Modelling Biogeochemical Cycles Across Scales: From Whole-Lake Phosphorus Dynamics to Microbial Reaction Systems

by

Igor Markelov

A thesis
presented to the University of Waterloo
in fulfillment of the
thesis requirement for the degree of
Doctor of Philosophy
in
Earth Sciences (Water)

Waterloo, Ontario, Canada, 2019

Examining Committee Membership

The following served on the Examining Committee for this thesis. The decision of the Examining Committee is by majority vote.

External Examiner:	Dr. Sergei Katsev Professor Large Lakes Observatory, Department of Physics University of Minnesota Duluth
Supervisor:	Dr. Philippe Van Cappellen Professor, Canada Excellence Research Chair Laureate Department of Earth and Environmental Sciences University of Waterloo
Committee member:	Dr. Nandita Basu Associate Professor Department of Earth and Environmental Sciences University of Waterloo
Committee member (adjunct):	Dr. George Arhonditsis Professor Department of Physical and Environmental Sciences University of Toronto
Internal external member:	Dr. Merrin Macrae Professor Department of Geography and Environmental Management University of Waterloo

Author's declaration

This thesis consists of material all of which I authored or co-authored: see Statement of Contributions included in the thesis. This is a true copy of the thesis, including any required final revisions, as accepted by my examiners.

I understand that my thesis may be made electronically available to the public.

Statement of contributions

This thesis consists of co-authored papers. As first author of each paper, I was primarily responsible of the study design and its execution. The following summarizes the contributions of the co-authors of each chapter.

Chapter 2

RMC and I designed the study. RMC, Sigrid Haande (SH), and Rachel Fisher designed and implemented sampling and sediment core extractions. I developed coupled lake-sediment model with input from RMC. RMC and I wrote the paper with input from PVC and SH.

Chapter 3

I designed the research questions and model with input from PVC, Ekaterina Markelova (EM), and RMC. EM and I wrote the chapter with input from RMC and PVC.

Chapter 4

I developed the research questions, collected and analyzed the data with input from Serghei A. Bocaniov (SAB), Homa Kheyrollah Pour (HKP), Raoul-Marie Couture (RMC), and Philippe Van Cappellen (PVC). I wrote the chapter with inputs from SAB, HKP, RMC, and PVC.

Chapter 5

I designed and developed the computer program. I wrote the chapter with the input from RMC and PVC.

Abstract

Lakes are ecologically, economically, and culturally significant resources that are, at the same time, very fragile and sensitive to human disturbances. During the last decades, intensified urbanization and discharge of nutrients lead to the increase of lake eutrophication in many regions of the world. Moreover, biogeochemical cycles within the lakes are changing due to climate warming, which increases water temperature and affects physical and hydrological lake regimes. In this thesis, I investigate a vast scope of the natural and anthropogenic processes affecting the biogeochemical cycles in lakes at different scales. In particular, I examine the cascading effect of the climate, regional weather, human interventions, and microbial control on phosphorus dynamics in lakes.

In Chapter 2, I demonstrate that on the lake scale, phosphorus cycle is driven by internal loading and iron recycling, while it is vulnerable to the reduction of ice cover. To achieve that, I expand the existing MyLake model by incorporating a sediment diagenesis module. Moreover, I develop the continuous reaction network that couples biogeochemical reactions taking place both in water column and sediment. In the modeling scenarios, I assess the importance of the sediment processes and the effects of the climatic and anthropogenic drivers on water quality in Lake Vansjø, Norway. I also highlight the importance of phosphorus accumulation within the lake that controls timing and magnitude of biogeochemical lake responses to external forcing. This includes projected changes in the air temperature, absence of ice cover, and potential management practices.

In Chapter 3, I contribute to the long-standing understanding that on the scales of microbial systems, the respiration reactions exert substantial control on biogeochemical cycles by regulating the availability of the electron donors and acceptors, secondary minerals, adsorption sites, and alkalinity. Moreover, I develop a new conceptual model to simulate the preferential catabolic reaction pathways based on power produced in reactions. In contrast to common kinetic rate expressions, I demonstrate that new thermodynamically based formulations can be applied to describe the microbial respiration of arbitrary large reaction networks. New approach substantially improves the robustness, transferability, and allows the generalization of the model-derived parameters.

In Chapter 4, I show that on the regional scale, weather defines hydrodynamic flush rates and water circulation patterns, which, in turn, control the phosphorus transport in Lake Erie, Canada. Specifically, precipitation controls the release of phosphorus from the watershed in the spring, while wind governs the water circulation and transport of the phosphorus released from sediment in the central basin during summer. I also illustrate that climate and weather in the upper Laurentian Great Lakes regulate changes in the water level of Lake Erie.

Overall, this thesis improves the fundamental understanding of the phosphorus cycle in lakes, which is being controlled by numerous biogeochemical and physical processes at various scales. In particular, I show that the climate has a cascading effect on the phosphorus cycle in lakes. First, climate controls regional precipitation, wind, and air temperature, which in turn control phosphorus supply from the watershed and basin-wide phosphorus transport. Second, being vulnerable to climate warming, the duration of ice cover impacts the phosphorus cycle through changes in light attenuation, water temperature, mixing regimes, and water column ventilation. Lastly, local environmental perturbations (*e.g.*, pH, temperature, or redox state) define thermodynamic properties of the sediment, which control microbial metabolism and, therefore, the internal phosphorus loading.

Finally, this thesis provides new open-source tools for reactive transport simulations in lakes as well as in saturated media. In addition to the coupled lake-sediment model developed in Chapter 3, I develop a computer program PorousMediaLab, which performs biogeochemical simulations in water-saturated media and described In Chapter 5. PorousMediaLab is the core component of the numerical investigations presented in the thesis. For example, PorousMediaLab is applied in Chapter 2 to design and test the initial reaction network, calculate fluxes at the sediment-water interface, and estimate reaction timescales. In Chapter 3, PorousMediaLab is used to simulate the reaction rates of batch and one-dimensional sediment column using a novel approach based on the thermodynamic switch function. In Chapter 4, PorousMediaLab is used to build a mass balance model and to improve the current understanding of the inter-basin exchange. Both tools

are open-source, and they are available online.

Acknowledgements

First, I would like to thank my supervisor Philippe Van Cappellen for giving me a chance to work in such a vibrant and innovative research group. I thank you for your guidance and limitless support in all adventures in many different countries that happened during all those years. You've been a true mentor and role model for me. Thank you!

I extend my sincerest gratitude to my co-supervisor, Raoul-Marie Couture, for his insightful comments, ideas, encouraging words, and immense knowledge of geochemistry. Thank you for all the time and efforts that you have generously invested in my career and personal growth. The completion of this thesis would not have been possible without your support.

In addition, I would like to thank my advisory committee members, Nandita Basu and George Arhonditsis, for committing your time and ensuring I stayed on track with my timeline. I also wish to thank Sergei Katsev and Merrin Macrae for agreeing to be a part of my examination committee.

To my friends and colleagues in the Ecohydrology research group. I am grateful to Adrian, Tatjana, Fereidoun, Homa, and Chris. I am especially grateful to my friends who made my stay in France, Germany, Canada, and Spain full of joy and support. Thank you my best friends Mark, Roma, Anzor, Mykhaylo, and Sergei. I am truly, truly blessed for being surrounded by such amazing people.

To my wife, who never ceases to amaze me. To my family, my Mom, my Dad, my brother, and my grandmother, for so much support in so many ways.

Lovingly dedicated to my wife

You are the light of my life

Table of Contents

List of Tables

List of Figures

Chapter 1

Introduction

1.1 Human Impact on Biogeochemical Cycles

Industrial revolution, mining and combustion of the planetary resources, disturbances of natural landscapes, and fast growth of the population dramatically change the environment. In the early 20th century, Russian biogeochemist Vernadskiy recognized that humans had become a "large scale geological force", and their impact could no longer be ignored. At present, human activity shapes biological, geochemical, aquatic, and climatic aspects of the environment.

One of such activities is the increase of one of the green-house gases in the atmosphere, namely carbon dioxide. In particular, 800,000-year-old ice cores extracted from Antarctic Dome C station indicate that carbon dioxide in the atmosphere has increased since the industrial revolution to the values never seen during the last millennium (Petit et al., 1999). Anthropogenic changes of the carbon cycle are responsible for this increase. More specifically, at the rate of about 0.2°C per decade, human-induced warming of the near-surface temperature reached 1°C above pre-industrial levels in 2017 (IPCC Report, 2018). Warming of the atmosphere resulted in regional weather instability and changes in hydrological cycles. Particularly, it resulted in heat waves, droughts, and desertification in the arid zones, and increase of storms with more frequent heavy downpours and floods in humid zones. As predicted by new generation climate models, further increase of carbon dioxide in the atmosphere with the "business as usual" will result in the air temperature rise from 2°C to 4°C by 2100 (IPCC Report, 2018).

The anthropogenic disturbances in the cycles of biogenic elements are also crucial. Phosphorus and nitrogen are essential elements required for plant growth and crop production and thus serve as a basis of the food chain. Therefore, modern phosphorus and nitrogen cycles are dominated by agricultural needs. Since World War II, fertilizer-based food production substantially altered global nitrogen and phosphorus cycles, increasing bioavailability and mobility over the large regions and even continents. Consequently, agricultural surplus application of the fertilizers increased the runoff of nitrogen and phosphorus to the land-ocean aquatic continuum by orders of magnitude (Filippelli, 2008, Mackenzie et al., 2002). Overall, the rise of the carbon dioxide in the atmosphere, increase of air temperature along with phosphorus and nitrogen load boost the biological productivity in the terrestrial and aquatic environments.

1.2 Impact on Lakes

Lakes are ecologically, economically, and culturally significant resources that play a vital role in providing habitat for birds, terrestrial and aquatic animals. However, many factors affect lakes and the temperature among the most influential. Recent studies have investigated the impact of climate warming on the water temperature of lakes (Livingstone, 2003, Parry, 2007, Sharma et al., 2015, Woolway et al., 2019). These studies and references therein provided evidences that water temperatures in the lakes rose rapidly, strengthened stratification, changed mixings rates, the metabolism and the life cycles of aquatic organisms. Long-term in-situ measurements in the Canadian Experimental Lakes Area also confirmed that water temperature is steadily increasing (Schindler et al., 1996, 1990). In high latitude regions, climate warming has the most profound effect on the lakes. Given the importance of freeze-thaw cycles and permafrost there, lakes experience significant changes in temperature, geomorphology, and hydrology (Quesada et al., 2006). In the comprehensive synthesis of in-situ and satellite-derived summer lake temperatures, O'Reilly et al. (2015) found that between 1985 and 2009, the water temperature rose 0.34°C per decade (global mean).

Given the impact on light, temperature, and mixing, ice characteristics demonstrate

the cascading effects on the flora, fauna, and water quality of the lakes (Bertilsson et al., 2013, Hampton et al., 2015, Lindenschmidt et al., 2018). In lakes with seasonal ice cover, the timing of ice cover is expected to define some of the most critical biotic and abiotic changes (Hampton et al., 2017). However, during the last century, the climate warming significantly reduced the period of ice cover in lakes. For example, in the Northern Hemisphere during the period from 1846 to 1995, the formation and break-up of ice occurred 0.57 days later and 0.63 days earlier per decade, respectively (Magnuson, 2000). The estimated projection for those lakes indicates that the overall rate of decrease of ice duration accelerates whereas the duration of ice cover is expected to be shorter by about 15–50 days in 2050 (Dibike et al., 2011). Lack of the complete understanding of the effect of ice cover on aquatic ecosystems highlights an urgent need for research focused on ecosystem changes in the seasonally ice-covered lakes (Hampton et al., 2017). It still remains unclear how disappearing ice affects biotic and abiotic systems, what ecological processes are at stake, as well as what are the potential feedbacks associated with these changes.

In addition to increasing surface water temperatures and shortening ice periods, climate warming is expected to change recurring global teleconnections and therefore precipitation patterns in watersheds of lakes (Abtew and Trimble, 2010). For example, El Nino – Southern Oscillation (ENSO) is responsible for the intensity of the precipitation across Canada and USA (Shabbar et al., 1996). Therefore, it is expected that ENSO has a major effect on hydrology and biology of lakes in North America. As such, cyclic variations in the rainfalls and increased droughts may stimulate the increase of harmful algae growth driven by weak dilution and therefore greater availability of the nutrients (Schaus et al., 2003). Moreover, modulated by global circulation patterns, water residence times define the retention of nutrients in lakes (Vollenweider, 1976). However, climate-related atmospheric circulation variability and its effect on the hydrology and biology of lakes has received little attention in the literature to date.

1.3 Lakes and Phosphorus Cycling

Lakes are crucial reservoirs in the regulation and maintenance of global biogeochemical cycles of carbon, nitrogen, and phosphorus. Synergistic effects of warming lake water, disappearing ice and increasing nutrient loads enhance the reproduction of algae and potentially could lead to anoxic conditions, fish stock changes, loss of biodiversity, and decrease of zooplankton which, in turn, intensify algal blooms (Conley et al., 2009, Havens and Paerl, 2015, Jeppesen et al., 2014, Paerl and Huisman, 2008, Sondergaard et al., 2003). In most lakes, phosphorus is the limiting nutrient for biological productivity (Correll, 1999, Dillon and Rigler, 1974). In turn, phosphorus behavior in the lakes is very dynamic, as it is extensively involved in biological cycles. Once it reaches the lake water, it is retained efficiently via uptake and incorporation by plants and subsequently deposited to the sediment in the organic form.

In the lakes, sediment accumulate allochthonous and autochthonous organic matter and solid inorganic particles that settle from the water column. Depending on geomorphology of the lake and wind exposure, the sediment could be resuspended back into water column, and therefore the sedimentation rates differ spatially and temporally (Håkanson, 1986). In nutrient rich lakes, the accumulation of the sediment typically happens in the deep parts with the rate of several millimeters per year (Sondergaard, 2007).

Sediments play an important role in the phosphorus cycle of the lakes and can be both sink and source of phosphorus. Phosphorus accumulated in the sediment can occur in dissolved and solid forms, as well as in a number of organic and inorganic species (Tables 1.1, 1.2). However, most of the phosphorus in the sediment is stored in the solid phase. Phosphorus mobilization from sediment into water column, termed "internal phosphorus loading", plays an important role in phosphorus availability (Boström et al., 1988). Various mechanisms, such as oscillating redox conditions, mineralization, microbial processes, and temperature control the release of phosphorus from the sediment (Boström et al., 1988, Gudasz et al., 2010, Jöhnk et al., 2008, Penn et al., 2000).

Redox conditions play an important role on phosphorus retention in the sediment.

Table 1.1: Reactions describing the transformation of organic phosphorus in water columns and sediments of lakes. R0a and R0b– algal growth dynamics; R1-R6 – typical redox sequence of organic matter degradation; x, y, z – define the C:N:P elemental composition of the organic matter produced or degraded in reactions R0-R6.

no.	**Reaction**
	Algae growth
R0a	$(x - y + 2\,z)CO_2 + (y - 2z)HCO_3^- + yNH_4^+ + zHPO_4^{2-} + (x - y + 2\,z)H_2O \longrightarrow (CH_2O)_x(NH_3)_y(H_3PO_4)_z + xO_2$
R0b	$(x + y + 2\,z)CO_2 + yNO_3^- + zHPO_4^{2-} + (x + 2\,y + 2\,z)H_2O \longrightarrow (CH_2O)_x(NH_3)_y(H_3PO_4)_z + (y + 2z)HCO_3^- + (x + 2\,y + 2\,z)O_2$
	Organic matter degradation
R1	$(CH_2O)_x(NH_3)_y(H_3PO_4)_z + xO_2 \longrightarrow (x - y + 2\,z)CO_2 + (y - 2z)HCO_3^- + + yNH_4^+ + zHPO_4^{2-} + (x - y + 2\,z)H_2O$
R2	$(CH_2O)_x(NH_3)_y(H_3PO_4)_z + 0.5xNO_3^- + (y - 2\,z)CO_2 + (0.5x + y - 2\,z)H_2O \longrightarrow 0.5xN_2(g) + (x + y - 2z)HCO_3^- + yNH_4^+ + zHPO_4^{2-}$
R3	$(CH_2O)_x(NH_3)_y(H_3PO_4)_z + 4xFe(OH)_3 + (7x + y - 2z)CO_2 \longrightarrow 4xFe^{2+} + (8\,x + y - 2\,z)HCO_3^- + yNH_4^+ + zHPO_4^{2-} + (3\,x - y + 2\,z)H_2O$
R4	$(CH_2O)_x(NH_3)_y(H_3PO_4)_z + 4xFeOOH + (7x + y - 2z)CO_2 + (x + y - 2\,z)H_2O \longrightarrow 4xFe^{2+} + (8\,x + y - 2\,z)HCO_3^- + yNH_4^+ + zHPO_4^{2-}$
R5	$(CH_2O)_x(NH_3)_y(H_3PO_4)_z + 0.5xSO_4^{2-} \longrightarrow 0.5xHS^- + (0.5\,x - y + 2z)CO_2 + + (0.5\,x + y - 2\,z)HCO_3^- + yNH_4^+ + zHPO_4^{2-} + (0.5\,x - y + 2z)H_2O$
R6	$(CH_2O)_x(NH_3)_y(H_3PO_4)_z + (y - 2z)H_2O \longrightarrow 0.5xCH_4(aq) + (0.5\,x - y + 2\,z)CO_2 + (y - 2\,z)HCO_3^- + yNH_4^+ + zHPO_4^{2-}$

Table 1.2: Reactions that have direct and indirect effects on the phosphorus cycle in lakes. R11-R16 — secondary redox reactions, R21-R28 — mineral precipitation–dissolution reactions, R31-R36 — phosphorus sorption and precipitation reactions, and R41-R45 — equilibrium reactions.

no.	**Reaction**
Secondary redox reactions	
R11	$HS^- + 2\,O_2 \longrightarrow H^+ + {SO_4}^{2-}$
R12	$HS^- + 2\,Fe(OH)_3 + 5\,H^+ \longrightarrow 2\,Fe^{2+} + S(0) + 6\,H_2O$
R13	$Fe^{2+} + \frac{1}{4}\,O_2 + 2\,{HCO_3}^- + \frac{1}{2}H_2O \longrightarrow Fe(OH)_3 + 2\,CO_2$
R14	$2\,O_2 + {NH_4}^+ + 2\,{HCO_3}^- \longrightarrow {NO_3}^- + 2\,CO_2 + 3\,H_2O$
R15	$CH_4 + O_2 \longrightarrow CO_2 + H_2O$
R16	$CH_4 + {SO_4}^{2-} + CO_2 \longrightarrow H_2S + 2\,{HCO_3}^-$
Mineral precipitation—dissolution reactions	
R21	$S(0) \longleftrightarrow S_8$
R22	$FeS_2 + 5\,O_2 + H^+ \longrightarrow FeOOH + 2\,{SO_4}^{2-}$
R23	$FeS + S(0) \longrightarrow FeS_2$
R24	$4\,FeS + 3\,O_2 + 2\,H_2O \longrightarrow 4\,S_8 + FeOOH$
R25	$FeS + HS^- + H^+ \longrightarrow FeS_2 + H_2$
R26	$Fe^{2+} + HS^- \longleftrightarrow FeS + H^+$
R27	$Ca^{2+} + {CO_3}^{2-} \longleftrightarrow CaCO_3$
R28	$Fe^{2+} + {CO_3}^{2-} \longleftrightarrow FeCO_3$
Phosphorus sorption and precipitation reactions	
R31	${HPO_4}^{2-} + Fe(OH)_3 \longleftrightarrow PO_4{\equiv}Fe(OH)_3 + H^+$
R32	${HPO_4}^{2-} + FeOOH \longleftrightarrow PO_4{\equiv}FeOOH + H^+$
R33	${HPO_4}^{2-} + Al(OH)_3 \longleftrightarrow PO_4{\equiv}Al(OH)_3 + H+$
R34	${HPO_4}^{2-} + CaCO_3 \longleftrightarrow PO_4{\equiv}CaCO_3 + H+$
R35	$3\,Fe^{2+} + 2\,{HPO_4}^{2-} \longleftrightarrow Fe_3(PO_4)_2 + 2\,H^+$
R36	$3\,Ca^{2+} + 2\,{HPO_4}^{2-} \longleftrightarrow Ca_3(PO_4)_2 + 2\,H^+$
Equilibrium reactions	
R41	$CO_2(aq) + H_2O{=}H_2CO_3{=}{HCO_3}^- + H^+{=}{CO_3}^{2-} + 2\,H^+$
R42	$H_3PO_4{=}{H_2PO_4}^- + H^+{=}{HPO_4}^{2-} + 2\,H^+{=}{PO_4}^{3-} + 3\,H^+$
R43	$H_2S{=}HS^- + H^+$
R44	${NH_4}^+{=}NH_3 + H^+$
R45	$H_2O{=}H^+ + OH^-$

For example, the concentration of iron has a strong influence on the mobilization and deposition of phosphorus to the sediment (Katsev and Dittrich, 2013, Orihel et al., 2016). The availability of iron-bearing minerals in the water column of a lake may result in the adsorption of phosphorus (R31, R32 in Table 1.2) and subsequent sedimentation in an inorganic form. Moreover, due to the redox control of phosphorus sorption on iron minerals, iron-bound phosphorus is a dynamic component of the sediment pool. That is, oxidized micro-layer at the sediment-water interface inhibits the release of sediment phosphorus due to the high affinity between particulate iron minerals Fe(III) and dissolved inorganic phosphorus (Penn et al., 2000). That is, under oxic and nitrate-rich conditions, the iron reduction is inhibited and iron remains in the oxidized form (McAuliffe et al., 1998). In contrast, under the reducing conditions, the reduction of iron minerals (R3, R4 in Table 1.1) generates dissolved Fe(II) and releases surface-bound phosphorus (R31, R32; Boström et al., 1988). As a result, elevated phosphorus concentrations may enhance internal phosphorus loading.

The release of phosphorus from the sediment also depends on the pH and alkalinity. With the increase of pH, surface-bound phosphorus may potentially be released from the surfaces of the oxidized minerals (R31, R32, R33, R34). For example, high microbial primary production (R0a and R0b) may increase pH and promote release of surface-bound phosphorus into water column from iron (R31, R32) and aluminum oxides (R33; Boström et al., 1988; Koski-Vähälä and Hartikainen, 2001). In contrast, in calcareous lakes with high pH conditions, the decrease of pH may potentially promote the dissolution of phosphorus bearing minerals, such as apatite and vivianite (R35, R36). Also, the dissolution of calcite increases at lower pH, which may release previously adsorbed phosphorus (R34; Otsuki and Wetzel, 2003).

Other factor that play a crucial role on the phosphorus mobilization is temperature. Temperature has a strong effect on thermodynamics of mineral formation, rates of abiotic reactions, and, most importantly, on the biological processes such as photosynthesis (Huisman et al., 2005, Jöhnk et al., 2008) and organic matter mineralization (Gudasz et al., 2010). Microbial processes in the sediments have a direct influence on phosphorus

mobilization through the degradation of organic matter with various electron acceptors (R1-R6), the rates of which are exponentially increasing with temperature. That is, the increase of water temperature during spring season promotes organic matter degradation in sediment and leads to the release of phosphate into water column.

Overall, the warming climate has the cascading effect on physical, hydrological and biogeochemical dynamics of lakes. It is expected that in response to warming climate the biological productivity of lakes will increase and lake water quality will worsen (Mantzouki et al., 2018). However, what consequences the warming climate cause on phosphorus cycle in lakes still remain poorly understood.

1.4 Lake and Sediment Models

Management needs and scientific interest in the understanding of fundamental processes in aquatic environments have driven development of the large number and wide variety of the lake models (Table 1.3, Mooij et al., 2010; Jørgensen, 2008; Jørgensen, 2010). Historically, eutrophication of lakes has sparked the development of first input-output models (Vollenweider, 1976). Later, depending on the relative importance of the specific process in lakes of interest, several directions of model development were initiated. These initiatives differ widely and can be broadly divided into three groups: hydrodynamic, functional, and water quality-focused models. The hydrodynamic models prevail in the studies focused on the spatial interactions such as lake thermal structure, circulation patterns, effects of transport on the biogeochemical cycles (Hodges, 2009). In the development of hydrodynamic models, special treatment is given to the accuracy of the transport processes and underlying model issues of dimensionality, boundary conditions, grid selection, time and space resolution (Hodges, 2009). Examples of such models include ELCOM, FVCOM, and MIKE 21 SW (Table 1.3). In contrast, functional aspects are of interest in the studies on flora and fauna including fish (Sondergaard et al., 2008), zooplankton (Hülsmann et al., 2005), phytoplankton (Huisman and Weissing, 1999), and aquatic plants such as macrophytes (Van Nes et al., 2003). Therefore, the functional models are focused on the accurate representation of the food webs and biological inter-

actions within lakes with the experiences gained mainly from the biomanipulation studies (Benndorf, 1995, Gulati et al., 1990, Sondergaard et al., 2008). Examples of such models include Charisma, SALMO, and RateCon (Table 1.3). Lastly, the models with water quality focus are of interest in studies of the transformation of chemical elements in the biogeochemical cycles of lakes (e.g., cycles of phosphorus, nitrogen, or carbon). Due to biogeochemical cycles controlled by both hydrodynamics and biology, the models of this group are the synergy of hydrodynamic and functional model groups and therefore the complexity of such models varies greatly. Examples of such models include Lake Shira Model, CE-QUAL-W2, ELCOM-CAEDYM, Delft 3D-ECO, and IPH-TRIM3D-PCLAKE (Table 1.3).

In lakes, a substantial part of the metabolism occurs in sediments (del Giorgio and Williams, 2005). The respiration of organic matter in sediment recycles phosphorus back to the inorganic form to support primary production. Respiration and primary production define the overall net balance of phosphorus in a lake. Due to the external input of allochthonous organic matter, the overall rate of respiration often exceeds the primary production, and sediment serves as the source of the phosphorus supply. Moreover, enhanced respiration in the sediment of eutrophic lakes often leads to oxygen depletion and anoxia. Depending on the geomorphology of a lake, biogeochemical processes in sediments could have a significant impact on water quality and biogeochemical cycles (Paraska et al., 2014, Sondergaard, 2007).

Initial development of the early diagenesis models started with the pioneering work on the analytical transport-reaction models by Berner (1980). Later, with the advance of the computational power, the numerical reactive-transport models of early diagenesis were further developed by Boudreau (1996), Soetaert et al. (1996), Van Cappellen and Wang (1996), Katsev et al. (2006), and Couture et al. (2010). In the extensive review, Paraska et al. (2014) described processes implemented in dozens of previously developed early diagenesis models. The authors concluded that the differences in the approach and complexity are minimal despite the diversity of the investigated environments (Paraska et al., 2014). Commonly, the transport part of the model accounts for molecular diffusion,

Table 1.3: Overview of the selected lake models and their components. Columns: Dim – dimensionality (H – horizontal, V – vertical), Str – stratification, H – hydrodynamics, T – temperature, L – light attenuation, Ice – ice and snow cover, Sed – sediment fluxes and dynamics, D – diagenesis, Lit – littoral zone. State variables: B – bacterial dynamics, Phy – phytoplankton dynamics, Zoo – zooplankton, F – fish , O – oxygen, P – phosphorus, N – nitrogen, Si – silica, OC – organic carbon, IC – inorganic carbon. In column "sed" ± stands for sediment oxygen demand constant flux, in column "D" ± stands for multi-layer box model. References: Vollenweider – Vollenweider (1976); BHM – Obenour et al. (2014); Piscator – Van Nes et al. (2002); ANN – Lam et al. (1987); RateCon – Rucinski et al. (2014); MyLake – Saloranta and Andersen (2007); Lake Shira Model – Prokopkin et al. (2010); PROTECH – Reynolds et al. (2001); SALMO – Recknagel et al. (2008); PCLake+ – Janssen et al. (2019); CLM – Schwab et al. (2009); GLIM (CIOM) – Wang et al. (2010); Charisma – Van Nes et al. (2003); CE-QUAL-W2 – Cole and Wells (2006); ICEPOM – Mellor et al. (2002); ELCOM+CAEDYM – Romero et al. (2004); FVCOM + ICM – Chen et al. (2006); DELFT3D-ECO – Los et al. (2008); MITgcm – Forget et al. (2015); GETM – Bruggeman and Bolding (2014); IPH-TRIM3D-PCLAKE – Fragoso Jr. et al. (2009); MIKE 21 SW – Moeini and Etemad-Shahidi (2007).

Model	**Dim**	**Str**	**H**	**T**	**L**	**Ice**	**Sed**	**D**	**Lit**	**B**	**Phy**	**Zoo**	**F**	**O**	**P**	**N**	**Si**	**OC**	**IC**
Vollenweider	0	-	-	-	-	-	+	-	-	-	+	-	-	-	+	+	-	-	-
BHM	0	-	-	-	-	-	-	-	-	-	+	-	-	-	-	-	-	-	-
Piscator	0	-	-	+	-	-	-	-	-	-	+	+	+	-	-	-	-	-	-
ANN	0+	-	-	-	-	-	±	-	-	-	+	-	-	+	+	-	-	-	-
RateCon	1V	+	+	+	-	-	±	-	-	-	+	+	-	+	+	-	-	+	-
MyLake	1V	+	+	+	+	+	+	-	-	-	+	-	-	+	+	-	-	+	+
Lake Shira Model	1V	+	+	+	+	-	-	-	-	+	+	+	-	+	+	+	-	+	-
PROTECH	1V	-	+	+	-	-	+	-	-	-	+	+	-	-	+	+	-	-	-
SALMO	1V	+	+	+	+	+	+	-	-	-	+	+	-	+	+	+	-	+	-
PCLake+	1V+	-	+	+	+	-	+	-	+	+	+	+	+	+	+	+	+	+	-
CLM	2H	+	+	+	-	-	-	-	-	-	-	-	-	-	+	-	-	-	-
GLIM (CIOM)	2H	-	-	+	+	+	-	-	-	-	-	-	-	-	-	-	-	-	-
Charisma	2H	-	-	+	-	-	+	-	-	-	-	-	+	-	-	-	-	-	-
CE-QUAL-W2	2HV	+	+	+	+	-	-	-	-	-	+	+	-	+	+	+	+	+	+
ICEPOM	3	+	+	+	+	+	-	-	-	-	-	-	-	-	-	-	-	-	-
ELCOM + CAEDYM	3	+	+	+	+	+	±	-	+	-	+	+	-	+	+	+	+	-	-
FVCOM + ICM	3	+	+	+	+	-	±	-	+	-	+	+	-	+	+	+	+	+	+
DELFT3D-ECO	3	+	+	+	+	+	+	±	+	+	+	+	-	+	+	+	+	+	+
MITgcm	3	+	+	+	+	-	-	-	-	-	-	-	-	-	-	-	-	-	-
GETM	3	+	+	+	+	-	-	-	-	-	-	-	-	-	-	-	-	-	-
IPH-TRIM3D-PCLAKE	3	+	+	+	+	-	±	-	-	+	+	+	+	+	+	+	+	+	-
MIKE 21 SW	3	-	+	-	-	-	-	-	-	-	-	-	-	-	-	-	-	-	-

bioturbation, irrigation, and burial. The reaction part of the models describes the oxygen consumption pathways and the cycling of carbon, nitrogen, phosphorus, manganese, iron, and sulfur. Phosphorus transformation in the sediment is described by organic matter degradation, adsorption on mineral surfaces, formation of phosphorus-bearing minerals, and acid-base speciation (R1-R6, R31-R36, and R42 in Tables 1.1 and 1.2). However, out of 83 reviewed models published since 1996, only five models examine phosphorus cycle as their primary focus of the study (Dale et al., 2013, Katsev and Dittrich, 2013, Katsev et al., 2006, McCulloch et al., 2013, Tromp et al., 1995).

The microbial respiration of organic phosphorus in the sediment determines if it will be converted into inorganic phosphorus or get buried. Thus, the microbial respiration defines the phosphorus cycle, controls oxygen levels and ecological conditions of lakes. The typical sequence of electron acceptors' consumption during organic matter degradation is shown in Table 1.1 (R1 to R6). This sequence of electron acceptor consumption runs from oxygen reduction through nitrate to iron and sulfate reductions to methanogenesis. Commonly, mathematical models of organic matter degradation are based on mass conservation principle where the redox sequences are described by Monod type equations with number of kinetic parameters and inhibition terms:

$$R = r_{max} \cdot X \cdot \frac{[ED]}{K_m^{ED} + [ED]} \cdot \frac{[EA]}{K_m^{EA} + [EA]} \cdot F_T \cdot \prod \frac{K_{in}}{K_{in} + [EA]} \tag{1.1}$$

where R – is the rate of the specific redox reaction, r_{max} – is the maximum rate per unit of biomass, X – is the biomass concentration, $\overline{r}_{max}$ – is the maximum rate constant per unit of biomass, $[ED]$ – is the concentration of electron donor, $[EA]$ – is the concentration of electron acceptor, K_m^{ED} and K_m^{EA} – are the limiting half-saturation constants of electron donor and electron acceptor, respectively, F_T – is the dimensionless thermodynamic factor of LaRowe et al. (2012) or Bethke et al. (2008), K_{in}^{EA} – are the inhibition constants for higher energy-yielding electron acceptors.

In this approach, the biogeochemical sequence of redox reactions (e.g., R1-R6 in Table 1.1) is represented by manually picked inhibition terms to prioritize one reaction

over another. However, multiplicative inhibition terms in eq. 1.1 do not take into account the dynamic nature of aquatic systems, such as changes in pH, temperature, ionic strength and redox state. These changes affect the thermodynamic driving force of energy-yielding reactions with the potential of shuffling the favorability of the specific elements and, thus, redox sequences. Therefore, the calibrated inhibition constants used to define the sequence of the redox reactions are usually site-specific and may lack general validity.

In summary, mechanistic lake models are useful tools for guiding and assessing long-term management strategies. The crucial requirement of such models is the ability to accurately represent biogeochemical cycles and their response to the external forcing. To achieve accurate representation of biogeochemical cycles, the dynamic model of the water column should be coupled with the dynamic vertically resolved biogeochemical model of the sediment (Soetaert et al., 2000). Although the diagenetic models reached their maturity, representation of sediment-water interactions is not a standard feature of lake models and is often greatly simplified (columns "Sed" and "D" in Table 1.3, Soetaert et al., 2000; Mooij et al., 2010; Jørgensen, 2008; Jørgensen, 2010).

1.5 Restoration of the Lakes

Eutrophication of the lakes is recognized world-wide problem which has implications on water quality and ecosystem services. The majority of restoration measures and practices focus on reducing external phosphorus loads to improve water quality in lakes. Unfortunately, external load reduction rarely led to the desired improvement of water quality (Jeppesen et al., 1991, Lürling et al., 2016, Sondergaard, 2007). Therefore, alternative chemical restoration practices have been applied. Some of them rely on the addition of reactive materials to the water column to sequester phosphorus in the sediments and reduce internal loading (Mackay et al., 2014). Because of the strong coupling of the early diagenetic cycling of phosphorus and iron (Doolittle et al., 2018, Molot et al., 2014, Verschoor et al., 2017), materials that have been used include salts of ferric iron (Engstrom, 2005, Orihel et al., 2016, Wilfert et al., 2015), but also aluminum (Huser et al., 2016, Schutz et al., 2017) and calcium phases (Gulati et al., 2012), as well as lanthanum

clays (Dithmer et al., 2015).

The comprehensive modelling studies of the restoration practices in lakes are barely (if at all) present. The complexity of the sediment water interactions complicates the building of the reliable models that can simulate the response of the water quality after the addition of reactive material. As a result, substantial uncertainties remains in terms of the scientific understanding of the restoration practices and their integration with other management measures. Therefore, often the most effective course of action for the particular lake remains unclear (Lürling et al., 2016).

1.6 Structure of the Thesis

The specific aims of this thesis are as follows:

1. Couple water column and sediment models in order to elucidate the specific physical, chemical and/or biological processes that govern phosphorus cycle in lakes;
2. Quantify and assess the effect of the climate warming and potential restoration measures on the phosphorus cycle and algal blooms in lakes;
3. Identify shortcomings and improve existing models of microbial reaction systems present in lakes;

The research portion of the thesis is organized into four chapters. In Chapter 2, I address my research question by expanding the existing one-dimensional MyLake model by introducing a vertically resolved sediment diagenesis module and integrate the continuous reaction network that couple the water column and sediment biogeochemistry. I use the coupled model to simulate the potential impacts of climate warming, shortening periods of ice cover, and restoration measures on the phosphorus cycle in Lake Vansjø, Norway. During the development and testing of the coupled model, I identify the shortcomings present in the models of microbial reaction systems.

Building on findings of Chapter 2, I suggest a new model that represents microbial respiration in aquatic environments (Chapter 3). I stress that commonly used inhibition

terms present in the reactions network of lake and sediment models are incapable of dealing with dynamically changing conditions. Therefore, I replace the inhibition terms with the thermodynamic switch function. I show that the model can simulate arbitrary large reaction networks, and it accounts for dynamic changes in the environmental conditions. Also, I show the example of how the new model can be applied to simulate early diagenetic processes in sediment.

In the study of Chapter 4, I show that on the regional scale, weather defines hydrodynamic flush rates and water circulation patterns, which, in turn, control the phosphorus transport in Lake Erie, Canada. Specifically, precipitation controls the release of phosphorus from the watershed in the spring, while wind governs the water circulation and transport of the phosphorus released from sediment in the central basin during summer. I also show that during the last century, the ratio of land runoff to precipitation in Lake Erie is increasing due to deforestation and urbanization of the watershed.

Finally, in Chapter 5, I develop PorousMediaLab, a tool for designing, developing, and quantifying the mechanisms of reactive transport within the aquatic environments. PorousMediaLab is the core component of the numerical investigations presented in the thesis. In Chapter 4, PorousMediaLab is used to build a mass balance model and to improve the current understanding of the inter-basin exchange. In Chapter 2, PorousMediaLab is applied to design and test the reaction network, estimate fluxes at the sediment-water interface, and reaction timescales. Lastly, PorousMediaLab is used in Chapter 3 to simulate the reaction rates using a novel approach based on the thermodynamic switch function.

Chapter 6 summarizes the major conclusions to the four Research Questions and elaborates on the research directions that should be pursued following the work in this thesis. In particular, I discuss the need for an improvement of the reactive modelling in lakes, simulation of alternative lake restoration measures, and modelling of the greenhouse gas fluxes from large and small lakes.

Chapter 2

Coupling Water Column and Sediment Biogeochemical Dynamics: Modelling Internal Phosphorus Loading, Climate Change Responses and Mitigation Measures in Lake Vansjø, Norway

Igor Markelov
Raoul-Marie Couture
Rachel Fisher
Sigrid Haande
Philippe Van Cappellen

Summary

We expanded the existing one-dimensional MyLake model by incorporating a vertically resolved sediment diagenesis module and developing a reaction network that seamlessly couples the water column and sediment biogeochemistry. The application of the MyLake-Sediment model to boreal Lake Vansjø illustrates the model's ability to reproduce daily water quality variables and predict sediment-water column exchange fluxes over a 20-year historical period. In prognostic scenarios, we assessed the importance of sediment processes and the effects of various climatic and anthropogenic drivers on the lake's biogeochemistry and phytoplankton dynamics. First, MyLake-Sediment was used to simulate the potential impacts of increasing air temperature on algal growth and water quality. Second, the key role of ice cover in controlling water column mixing and biogeochemical cycles was analyzed in a series of scenarios that included a fully ice-free end-member. Third, in another end-member scenario P loading from the watershed to the lake was abruptly halted. The model results suggest that remobilization of legacy P stored in the bottom sediments could sustain the lake's primary productivity on a time scale of several centuries. Finally, while the majority of management practices to reduce excessive algal growth in lakes focus on reducing external P loads, other efforts rely on the addition of reactive materials that sequester P in the sediment. Therefore, we investigated the effectiveness of ferric iron additions in decreasing the dissolved phosphate efflux from the sediment and, consequently, limit phytoplankton growth in Lake Vansjø.

2.1 Introduction

Lakes play a crucial role in water supply, food production, recreation, and climate regulation (Franz et al., 2018, Mueller et al., 2016, Tranvik et al., 2009). During the last century, changing climate, intensified agriculture and urbanization have been exerting increasing pressures on lake ecosystem functioning and services (Adrian et al., 2009, Carvalho et al., 2013, Shimoda et al., 2011). Rising air temperatures and nutrient loadings have direct effects on lake physical and ecological properties (Ludsin et al., 2001, Schmid

et al., 2014, Stefan et al., 2001, Winder and Sommer, 2012, Woolway and Merchant, 2019). Air and water temperatures are the key controlling factors of lake thermal regimes (Dibike et al., 2011, Livingstone, 2008), ice characteristics (Couture et al., 2015, Magnuson et al., 2000), and ecosystem metabolism (Winder and Sommer, 2012, Yvon-Durocher et al., 2012). Along with the meteorological drivers, increased P loading degrades lake water quality by intensifying primary production, potentially resulting in nuisance algal blooms and deoxygenation of bottom waters (Carvalho et al., 2013, Smith et al., 1999). A fraction of particulate inorganic and organic P, either externally derived (allochthonous) or produced in the lake (autochthonous), ultimately settles at the sediment-water interface (SWI), where a host of early diagenetic processes cycles P, leading either to the return of dissolved P to the hypolimnion or to permanent burial in the sediments. The fate of deposited P is highly variable as it depends on many different physical, biological and geochemical properties and processes of the sedimentary reservoir (Dittrich et al., 2009, Katsev and Dittrich, 2013, Xiong et al., 2019).

After decades of sustained external P inputs, lakes have been shown to accumulate legacy P and experience mobilization of P from the sediment (*i.e., internal loading*), a phenomenon extensively reviewed in the literature (*e.g.*, Orihel et al. (2017)). Internal P load is a significant concern for stakeholders due to continued water quality deterioration, with associated social and economic costs, and despite measures put in place to reduce external P loads (Matisoff et al., 2016, Mueller et al., 2016). Therefore, a predictive understanding of nutrient cycles within lake systems, and internal P loads in particular, is a primary research focus for maintaining and restoring healthy lake ecosystems.

Process-oriented lake modelling is a useful tool for guiding and assessing long-term management strategies and governance models. The crucial requirement of such modelling is the ability to accurately represent biogeochemical cycles in lakes and their response to the external drivers. Such models often rely on the assumption of lateral homogeneity, suitable in a vertically stratified environment, and are thus underpinned by 1D hydrodynamic simulations coupled with ecological and biogeochemical modules of appropriate complexity (Janssen et al., 2015). However, representation of sediment-water interactions

is not a standard feature of lake models and is often greatly simplified (Mooij et al., 2010, Soetaert et al., 2000).

Lacustrine sediments are a hotspot of enhanced biological activity. Multiple studies stress the vital importance of early diagenetic processes in controlling internal P loading in a variety of lake systems (Amirbahman et al., 2012, James, 2017, Loh, 2013, Nurnberg et al., 2013). While early diagenetic models can capture the drivers and timing of P release from sediment (Katsev, 2017, Katsev and Dittrich, 2013, Katsev et al., 2006, Li et al., 2018, McCulloch et al., 2013), these detailed models are not routinely coupled to lake water column models (Janssen et al., 2015, Paraska et al., 2014, Robson, 2014). Computational expense, complexity and, possibly, the underestimated importance of early diagenetic processes have led model designers to simplify interactions between the sediment and the overlying water. Numerous empirical lake models have been developed for internal P loading (*e.g.*, Schauser et al. (2006), Bryhn and Haakanson (2007)), but their generalization is unlikely as their applicability tends to be site-specific. Popular approaches to couple sediment processes to lake water column models have included the incorporation of an empirical bottom flux boundary (Schmid et al., 2017), and vertically integrated sub-modules (*e.g.*, oxic and anoxic layers) (Janssen et al., 2015, Matzinger et al., 2010, Mooij et al., 2010, Schmid et al., 2017). Several well-established lake models, such as FABM-PCLake (Hu et al., 2016), DYRESM-CAEDYM (Trolle et al., 2008), CE-QUAL-W2 (Zhang et al., 2015), GLM (Hipsey et al., 2017), and DELWAQ (Smits and van Beek, 2013) were built on variations of those approaches in order to represent sediment-water interactions.

Here, we build upon two existing Matlab-based models: MyLake focuses on the reactions of P (Saloranta and Andersen, 2007), oxygen (O) (Couture et al., 2015), and carbon (C) (de Wit et al., 2018, Kiuru et al., 2018), while Matsedlab focuses on the reactions of O, C, iron (Fe) (Couture et al., 2010), sulphur (S) (Couture et al., 2016) and nitrogen (N) (Akbarzadeh et al., 2018). In order to couple the two individual models into the 1.5-dimensional Lake-Sediment model, we integrated their reactions networks. The goal is to deliver an open-access tool for the combined modelling of water column

and sediment that uses a consistent biogeochemical reaction network. Consequently, we updated Matsetlab with reactions of Al, Ca and P and MyLake with reactions of N, Fe, S, Al and Ca (Ahlgren et al., 2011, Canavan et al., 2006, Couture et al., 2010, Dijkstra et al., 2018, Dittrich et al., 2009, Doan et al., 2018, Gudimov et al., 2016, Katsev and Dittrich, 2013, Katsev et al., 2006, Li et al., 2018, Parsons et al., 2017, Testa et al., 2013, Van Cappellen and Wang, 1996).

We evaluate the coupled Lake-Sediment model against both time-series and vertical water column, solid-phase sediment and sediment pore water profiles of eutrophied Lake Vansjø in Norway. We simulate the responses to: (1) variable climate (air temperature); (2) absence of ice cover; and (3) external P load cut-off. We further showcase the use of the model to assess a management practice aimed at reducing internal P loads via the addition of reactive iron to the water column.

2.2 Model Development, Study Site and Methods

2.2.1 Model Formulation

MyLake is a one-dimensional, process-based model that simulates daily vertical distributions of lake water temperature, density stratification and mixing, and accounts for seasonal lake ice and snow cover. It further represents simplified phosphorus-phytoplankton dynamics where growth is limited by temperature, light and nutrient availability (Saloranta and Andersen, 2007). In the current study, the existing physical hydrodynamic, ice and snow cover modules of MyLake were used, and the phosphorus-phytoplankton module was reformulated for direct coupling to the reaction network in the sediment. Biogeochemical reactions involving oxygen (Couture et al., 2015) and carbon (de Wit et al., 2018, Kiuru et al., 2018), as well as reactions of iron (Fe), manganese (Mn), aluminum (Al), calcium (Ca) and sulfur (S) were similarly coupled between sediment and water column (Figure 2.1, Table 2.1 and 2.2).

The sediment module is a modified and adapted version of Matsetlab (Couture et al., 2016) rewritten specifically for coupling to the water column module. The math-

Table 2.1: Algal dynamics and organic matter (OM) degradation reactions (primary reactions) included in the MyLake-Sediment model. x, y, z – define the C:N:P elemental composition of the organic matter produced or degraded in reactions R0-R6, $\mu(20)$ – is the specific growth rate of algae at $20°C$, Q_{10} – the Q_{10} temperature coefficient, $[A]$ – is the concentration of algae, λ – is the fractional day length, ϵ_i – is the attenuation coefficient for layer i, Δz_i – is the thickness of the layer i, H – is the light limitation function (Saloranta and Andersen, 2007), I'_{zi} – is the photosynthetically active irradiance at noon at the depth level z_i, I' – is the light saturation level of photosynthesis, $N^\star$ stands for NH_4^+ in the rate equation of reaction R0a and for NO_3^- in R0b, N' – is the limiting concentration of nitrogen for algal growth (NH_4^+ in the rate equation of reaction R0a and NO_3^- in that of R0b), P' – is the limiting concentration of HPO_4^{2-}, $m(20)$ – is the algae loss rate at $20°C$, $k(5)$ – is the degradation rate constant at $5°C$, $[OM]$ – is the concentration of organic matter (*i.e.,* POP, DOP, POC, and DOC), $[EA]_i$ – is the concentration of the electron acceptor (*i.e.*, O_2, NO_3^-, $Fe(OH)_3$, FeOOH, and SO_4^{2-}), K_{mi}^{EA} – is the half-saturation constant. Parameter values used in the simulation are listed in Tables S2 and S4.

no.	**Reaction**	**Equation**
Algae dynamics		
R0a	$(x-y+2z)CO_2 + (y-2z)HCO_3^- + yNH_4^+ + zHPO_4^{2-} + (x-y+2z)H_2O$	$\mu(20)Q_{10}^{(T-20)/10}[A]\frac{\lambda}{\epsilon_i \Delta z_i}\times$
	$\longleftrightarrow (CH_2O)_x(NH_3)_y(H_3PO_4)_z + xO_2$	$\left[H\left(\frac{I'_{zi}}{I'}\right) - H\left(\frac{I'_{zi+1}}{I'}\right)\right]\times$
R0b	$(x+y+2z)CO_2 + yNO_3^- + zHPO_4^{2-} + (x+2y+2z)H_2O$	$\frac{[HPO_4^{2-}]}{[HPO_4^{2-}]+P'}\frac{[N^\star]}{[N^\star]+N'}$
	$\longleftrightarrow (CH_2O)_x(NH_3)_y(H_3PO_4)_z + (y+2z)HCO_3^- + (x+2y+2z)O_2$	$-m(20)Q_{10}^{(T-20)/10}[A]$
Primary redox reactions		
R1	$OM + xO_2 \longrightarrow (x-y+2z)CO_2 + (y-2z)HCO_3^- + + yNH_4^+ + zHPO_4^{2-} + (x-y+2z)H_2O$	
R2	$OM + 0.5xNO_3^- + (y-2z)CO_2 + (0.5x+y-2z)H_2O \longrightarrow 0.5xN_2(g) + (x+y-2z)HCO_3^- + yNH_4^+ + zHPO_4^{2-}$	$k(5)[OM]f_iQ_{10}^{(T-5)/10}$
R3	$OM + 4xFe(OH)_3 + (7x+y-2z)CO_2 \longrightarrow 4xFe^{2+} + (8x+y-2z)HCO_3^- + yNH_4^+ + zHPO_4^{2-} + (3x-y+2z)H_2O$	where
R4	$OM + 4xFeOOH + (7x+y-2z)CO_2 + (x+y-2z)H_2O \longrightarrow 4xFe^{2+} + (8x+y-2z)HCO_3^- + yNH_4^+ + zHPO_4^{2-}$	$f_i = \frac{[EA]_i}{[EA]_i+K_{mi}^{EA}}\times$
R5	$OM + 0.5xSO_4^{2-} \longrightarrow 0.5xHS^- + (0.5x-y+2z)CO_2 + + (0.5x+y-2z)HCO_3^- + yNH_4^+ + zHPO_4^{2-} + (0.5x-y+2z)H_2O$	$\times \prod_{j=1}^{N-1}\frac{K_{mj}^{EA}}{[EA]_j+K_{mj}^{EA}}$
R6	$OM + (y-2z)H_2O \longrightarrow 0.5xCH_4(aq) + (0.5x-y+2z)CO_2 + (y-2z)HCO_3^- + yNH_4^+ + zHPO_4^{2-}$	

Table 2.2: Secondary redox reactions, mineral precipitation - dissolution reactions, phosphorus sorption and precipitation reactions, and equilibrium reactions in the coupled MyLake-Sediment model. Two pools of Fe(III) are used to represent two pathways of Fe (oxy)hydroxide formation that yield minerals with different reactivities (Couture et al., 2016).The first pathway produces reactive $Fe(OH)_3$ upon oxidation of ferrous Fe (R13); the second pathway yields less reactive FeOOH through the oxidation of pyrite and mackinawite (R23, R25). Parameter values used in the simulation are listed in Table A4.

no.	Reaction	Kinetic or Equilibrium
Secondary redox reactions		
R11	$HS^- + 2\,O_2 \longrightarrow H^+ + SO_4{}^{2-}$	$k_{tsox}[O_2][\sum S(-II)]$
R12	$HS^- + 2\,Fe(OH)_3 + 5\,H^+ \longrightarrow 2\,Fe^{2+} + S(0) + 6\,H_2O$	$k_{tsfe}[Fe(OH)_3][\sum S(-II)]$
R13	$Fe^{2+} + \frac{1}{4}\,O_2 + 2\,HCO_3{}^- + \frac{1}{2}H_2O \longrightarrow Fe(OH)_3 + 2\,CO_2$	$k_{feox}[Fe^{2+}][O_2]$
R14	$2\,O_2 + NH_4{}^+ + 2\,HCO_3{}^- \longrightarrow NO_3{}^- + 2\,CO_2 + 3\,H_2O$	$k_{amox}[O_2][NH_4{}^+]$
R15	$CH_4 + O_2 \longrightarrow CO_2 + H_2O$	$k_{ch4o2}[CH_4][O_2]$
R16	$CH_4 + SO_4{}^{2-} + CO_2 \longrightarrow H_2S + 2\,HCO_3{}^-$	$k_{ch4so4}[CH_4][SO_4{}^{2-}]$
Mineral precipitation - dissolution reactions		
R21	$OM + HS^- \longrightarrow OMS$	$k_{oms}[\sum OM][\sum S(-II)]$
R22a	$S(0) \longrightarrow S_8$	$k_{spre}[S(0)]$
R22b	$S_8 \longrightarrow S(0)$	$k_{sdis}[S_8]$
R23	$FeS_2 + 5\,O_2 + H^+ \longrightarrow FeOOH + 2\,SO_4{}^{2-}$	$k_{fes2ox}[FeS_2][O_2]$
R24	$FeS + S(0) \longrightarrow FeS_2$	$k_{fespre}[FeS][S(0)]$
R25	$4\,FeS + 3\,O_2 + 2\,H_2O \longrightarrow 4\,S_8 + FeOOH$	$k_{fesox}[FeS][O_2]$
R26	$FeS + HS^- + H^+ \longrightarrow FeS_2 + H_2$	$k_{fes2pre}[FeS][\sum S(-II)]$
R27a	$Fe^{2+} + HS^- \longrightarrow FeS + H^+$	$k_{fepre}(\Omega_{FeS} - 1)$
R27b	$FeS + H^+ \longrightarrow Fe^{2+} + HS^-$	$k_{fedis}[FeS](1 - \Omega_{FeS})$
R28a	$Ca^{2+} + CO_3{}^{2-} \longrightarrow CaCO_3$	$k_{CCpre}(\Omega_{CC} - 1)$
R28b	$CaCO_3 \longrightarrow Ca^{2+} + CO_3{}^{2-}$	$k_{CCdis}[CaCO_3](1 - \Omega_{CC})$
R29a	$Fe^{2+} + CO_3{}^{2-} \longrightarrow FeCO_3$	$k_{FCpre}(\Omega_{FC} - 1)$
R29b	$FeCO_3 \longrightarrow Fe^{2+} + CO_3{}^{2-}$	$k_{FCdis}[FeCO_3](1 - \Omega_{FC})$
Phosphorus sorption and precipitation reactions		
R31a	$HPO_4{}^{2-} + Fe(OH)_3 \longrightarrow PO_4{\equiv}Fe(OH)_3 + H^+$	$k_{psorb}^{Fe(IIIa)}[Fe(OH)_3][HPO_4{}^{2-}]$
R31b	$PO_4{\equiv}Fe(OH)_3 + H^+ \longrightarrow HPO_4{}^{2-} + Fe(OH)_3$	$4R3 + 2R12$
R32a	$HPO_4{}^{2-} + FeOOH \longrightarrow PO_4{\equiv}FeOOH + H^+$	$k_{psorb}^{Fe(IIIb)}[FeOOH][HPO_4{}^{2-}]$
R32b	$PO_4{\equiv}FeOOH + H^+ \longrightarrow HPO_4{}^{2-} + FeOOH$	$4R4$
R33a	$3\,Fe^{2+} + 2\,HPO_4{}^{2-} \longrightarrow Fe_3(PO_4)_2 + 2\,H^+$	$k_{Vpre}(\Omega_V - 1)$
R33b	$Fe_3(PO_4)_2 + 2\,H^+ \longrightarrow 3\,Fe^{2+} + 2\,HPO_4{}^{2-}$	$k_{Vdis}[Fe_3(PO_4)_2](1 - \Omega_V)$
R34a	$3\,Ca^{2+} + 2\,HPO_4{}^{2-} \longrightarrow Ca_3(PO_4)_2 + 2\,H^+$	$k_{Apre}(\Omega_A - 1)$
R34b	$Ca_3(PO_4)_2 + 2\,H^+ \longrightarrow 3\,Ca^{2+} + 2\,HPO_4{}^{2-}$	$k_{Adis}[Ca_3(PO_4)_2](1 - \Omega_A)$
R35a	$HPO_4{}^{2-} + Al(OH)_3 \longrightarrow H^+ + PO_4{\equiv}Al(OH)_3$	$k_{psorb}^{Al}[Al(OH)_3][HPO_4{}^{2-}]$
Equilibrium reactions		
R41	$CO_2(aq) + H_2O{=}H_2CO_3{=}HCO_3{}^- + H^+{=}CO_3{}^{2-} + 2\,H^+$	$K_{C0}\ K_{C1}\ K_{C2}$
R42	$H_3PO_4{=}H_2PO_4{}^- + H^+{=}HPO_4{}^{2-} + 2\,H^+{=}PO_4{}^{3-} + 3\,H^+$	$K_{P1}\ K_{P2}\ K_{P3}\ K_{P4}$
R43	$H_2S{=}HS^- + H^+$	K_{H_2S}
R44	$NH_4{}^+{=}NH_3 + H^+$	K_{NH_4}
R45	$H_2O{=}H^+ + OH^-$	K_{H_2O}

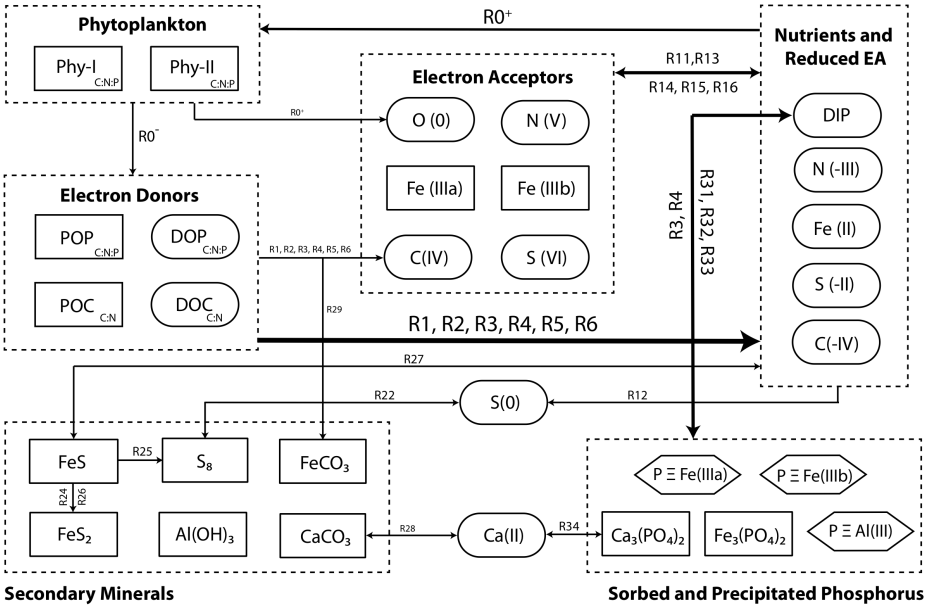

Figure 2.1: Reaction network in water column and bottom sediment. Squared boxes represent particulate organic and mineral phases, boxes with rounded corners are aqueous species and polygons indicate phosphorus sorbed onto ferric Fe and Al (hydr)oxides.

ematical representation of the sediment module consists of coupled nonlinear advection-diffusion-reaction equations which represent reactive transport processes of solid and aqueous species in the sediment. Transport processes such as bioturbation, molecular diffusion, burial of solids, solute irrigation, and compaction are implemented according to Boudreau (1997). Finally, MATLAB's *pdepe* solver used in Matsedlab has been replaced by operator splitting algorithm with the Crank-Nicolson method for the transport step and Butcher's Fifth-Order Runge-Kutta method for the reaction step.

In addition to P, the continuous (*i.e.*, in water column and sediment) reaction network takes into account the coupled cycles of key biogeochemical elements (Fe, Mn, Al, Ca, and S), which play important roles in controlling P cycling in the water column and sediments (Hadley et al., 2012, Iho et al., 2017, Lehtoranta et al., 2009, Verschoor et al., 2017). The model has been designed to study P partitioning among major P-binding forms commonly quantified by operational P-fractionation schemes (Doan et al., 2018). The reaction network includes microbially mediated primary and secondary redox reactions, aqueous speciation, mineral dissolution and precipitation (Figure 2.1, Tables 2.1, 2.2 and A.1). Microbially mediated organic matter degradation (*i.e.*, aerobic respira-

tion, denitrification, iron and sulphate reduction, methanogenesis) are implemented using Michaelis-Menten rate laws. Bimolecular reaction rate laws are used for secondary redox reactions (*e.g.*, oxidation of Fe^{2+}, $NH_4{}^+$, and HS^-), whereas precipitation and dissolution kinetics of the minerals depend on the corresponding degree of saturation and pH. In MyLake-Sediment, pH can be either a) fixed by the user, as was done here, or calculated via b) the electroneutrality equation, or c) by calling a compiled version of PhreeqC (Parkhurst and Appelo, 2013). The majority of the reaction network parameters are set according to previous studies (Atkin and Tjoelker, 2003, Canavan et al., 2006, Couture et al., 2016, Dijkstra et al., 2018, Katsev and Dittrich, 2013, Parkhurst and Appelo, 2013, Van Cappellen and Wang, 1996), while others were either calibrated using the global optimization toolbox in MATLAB which relies on a genetic algorithm or manually fine-tuned to obtain the best overall fit to the observations.

Coupling of the water column and sediment across the SWI accounts for fluxes of dissolved and solid species. Each time step of the two-way coupled model involves the following three sequential operations: (i) MyLake provides boundary conditions for solid (Neumann type) and aqueous (Dirichlet type) species to the sediment module; (ii) results of the sediment module run are used to estimate the diffusive and nonlocal transport fluxes of dissolved species across the SWI; (iii) these fluxes across the SWI are used to update the concentrations of dissolved species in the benthic boundary layer of the water column; (iv) MyLake then proceeds to the next time step.

Specifically, MyLake provides boundary conditions for the sediment solid and aqueous species. The settling (advective) flux of a solid constituent from the water column to the sediment is proportional to its concentration in the water column C_i^s times its settling velocity w_s. Additionally, in the coupled model, significant accumulation of sediment is assumed to be restricted to water depths exceeding a user-specified "sediment effective depth" (Figure 2.2). Thus, for the solid s, the one-dimensional, sediment surface area-weighted deposition flux at the SWI is estimated as follows:

$$F_j^s = \sum_1^n \omega_s \cdot C_{i,j}^s \cdot \frac{A_i - A_{i-1}}{A_{sed}} \tag{2.1}$$

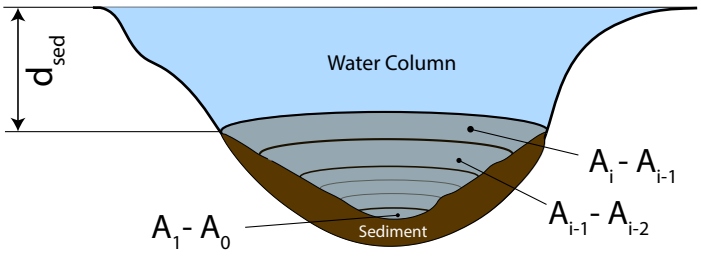

Figure 2.2: Representation of sediment in the model. Due to sediment focusing toward the deeper parts of the lake, significant accumulation of sediment is assumed to only occur below a user-defined "sediment effective depth", d_{sed}. If A_i is the surface area of the water column layer that intersects the SWI at depth d_{sed} and A_{i-1} that of the water column layer below it, then $A_i - A_{i-1}$ is the area of the SWI that captures the particulate matter deposited at water depth d_{sed} and across which solutes are exchanged between the sediment pore water and the i^{th} water layer. The SWI is similarly divided until the lowest water depth is reached where $A_0 = 0$. Thus, the model calculations can be considered to be 1.5 dimensional as the horizontal two-dimensional morphology of the lake is taken into account.

where spatial and temporal grids points are represented by indices i and j respectively, ω_s — is the settling velocity of the solid particles in the water column, $C^s_{i,j}$ – is the concentration of the solid constituent in the water column, A_i – is the area of the sediment below i^{th} layer of water column, A_{i-1} – is the area of the sediment below $(i-1)^{th}$ layer of water column, A_{sed} – is the total area of the sediment below the "sediment effective depth". The numbering of the layers starts at the deepest point of the lake with $A_0 = 0$. The sediment boundary condition for solute a is the area weighted mean concentration in the water column below the "sediment effective depth":

$$C^a_j = \sum_1^n C^a_{i,j} \cdot \frac{A_i - A_{i-1}}{A_{sed}} \tag{2.2}$$

Pore water profiles modelled in the sediment are used to estimate fluxes at the SWI. Thus, the flux of solute a at the SWI is estimated as the sum of diffusive and nonlocal bioirrigation fluxes:

$$F^a_j = -\frac{\varphi D^a_o}{\theta^2}\frac{\partial C^a_{i,j}}{\partial z} + \alpha \int_0^L (C^a_{i,j}(z) - C^a_{0,j})dz \tag{2.3}$$

where φ – is the porosity, D^a_o – is the temperature corrected molecular diffusion coefficient

of solute a, θ – is the tortuosity, $C^a_{i,j}$ – is the concentration of dissolved species, $C^a_{0,j}$ – is the concentration of dissolved species at the SWI (*i.e.*, bottom water concentration), z – is depth in the sediment with $z = 0$ at the SWI, α – is the irrigation coefficient, L – is the the depth of irrigation. The diffusive flux is estimated using a fourth-order finite-difference approximation. The integral is estimated using the trapezoidal method.

Finally, the flux of solute a across the SWI leads to a change of the water column concentration, which is estimated at each time step for each layer below the "sediment effective depth":

$$C^a_{i,j+1} = C^a_{i,j} + F^a_j \frac{A_i - A_{i-1}}{V_i} \Delta t \tag{2.4}$$

where V_i – is the volume of i^{th} layer of water column, Δt – is the time-step of the coupled model. A mass balance check of the coupled model revealed less than 1% error in fluxes across SWI for a ten-year simulation.

The model's short execution time and its execution as a Matlab function (taking parameter values as input and returning performance metrics as output) make it suitable for sensitivity and uncertainty analyses. It enables users to evaluate if parameter values found after optimization are unique and determine if the parameters agree with field data and process knowledge (Jackson-Blake and Starrfelt, 2015). Low model sensitivity to a given parameter or the response of the parameter value to changes in other parameters may lower confidence in the values emerging from the optimization (Dittrich et al., 2009).

2.2.2 Study Site

Lake Vansjø (59°23′N, 10°50′E) is located in the southeastern part of Norway. Its catchment was formed during the last ice-age and consists of an accumulation of unconsolidated glacial debris (coarse moraines). The area surrounding the lake presently comprises mainly forest (78%), agricultural area (15%) and open-water (7%) (Skarbøvik et al., 2019). Lake Vansjø has a surface area of 36 km^2 and comprises several sub-basins, the two largest being Storefjorden (eastern basin, draining a catchment of 244 km^2) and

Vanemfjorden (western basin, draining a catchment of 58 km^2). The water column of both basins remains oxygenated throughout the year. In this study, we focus on the deeper Storefjorden basin (max depth 41 m, mean depth 8.7 m, residence time 10 months) which drains into the Vanemfjorden basin through a shallow channel. The hydraulic residence time for the two basins together is estimated at 13 months.

The lake is an important drinking water source for three surrounding municipalities and is used for fishing and recreation. It has a long history of eutrophication from, at least, the 1970s when the systematic monitoring of the lake began. Total P concentrations in Storefjorden typically vary between 20 and 40 $\mu g\text{-}P\ L^{-1}$ (Skarbøvik et al., 2019), that is above the threshold of good ecological status set by the European Water Framework Directive. Lake Vansjø has experienced blooms of cyanobacteria causing beach closures (Moe et al., 2016). Measures to reduce inputs of phosphorus have not been met with a proportionate level of success (Skarbøvik et al., 2019).

2.2.3 Sampling, Analysis and Data Sources

Historical precipitation, temperature, insolation and wind records for Lake Vansjø were obtained from daily weather data at the Norwegian Meteorological Institute stations 1715 (Rygge), 1750 (Floter), and 378 (Igsi), located between the two lake basins (59°38′N, 10°79′E). Future climatic conditions were obtained from an ensemble of models used by the Inter-Sectoral Impact Model Intercomparison Project (ISIMIP), and downloaded from the Centre for Environmental Data Analysis database (Warszawski et al., 2014). The Institute Pierre Simon Laplace General Circulation Model (Dufresne et al., 2013), Geophysical Fluid Dynamics Laboratory Climate Model (Delworth et al., 2012), and Norwegian Earth System Model (Bentsen et al., 2013) provided air temperature projections for the period from 2018 to 2100. We retrieved the results of two representative concentration pathways (RCP) of radiative forcing, 4.5 and 8.5 $W\ m^{-2}$, for each model. The data were linearly interpolated over Lake Vansjø using the nearest 3 grid-points. For weather projections without climate change, the statistically consistent future weather was generated after Chen et al. (2010).

Catchment hydrology and loads of suspended sediments, particulate P and dissolved species were compiled previously (Couture et al., 2018), using daily measurements of flow and bi-weekly measurements of water chemistry over a 30-yr period (01/01/1983–31/12/2013) measured at the gauging station at Hogfoss (Station 3.22.0.1000.1; Norwegian Water Resources and Energy Directorate, NVE). Lake water chemistry and temperature data were provided by the Vansjø-Hobøl monitoring programme, conducted by the Norwegian Institute for Bioeconomy Research (NIBIO) and by the Norwegian Institute for Water Research (NIVA) (Haande et al., 2016). The measurements include temperature, concentrations of dissolved oxygen (DO), total P (TP), orthophosphate-P (DIP), particulate organic phosphorus (POP), and chlorophyll a (Chl-a). These data are available freely through NIVA's online database (http://www.aquamonitor.no) until 2015 and on the Norwegian national database (https://vannmiljo.miljodirektoratet.no).

An undisturbed sediment core was collected at the deepest point of the Storefjorden basin using a modified Kajak-Brinkhurst gravity-type corer with an inner diameter of 8.3 cm. The core was sectioned anaerobically at 1 cm intervals from the SWI down to 5 cm, at 2 cm intervals from 5 to 15 cm depth and at 5 cm intervals from 15 to 30 cm depth. Samples were transported at 4°C before centrifugation at 500 g under nitrogen atmosphere (N2:H2 97:3%, O2 $<$ 1 $ppmv$). The supernatant, hereafter referred to as the pore water fraction, was filtered through a 0.2 μm pore size polypropylene membrane filter (Whatman).

Phosphorus partitioning within the sediment was evaluated using the 5-step sequential extraction scheme from Hieltjes and Lijklema (1980), Paludan and Jensen (1995) and Reitzel et al. (2006), where steps 1 and 2 were carried out under an N_2 atmosphere. Briefly, samples were treated, at a 1:25 sediment:solution ratio, with 1) deionized water for 16 h at 40°C, 2) bicarbonate buffered dithionite (BD) solution for 1 hour at 40 °C, 3) 0.1 M NaOH for 16 h at 40°C, 4) 0.5 M HCl for 16 h at 40°C, 5) ashed for 8 h at 520°C and 1.0 M HCl for 16 h at 120°C. Between steps, the supernatant was recovered and filtered through a 0.2 μm pore size polypropylene membrane filter. The following operationally defined fractions are associated with the corresponding sequential extraction steps: loosely bound-P,

Fe-P, Al-P, Ca-P, and unreactive-P. Particulate organic phosphorus (POP) is estimated by subtracting the molybdate-reactive phosphorus from total phosphorus measured in the NaOH extract (Ahlgren et al., 2011). All solutions were prepared using analytical grade reagents from Fluka, Sigma-Aldrich or Merck and prepared with 18 *Ohm* water (Millipore) deoxygenated by cooling boiled water using a N_2 stream. Total Fe, Al, Ca, P and Si concentrations of the pore water samples and extracts were measured by ICP-OES (Thermo Scientific iCAP 6300) after acidification with HNO_3 to pH < 2. Total P and soluble reactive P (SRP) were measured by the molybdenum blue/ascorbic acid method on a LaChat QuickChem 8500 flow injection analyzer system. Matrix-matched standards were used for all calibrations, and NIST validated multi-elemental solutions were used as controls.

2.3 Results and Discussion

2.3.1 Water Column Temperature and Chemistry

Because of the relatively short hydraulic residence time of the lake, initial conditions in the water column only affect the result during the first 10 years of simulation. In contrast to the water column, the sediment contains slowly reacting solid phases and the module could not be spinned up with measured data only. Instead, the 1983-1995 cycle was repeated until the sediment column reached steady-state, at which point the concentration distributions were saved and used as initial conditions in the further simulations of the historical period (1995-2015), open water scenario (1995-2015), climate warming (1995-2070), external P reduction scenario (1995-2200), Fe amendment scenario (1995-2070).

Six model parameters were necessary to fit the simulated temperatures to observations in the water column of the lake: the open water diffusion a_k, the ice covered period diffusion parameter a_k^{ice}, the minimum stability frequency N^2, the light attenuation coefficients (photosynthetically $\hat{\varepsilon}$ and non-photosynthetically active $\bar{\hat{\varepsilon}}$), and the win sheltering coefficient W_{str} (Supplemental material, Table A.2). These parameters were taken from

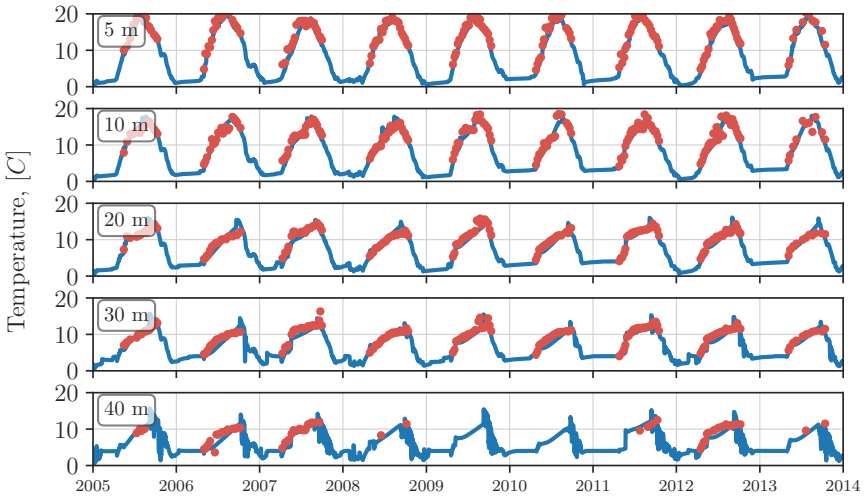

Figure 2.3: Observed temperatures (symbols) at different depths in Lake Vansjø compared to simulations (lines) with the calibrated physical model for the period from 2005 to 2014.

previous modelling studies on Lake Vansjø Couture et al. (2014), Saloranta and Andersen (2007). Details on the description of the parameters can be obtained from Saloranta and Andersen (2007).

Figure 2.3 highlights the good agreement between simulated and observed temperatures. The mean absolute error (MAE) for all depths was 1.07°C, RMSE was 1.34°C, the correlation coefficient (r) was 0.91, the coefficient of determination (R^2) was 0.7, and the bias was -0.6°C (supplemental material, Table A3). In general, the model tended to slightly underestimate the warming of the hypolimnion during summer periods.

Of the 43 parameters values needed for the reaction network, 30 were taken from the literature (Atkin and Tjoelker, 2003, Canavan et al., 2006, Couture et al., 2016, Dijkstra et al., 2018, Katsev and Dittrich, 2013, Parkhurst and Appelo, 2013, Van Cappellen and Wang, 1996) and 13 were fitted to reproduce the observations. The calibrated parameters relate to organic matter degradation, the half-saturation constants of microbial Fe reduction, and P sorption and mineral precipitation parameters. The values remained within the range of previously reported values, as shown in the supplemental material (Table A4).

The dissolved oxygen (DO) concentration in the water column declined throughout

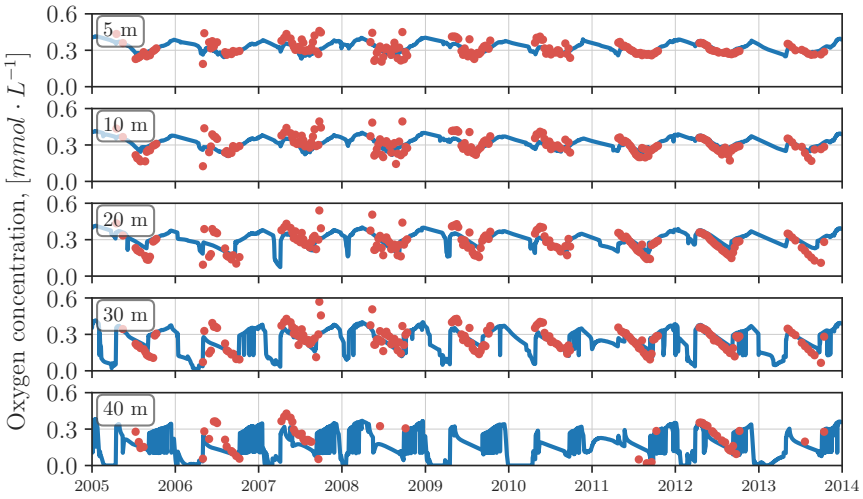

Figure 2.4: Observed dissolved oxygen concentrations (symbols) at different depths in Lake Vansjø compared to simulations (lines) of calibrated model for the period from 2005 to 2014.

annual periods of high productivity, reaching minimum values in the hypolimnion at about 0.1 $mmol\ L^{-1}$ (Figure 2.4). The measurements are more scattered before the year 2010 than afterwards, likely reflecting the improved DO measurement protocols introduced in 2010. As can be seen in Figure 2.4, the model was able to reproduce the observed DO concentration time-series in the water column with a bias of less than 9% for the DO concentrations in the hypolimnion. The RMSE gradually increased with the depth, from 0.03 $mmol\ L^{-1}$ at the surface to 0.1 $mmol\ L^{-1}$ at 40 m (Table A3). Although the timing and magnitude of the DO peaks are well captured, in the specific case of DO at 40 m depth, the model struggles to fully capture the trends, which results in the low statistical correlation metrics (Table A3). The model satisfactorily captured the seasonal variations of total phosphorus (TP), phytoplankton (Phy-P), DIP and particulate phosphorus (PP) in the mixed layer of the lake (Figure 2.5). The simulated P dynamics in the lake reproduced the observed strong seasonal features, with Phy-P reaching maximum values during the summer when the lake is most productive. By contrast, surface DIP is at a minimum during the summer, consistent with its uptake by phytoplankton. Discrepancies between measured and model P distributions in the water column may be due to the simplicity of the algal dynamics in MyLake. The current version of MyLake does not yet

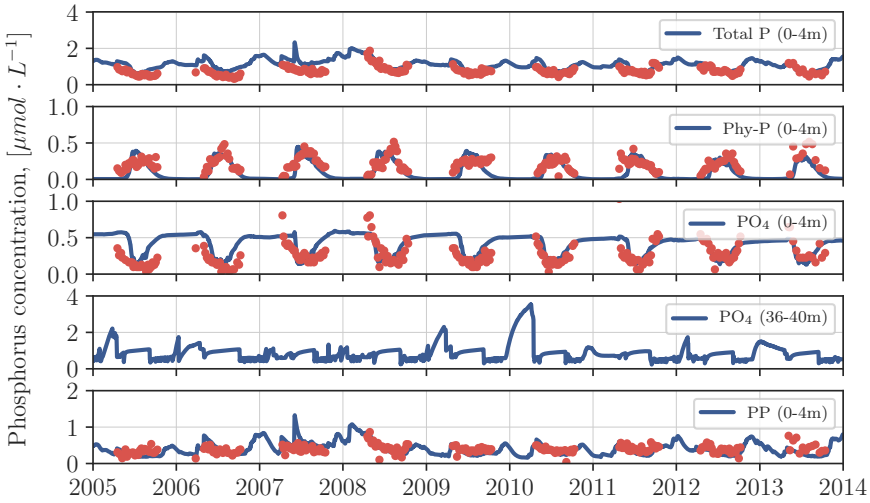

Figure 2.5: Observed concentrations (symbols) of total phosphorus (Total P) in surface water (0-4 m), phosphorus in phytoplankton (Phy-P) in surface water (0-4 m), dissolved inorganic phosphorus (DIP) in surface and bottom water (36-40 m), and particulate phosphorus (PP) in surface water (0-4 m) compared to simulations (lines) of the calibrated model for the period from 2005 to 2014. Total P is the sum of all phosphorus compounds, *i.e.*, Phy-P, DIP, and particulate organic and inorganic P. Measured Phy-P concentrations are derived from Chl-a measurements using C:Chl-a=40:1 (g/g) and C:P=106:1(mol/mol) ratios (Cloern et al., 1995). PP is the sum of allochthonous particulate organic phosphorus and solid inorganic phosphorus.

simulate phytoplankton community dynamics or N-limitation to algal growth, as is done in other models such as PROTECH (Reynolds et al., 2001), thus community shifts due to changing climate and N recycling from the sediments are not captured. Other processes, such as cell buoyancy effects (Gemmell et al., 2016) and grazing by zooplankton (George and Reynolds, 1997), are also not included.

2.3.2 Sediment Pore Water and Solid Phase Geochemistry

In the sediment, the pore water concentration of DIP gradually increased with depth from near 0 mM at SWI to about 0.06 mM at 16 cm, then steadily decreased to 0.04 mM at 30 cm (Figure 2.6.1). In the upper 10 cm, the concentrations of dissolved Fe and Ca increased steadily with depth to their highest values of 0.5 mM and 0.27 mM, respectively, remaining fairly constant at greater depths. The model captured the main features of the pore water profiles, both the depth of the phosphate and calcium peaks and the

magnitudes of the concentrations. The total solid fraction of P in the sediment was about 0.7 $mmol\ g^{-1}$ of dry sediment (2% by weight). Solid phase P speciation was dominated by iron-bound phosphorus (Fe-P), followed by aluminum bound (Al-P), POP and calcium bound phosphorus (Ca-P). In the model, Fe-P is represented by P sorbed on iron minerals and vivianite, Al-P by P sorbed on Al, POP by allochthonous particulate P and Phy-P, and Ca-P by calcium phosphate precipitate. By adjusting the parameters of first-order rate constants of organic matter degradation, dissolution and precipitation constants of apatite and vivianite, and phosphate adsorption constants on aluminum and iron oxides, the model also captured the distribution of P in the operationally-defined pools (Figure 2.6.2). The modelling results indicate that the most significant parameters, with respect to P release from the sediment to the water column, are the parameters values describing organic matter lability (first-order rate constants of organic matter degradation), the reductive dissolution of Fe (oxy)hydroxides (half-saturation constants of the terminal electron acceptors), and the sorption of P onto Fe and Al oxides (Table A4). The model consistent average sediment burial rate of 0.1 $cm \cdot y^{-1}$ agrees with the estimations of 0.17 $cm \cdot y^{-1}$ at 14 cm depth for the previously collected cores (Solheim et al., 2006). Thus, the burial rate suggests that the top 15 cm of the sediment represent about 100-150 years of sediment deposition. Finally, although the pore water DO was not measured in the sediment cores, modelling results predict that it was depleted within the uppermost 0.3 cm of sediment. Such DO penetration depth is consistent with high rates of organic matter degradation following the season of high biological productivity (Maerki et al., 2009).

2.3.3 Baseline Simulation

Depth-integrated P reaction rates, fluxes and inventories are shown in Figure 2.7. The simulation results for the historical 1995-2015 period, hereafter referred to as the baseline, indicate that about one-third of P deposited at the SWI is sorbed to ferric Fe (oxy)hydroxides and the remaining consists of POP. Upon reductive dissolution of the Fe oxides and microbial degradation of POP, on average 60% of the deposited P is returned

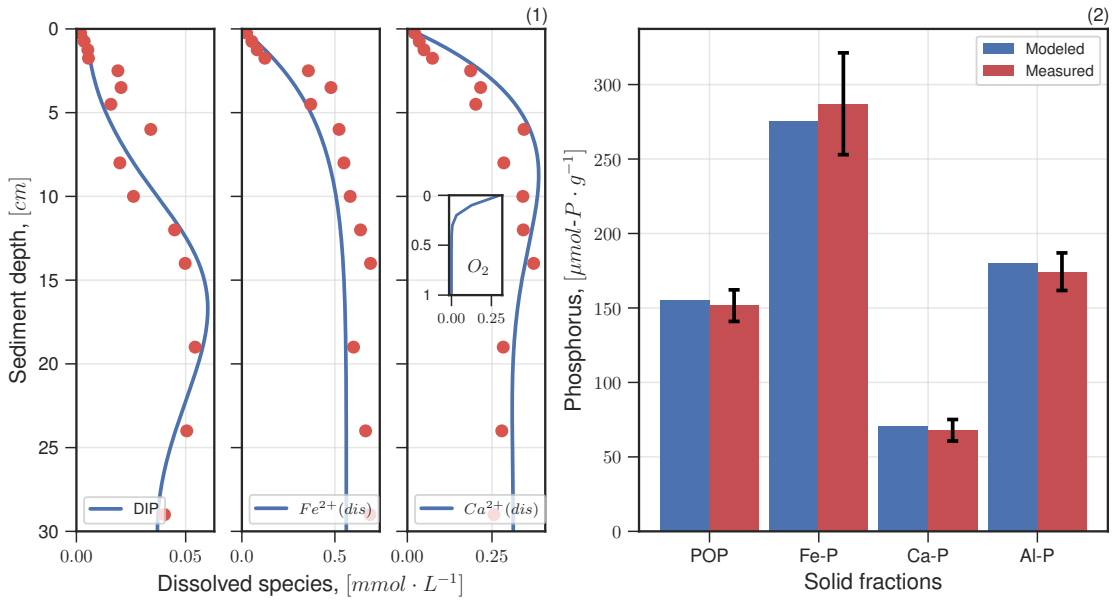

Figure 2.6: Sediment geochemistry. Panel (1) compares the simulated and measured pore water profiles of DIP, ferrous iron and calcium; panel (2) compares the simulated and measured average concentrations of the solid-phase pools of phosphorus in depth interval 0-30 cm. The pore water and solid-phase data were measured on sediment cores collected in October 2014 in the deepest part of Lake Vansjø.

as DIP to the overlying water, while 40% remains trapped in the iron redox cycle or precipitates as mineral Ca phosphate. Below the upper (0-15 cm) sediment interval of P recycling associated with the reductive dissolution and oxidative precipitation of ferric Fe (oxy)hydroxides, P is permanently removed via the burial of Ca and Fe phosphate mineral phases and P sorbed to Al oxides. Over the historical period, the bottom sediments act as a net sink for P. The P exchanges between the sediments and the overlying water vary significantly along a single year, however. In particular, the sediments become a more pronounced source of P to the water column during the growing season (Figure 2.8). In the following sections, the baseline serves as the starting point of additional simulations in which various perturbations are imposed on the lake-sediment system, namely 1) projected future changes in air temperature, 2) disappearing ice-cover, 3) stoppage of external P input, and 4) Fe-amendments as a remediation strategy.

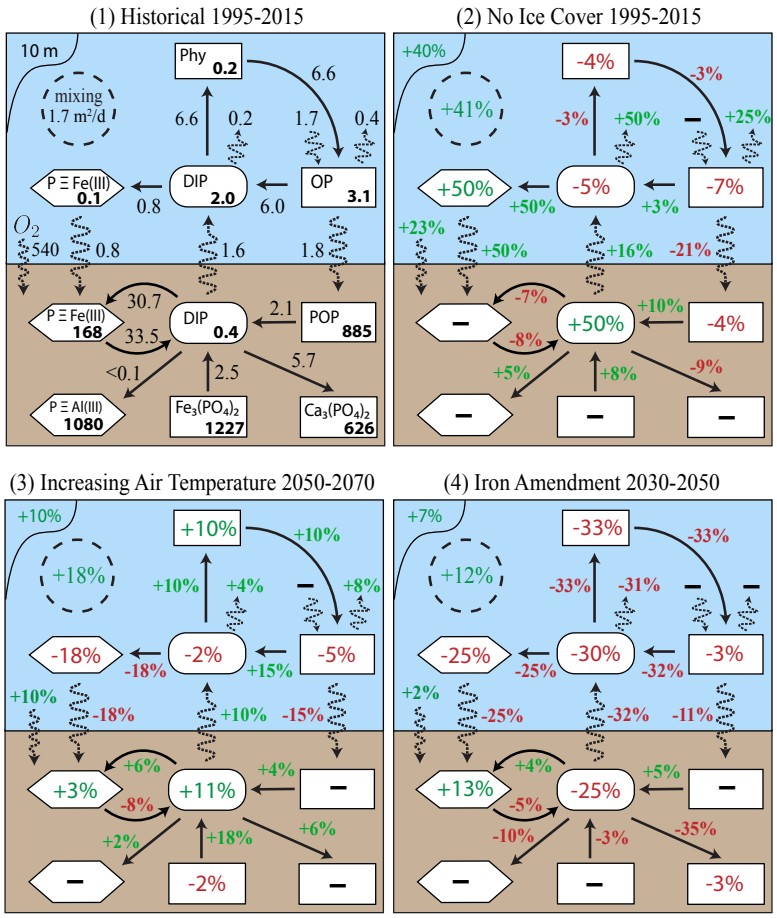

Figure 2.7: Calculated 20-year average values of phosphorus fluxes ($\mu mol\text{-}P \cdot cm^{-2} \cdot y^{-1}$) and depth-integrated P inventories ($\mu mol\text{-}P \cdot cm^{-2}$) in the water-column and sediment: (1) historical 1995-2015 simulation, (2) no ice cover 1995-2015, (3) increasing air temperatures 2050-2070, and (4) iron amendment scenario 2030-2050. IPSL, GFDL, and NorESM climate models provided the atmospheric forcing for scenario 3 and 4. Dashed zigzag lines represents fluxes in and out of the water column due to lake inflows and outflows as well as transfers across the SWI. Red and green colors represent relative change in values compared to the historical 1995-2015 simulated values. Percentage change within 1% of the original values are noted with dash (no change). OP stands for the sum of particulate and dissolved organic phosphorus.

2.3.4 Climate Warming Scenarios

Lakes are warming under climate change worldwide (Woolway and Merchant, 2019). Surface temperatures in seasonally ice-covered lakes have been reported to increase faster than in ice-free lakes (O'Reilly et al., 2015, Winslow et al., 2018). At the same time, significant decreases in the duration of ice cover have been observed and are projected to continue (Austin and Colman, 2008, Butcher et al., 2015, Fang and Stefan, 2009), with profound impacts on water-column processes, as summarized in Lindenschmidt et al.

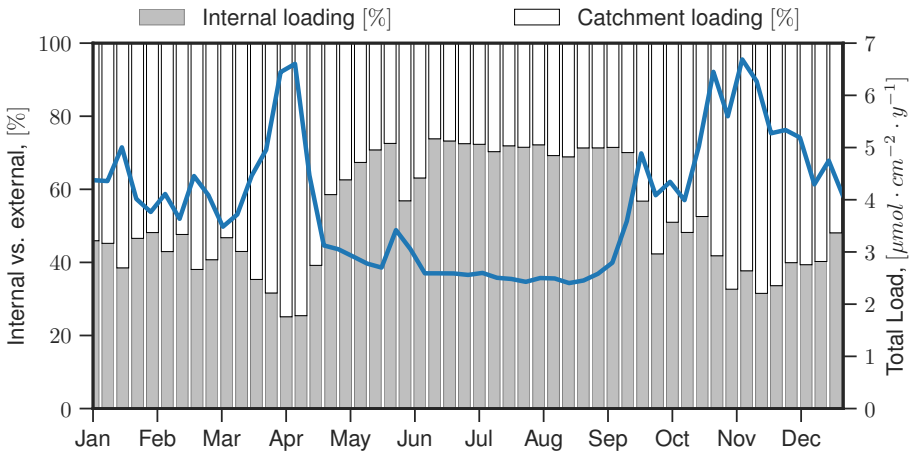

Figure 2.8: Weekly total P loading (external plus internal) to the water column of Lake Vansjø (blue line), and relative contributions (in %) of P supplied from the catchment (white bars) and from the sediments (gray bars). The results shown are average values for the period 1995-2015.

(2018). Lake water quality and harmful algal blooms are expected to worsen as a result of higher water temperatures (Mantzouki et al., 2018), droughts and longer hydraulic residence times (Mosley, 2015, Visser et al., 2016).

Here we analyze how Lake Vansjø may respond to changing air temperatures and, in particular, how this may affect P exchanges between the bottom sediments and the water column. Historical air temperatures for the period 1995-2015 and those from the climate models described in section 2.2.3 for the period from 2015 to 2070 were imposed to the model. The largest differences in the projected air temperatures are between the climate models rather than between RCPs: IPSL and GFDL both predict warmer winters (+7°C for IPSL and +3°C for GFDL) and summers (+3°C for IPSL and +0.5°C for GFDL), while NorESM predicts warmer winters (+3°C) but colder summers (−3°C) compared to the historical period (Figure A.3). Trends of selected model variables under the climate warming scenarios are summarized in Figure 2.9 (Note that seasonal ice formation is still taking place in the warming scenarios, in contrast to the open water scenario discussed in section 2.3.5).

In agreement with previous studies (Gebre et al., 2014), the model results predict that, on an annual basis, with every degree of air temperature increase the duration of lake ice shortens by about 21 day (Figure A4). In the ”warmest” IPSL RCP 8.5 scenario,

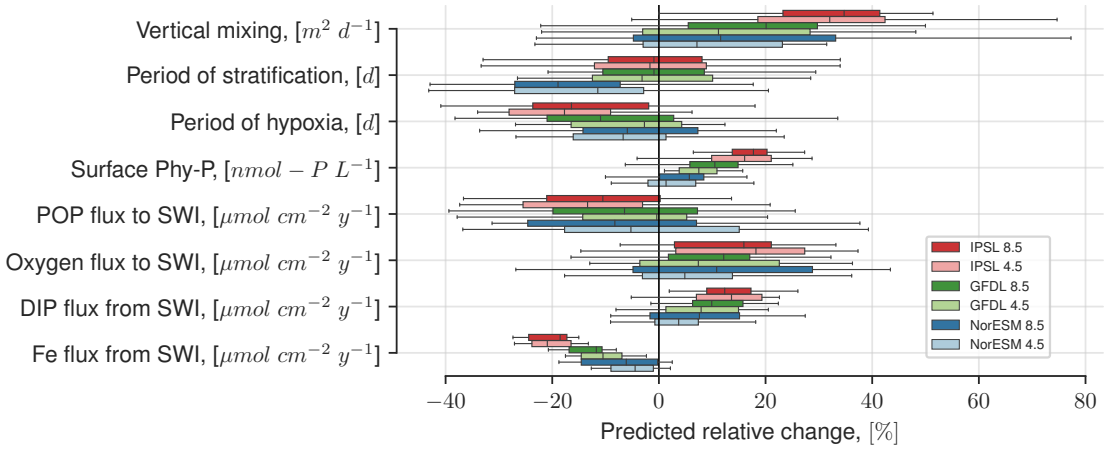

Figure 2.9: Trends of selected MyLake-Sediment variables in the climate warming scenarios, according to the projections of the climate models for RCP 4.5 and RCP 8.5, over the period of 2050-2070 relative to average historical values for the period 1995-2015.

the model yields a reduction in ice cover duration from 105 days during the historical period (1995-2015) to less than 20 days for the 2050-2070 period.

Increasing air temperature and decreasing ice cover have antagonistic effects on water column stability. As summarized in Obertegger et al. (2017), decreasing ice cover duration enhances spring mixing as a result of prolonged periods of open water and subsequent wind exposure, an effect that is offset by earlier stratification due to warming air temperatures (Adrian et al., 2009), which in turn slows down DO replenishment of the lower lake waters. Despite a more extended period of water stratification by up to 10 days, compared to the historical 1995-2015 period, the cumulative effect of both imposed environmental variations is the gradual deepening of the thermocline, together with increasing vertical mixing (on average) and decreasing duration of hypoxia (Figures 2.7 and 2.9). These results are in line with a previous study where shorter ice cover duration is the governing factor driving increasing dissolved oxygen concentrations in the water column (Couture et al., 2015, Fang and Stefan, 2009).

The model results suggest that earlier water column ventilation and late-season warming of the hypolimnion have cascading effects on the biogeochemical dynamics in the sediments. First, increased bottom DO concentration favors both the degradation of organic matter in the sediment and the oxidation of Fe(II). The former releases DIP to the

porewater, while the latter forms Fe(III) (oxy)hydroxides that sequester DIP. The model predicts that DIP release exceeds DIP sorption by newly formed Fe (oxy)hydroxides. The net result is a decrease of the Fe(II) and an increase of the DIP flux from the sediment (Figure 2.9). Next, phytoplankton growth and abundance respond to the increasing internal P loading and the warming water temperature yielding a summer bloom that lasts about 10 days longer by the end of the simulation period (not shown).

2.3.5 Open Water Scenario

Given the key role of ice cover in controlling water column stability and the biogeochemical dynamics of the lake, we simulate the response to a complete absence of ice cover. This is done by imposing open water conditions throughout the entire simulation period, hence allowing for enhanced gas exchange and wind-induced mixing during the otherwise ice-covered time of the year. The integrated P fluxes and inventories for the open water scenario during the 1995-2015 period, compared to the baseline values, are shown in Figure 2.7.2.

The model results yield averaged vertical diffusivity coefficients that are up to 41% higher without ice than with ice as a result of the enhanced wind-induced mixing. During the course of year, the durations of stratification and hypoxia decrease at first stepwise by about 20% and 50%, respectively (Figure A4), until increasing temperature gradually reverts the trend causing the extension of the period of stratification. As also seen for the shorter ice-covered durations in the climate warming scenarios, the complete absence of ice cover leads to higher dissolved oxygen concentrations in the water column and a 23% rise in the oxygen influx to the sediment. The enhanced mixing and more oxygenated water column further result in more P to be deposited at the SWI in the form of P sorbed to ferric Fe (oxy)hydroxides, and less as POP. The increased efflux of DIP from the sediments in the year-round open water scenario, however, is mostly supported by the faster early diagenetic mineralization of POP under the more oxic conditions. The enhanced upward vertical mixing of DIP also increases P export via the lake outflow. That is, overall, the lake's sediments become less efficient at retaining P. Nonetheless,

despite the profound reorganization of P cycling in the lake, the complete absence of ice cover has only a relatively small impact on the phytoplankton biomass (4% decrease).

2.3.6 External P Reduction Scenario

To further evaluate the role of internal P loading in the biogeochemical functioning of Lake Vansjø, a simulation is performed where the external loads of all P-containing species are set to zero after 2015, all other conditions remaining unchanged (Figure A5). The simulation is run until 2195, that is, the 20-year historical cycle (1995-2015) is repeated ten times but without any new addition of P to the lake. Thus, all phytoplankton biomass growth after 2015 is supported by P recycling within the lake-sediment system.

The results indicate that after the external P cutoff internal loading from the sediments provides a long-term source of P to the water column (Figure A5). Prior to the external P cutoff, the efflux of DIP from the sediments represents 25-75% of the total P loading to the water column (Figure 2.8). After the external P cutoff, it becomes 100% of the total loading. From 2015 onwards, the magnitude of the internal DIP loading is predicted to decay exponentially. Such decay can be also simulated with a half-life of 229 years according to the best-fit equation: $F_0 \cdot exp(-t/330)$, where F_0 is the DIP efflux before the cutoff and t is the number of years after 2015. The long decay period reflects the slow depletion of the large solid-phase P pools accumulated in the sediment, mainly via DIP production by the degradation of refractory POP, P desorption from Fe and Al mineral phases and dissolution of vivianite (Figure A5).

The important role of legacy P stored in the sediments is further illustrated by conducting the same simulation but with the sediment module turned off (Figure A5, panel 3). In the absence of internal DIP loading, the lake's temporal response to the external P cutoff is instead driven by the water residence time. The depletion of water column DIP can be approximated by the following fitted curve: $P_0 \cdot exp(-t/3\tau)$, where P_0 is the concentration of DIP before the cutoff and τ is the hydraulic residence time (0.85 years). The factor 3 in the denominator of the exponent indicates that the decay of the DIP concentration is slower than that expected for an unreactive tracer, because the

biological cycling of P in the water column increases the residence time of DIP. That is, nine hydraulic residence times are needed to flush out 95% of DIP. Thus, overall, internal DIP loading extends the response time scale of Lake Vansjø with respect to the cessation of external P loading by more than two orders of magnitude relative to the no-sediment scenario.

Under the current climate conditions, the modelled P concentration time series can be used to derive the following predictive model emulator of the average annual TP concentration in the water column of Lake Vansjø, as a function of the external and internal P loadings:

$$TP = 3 \cdot \tau \cdot (F_{ext} + F_{sed}) - (3 \cdot \tau \cdot (F_{ext} + F_{sed}) - P_0) \cdot exp(-t/3\tau) \tag{2.5}$$

where TP is expressed in units of $\mu mol\ L^{-1}$, and F_{ext} and F_{sed} are the P fluxes to the water column from the catchment and from the sediments, respectively, both expressed in units of $\mu mol\ L^{-1}\ y^{-1}$. This lake-specific equation would predict, for instance, that best management practices that would reduce the external P load by half would decrease the water column TP concentration by about 20% over a 10-year period.

2.3.7 Iron Amendment Scenario

While the majority of management measures and practices focus on reducing external P loads to improve water quality in lakes, alternative mitigation approaches rely on the addition of reactive materials to the water column to sequester P in the sediments (Mackay et al., 2014). Because of the strong coupling of the early diagenetic cycling of P and Fe (Doolittle et al., 2018, Molot et al., 2014, Verschoor et al., 2017), materials that have been used include salts of ferric Fe (Engstrom, 2005, Orihel et al., 2016, Wilfert et al., 2015), but also Al (Huser et al., 2016, Schutz et al., 2017) and Ca phases (Gulati et al., 2012), as well as lanthanum clays (Dithmer et al., 2015).

Here, we simulate the outcomes of a ferric Fe addition to Lake Vansjø. The imposed scenario consists of yearly additions, from 2030 to 2050, of 200 $g\ m^{-2}$ (0.3 $mmol\ cm^{-2}$)

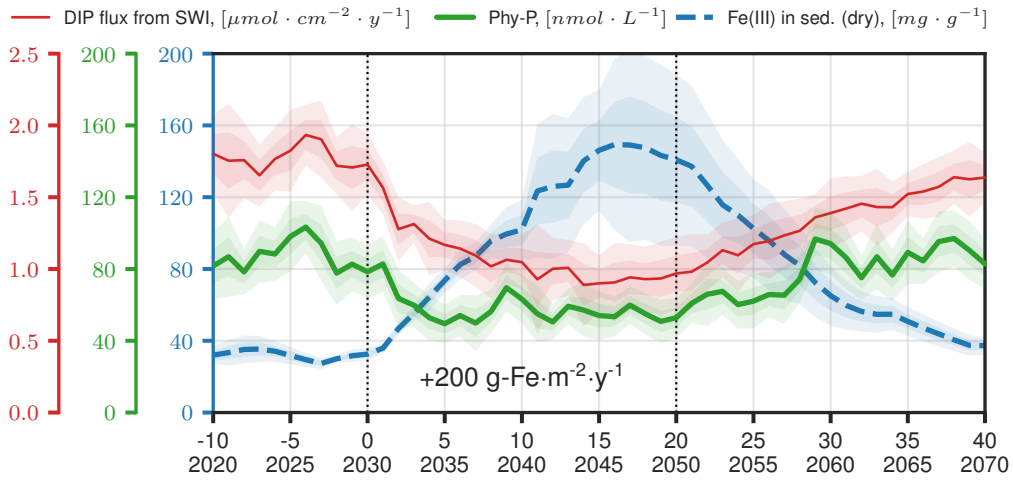

Figure 2.10: Response of the benthic DIP flux (thin red line), water-column phytoplankton biomass (thick green line) and sediment Fe inventory (dashed blue line) to the addition of 200 $g\text{-}Fe \cdot m^{-2} \cdot y^{-1}$, starting in 2030 and continuing until 2050. The shaded areas represent the ranges obtained for the different air temperature projections from the GFDL, IPSL and NorESM models shown in Figure A.3. Dark and light shaded areas represent 68 and 95 confidence intervals, respectively.

of Fe(III) added via the lake inlet just before ice breakup. The resulting 20-year averaged fluxes and inventories of the P cycle during the iron treatment are compared to the historical 1995-2015 values in Figure 2.7, while Figure 2.10 shows the timing and magnitude of the changes in the DIP efflux from the SWI, phytoplankton biomass, and Fe inventory of the sediments. Figure 2.11 further shows the relationship between benthic DIP fluxes and annual iron loads before, during and after iron treatment. The figure illustrates the hysteresis in the internal DIP loading response after the amendment is terminated in 2050.

During the first 10 years of iron amendment, the model predicts that the DIP flux from the sediments decreases by 43% from an average annual value of 1.75 to 1 $\mu mol\ cm^{-2}\ y^{-1}$ (Figure 2.10). This decline in internal P loading is due to enhanced P retention in the sediments by Fe(III) (oxy)hydroxide minerals in the upper oxic layer and by ferrous Fe minerals, such as vivianite, in the deeper anoxic layer (Bostrom et al., 1988, Smolders et al., 2006). The decreased internal P loading in turn results in lower phytoplankton biomass, which decreases by 30% from 85 to 60 $nmol - P\ L^{-1}$ during the period of amendment (Figure 2.10). Once the treatment is terminated (*i.e.*, from 2050 onward)

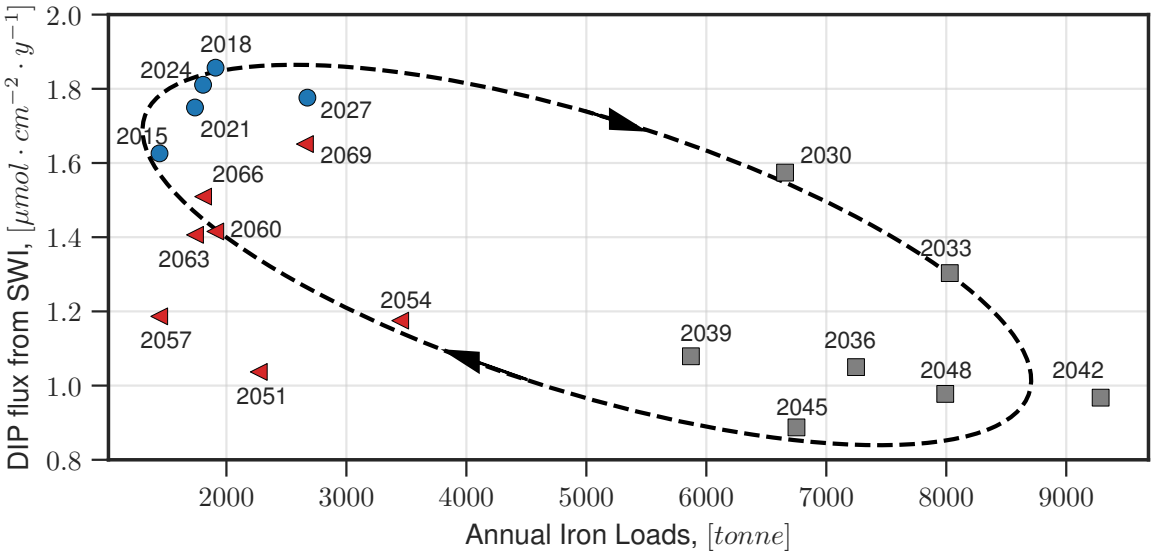

Figure 2.11: Relationship between the annual benthic flux of DIP from sediment to water column (*i.e.*, the internal P loading) and the corresponding annual ferric Fe loading to the lake before the iron amendment (2015-2030; circles), throughout the amendment period (2030-2050; squares) and after the amendment (2050-2070; triangles). Dashed line and arrows highlight the direction of the hysteresis of the relationship.

the lake's phytoplankton biomass returns to its pre-treatment level within about 15 years (Figure 2.10). The imposed Fe treatment and the predicted responses are consistent with observations reported for 15 actual treatments worldwide (Orihel et al., 2016), in which lakes with low natural Fe levels show stronger responses than Fe-rich lakes.

The efficiency with which Fe amendments are likely to decrease algal growth depends on the existing Fe inventory in the sediments, and on whether or not internal loading is a major source of DIP to the water column. For example, in Lake Simcoe (Ontario, Canada), similar to Lake Vansjø, internal loading supplies between a third to one half of P to the water column (Loh, 2013). In contrast, the estimated internal loading in the eastern basin of Lake Erie (Ontario, Canada) only accounts for 3-7% of the total phosphorus load (Matisoff et al., 2016). In such a case, even if the addition of iron reduces the internal loading by half, the overall effect will be insignificant.

Finally, internal P loading has been shown to be naturally supressed in lakes with sediments containing high concentrations of Al (Kopáček et al., 2005, Lake et al., 2007, Ostrofsky, 2019). Additions of Al have been used as a lake remediation measure, and

studies of Al-treated lakes show that Al enhances P sorption in sediments and prevent P release to the water column during the reductive dissolution of Fe(III) minerals (Huser et al., 2016). The use of MyLake-Sediment model to simulate a lake's response to Al addition will require careful modelling of lake and porewater pH in order to capture pH dependent P sorption to Al mineral phases (Reitzel et al., 2013).

2.4 Concluding Remarks

Internal nutrient recycling from sediments plays a key role in the biogeochemical cycling and biological productivity of lakes. Here, we present a Lake-Sediment model meant to diagnose the processes driving internal P loading in lakes and predict how these processes respond to changes in climate conditions, inputs from the catchment, and lake restoration measures. The model directly couples the biogeochemical reaction networks of water column and sediments in order to simulate P exchanges across the SWI. We use the model to assess the effectiveness of P loading targets and other mitigation strategies aimed at controlling excessive algal growth in a eutrophic lake in Norway, Lake Vansjø. The results clearly illustrate the importance of the accumulated legacy P in the lake's sediments in controlling the timing and magnitude of the response of internal P loading to external forcings, including projected changes in air temperature and ice cover, as well as management interventions.

With a strong focus on coupled biogeochemical processes across the SWI, this code can serve as a stepping stone to generate lake restoration scenarios (Lürling et al., 2016), test hypotheses on the response of algal biomass to external and internal fluxes of P and Fe (Verschoor et al., 2017), and help with "climate-proofing" remediation measures, whose effectiveness will likely be modulated by ongoing climate change (Trolle et al., 2011). To this end, further model development and evaluation avenues should focus on capturing the temporal (*e.g.,* Amirbahman et al. (2012), Katsev and Dittrich (2013)) and, in particular, spatial heterogeneity in sediment P distributions and recycling efficiencies (*e.g.,* Dittrich et al. (2013), Doan et al. (2018), Gudimov et al. (2015), Matisoff et al. (2016, 2017)).

Chapter 3

Dynamic Modelling of Preferential Catabolic Reaction Pathways Using Thermodynamic Switch Function

Igor Markelov
Ekaterina Markelova
Raoul-Marie Couture
Philippe Van Cappellen

Summary

We present a new conceptual model of microbial functioning by describing redox cascades that are commonly observed in the aquatic environments. In a classical approach, the biogeochemical sequence of nutrients in redox fluctuating environments (e.g., sediments, riparian zones) is represented by the Monod equation supplemented by the inhibition terms. Such terms involve a wide range of assumptions to prioritize one reaction over another, whereas they lack generalization and are limited to particular case-studies. To decrease the number of subjective assumptions and improve model robustness, we replace the inhibition terms by introducing a thermodynamic switch function. The thermodynamic switch function accounts for the overall energy supply rate (power) of each individual microbial reaction in the reaction network. The thermodynamic switch function does not require any calibrated parameters and provides a unique feature for the continuous simulation of ecosystem evolution in time and space. The model demonstrates the ability to reproduce the experimental data of highly complex redox systems comprising numerous electron acceptors (O_2, NO_3^-, MnO_2, $Fe(OH)_3$, SO_4^{2-}, HCO_3^-) and electron donors ($C_6H_{12}O$, CH_3COO^-, H_2) at once. Such abundance and variability of nutrients are expected in the microbial aquatic models. With the recent growth of the genomics, transcriptomics, proteomics, and metabolomics data, the complexity of such models will likely expand. The thermodynamic switch function is an ideal candidate to model the sequence of less-known reactions for which microbial redox sequence has not been defined experimentally yet. Since the model incorporates the real values of major geochemical parameters (temperature, pH, ionic strength, solute concentrations), it could be well integrated into more sophisticated simulations of the aquatic environments where the environmental changes are expected to occur.

3.1 Introduction

Natural waters are dynamic systems with a continuous flow of mass and energy. By breaking down organic matter from dead plants and animals, many microorganisms har-

vest energy stored in reduced compounds and release nutrients to the ecosystem's food chain. Therefore, aquatic microorganisms play crucial roles in the cycling of nutrients within their environment, imposing the ultimate control on water quality and ecosystem sustainability. Vigorous microbial activity is often found at the environmental interfaces that are rich in nutrients and span over large redox gradients (Megonigal et al., 2003). A variety of redox-sensitive compounds imposes microbial competition for the most energy gaining reactions that result in the spatial and temporal distribution of nutrient concentrations.

The global cycles of major nutrients (*i.e.*, carbon, nitrogen, phosphorus, iron, sulfur) are interconnected with one another. Understanding of the mechanisms and regulatory factors of such complex biogeochemical systems requires laboratory investigations and numerical simulations. Never in equilibrium and orchestrated by microbial metabolism, the nutrient cycles are driven by the dissipation of energy from high-energy to low-energy state (Canfield et al., 2005). It translates to the ecosystems in a way that the overall metabolism with the largest free energy yield outcompetes less thermodynamically favored processes.

The typical redox sequence is schematically demonstrated in Figure 3.1. The sequence runs from oxygen reduction through nitrate and manganese to iron and sulfate

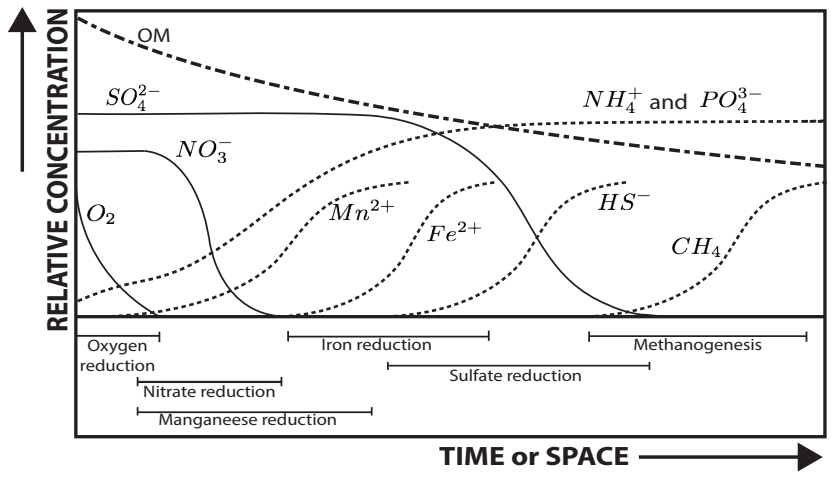

Figure 3.1: Transitional environments show a distinct redox zones in space or time with sequential reduction of oxygen, nitrate, manganese, iron and sulfate followed by methanogenesis.

reductions being coupled to organic matter oxidation and finishes by methanogenesis. So-called, redox cascades are often observed in wetlands (Achtnich and Schuhmann, 1995, Ponnamperuma, 1972, Yao et al., 1999) and upland soils (Peters and Conrad, 1996), in sediments (Froelich et al., 1979, Reeburgh, 1983) and stratified water bodies (Canfield and Thamdrup, 2009), in groundwater (Lovley et al., 1994) and contaminant plumes (Watson et al., 2005) in vadose zones (Rezanezhad et al., 2014) and hyporheic zones (Stegen et al., 2016, Van Cappellen and Slomp, 2004).

The rate of organic matter utilization is commonly modeled as a function of microbial growth rate. The empirical formulation of this model was first introduced in 1950 by Jacques Monod (Monod, 1950). Since then, for about 70 years, Monod type kinetics is being widely applied to simulate nutrient fluxes in biogeochemical systems. This model was initially developed to reproduce the maximum growth of a specific microbial culture by accounting for a single reaction. It explains the major limitation of the Monod equation, which does not allow its application for natural ecosystems full of simultaneous microbially mediated reactions.

The drawback of the Monod equation is in its failure to account for more than one redox reaction at a time when numerous electron acceptors (*e.g.*, oxygen, nitrate, sulfate) are present in the aquatic environment. Based on the laboratory and field observations, the oxidants are often consumed stepwise, creating the redox cascade of biogeochemical reactions. So that an additional multiplier is generally added to the Monod equation to limit the reaction as long as the other stronger oxidant is present in the system. It is done by introducing either conditional switches or inhibition terms that artificially prioritize one reaction over another (Arndt et al., 2013, Roden, 2008). Blanch (1981) summarized a wide variety of equations to describe the inhibition of metabolic pathways (Aiba et al., 1968, Boon and Laudelout, 1962, Humphrey, 1972, Yano et al., 1966). The inhibition constants are commonly used to represent the suppression of a given electron acceptor by a more favorable one (Aguilera et al., 2005, Haeckel et al., 2007, Jourabchi, 2007, Katsev and Dittrich, 2013, Markelova et al., 2018, Regnier et al., 2003, Thullner et al., 2009, Wang and Van Cappellen, 1996).

All biogeochemical models always represent significant simplifications of complex natural ecosystems that are coupled with a set of conceptual assumptions. The assumptions of the Monod equations with the multiplicative inhibition terms are simple, but at the same time, they lack general validity. In most cases, such models rely on the chain of kinetic switches to find the best fit to the experimental data without substantial fundamental justification. The model becomes highly specific to the physicochemical parameters of the system and cannot be applied for alternative conditions. Such models cannot be easily translated to other case studies. Moreover, purely kinetic representations of inhibition terms do not take into account the dynamic nature of environmental systems, such as changes in pH, temperature, ionic strength or redox state. These changes affect the thermodynamic driving force of energy-yielding reactions with the potential of shuffling the favorability of the specific elements and, thus, biogeochemical sequences.

Another common assumption of biogeochemical models is based on the constant (not-changing) conditions of the systems. Although laboratory studies aim to control system conditions manually, the environmental conditions in nature are highly dynamic. Therefore, most of the biogeochemical models remain study-specific and are incapable of reproducing high dynamic variability of the ecosystem in space and time. In order to scale-up model application from the laboratory to the field investigations, biogeochemical models should be able to account for the evolution of modelling parameters. Overall, the number of assumptions and calibrated parameters become rather formidable, and models seem to lose the sense of ecosystem functioning as a whole. A systematic understanding of how the sequence of redox reactions operates in the environment is still lacking.

Due to the high complexity of natural systems, observed redox sequences are seldom backed up with thermodynamic calculations. One of the most striking observations accounting for thermodynamic driving force was demonstrated by Lovley and Goodwin (1988) and Hoehler et al. (1998). In their separate studies, they noticed that in the particular cases, H_2 concentration can serve as a proxy to define the predominant terminal electron-accepting reactions in anoxic sediments. They conclude that *"this close link derives from a competition-induced necessity for terminal metabolic bacteria to maintain* H_2

concentrations as low as possible", *i.e.*, operate at their thermodynamic or physiological feasibility boundaries.

Depending on the dominant process consuming terminal electron acceptors, redox gradient zones have specific concentrations of electron donors, such as hydrogen gas and low-molecular-weight organic acids (Lovley and Goodwin, 1988). The observed pattern is attributed to the competitive exclusion process, whereby a microbial community outcompetes other contenders by maintaining the concentrations of electron donors near the threshold of the thermodynamic or kinetic feasibility (Lovley and Goodwin, 1988). To take into account these findings, Bethke et al. (2011) and LaRowe et al. (2012) have proposed factors to expand the Monod equation for the use in the energy-limited environments. The equation incorporate thermodynamic potential factor (F_T term), describing how rates may vary depending on the Gibbs Free Energy available in the environment.

When the thermodynamic limiting term supplements the Monod equation, the model becomes capable of calculating nutrient concentrations in low-energy environments. This expands the capacity of the Monod equation, which now can be applied in the energy-limited environment, such as pristine freshwater aquifers (Bethke et al., 2008) or deep marine sediments (LaRowe and Amend, 2015). Although, the F_T term suppress the reaction on the lower end, but it is careless for the simultaneous presence of other nutrients with higher energy yields under the non-limiting conditions. This motivated several scientific groups to investigate the application of the maximum entropy production principle to describe the internal organizations of the ecosystems (Vallino and Algar, 2016).

Vallino (2010) and Algar and Vallino (2014) examined the application of the maximum entropy production principle for describing ecosystem biogeochemistry. The authors introduced the novel rate expressions with new, although hard to justify, parameters, such as the characteristic timescale over which the optimization is performed and weighting term accounting for how much the optimization considers future events. They showed the modelling results for microbial community utilizing methanogenesis (Vallino, 2010) and three nitrate reduction pathways (Algar and Vallino, 2014). The authors concluded

that the regulation of biogeochemical reactions could be determined via the solution of an optimal control problem. Although the approach looks promising, an implementation of the numerically efficient optimization problem in ecological models along with *a priori* determination of the additional new parameters for the receding horizon functions of different biological systems are quite challenging tasks.

Our objective was to create a new model that would represent not only energy-limited systems, but also nutrient rich conditions, while avoiding numerous artificial assumptions. A new concept presented here accounts for dynamic conditions and provides a convenient and numerically efficient way to model the temporal and spatial sequencing of electron donors and acceptors based on energy supply rate. Below, we show three examples to illustrate it. First, we simulate the batch system of anoxic wetland sediment (Figure 3.31). Second, we simulate batch reactor of the syntrophic biodegradation in an anaerobic laboratory system of contaminant plume derived from sandstone material (Figure 3.32). Finally, we simulate reactions and transport in one-dimensional column of the lacustrine sediment (Figure 3.33).

3.2 Model Formulation

Microorganisms maintain their organized structure by harvesting energy from the low-entropy substrates while discarding high-entropy waste (Schrödinger, 1944). Although metabolic functioning is controlled by the laws of thermodynamics, it is rather impractical to measure the thermodynamic properties of the living organism due to the complexity of its structure. Thus, one may estimate the activity of a given microbial community by the net flow of chemical compounds (nutrients) and energy it consumes to grow and maintain their structure. In particular, by calculating the amount of energy that microorganisms harvest via the net flow of nutrients for the growth and maintenance:

$$\Delta G_i = \Delta G_i^{\circ} + R \cdot T \cdot \ln \prod_j (a_j)^{\nu_j} \tag{3.1}$$

where ΔG_i° – Gibbs energy of reaction at standard conditions ($J \cdot mol - e^{-1}$), a_j – activity of products and reactants, ν_j – stoichiometric coefficients, R – is the gas constant ($J \cdot mol^{-1} \cdot K^{-1}$), T – is the temperature (K).

As reviewed in the introduction, dual-Monod equation provides state of the art for the calculation of reaction rates driven by microbial activity, which can be generalized as follows:

$$R = \overline{r} \cdot X = \overline{r}_{max} \cdot \frac{[ED]}{K_m^{ED} + [ED]} \cdot \frac{[EA]}{K_m^{EA} + [EA]} \cdot X = \overline{r}_{max} \cdot F_K \cdot X \tag{3.2}$$

where R – is the substrate utilization rate ($mol \cdot L^{-1} \cdot s^{-1}$), $\overline{r}$ – is the substrate utilization rate per unit of biomass ($mol \cdot mol - C^{-1} \cdot s^{-1}$), X – is the biomass concentration ($mol - C \cdot L^{-1}$), $\overline{r}_{max}$ – is the maximum rate constant per unit of biomass ($mol \cdot mol - C^{-1} \cdot s^{-1}$), $[ED]$ – is the concentration of electron donor ($mol \cdot L^{-1}$), $[EA]$ – is the concentration of electron acceptor ($mol \cdot L^{-1}$), K_m^{ED} and K_m^{EA} – are the limiting half-saturation constants of ED and EA respectively ($mol \cdot L^{-1}$). F_K – is the dimensionless kinetic limitation factor.

In order to apply Monod equation to oligotrophic environments, a thermodynamic limiting factor F_T needs to be taken into account:

$$R = \overline{r}_{max} \cdot F_K \cdot F_T \cdot X \tag{3.3}$$

where F_T – is the dimensionless thermodynamic factor of LaRowe et al. (2012) or Bethke et al. (2011). In turn, the F_T accounts for specific parameters, such as the membrane potential and Gibbs Free Energy, and in LaRowe et al. (2012) form it is expressed as follows:

$$F_T = \frac{1}{exp\left(\frac{\Delta G_i + F\Delta\Psi}{RT}\right) + 1} \tag{3.4}$$

where F – is the Faraday constant ($J \cdot V^{-1} \cdot mol - e^{-1}$), $\Delta\Psi$ – is the membrane potential (V).

In order to take into account the presence of other nutrients with higher energy yield and dynamic nature of the reactive systems, we suggest modelling competitive catabolic

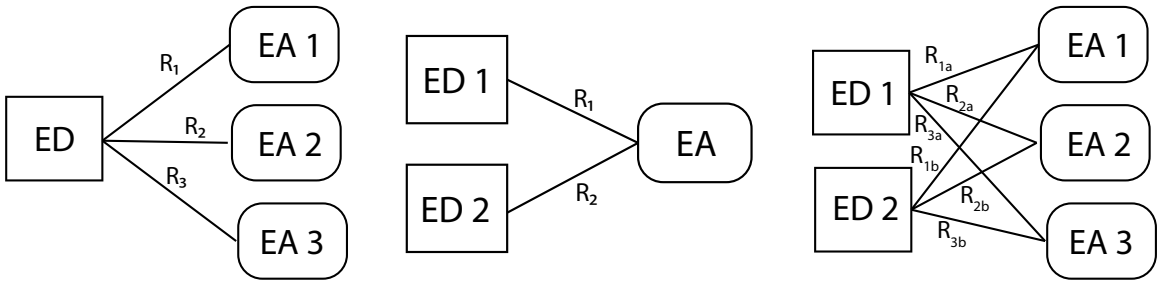

(a) EA_i (b) ED_i (c) $ED_i \cap EA_i$

Figure 3.2: Microbial consumption of: a) the most energetic electron acceptor, b) the most energetic electron donor, and c) combination of both.

reactions using thermodynamic switch function, F_E. Then the overall generalized equation that accounts for multicomponent systems is as follows:

$$R = \overline{r}_{max} \cdot F_K \cdot F_T \cdot F_E \cdot X \tag{3.5}$$

Dimensionless thermodynamic switch function is estimated for every catabolic reaction as a fraction of potential power produced via this reaction pathway to the total potential power available in the system where this specific function group is involved in the given moment of time:

$$F_{Ei} = \frac{\overline{P_i}}{\sum_{j=1}^{M} \overline{P_j}} \tag{3.6}$$

where $\overline{P_i}$ – is the potential energy supply rate, or power, per unit of biomass of the catabolic reaction and presented as follows:

$$\overline{P_i} = \Delta G_i \cdot \overline{r}_i \tag{3.7}$$

As an example, consider a simple case with one electron donor and three electron acceptors (Figure 3.2a). Possible reaction pathways are R_1, R_2, and R_3. Thus, the thermodynamic switch function of the reaction pathway R_2 could be estimated as the fraction of the potential energy supply by reaction R_2 to the sum of potential energy

supplies by all possible reaction pathways with the given electron donor, ED:

$$F_{e2} = \frac{P_2}{P_1 + P_2 + P_3} = \frac{\Delta G_2 \cdot \overline{r}_2}{\Delta G_1 \cdot \overline{r}_1 + \Delta G_2 \cdot \overline{r}_2 + \Delta G_3 \cdot \overline{r}_3} \tag{3.8}$$

where $\overline{r}_i$ – is the electron transfer rate per unit of biomass for i^{th} reaction eE.n 3.2), ΔG_i – is the Gibbs Free Energy of the reaction (eq. 3.1). Then, the overall reaction rate equation becomes:

$$R_2 = \overline{r}_2 \cdot X_2 \cdot \frac{\Delta G_2 \cdot \overline{r}_2}{\Delta G_1 \cdot \overline{r}_1 + \Delta G_2 \cdot \overline{r}_2 + \Delta G_3 \cdot \overline{r}_3} \tag{3.9}$$

The second example demonstrates the modelling of the rate of the preferential catabolic reaction between two electron donors and a sole electron acceptor (Figure 3.2b). Then, the energy supply term for the reaction pathway R_1 becomes the following:

$$F_{e1} = \frac{P_1}{P_1 + P_2} = \frac{\Delta G_1 \cdot \overline{r}_1}{\Delta G_1 \cdot \overline{r}_1 + \Delta G_2 \cdot \overline{r}_2} \tag{3.10}$$

As for more complex example, consider the case when microbially mediated reaction network consists of two electron donors and three electron acceptors (Figure 3.2c). In this case, the energy supply term for the reaction pathway R_{2b}, for example, is the product of the energy supply terms of the reactions involving both electron donor ED2 and electron acceptor EA2:

$$\begin{aligned} F_{e2b} &= \frac{P_{2b}}{P_{2a} + P_{2b}} \times \frac{P_{2b}}{P_{1b} + P_{2b} + P_{3b}} = \\ &= \frac{\Delta G_{2b} \cdot \overline{r}_{2b}}{\Delta G_{2b} \cdot \overline{r}_{2b} + \Delta G_{2a} \cdot \overline{r}_{2a}} \times \frac{\Delta G_{2b} \cdot \overline{r}_{2b}}{\Delta G_{1b} \cdot \overline{r}_{1b} + \Delta G_{2b} \cdot \overline{r}_{2b} + \Delta G_{3b} \cdot \overline{r}_{3b}} \end{aligned} \tag{3.11}$$

The primary advantage of the thermodynamic switch function is that it takes into account the dynamics of the system that can change the energetics of the reactions and

produce tipping points. Below, we show several examples to demonstrate the capabilities of the thermodynamic switch function.

3.3 Model Application and Discussion

The model of microbial functioning under dynamic conditions is represented by a set of differential equations that can be solved in any simulation program (e.g., Comsol, PHREEQC *etc.*). The Gibbs Free Energy values of reactions shall be calculated based on the thermodynamic databases. In this study, we calculated dynamic Gibbs Free Energy values by using a comprehensive database and numerical solver implemented in PorousMediaLab. PorousMediaLab is a computer program written in Python programming language that is designed to perform a wide variety of kinetic and thermodynamic biogeochemical simulations in the aquatic environment (Markelov, 2019). By automatic calculation of dynamic Gibbs Free Energy values, we derived the thermodynamic switch function at every simulation timestep.

Although the results of laboratory studies could not be simply extrapolated to the natural complexity of aquatic systems, they provide advantages to compare our understanding of the real systems with their idealized counterparts. Below, we test the model against measured data acquired from the laboratory experiments of the batch system with

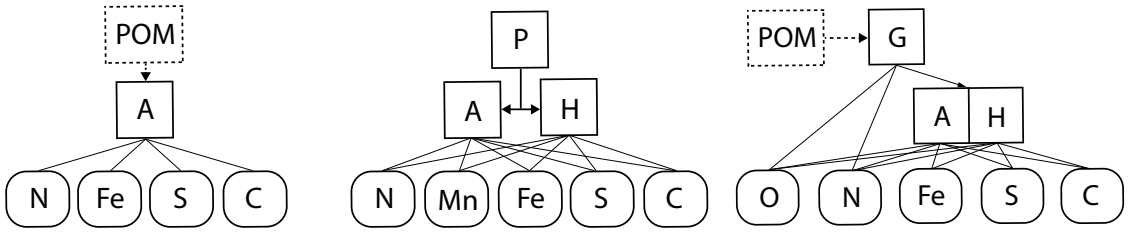

(1) Roden (2008) (2) Watson et al. (2003) (3) Sediment example

Figure 3.3: Competitive reaction pathways considered in the experimental work of (1) Roden (2008), (2) Watson et al. (2003) as well as (3) sediment example, where POM stands for particulate organic matter, P - phenol, G - glucose, A - acetate, H - hydrogen, O - oxygen, N - nitrogen, Mn - manganese, Fe - iron, S - sulfur, and C - carbon. Dashed arrows represent hydrolysis, solid lines - catabolic (fermentation and respiration) reaction pathways. Preference of the particular reaction pathway is defined by the energy supply term.

Table 3.1: Stoichiometry and standard Gibbs Free Energy of microbially mediated reactions considered in **1** - example 1: wetland sediment (Roden, 2008), **2** - example 2: contaminant degradation in sandstone material (Watson et al., 2003), and **3** - example 3: freshwater sediment example. The units of Gibbs Free Energy are kJ per $mol \cdot \overline{e}$.

no.	**1**	**2**	**3**	**Stoichiometry**	ΔG^0
R1G			•	$C_6H_{12}O_6 + 6\,O_2 \longrightarrow 6HCO_3^- + 6H^+$	-112.6
R2G			•	$C_6H_{12}O_6 + 4.8\,NO_3^- + \longrightarrow 6\,HCO_3^- + 1.2\,H^+ + 2.4\,N_2(aq) + 2.4\,H_2O$	-107.9
R3G			•	$C_6H_{12}O_6 + 4\,H_2O \longrightarrow 2\,CH_3COO^- + 2\,HCO_3^- + 4\,H^+ + 4\,H_2$	3
R1P		•		$C_6H_6O + 5\,H_2O \longrightarrow 3\,CH_3COO^- + 2\,H_2 + 3\,H^+$	20.3
R1A			•	$CH_3COO^- + 2\,O_2 \longrightarrow 2\,HCO_3^- + 8\,H^+$	-104.7
R2A	•	•	•	$CH_3COO^- + 1.6\,NO_3^- + 0.6\,H^+ \longrightarrow 0.8\,N_2 + 2\,HCO_3^- + 0.8\,H_2O$	-100
R3A		•		$CH_3COO^- + 4\,MnO_2 + 5\,H^+ \longrightarrow 4\,Mn^{2+} + 2\,HCO_3^- + 4\,H_2O$	-100.7
R4A1	•			$CH_3COO^- + 8\,Fe(OH)_3 + 15\,H^+ \longrightarrow 8\,Fe^{2+} + 2\,HCO_3^- + 20\,H_2O$	-84.5*
R4A2		•	•	$CH_3COO^- + 8\,FeOOH + 15\,H^+ \longrightarrow 8\,Fe^{2+} + 2\,HCO_3^- + 12\,H_2O$	-55.5*
R5A	•	•	•	$CH_3COO^- + {SO_4}^{2-} \longrightarrow 2\,HCO_3^- + HS^-$	-5.9
R6A	•	•	•	$CH_3COO^- + H_2O \longrightarrow HCO_3^- + CH_4$	-1.8
R1H			•	$H_2 + 0.5\,O_2 \longrightarrow H_2O$	-131.6
R2H		•	•	$H_2 + 0.4\,NO_3^- + 0.4\,H^+ \longrightarrow 1.2\,H_2O + 0.2\,N_2$	-126.9
R3H		•		$H_2 + MnO_2 + 2\,H^+ \longrightarrow 2\,H_2O + Mn^{2+}$	-127.6
R4H		•	•	$H_2 + 2\,FeOOH + 4\,H^+ \longrightarrow 4\,H_2O + 2\,Fe^{2+}$	-82.4*
R5H		•	•	$H_2 + 0.25\,{SO_4}^{2-} + 0.25\,H^+ \longrightarrow H_2O + 0.25\,HS^-$	-32.7
R6H		•	•	$H_2 + 0.25\,HCO_3^- + 0.25\,H^+ \longrightarrow 0.75\,H_2O + 0.25\,CH_4$	-28.7

anoxic wetland sediment, a batch reactor with contaminant derived from sandstone material. Finally, we showcase an example of reactions and transport in a one-dimensional column of the lacustrine sediment.

3.3.1 Example 1: Batch Reactor with Wetland Sediment

In the first example, we demonstrate the application of thermodynamic switch function to reproduce the experimental results of organic matter degradation with a set of terminal electron acceptors present in the slurry of wetland sediments published by Roden (2008). In the experimental work, organic-rich (20-30% dry weight) and iron-rich (5% dry weight) sediments were obtained from an artificially flooded freshwater wetland located in the Talladega National Forest, USA (Roden and Wetzel, 2002). Batch reactor experiments were performed in homogenized anaerobic sediments mixed with synthetic groundwater to provide nitrate (NO_3^-) and sulfate (${SO_4}^{2-}$). Concentrations of NO_3^-, ${SO_4}^{2-}$, HCl-extractable amorphous Fe(III) and Fe(II), total CO_2 and CH_4 were measured using methods described in Roden and Wetzel (1996). Experimental data shows a typical

case when electron acceptors are consumed sequentially from the most energy-yielding NO_3^- to a less energy-yielding SO_4^{2-}, followed by methanogenesis (Figure 3.4).

In the original paper, Roden (2008) created three models representing experimental results. The author increased the complexity of the models to showcase different approaches for imposing the segregation of microbial redox processes. In the first and second modelling examples, the author used first-order kinetics with conditional switches and inhibition constants to artificially impose the separation of redox processes. In the third model, the degradation of organic matter was model through two sequential steps: hydrolysis of particulate organic matter and respiration of acetate. The author used a dual-Monod equation without inhibition terms but imposed the reaction sequence by limiting the concentration of the acetate produced during hydrolysis. Additionally, the parameters of the initial population densities of microorganisms capable of nitrate, sulfate, and iron reduction, as well as methanogenesis, were calibrated to fit the experimental data. That is, by setting low initial value of the particulate microbial community, the corresponding redox reaction was artificially delayed due to the slow microbial growth in the initial phase. Overall, all models presented in the original work were able to reproduce the reaction sequence quite well. However, it required numerous calibrated and kinetic parameters. In the third model, for instance, 21 kinetic parameters were supplemented by 4 adusted initial microbial population densities (Table 8.6 in Roden, 2008).

In the model presented here, the degradation of organic matter is considered in two sequential steps (Figure 3.31). In the first step, the hydrolysis of the organic matter produces acetate, which is being oxidized at the second step. The hydrolysis reaction is modeled as a first-order rate law with a hydrolysis constant of 0.1 d^{-1}, which was derived in the original work of the experimental study. The oxidation of acetate is coupled to a set of the reduction reactions with nitrate (reaction R2A in Table 3.1), iron oxide (R4A1), sulfate (R5A) and carbon dioxide (R6A). At this step, the dual-Monod equation supplemented by thermodynamic term F_T and thermodynamic switch function F_E was applied to reproduce catabolic reaction pathways. The thermodynamic term was calculated with the membrane voltage potential, $\Delta\Psi$, of 160 mV for all reactions. For simplicity, the concentration of the

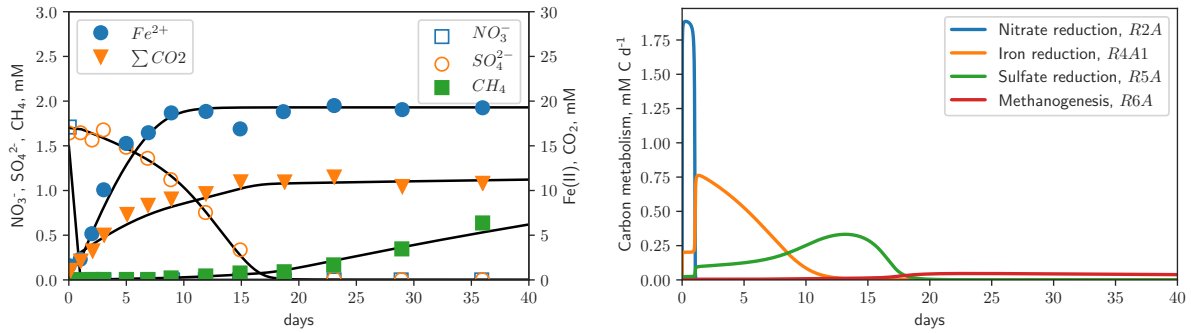

(a) Concentrations

(b) Rates

Figure 3.4: Experimental data of organic matter degradation with a set of terminal electron acceptors in slurry of anoxic wetland sediment (Roden, 2008) and simulation using thermodynamic switch function. The experiment . a) Simulated (solid lines) and measured (symbols) concentrations of NO_3^-, SO_4^{2-}, Fe(II), $\sum CO_2$, and CH_4(g). b) Simulated rates of carbon metabolism in the reactions of denitrification $R2A$, iron reduction $R4A1$, sulfate reduction $R5A$ and methanogenesis $R6A$ (Table 3.1). The experimental data were taken from the original work (Roden, 2008).

biomass concentration was kept constant incorporated in the maximum rate constants, *i.e.*, $\hat{r}_{max} = \overline{r}_{max} \cdot X$. The maximum rate constants $\hat{r}_{max}$ of nitrate, iron, and sulfate reduction as well as of methanogenesis equal to 2.6, 1.7, 0.7, 0.2 d^{-1}, respectively. Limiting concentrations of 0.2, 0.01, 3, and 0.006 $mmol \cdot L^{-1}$ were assumed for CH_3COO^-, NO_3^-, Fe(III) oxide surface sites, and SO_4^{2-}, respectively. Parameters used in the simulation are in the ranges of the values reported in the literature (Supplemental information, Table C1). Overall, the application of the thermodynamic switch function decreases the number of calibrated parameters from 25 in the original model to 10 used in our model. Our model with the thermodynamic switch funciton represents experimental data quite well and eliminates unnecessary assumptions.

3.3.2 Example 2: Batch Reactor with Sandstone Material

In the second example, the thermodynamic switch function is applied to simulate the 600-day experiment of phenol degradation in the sandstone suspension (Watson et al., 2003). The rock sample was acquired from the aqueous plume area of the Four Ashes site (Thornton et al., 2001). A batch study was set with the sandstone material serving as a source of microbial community nourishing in iron- and manganese-bearing minerals.

Additionally, to the solid electron acceptors, natural sandstone was dispersed in sterile synthetic groundwater carrying aqueous electron acceptors (NO_3^- and SO_4^{2-}) to empower microbial phenol oxidation.

We applied the thermodynamic switch function not only to reproduce the experimental results of this study, but also to improve fundamental system understanding. In the original model of this study, a number of kinetic parameters were chosen arbitrarily to obtain the best fit between the model and the measurements. At least six parameters were based on manually imposed inhibition terms, which were applied non-consistently thought the model.

For example, different inhibition terms defining microbial preferences were assumed for different electron donors. So that, acetate oxidation incorporated two inhibitors (NO_3^- and SO_4^{2-}), while neglected two other possible inhibitors (manganese- and iron-bearing minerals). Meanwhile, in the reactions of hydrogen oxidation, the inhibitors were iron minerals and sulfate. Moreover, in reactions with hydrogen, the availability of Fe was constrained by the implementation two artificial pools: highly and slowly reactive mineral phases (Table 2 in Watson et al., 2003). The definition of the inhibition constants was rather complicated and non-straightforward most likely due to the absence of experimental evidence of such complex biogeochemical interplay.

Therefore, our goal was to represent experimental data by closely following the original model formulation and at the same time, minimizing a number of assumptions and calibrated parameters. The key concept of syntrophic phenol biodegradation via fermentation and respiration is preserved in our model (Christensen et al., 2000). Whereas, dual-Monod kinetic formulation coupled with thermodynamic switch F_E (eq. 3.5) replaces a number of calibrated inhibition terms. Moreover, in order to keep the consistency of modelling assumptions, we apply the same parameters for both electron donors, i.e., acetate and hydrogen. The overall Gibbs Free energies of the reactions are summarized in Table 3.1 and detailed parameters are provided in the supplemental information (Table C1).

By decreasing a number of calibrated parameters and assumptions, the model be-

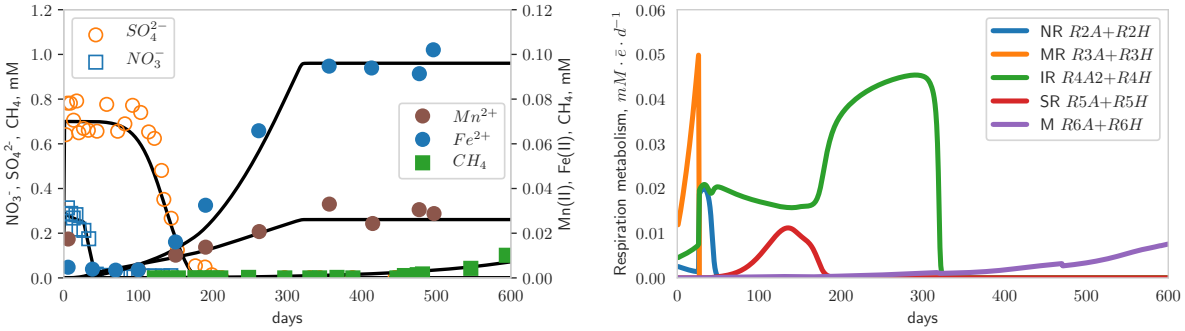

(a) Concentrations (b) Rates

Figure 3.5: Results of microcosm simulation of the experimental work of Watson et al. (2003). a) Concentrations of selected species reported in the original work. Symbols represent digitalized experimental data, lines are simulated by the model with thermodynamic switch function. b) Overall respiration rates utilizing both acetate and hydrogen of nitrate reduction (NR), manganese reduction (MR), iron reduction (IR), sulfate reduction (SR), and methanogenesis (M). The experimental data were taken from the original paper.

came robust and was able to closely reproduce experimental results. The application of the thermodynamic switch function indicated that there is no need to artificially increase complexity of the modeled system for understanding the consumption of Fe, as it can be modeled as a homogeneous mineral phase. Moreover, it is evident from the model, that both iron and nitrate reductions start at the beginning of the experiment, but are suppressed by manganese reduction, which is in agreement with other studies with acetate and hydrogen (DiChristina, 1992). The most striking outcome of the model is that iron and sulfate reductions are found to occur simultaneously from day 100 to 200. Such complex interplay of reaction power and kinetics implies that simplified inhibition terms are of no use for data interpretation. A more detailed comparison of the original model Watson et al. (2003) with the modified model of this study is provided in the supplemental information (Figure C1).

3.3.3 Example 3: Freshwater Sediment Column

In the third example, the model is tested for the complex multi-component system, that is more likely to better represent the natural diversity of aquifers. However, most of the experimental studies employ limited number of redox-active species. Therefore,

the biogeochemical system of organic matter degradation in aquatic sediment used in this example is a hypothetical, rather than experimentally derived one. As a typical case-study, we assume one-dimensional sediment column that consists of the organic material and iron minerals providing suitable conditions for microbial activity. Physical properties of the sediment column, system boundary conditions, transport and reaction parameters used in the simulation are listed in (Tables C1, C2, and C3).

The model assumes that aqueous electron acceptors (oxygen, nitrate and sulfate) diffuse from the top of the sediment column, where a constant flux of solid settling material is imposed. The fate of organic matter is assumed to be driven by an interplay of hydrolysis, fermentation, and oxidation reactions coupled to all available electron donors and acceptors (Figure 3.33 and Table 3.1). Overall, the model is tested to predict the biogeochemical interplay and sequence of 13 redox reactions comprising 3 electron donors and 5 electron acceptors. The simulations address two scenarios of environmental conditions, such as pH 6.5 and 7.5, to demonstrate that the model is capable of reflecting natural dynamics.

The modelling results at steady-states demonstrate the increase of pH from 6.5 to 7.5 causes the decrease of thermodynamic favorability for 9 biogeochemical reactions (Table 3.1). However, the kinetic rates of only five catabolic reactions are decreasing and that ultimately defines the system overall behavior. Significant thermodynamic suppression of the iron reduction has led to excess availability of the acetate and hydrogen for other respiration pathways. As a result, seven different catabolic reaction rates are increased (Table 3.2). The highest increase in the overall rate is estimated for the aerobic respiration of acetate (more than five times of growth). Although the total sediment oxygen demand

Table 3.2: Integrated over the depth steady state rates of two microcosm simulations in sediment with fixed pH of 6.5 and pH 7.5. The units of the rates are $mM \cdot cm^{-2} \cdot d^{-1}$.

no.	**R1G**	**R2G**	**R3G**	**R1A**	**R2A**	**R4A2**	**R5A**	**R6A**	**R1H**	**R2H**	**R4H**	**R5H**	**R6H**
pH 6.5	0.09	0.12	0.94	0.01	0.02	0.55	0.05	0.046	0.002	0.005	0.147	0.046	0.102
pH 7.5	0.12	0.08	0.89	0.07	0.05	0.22	0.08	0.039	0.002	0.009	0.152	0.048	0.073
Δ, %	18	-35	-5	580	181	-60	58	-15	0	80	4	4	-28

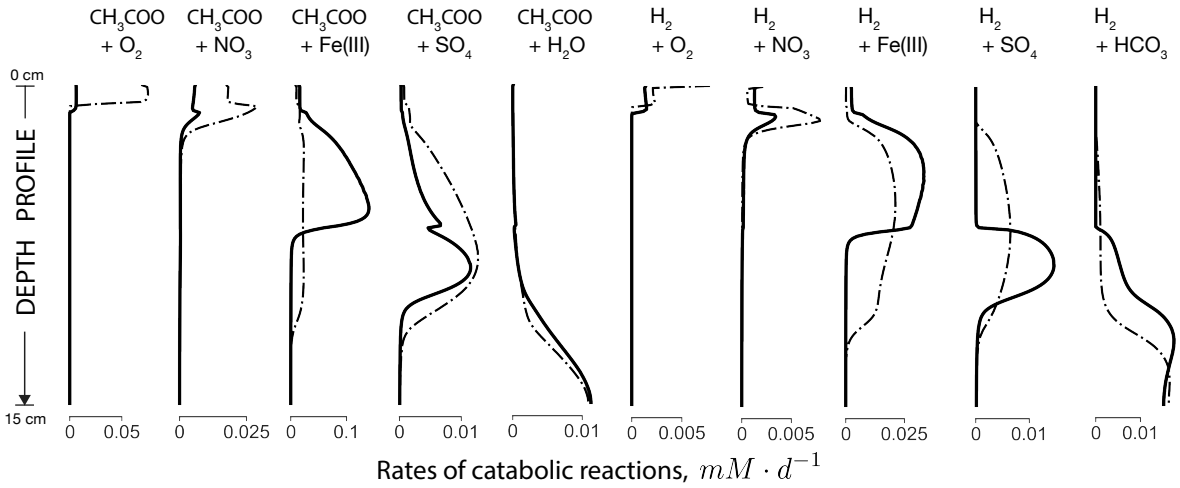

Figure 3.6: Steady state rates of the acetate and hydrogen catabolic reactions. Solid lines represent rates under pH 6.5, dash-dotted lines represent rates at pH 7.5. The units are $mM \cdot d^{-1}$.

stays about the same (not shown), there is a re-distribution of the oxygen consumption from the oxidation of less produced Fe (II) to oxidation of the building acetate (Table 3.2). At the same time, the increase of pH makes the reaction iron reduction with acetate R4A2 less favorable, and, as a result, an integrated over the depth rate drops significantly (Table 3.2). The potential energy supply rate of the reaction becomes comparable with that of the sulfate reducing reaction R5A, and, as a result, the reactions co-occur and overlap at the depths from 2 to 12 *cm* (Figure 3.6). In contrast, there is an overlap of the sulfate reduction with methanogenesis at pH 6.5, whereas, the reductive pathway zones are more distinct at pH 7.5.

Although it is out of the scope of this study, suppressed Fe(II) recycling in the lacustrine sediment may potentially result in harmful effects to the lake. Firstly, lower concentrations Fe(II) may lead to an increase of the internal P load in the water column of the lake from the sediment due to the decrease of the co-precipitation and formation of Fe and P bearing minerals (Markelov et al., in review). Likewise, the absence of ferrous iron and formation of fresh iron minerals in sediment could result in the increased efflux of the toxic sulfide to the bottom waters due to i) enchased reduction of sulfate in the deficiency of iron reduction (as shown here), and ii) decreased precipitation of the secondary minerals such as mackinawite and pyrite in the lack of ferrous iron (Smolders et al., 1995). Those simulations would not be possible using standard kinetic approaches with inhibition or

conditional switches.

3.4 Concluding Remarks

Presently, redox sequences are mainly described by number of calibrated kinetic parameters and are seldom backed up with thermodynamic calculations. Previously developed conditional switches or inhibition terms would work in relatively simple systems, however, they are incapable of dealing with dynamic changing conditions and multiple reactions taking place in parallel. In this study, we provide a new concept that goes beyond the kinetic calibrations and accounts for thermodynamics of the whole reaction network. We created a new model which is able to reproduce segregation of microbial redox processes while avoiding numerous artificial assumptions and calibrated parameters. In particular, by introducing the thermodynamic switch function to Monod kinetics, the model becomes a powerful tool in predicting future system behavior accounting for dynamic environmental conditions. Potentially, the model could become useful not only for the description of experimental results, but also for providing fruitful generalizations and valuable insights from laboratory to field scale observations.

The thermodynamic switch function can be applied for the systems with other less-known redox reactions for which the redox sequence has not been evaluated experimentally yet. As Gallagher et al. (2014) noted, using a generalized formula for electron donors can miss the potentially important link between electron donors and alkalinity. Depending on the available electron donor such as hydrogen, formate, acetate, propionate, butyrate, ethanol, methanol, and lactate, net community metabolism may differently change pH, and therefore, shuffle redox sequences and change saturation states of the minerals. As a result, the use of the generalized formula for electron donors may undervalue the role of net community metabolism on environmental conditions and misinterpret the direction of the ecosystem change.

Moreover, presently, in state of the art diagenetic models, the microbial oxidation of the methane, sulfide, ferrous iron, and ammonia are entirely disregarded. Instead, these

reactions are usually represented by the abiotic second order rates. An interplay of microbial oxidation reactions with organic matter degradation under changing environmental conditions may have substantial implications on ecosystem functioning. In these cases, the model with the thermodynamic switch function can be applied as a predictive tool with an arbitrary large reactive networks to guide long-term management strategies and governance of aquatic environments.

Finally, with the expansion of the "omics" data (Perez-Riverol et al., 2017), new previously unknown reaction pathways will likely emerge, and the parameterization of the microbial redox models will be impractical or even impossible task. Instead, model representation with the thermodynamic switch function where each reaction is coupled to the specific groups of functional genes can directly link the "omics" measurements with simulated results. All of the above let us conclude that models such as ours will be well suited not only to compare with the data but also to make predictions for scenarios of the evolving natural ecosystems.

Chapter 4

Variations of the Water Balance of a Large Temperate Lake (Lake Erie, Canada-USA) from 1917 to 2017

Igor Markelov
Serghei A. Bocaniov
Homa Kheyrollah Pour
Raoul-Marie Couture
Philippe Van Cappellen

Summary

We analyzed and constrained the water budget of Lake Erie using a century-long data of separate hydrological components, such as river discharges, over-lake precipitation, evaporation, consumptive use, and diversions. Our water budget estimates indicate that (i) ratio of land runoff to precipitation is steadily increasing since the early 20^{th} century, (ii) surface water elevation dynamics is driven by the outflow from the upper Laurentian Great Lakes, and (iii) variations in annual water budgets of Lake Erie are influenced by El Niño-Southern Oscillation cycle and weather in the upper Laurentian Great Lakes. Our study confirms that spring precipitation and runoff are significant additional contributing factors in the resurgence of algal blooms. In addition, summer circulation patterns in Lake Erie simulated by 3D hydrodynamic models (Beletsky et al., 2013, Niu et al., 2015) and wave direction measurements from buoy 45005 (West of Lake Erie) suggest that recent resurgence of the algal blooms can be attributed to the westward transport of the DRP from the central basin accumulated during the extended periods of the summer hypoxia.

4.1 Introduction

Accurate estimates of the water balance of lakes are required for formulation of regulatory plans, operational regulation, and forecasting of water level. Rising and falling water levels may affect navigation, water supply, and intensify of the erosion of the coastal areas. Lake Erie, the fourth largest lake by surface area shared by two countries, spans three United-States states and one Canadian province. It is an economically and ecologically important lake within the Laurentian Great Lakes (LGLs). Quantifying the mass water balance of Lake Erie is one of the preliminary steps for developing hydrological and lake water quality models, maintaining the quality of the ecosystem services. The first estimates of the water budget of Lake Erie dates back as early as 1927 (Horton, 1927). Previous studies focused either on the Lake Erie water budget (Derecki, 1976b, Quinn and Guerra, 1986) or on the lake as a part of Great Lakes system (Bengtsson et al., 2012, Chapra and Dolan, 2012, Gronewold et al., 2016).

Human activities and an increasing rate of urbanization have resulted in more frequent floods and faster over-land flow regimes (Burns et al., 2005, Nirupama and Simonovic, 2006, Poff et al., 2006). The long-term human activities in the Lake Erie basin, such as deforestation, including all other types of land clearing, and urbanization, contribute to the increase of the runoff coefficient, *i.e.,* the ratio between surface runoff and precipitation. However, minimal attempts have been made to show the long-term effects of land-use on surface runoff and differentiate them from hydrological responses of climate change.

There have been a number of studies focusing on the water budget of Lake Erie, however, large uncertainty still remains as corresponding role of the upstream LGLs system has not been clearly demonstrated (Bengtsson et al., 2012, Chapra and Dolan, 2012, Derecki, 1976b, Quinn and Guerra, 1986). The upper LGLs (Superior, Michigan and Huron), located upstream of Lake Erie, have a total watershed area of five times that of Lake Erie. Therefore, it is reasonable to expect that the water budget of Lake Erie could be responsive to the inflow water volume from connecting (upstream) channels, which are comparable to that from the lake's own watershed. Nevertheless, the relative roles of Lake Erie's precipitation and inflow from the upstream lakes have not been sufficiently demonstrated with regard to observed fluctuations in lake water levels.

An additional factor influencing water budget of lakes with large basin area is atmospheric circulation (Scott and Huff, 1996, Winter, 1995). The basin area of LGLs is more than 500,000 km^2 (Neff and Nicholas, 2004). Large-scale atmospheric circulations and decadal land-ocean variability operates over similar or larger spatial scales (>1000 km). For example, the east-central Equatorial Pacific Circulation (El Niño-Southern Oscillation cycle: ENSO) affects over-land precipitation, temperature and it is responsible for warmer (El Niño) and colder (La Niña) weather conditions across Canada and USA. However, climate-related atmospheric circulation variability and its effect on the water budget of LGLs has received little attention in the literature to date.

Lake Erie suffered from deteriorating quality of the ecosystem services that it provides, mainly due to intense algal blooms since the 1970s. Two decades ago, after changing

the policy on using phosphorus in detergent and setting up the target on total phosphorus (TP) load stemming from fertilizer applications, the blooms disappeared (Scavia et al., 2014). Nevertheless, Lake Erie experienced a revival of the algal blooms since 2008. Previous studies suggest that causes for the recent events include an increase of bioavailable phosphorus (Jarvie et al., 2017), internal phosphorus loading (Matisoff et al., 2016), invasive mussel species (Karatayev et al., 2014), and meteorological conditions (Michalak et al., 2013). Systematic identification and quantification of the drivers of the algal blooms are essential for regulators, stakeholders, and the scientific community. Therefore, statistical, probabilistic, and mechanistic model forecasts are active fields of the research for water quality forecasting and bloom predictions in Lake Erie. The water mass balance is the essential preliminary step for the building of such models.

Herein, we hypothesize that: (i) the ratio of land runoff to precipitation (runoff coefficient) in Lake Erie basin should be increasing over the historical period of observations since the early 20^{th} century due to deforestation and urbanization of the watershed; (ii) the outflow from the upper LGLs is significant factor that drives variations in the annual water budget of Lake Erie; and (iii) the long-term water budgets of Lake Erie are correlated with the modes of large-scale atmospheric ENSO cycle. To check our hypotheses, first, we examine the century-long (1917-2003) variations of water level, precipitation, evaporation, and runoff to study the effect of climate forcing on the water budget of Lake Erie. For that, we perform statistical as well as time-frequency analyses. Secondly, this paper estimates the net basin-wide water mass balance of Lake Erie that covers 15 years, from 2003 to 2017. Based on previous estimates of Michalak et al. (2013) for 2011, we hypothesize that timings and magnitude of precipitation and runoff are significant contributing factors in algal blooms during the recent decade. Moreover, we suggest that future bloom forecast models should give special attention to inter-basin and basin-wide circulation, emphasizing the importance of the spatial hydrodynamic circulation.

4.2 Methods

4.2.1 Site Description

The LGLs constitute the largest amount of fresh surface water in the western hemisphere. Out of five lakes, Lake Erie is the fourth-largest, southernmost, shallowest, and most biologically productive. The lake serves as a water source for public water supply, and supports recreation and fishing activities, industrial and agricultural needs. It is 400 km long, about 90 km wide, it covers 25,700 km^2 and contains approx. 484 km^3 of water (Figure 4.1). Lake Erie consists of three different basins: the western (WB), central (CB), and eastern (EB). The western basin is the shallowest basin (mean depth = 7.3 m, volume = 24 km^3) with a water residence time of 0.13 *years* (Matisoff et al., 2016). The central basin is the intermediate by depth and the largest by volume (mean depth = 18.5 m; volume = 305 km^3) with a water residence time of 1.74 *years* (Bocaniov et al., 2016). The eastern basin is the deepest basin and intermediate by volume (mean depth = 24.4 m; volume = 154 km^3), and a water residence time of 0.89 *years* (Bocaniov et al., 2016). Lake Erie basin also includes Lake St. Clair, a large shallow lake (mean depth = 3.8 m, volume 4.25 km^3; Bocaniov et al., 2018) with two connecting channels, St. Clair and Detroit rivers (Figure 4.1).

The total drainage area of Lake Erie including the Huron-Erie corridor (HEC), which itself consists of the St. Clair and Detroit Rivers and Lake St. Clair sub-watersheds has an area of 77,213 km^2 with 71% and 29% of the watershed area located in the USA and Canada, respectively (Figure 4.1, Table 4.1).

4.2.2 Water Mass Balance

Here, the water mass balance (Equation 4.1) has been estimated for the period from 2003 to 2017 as the difference between the inflows and the outflows of the hydrological components such as over-lake precipitation (P), surface runoff (R), inflow and outflow via the connecting channels (C_{in} and C_{out}), over-lake evaporation (E), consumptive use (W),

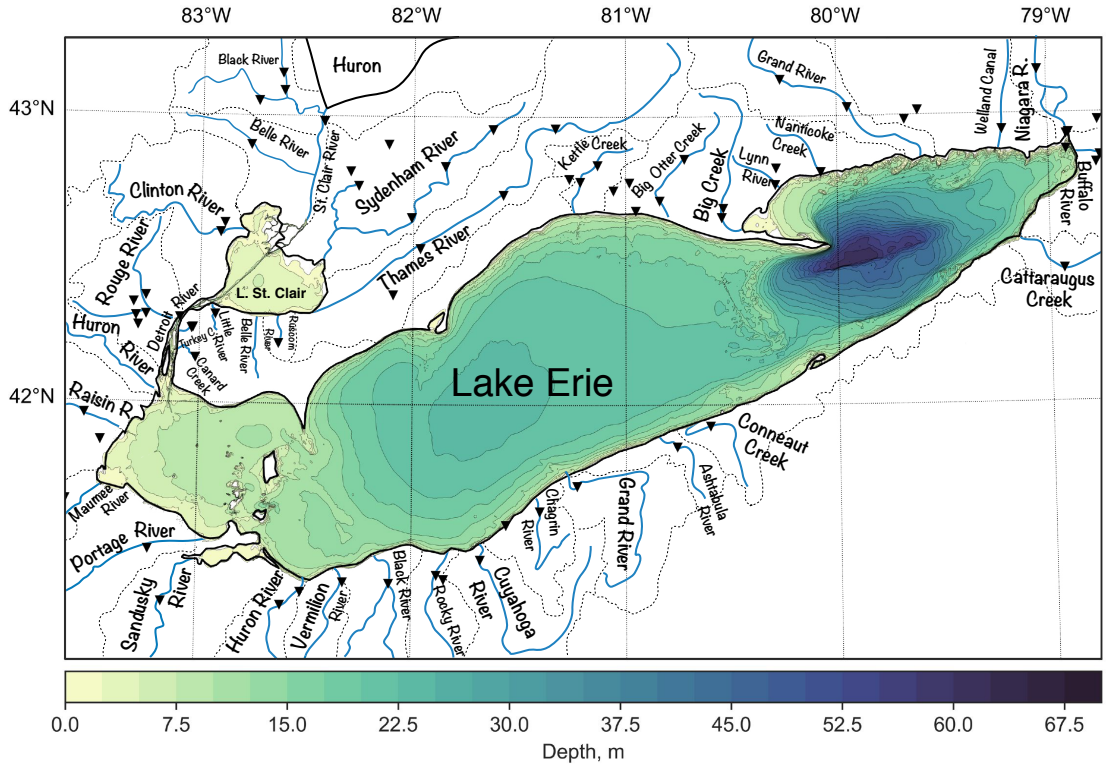

Figure 4.1: Bathymetry of Lake Erie and Lake St. Clair with the largest rivers and their corresponding watersheds (thin dashed lines). Triangles represent the locations of gauging stations (Table C1, supporting information).

and outflow via lake diversions (D):

$$dV/dt = P + R + C_{in} - E - C_{out} - W - D \tag{4.1}$$

Previous studies suggest that groundwater inputs to the Lake Erie and Lake St. Clair are not likely to be a significant component of the total water budget with varying fluxes in the range from 0.9 to 3.7 cubic meters per second (cms) per 100 km of the shoreline (Neff and Nicholas, 2004). Isostatic rebound and thermal expansion are considered to have relatively negligible contributions to the water budget (Derecki, 1976a, Mainville and Craymer, 2005, Meredith, 1975, Quinn and Guerra, 1986). The annual water balance is calculated for the standard water year (October 1 to September 30). Below, we discuss the potential uncertainties associated with each hydrological component used in this study.

4.2.3 Data

Due to the unavailability of the high-resolution historical data, hydrological components of Lake Erie were analyzed for two periods: from 1900 to 2017 and from 2003 to 2017. We analyzed hydrological components during the historical period (1917-2017) using monthly average values. Meanwhile, detailed water mass balance was evaluated for the period from 2003 to 2017 using the daily values of hydrological components.

Precipitation

The precipitation data were acquired from the National Oceanic and Atmospheric Administration (NOAA), from gage measurements collected at the inland weather stations (https://www.glerl.noaa.gov/data/dashboard/data). IN the database, monthly values of over-lake precipitation are available starting from 1900. Daily values of the recent precipitation for 2003 to 2017 were obtained via personal communication with Tim Hunter (Great Lakes Environmental Research Laboratory, GLERL). There is a potential bias in the precipitation measurements caused by instrumental shortcomings, which has been estimated to vary from 5% to up to 45%, reportedly inconsistent from year to year (DeMarchi et al., 2009, Groisman and Legates, 1994, Neff and Nicholas, 2004, Winter, 1981). An additional source of uncertainty could arise from data interpolation between land gages, which may inaccurately represent meteorological conditions at the lake surface itself (Eichenlaub, 1979, Neff and Nicholas, 2004). However, the overall data uncertainty remains unknown due to the lack of precipitation measurements on the water surface.

Runoff and Streamflow

The precipitation that falls into the drainage basin of Lake Erie is collected into more than 60 large rivers and small creeks, which eventually discharge into the lake (Table C1). Monthly values of the runoff collected by NOAA (https://www.glerl.noaa.gov/data/dashboard/data) partially cover the period from 1900 to 2017. Daily data of streamflow measurements for 2003-2017 for the US tributaries were retrieved from the United States Geological Survey

Table 4.1: Characterization of the sub-watersheds in Lake Erie basin. Abbreviations: Huron-Erie Corridor (HEC), Lake Erie (LE), watershed area (WA).

#	System	Total WA (TA) $[km^2]$			Monitored WA (MA) $[km^2]$			MA as % of TA [%]		
		Canada	USA	Total	Canada	USA	Total	Canada	USA	Total
1	HEC, including:	10469	7242	17711	6854	4936	11790	65.5	68.2	66.6
1.1	St. Clair River	502	2997	3499	0	2031	2031	0	67.8	58
1.2	Lake St. Clair	9499	2727	12226	6625	1901	8526	69.7	69.7	69.7
1.3	Detroit River	468	1518	1986	229	1005	1234	48.9	66.2	62.1
2	LE, including:	12174	47327	59501	8724	36594	45318	70.4	77.3	75.9
2.1	West Basin	431	26467	26898	0	22742	22742	0	85.9	84.5
2.2	Central Basin	2710	14764	17474	1331	11748	13079	49.1	79.6	74.8
2.3	East Basin	9033	6096	15129	7239	2104	9497	80.1	34.5	61.8
	Total (HEC + LE)	22643	54570	77213	15424	41531	56955	68.1	76.1	73.8

(USGS) service (https://maps.waterdata.usgs.gov) and for the Canadian tributaries from Water Survey of Canada (WSC) hydrometric database (http://collaboration.cmc.ec.gc.ca/cmc/hydrome Briefly, the daily runoff was estimated at gauged stations for the watershed for Canadian and US datasets, and then extrapolated to account for the ungauged area of the watershed using the area-to-runoff ratios (Table 4.1, Table C1). The uncertainty in the streamflow measurements arises from the two main constituents: procedural inaccuracies and errors associated with extreme events such as flooding (Neff and Nicholas, 2004). Previous studies estimated that the uncertainty on average is between 5 and 15%, depending on the vegetation and ice dynamics (Herschy, 1971, Neff and Nicholas, 2004, Pelletier, 1988, Quinn, 1979, Sauer and Meyer, 1992). However, the flooding increases estimation inaccuracies drastically when the stream overflows the river banks and the established stage-discharge or velocity-discharge relations become inadequate.

Evaporation

The evaporation data of NOAA is estimated using the Great Lakes Evaporation Model (GLEM; Croley, 1989, 2005). The model relies on meteorological data from the lake

shoreline and inherently carries error percentages similar to precipitation data. Moreover, GLEM was initially created for deep lakes and, thus, may provide more reasonable data for Lake Erie than for shallow Lake St Clair. Thus, errors in evaporation can also vary widely and are assumed to be in 10 – 15% range on par with previous studies (Croley, 1989, 2005, Quinn and Guerra, 1986, Winter, 1981). Model derived monthly average values since 1950 were obtained from NOAA website (https://www.glerl.noaa.gov/data/dashboard/data), while daily values for 2003-2017 via personal communication with Tim Hunter (GLERL).

Connecting Channels and Diversions

In the Huron-Erie corridor (HEC) and Lake Erie, there are three connecting channels (Figure 4.1). The first channel, the outflow of the Lake Huron, is connected with the relatively shallow Lake St. Clair via the St. Clair River. The second channel, the Detroit River, flows from Lake St. Clair into Lake Erie. Finally, the third channel supplies water from Lake Erie into Lake Ontario via the Niagara River. For the St. Clair and Detroit rivers, estimated flows were taken from the previous work on Lake St. Clair, where partially missing daily flows were calculated using daily mean water levels (Scavia et al., 2018). For the Niagara River, flows for station USGS-04216000 at Buffalo, New York are available in the National Water Information System (NWIS) database for the period from 1926 to 2017.

The connecting channels have the most significant contribution to the water balance of Lake St. Clair and Lake Erie. Therefore, accurate measurements of the connecting channels are critical for correct water balance. An average range of uncertainty in monthly non-ice-affected-flow is estimated within 3.5–4% (Neff and Nicholas, 2004). However, during the winter period, ice accumulation affects the accuracy of the discharge measurements, and it falls in the range from 5 to 15%.

The Welland Canal diverts water from Lake Erie to Lake Ontario to allow navigation of ships between the lakes. It was taken into service in 1829 and records have been kept since 1860. As described above, the uncertainty of streamflow estimation is likely to be in the range from 5 to 15%. On average, the diversion through the canal is 191 *cms* or

about 3% of Niagara River flow (Quinn and Edstrom, 2000). Hence, the contribution of the Welland Canal uncertainty is likely below 1 percent of the total mass balance.

Statistical data on withdrawals from Lake Erie is available in the Great Lakes Regional Water Use Database reports (https://waterusedata.glc.org), starting in year 1987. The reports include annual average consumptive use for the industrial, commercial, institutional, power production and public water supply, self-supply for irrigation and livestock. However, data uncertainty is not reported.

El Niño–Southern Oscillation Index

To study the effect of the climate on the water budget of Lake Erie, we analyzed irregular, periodic variation patterns of winds and sea surface temperatures over the Pacific Ocean. One such standardized measure of variation is El Niño–Southern Oscillation Index (ENSO). The index is based on the observed water temperature and air pressure differences in the western and eastern tropical Pacific (Shabbar et al., 1996). The oscillating pattern of ENSO has a direct effect on the wind across the Pacific, which results in the rainfalls and weather changes in Canada and the United States (Shabbar et al., 1996). The impact of ENSO on the air temperatures in Canada has the most substantial effect between the late fall and early spring (November to May). Throughout the positive phase of ENSO (warm El Niño event), Manitoba and Ontario experience the most significant positive air temperature anomalies (up to 3°C higher), while the maximum negative anomalies in the air temperature over the south and central Canada are reported in the case of the negative and cold La Niña event (Shabbar et al., 1996, 1997). Monthly values of the historical time series (1900-2017) of El Niño 4 sea surface temperature index were obtained from the NOAA website (https://www.esrl.noaa.gov/psd/gcos_wgsp/Timeseries).

4.3 Results and Discussion

4.3.1 Historical Trends (1917-2017)

Figure 4.2 shows yearly average values of precipitation, runoff, and the ratio of runoff to precipitation for the entire Lake Erie from 1900 to 2017. Linear regression of the precipitation shows a slightly increasing trend of about 0.5 *mm* per year with an average value of 840 *mm* in 1900, increasing up to 898 *mm* in 2017. Not only did the average value rise, but the amplitude of the variations in precipitation increased. Increased variations could be attributed to improved measurement techniques and/or increased frequency of extreme weather events. An additional interesting feature in the historical precipitation is the 30-year periodicity that is seen in the ten-year moving average (solid black line, Figure 4.2). Relatively "wet" 15-year intervals are succeeded by relatively "dry" 15 year periods. The last "dry" period started in the late 1990s, and currently, Lake Erie is undergoing a "wet" period. During the current period, the average annual precipitation is from 10% to 20% higher compared to the previous "dry" period (1990-2005). As reported by Quinn and Guerra (1986), the mean precipitation of Lake Erie for the period 1940-79 (900 *mm*) was about 5% higher than that during 1900-39 (850 *mm*). The average precipitation for the period 1980-2017 is 875 *mm*, the lowest value of 565 *mm* was observed in 1988 whereas the year 2011 set a new historical high of 1330 *mm*.

The central panel of Figure 4.2 shows the total runoff. In general, the runoff repli-

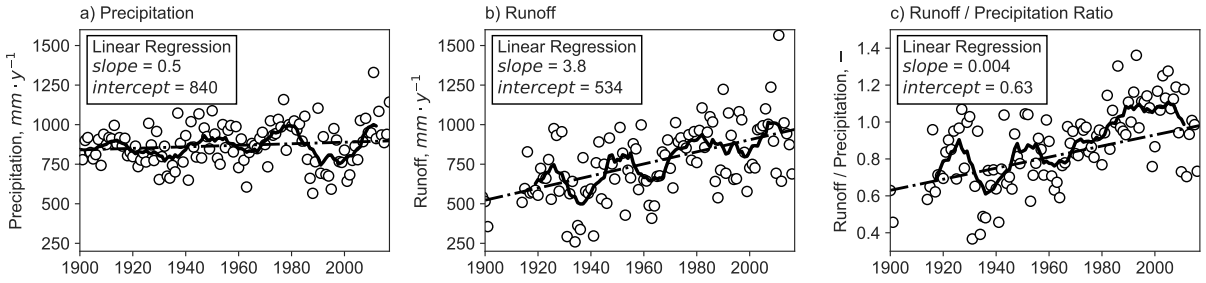

Figure 4.2: a) Historical 1900-2017 precipitation over the Lake Erie, b) runoff to the Lake Erie, c) runoff to precipitation ratio. Black circles represent actual measured values using methods described in section section 4.2, dot-dashed lines – linear regression trends estimated using ordinary least squares method, and solid lines – 10-year moving averages.

cates the same 30-year patterns found in the precipitation estimates, however, there are some differences. Firstly, the runoff has a steeper regression line than that of precipitation with an average increase of 3.8 *mm* per year. As a result, the mean value estimated by the regression in 1917 (598 *mm*) almost doubled by the year 2017 (980 *mm*). As for absolute values, the value of 259 *mm* estimated for runoff in 1934 is six-fold lower than the highest value of 1564 *mm* recorded in 2011. Additionally, in contrast to the years before 1980, the runoff in the recent 3 decades delivers about the same volume of water as precipitation. Quinn and Guerra (1986) reported that the mean runoff during 1940-79 (763 *mm*) was considerably higher than that of 1900-39. The same could be said about the period from 1980 through 2017: the average runoff (893 *mm*) is considerably higher than that of 1940-79. Changes in land-use with the urbanization of surrounding watersheds, as well as changes in seasonal precipitation patterns, therefore increased the average runoff-precipitation ratio from 0.6 at the beginning of the 20^{th} century to 1.01 in 2018 (Figure 4.2). In other words, due to land-use changes during the last century, about the same precipitation produces substantially higher runoff and increases the risk of the flooding.

Quinn and Guerra (1986) estimated annual average evaporation as a separate hydrological component for the 1940-79 period to be 687 *mm* and reported an error within the 10-20% range. In contrast, through the continuous historical estimates from 1950 to 2017, NOAA reports a 25% larger average value of 872 *mm*, highlighting a slightly increasing trend of 1 *mm* per year (Figure C1, supplemental material).

During the last century, St. Clair River delivers about 74% of the total water supply to Lake Erie. Consequently, water level changes in Lake Erie strongly correlate with the water level variations of St. Clair River (Figure C2; $r = 0.95$, $p \ll 0.001$), water level of Lakes Michigan and Huron (Figure C2; $r = 0.82$, $p \ll 0.001$), and somewhat with water level Lake Superior (Figure C2; $r = 0.38$, $p \ll 0.001$). Therefore, it is expected that the water level of Lake Erie strongly depends on large-scale atmospheric circulation over the upper LGLs. Moreover, the signals of ENSO should be reflected in the patterns of the level fluctuations, which we discuss below.

The wavelet transform is used to analyze time series of Lake Erie water level, runoff, precipitation along with ENSO (Figure 4.3). By decomposing a one-dimensional time series into two-dimensional time-frequency space, one can determine both the dominant modes of variation and how they evolve in time. Here, time series of water level contain modes at many different time scales (Figure 4.3). That is, in contrast to precipitation and runoff where the spectrum values are dominant on annual and seasonal time scales, the spectrum values of water level over the synoptic time scales are comparable to those on the annual time scales. Moreover, ENSO shows synoptic time scale dominance, and some of its power spectrum peaks match those of the water level (Figure 4.3, white ellipses). As

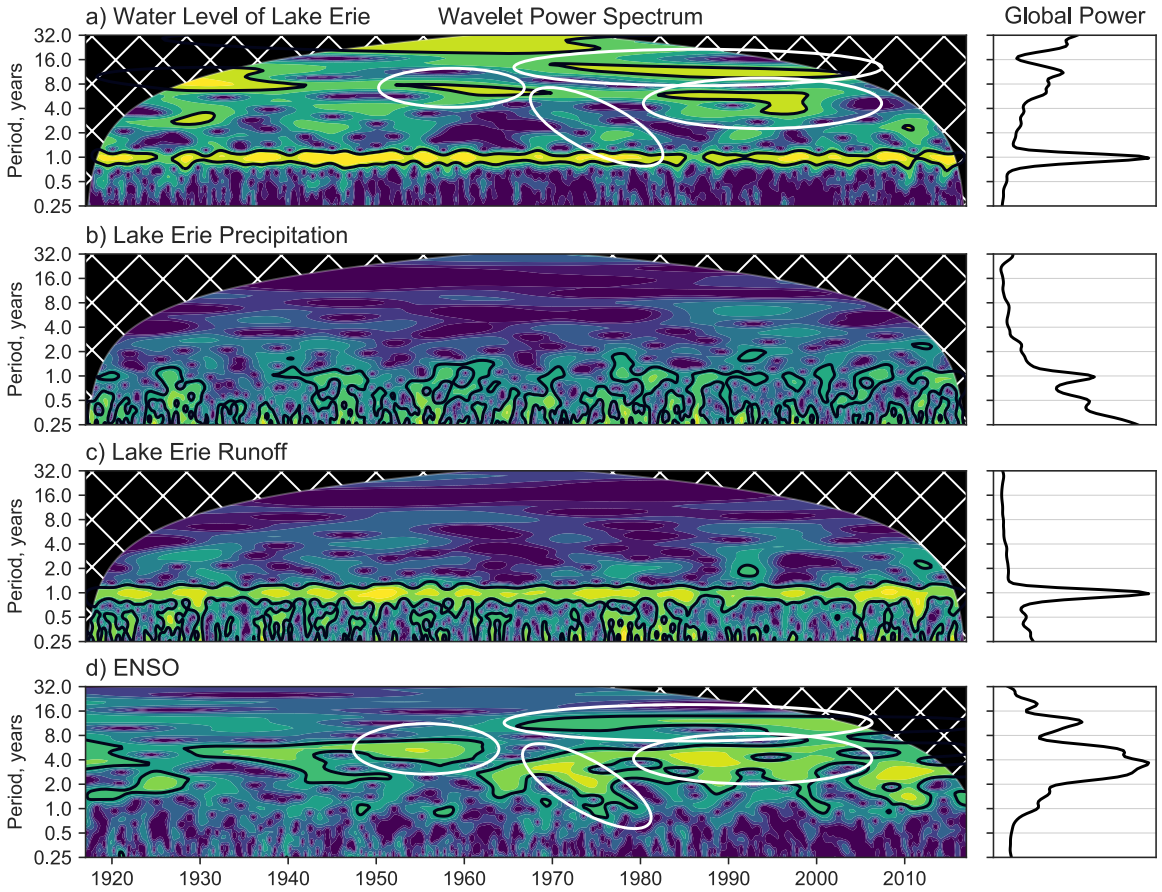

Figure 4.3: Wavelet power spectrums for the period from 1917 to 2017 of a) water level in Lake Erie, b) over-lake precipitation, c) runoff, d) El Niño - Southern Oscillation Index (ENSO). Plots on the right side represent the normalized unitless global wavelet power spectra. The cross-hatched area shows the regions where the boundary effects of the time series are significant. The black contour indicates 90% confidence regions. White ellipses show matching power spectrum peaks. More detailed frequency analysis is in the supplemental information.

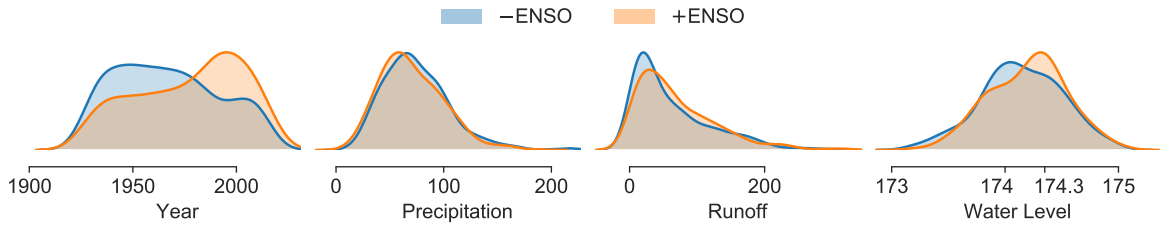

Figure 4.4: Categorical kernel density estimations of a) ENSO through the historical period, b) Lake Erie monthly precipitation, c) Lake Erie monthly runoff, and d) the water level in Lake Erie. Colours represent categories when ENSO is either positive (orange colour) or negative (blue colour).

a result, the annual change of water level also slightly correlates with ENSO (Figure C3, $r = 0.23$, $p = 0.01$).

Categorical kernel density estimations of ENSO as well as of precipitation, runoff and water level of Lake Erie support these findings (Figure 4.4). During recent years, the positive phase of ENSO was more frequent than the negative phase. Although the precipitation over the lake has a generally increasing trend, during the negative phase it is slightly lower than that of throughout the positive phase. Additionally, the water level in Lake Erie has two distinguishable peaks depending on the phase of ENSO. When the phase is negative, the mean water level is 174 m, while the average water level during the positive phase is 174.3 m.

Together, the evidences suggest that during the historical 1900-2003 period, the ratio of runoff to direct precipitation is steadily increasing. Also, surface water elevation dynamics in Lake Erie are driven by the outflow from the upper LGLs with St. Clair River being the largest contributor in water balance of Lake Erie. As a result, variations in the annual water level of Lake Erie depends on climate and weather in the upper LGLs.

4.3.2 Recent Trends (2003-2017)

During the 2003-2017 period, the average year of St. Clair River delivers 5081 cms of water to Lake St Clair (Figure 4.5, Table 4.2). This channel transfers 96% of the total water supply of the lake (Figure C4). Since 2003 the discharge of St. Clair River has fluctuated below the average value (except the year 2009). Following 2013, St. Clair

River discharge increased, and by 2017, it was 15% higher than average. High discharge of the channel and a relatively small volume of Lake St. Clair (4.17 km^3) result in a short residence time of 9 days (Bocaniov et al., 2018).

The second-largest water source of Lake St. Clair is the runoff. The runoff has the most significant annual variations and brings 174 *cms* with the Thames and Sydenham rivers being the most substantial contributors (but less than 3% of the total water supply). Lastly, precipitation brings 32 *cms* on average with the highest amount of 46 *cms* recorded in 2011 (less than 1%). In contrary, evaporation stayed close to the average value of 31 *cms* with the lowest values of 27 *cms* in 2003 and the highest of 37 *cms* in 2016 (<1% of total water loss). Thus, the net basin supply of Lake St. Clair is 5287 *cms*, and the

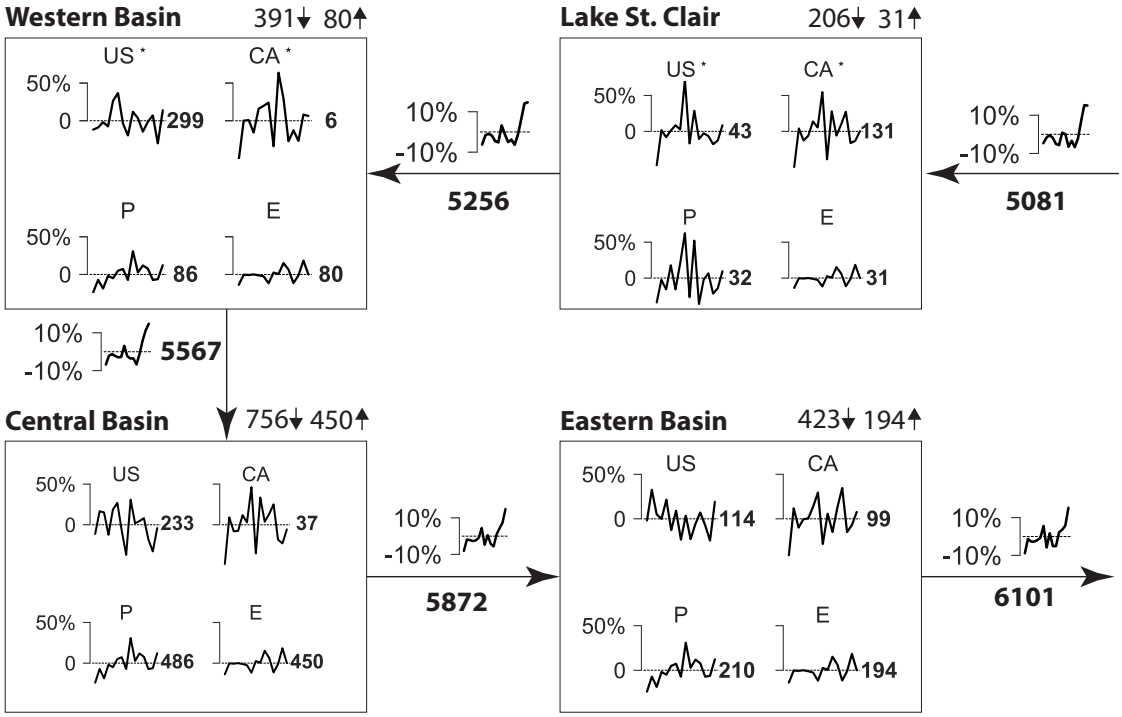

Figure 4.5: Average water balance of Lake Erie and Lake St. Clair for the period 2003-2017. The boxes represent three basins of Lake Erie and one basin of Lake St. Clair (top right box). The two numbers on top of each box represent water gained of water via runoff and precipitation (downward arrows) or lost via evaporation (upward arrow). Graphs inside the boxes indicate changes in US runoff (US), Canadian runoff (CA), precipitation (P) and evaporation (E) relative to the average value over the time period 2003-2017. The numbers on the right side of each graph show the average value for the period from 2003 to 2017. The arrows connecting the boxes represent the flows through connecting channels or inter- basin water transfer. Yearly average values could be found in Table 4.2. The units are *cms*.

St. Clair River is the most significant contributor to the Lake St. Clair water budget. As a result, Detroit River, the outflow of Lake St. Clair and connecting channel with the WB of Lake Erie, has the same pattern of the discharge as the St. Clair River ($r = 0.82$, $p \ll 0.001$).

Detroit River flows into the WB and delivers 94% (5256 *cms*) of the total water supply of WB (Table 4.2). In addition, 5% (305 *cms*) is delivered through the runoff, and less than 1% (86 *cms*) via the precipitation. Increased discharge from St Clair River and, as a result, Detroit River, after 2013, resulted in the increased the water level of Lake Erie by 64 *cm* (Table 4.2).

Due to the large surface area of the CB, the precipitation and evaporation constitute the substantial part of its water balance. Precipitation delivers 8% (486 *cms*) of water annually, while runoff delivers only 5% (270 *cms*). The rest of the water comes from the WB through the net inter-basin exchange (5567 *cms*, 87%). CB delivers 94% (5872 *cms*) of water annually to EB via the net inter-basin exchange. In contrast to the CB, EB has a smaller surface area, therefore, precipitation and runoff together deliver only 6% of the total water supply (210 *cms* and 213 *cms*, respectively).

In summary, the overall water mass balance, essential for building mechanistic models, is reasonably well satisfied with the average absolute residual of less than 3%. St. Clair River, connecting channel with Lake Huron, delivers 74% (5081 *cms*) of total water supply for both lakes (6857 *cms*) while precipitation and runoff deliver only 11% (808 *cms*) and 14% (961 *cms*), respectively. In 2011, precipitation and runoff reached the maximum values of 1073 and 1143 *cms*, respectively. During the last 15 years both Lake St. Clair and Lake Erie have very high input of water from the connecting channels, and relatively low inputs from precipitation and runoff. Our estimates stress the importance of climate and meteorological conditions in the upstream LGLs.

Table 4.2: Annual water budget of Lake Erie and Lake St. Clair for the period from 2003 to 2017. The residual represents the difference between the inflow and the outflow. WB* stands for the water body, † the mean and ‡ the sum of absolute values of the residuals. All units are in *cms* except for the last two rows of the table.

WB*	Component	2003	2004	2005	2006	2007	2008	2009	2010	2011	2012	2013	2014	2015	2016	2017	Mean
SCR	Outflow LH	4845	4991	5059	4989	4825	4794	5125	5083	4751	4910	4739	4971	5436	5856	5847	5081
	US Runoff	4	10	10	9	11	9	16	6	12	7	9	7	7	9	9	9
	CA Runoff	1	2	2	2	2	1	3	1	2	1	2	1	1	2	1	2
	Outflow	4849	5003	5071	4999	4837	4804	5144	5091	4765	4918	4750	4979	5444	5867	5857	5092
LSC	US Runoff	19	33	30	35	36	36	58	30	44	32	33	33	29	29	38	34
	CA Runoff	65	134	112	121	147	136	199	79	165	122	142	165	108	112	129	129
	Precipitation	21	32	27	38	27	39	53	24	49	21	32	35	25	28	35	32
	Evaporation	27	31	31	31	31	31	28	32	31	36	33	28	31	37	31	31
	Outflow	4928	5171	5209	5162	5017	4984	5426	5191	4992	5056	4923	5184	5575	5998	6029	5256
DR	US Runoff	11	16	15	18	19	17	16	10	15	11	14	15	15	14	17	15
	CA Runoff	3	6	6	5	7	7	7	4	9	7	4	5	4	6	6	6
	Outflow	4941	5193	5230	5184	5043	5009	5450	5205	5016	5074	4941	5204	5594	6018	6051	5277
WB	US Runoff	253	256	278	259	358	391	271	231	320	298	241	280	305	195	324	284
	CA Runoff	0	0	0	0	0	0	0	0	0	0	0	0	0	0	0	0
	Precipitation	66	80	70	85	82	91	93	80	113	89	97	93	80	81	97	86
	Evaporation	69	80	79	80	79	78	71	82	80	92	85	71	79	95	80	80
	Outflow	5191	5449	5499	5447	5404	5413	5743	5433	5368	5369	5194	5506	5900	6200	6392	5567
CB	US Runoff	206	271	268	204	276	295	215	146	304	237	243	251	191	156	223	233
	CA Runoff	19	40	34	34	41	38	53	24	49	38	41	46	30	28	34	37
	Precipitation	369	451	395	476	462	510	521	450	636	499	543	524	450	455	545	486
	Evaporation	388	449	447	450	445	438	397	461	452	518	479	398	444	533	450	450
	Outflow	5397	5762	5748	5711	5737	5817	6136	5592	5905	5625	5543	5929	6127	6307	6745	5872
EB	US Runoff	112	151	120	114	139	100	125	87	118	88	108	122	106	86	136	114
	CA Runoff	59	111	90	99	100	113	129	71	105	85	112	134	85	92	107	99
	Precipitation	159	195	171	206	199	220	225	194	275	216	235	226	195	197	236	210
	Evaporation	168	194	193	194	192	189	172	199	195	224	207	172	192	230	194	194
	Outflow	5560	6025	5935	5936	5983	6060	6442	5746	6207	5789	5790	6239	6321	6452	7029	6101
Outflow	Niagara River	5255	5575	5788	5544	5747	5642	5836	5628	5700	5944	5439	5773	6114	6356	6660	5800
	Welland Canal	200	201	223	171	175	205	195	187	132	218	166	193	226	221	146	191
	Consumptive Use	22	21	22	21	23	22	22	23	19	19	19	19	19	20	20	21
	Total	5477	5797	6033	5737	5945	5869	6053	5837	5852	6181	5625	5985	6359	6597	6826	6011
	Δ (In-Out)	83	228	-97	199	38	192	389	-92	356	-392	166	254	-38	-145	203	90† | 191‡
	Δ WL SC, *cm*	-14	25	-17	2	-9	18	12	-21	16	-33	21	30	16	-1	17	4
	Δ WL LE, *cm*	0	21	-17	6	-6	4	12	-22	28	-35	21	15	19	-11	20	4

4.3.3 Remarks on Building Mechanistic Models

Local and upstream LGL meteorological conditions not only play essential roles in the water budget of Lake Erie but also control the algal bloom by i) flashing out dissolved reactive phosphorus (DRP) from the agricultural fields in spring, and by ii) modifying the circulation in the CB. With regard to former, in the analysis of the severe algal blooms of 2011, Michalak et al. (2013) conclude that high precipitation from March to June (75% above the prior 20-year average) had the most substantial influence on DRP release from the Maumee watershed in spring, the vital period for incubating algal blooms (Michalak et al., 2013, Stumpf et al., 2012). Moreover, weaker circulation in WB in summer of 2011 has led to the longer water residence times that prevented from the flushing of nutrients from shallow WB, led to the minimal dilution of the nutrient-rich Maumee River, and therefore incubated the bloom (Michalak et al., 2013). As a result, during 2003-2017 period, the severity of algal blooms strongly correlates with the late spring over the lake precipitation ($r = 0.84$, $p \ll 0.001$; Figure 4.6a) and the runoff ($r = 0.71$, $p = 0.005$; Figure 4.6b). In other words, timing and intensity of precipitation in Lake Erie and upstream LGLs modify the magnitude of the bloom by flashing rate of the DRP from the fields and by varying the circulation in WB.

Likewise, circulation in CB has direct control on the algal blooms as it could deliver

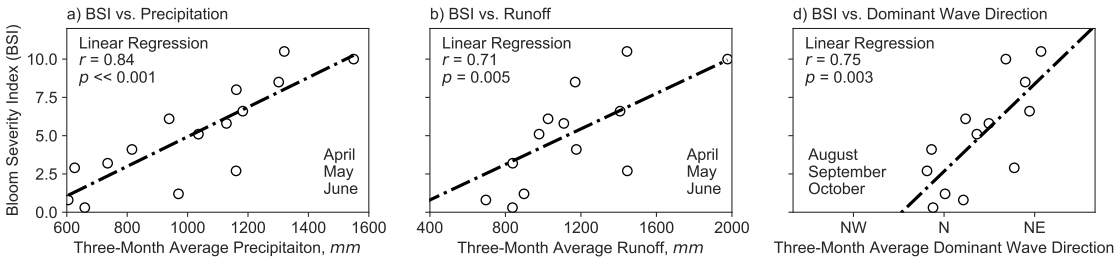

Figure 4.6: Correlations of bloom severity index (BSI) with a) precipitation, b) runoff, and c) dominant wave direction. Wave direction is the direction from which the highest energetic waves at the dominant period are coming. Three-month average values for precipitation and runoff are estimated for April, May and June, while three-month average values of dominant wave direction are estimated for August, September, and October. Wave direction measurements are taken from buoy 45005, West of Lake Erie. Bloom severity index is obtained from NOAA website.

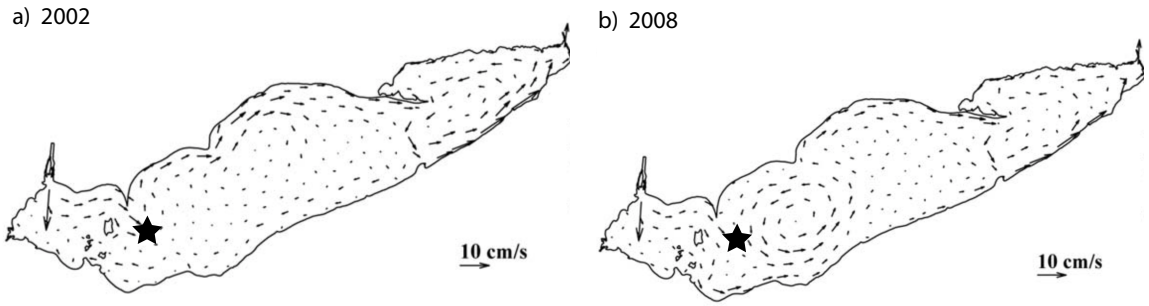

Figure 4.7: The depth-averaged circulation in Lake Erie during a) summer of 2002 and b) summer of 2008. The images are taken from Niu et al. (2015). The star represents the location of the station 450005, West of Lake Erie. In 2002, Lake Erie experienced the lowest algal blooms during the last two decades. In contrast, 2008 was the first year in the sequence of large and continuous algal blooms during the last 15 years (Figure C5).

westwards DRP released from the sediment during hypoxia in CB (Scavia et al., 2014). The summer circulation patterns in the CB vary significantly year by year (Niu et al., 2015). For instance, in 2002 and 2005, weak anticyclonic gyres were formed in the CB (Figure 4.7b; Niu et al., 2015; Beletsky et al., 2013). At the same time, in 2002 and 2005, Lake Erie had the lowest algal blooms throughout the recent two decades as reported by NOAA (Supplemental information, Figure C5). In contrast, during severe algal bloom of 2008, the summer circulation of the CB had a two-gyre pattern, with a powerful cyclonic gyre, which delivers water and nutrients from the middle of the CB to the boundary with the WB (Figure 4.7b; Niu et al., 2015. Such distinct inter-annual variability of circulation dynamics in the CB is induced by the variation of the surface wind stress (Beletsky et al., 2013, Niu et al., 2015). Also, measurements of the average direction of the dominant wave in August, September, and October at Station 45005, located on the border of the WB and CB (Figure 4.7), show a strong correlation with the severity of algal blooms ($r = 0.75$, $p = 0.003$; Figures 4.6c). Thus, when the most energetic waves formed by the summer winds come from the North-East, then there is an increase in the intensity of algal bloom that year. That is, the results indirectly suggest that, in addition to the phosphorus load from the watershed, algal blooms could be fueled by the westward transport of the DRP from the CB accumulated during the extended periods of the summer hypoxia.

Thus, basin-wide circulation and inter-basin exchange are significant factors in the spatial transport of water and nutrients in Lake Erie. Michalak et al. (2013) reported that

weaker WB circulation in summer of 2011 has prevented from the flushing of nutrients and drove to the minimum dilution of the phosphorus-rich Maumee River waters. Currently it seems that algal blooms are sustained by the DRP delivered from the central basin that accumulated during the extended period of summer hypoxia. Therefore, one- and two-dimensional ecological models of Lake Erie will not likely provide the robust results in water quality and bloom forecasting.

4.4 Summary and Conclusions

We have demonstrated that along with strong seasonal and annual patterns, precipitation and runoff in the Lake Erie basin exhibit 30 years cycles. These cycles correlate with the water level of Lake Erie. Since the early 20^{th} century deforestation and urbanization of the Lake Erie watershed, as well as changes in seasonal precipitation patterns increased the land runoff to precipitation ratio, *i.e.*, the same precipitation produces substantially higher runoff. From 2003 to 2013, the water level fluctuated around its average values. The year 2011 saw the delivery of record volumes of waters through precipitation and runoffs and increased the water level of Lake Erie by 28 *cm*.

Predominantly, the water level of Lake Erie depends on the supply of water via connecting channels from Lake Huron and Lake Superior with large corresponding watersheds. In those lakes, the water rise during the recent years was due to changes in weather patterns: persistent over-lake precipitation and above-average spring runoff (Gronewold et al., 2016). As a result, the water level of Lake Erie reflects signals of the large scale atmospheric circulation modes of ENSO. During recent years, the warm El Niño occurred more often than cold La Niña, and the positive phase of ENSO also contributed to the increase of the water supply from the upper LGLs. From 2013 onwards, all of the above increased the inflow of water into the Lake Erie and the water level rose by 64 *cm* increasing the outflow by 16% (more than 1000 *cms*).

Basin-wide water budget estimated for the 2003-2017 period will be used for building the hydrodynamic model of Lake Erie to advance the predictive understanding of the bio-

geochemical responses of large lakes to climate warming. Basin-wide daily measurements, source code, and our estimates are publicly available in the open GitHub repository: `https://github.com/pycckuu/Great-Lakes-Data`.

Chapter 5

PorousMediaLab: The Toolbox For Batch And 1-D Reactive Transport Modelling

Igor Markelov
Raoul-Marie Couture
Philippe Van Cappellen

Summary

PorousMediaLab is a computer program written in Python programming language that is designed to perform a wide variety of biogeochemical modelling in the aquatic environment. PorousMediaLab is designed for batch reactions and one-dimensional saturated transport calculation with transient boundary conditions involving equilibrium and kinetically controlled aqueous and mineral reactions with user-defined rate expressions. Automated code generation and parameter estimation allow for the development and evaluation of mechanistic process models with an arbitrary number of user-defined reactions and species. Having a text user interface, PorousMediaLab makes new model applications effortless, very flexible, less error-prone, and less time-demanding. In the examples below, the application of PorousMediaLab demonstrates capabilities of the program to simulate (1) titration of a strong acid with the base, (2) simulation of anoxic freshwater wetland sediment, (3) freeze-thaw cycles of saturated soil column with transient temperature boundary conditions. Built on top of the robust, efficient and tested mathematical frameworks, PorousMediaLab is an ideal candidate for solving scientific and practical applications related to aquatic chemistry.

5.1 Introduction

All biogeochemical transformations on the Earth are the result of the complex natural processes and anthropogenic influence. Transport, chemical, mechanical, and biological processes in Earth systems are coupled, and often individual features and mechanisms play a crucial role in the overall system functioning (Steefel et al., 2005). Growing scientific knowledge of those systems and the necessity of connecting laboratory and field observations creates a need for development and application of flexible and efficient reactive transport models (RTMs). RMTs are powerful tools for capturing interplay between physical, chemical, and biological processes (Steefel and Van Cappellen, 1998). RTMs have been widely applied to study contaminant reactive transport in groundwater (*e.g.,* Saaltink et al. 2004), rock and soil weathering (*e.g.,* Ayora et al. 1998, Lawrence et al.

2014), greenhouse gas emissions from peat soils (*e.g.,* Rezanezhad et al. 2016), early diagenetic transformations in sediments (*e.g.,* Van Cappellen and Wang 1996 and Couture et al. 2016), nutrient dynamics in rivers and lakes (*e.g.,* Vanderborght et al. 2007 and Schmid et al. 2017).

Conventional RTMs perform model simulation based on the transport and processes pre-defined by the developer of the program. In such cases, a user makes use of an already defined reaction network or can select reactions from the available ones in the program database. On the one hand, such approach offers the robustness and efficiency of numerical computation (*e.g.*, the Jacobians are already defined for equilibrium reactions), but, on the other hand, the approach does not provide flexibility for the scientists to test new theories and identify novel reaction pathways.

Here, a modelling program PorousMediaLab is presented. PorousMediaLab is a computer program designed to simulate a wide variety of biogeochemical systems in aquatic environments. The flexibility of PorousMediaLab is a critical feature since the tool is designed for scientists or students who wish to assess interplays between biotic and abiotic processes, describe biological community structures, identify novel reaction pathways, or simply quantify reaction rates. PorousMediaLab is designed for simulation of reactor or batch experiments as well as a reactive system with one-dimensional transport and transient boundary conditions. General representation of processes in PorousMediaLab allows (i) to deal with arbitrary large reaction networks defined by a user, (ii) it can be used for predictive modelling to design experiments, (iii) it can be used for inverse modelling and parameter identification problems. PorousMediaLab has been used in the design and analysis of the laboratory experiments to study the effect of reactive transport on biotic and abiotic geochemical systems. PorousMediaLab is written in Python, and its modular structure makes it relatively easy to use and expand. The following chapters briefly discuss the computational approach as well as show three examples demonstrating the capabilities of the program.

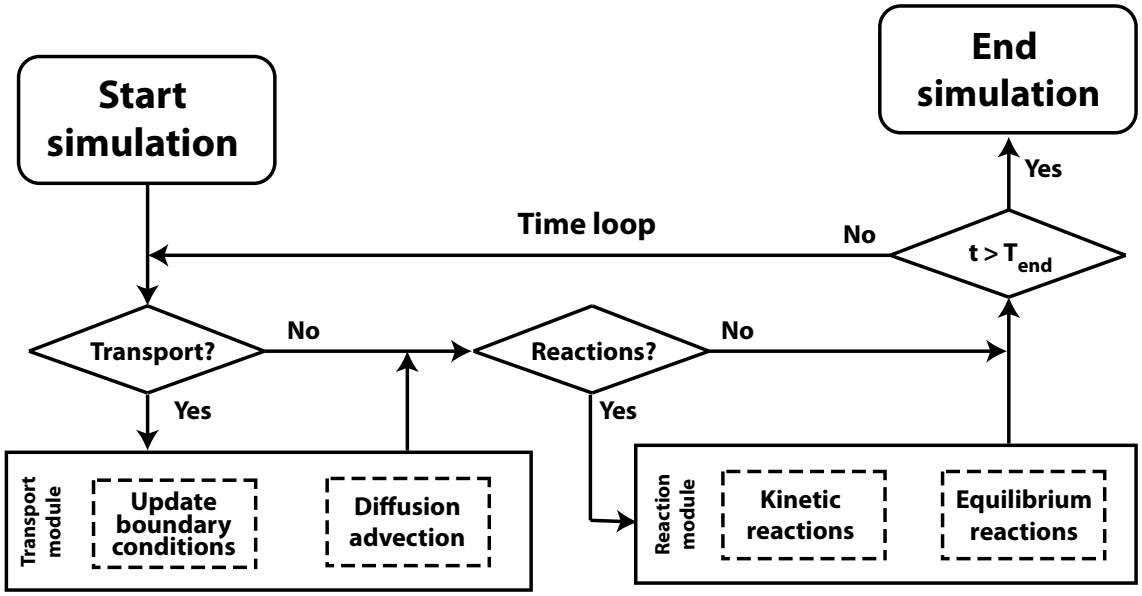

Figure 5.1: Generic program flow for a reactive transport simulator using operator splitting.

5.2 Overview of PorousMediaLab

PorousMediaLab is a general-purpose numerical simulator that solves mass balance equations in aquatic chemistry applications. The mathematical representation of the model consist of the coupled nonlinear partial differential equations representing transport and reactions processes of solid and aqueous species:

$$\frac{\partial(\theta C_i)}{\partial t} = \frac{\partial}{\partial x}\left(\theta D_i \frac{\partial C_i}{\partial x}\right) - \frac{\partial}{\partial x}\left(\omega \theta C_i\right) + \theta \sum R(x, t, C_i, ...) \tag{5.1}$$

where C_i is concentration of i^{th} reactant; θ is the porosity φ for dissolved species and $(1 - \varphi)$ for solid species; D_i is effective diffusion; ω is advective term; $\sum R(x, t, C_i, ...)$ represents mass-conservation of the reaction term, i.e. sum of all sources and sinks of particular reactant. The computational results of transport and reaction modules have been tested against analytical solutions (appendix D.1).

Figure 5.1 shows the main program flow. Using the operator splitting technique, the transport and reactive terms are decoupled and solved sequentially. If no transport present in the simulation, i.e., the simulation of batch or well-mixed reactor, then the

transport module is skipped in the time loop, and only the reaction module is executed. Otherwise, when reactions are absent, then the program estimates only the transport.

In PorousMediLab one-dimensional advective-diffusive transport can be solved using either finite volume or finite difference discretization schemes. By default, the transport integration of Crank-Nicolson finite difference scheme is applied. A Finite volume partial differential equation solver *FiPy* (Guyer et al., 2009) is used for the cases when the transport part of equations is non-linear (*e.g.*, a diffusivity that depends on concentration) or when multiple transport equations are coupled (*e.g.*, if diffusivity depends on temperature and thermal conductivity depends on concentration). Kinetic reactions are solved using Fortran solver *LSODA* from *scipy.integrate* package (Jones et al., 2001). To ensure the stability of the solution, a robust numerical Nelder-Mead method from *scipy.optimize* package is used to find a solution to the non-linear algebraic equations in equilibrium reactions. The approach of solving equilibrium reactions is taken from *Aquatic Chemistry* (Stuum and Morgan, 1996) and it involves several steps: (1) the establishment of the system in the equilibrium, (2) selection of the unknowns, (3) writing expressions for other species based on the equilibrium expressions, (4) the minimization of the balance squared error until a charge balance is achieved. When the numerical methods do not converge, the PorousMediaLab alerts the user to make the corresponding changes in spatial or temporal discretization; a user may also change the solvers in kinetic and equilibrium modules to any of those available in *scipy* package.

PorousMediaLab has a modular architectural design, which makes the structure of the code clearer and provides the flexibility for users to modify submodules according to their own needs. The computer code for PorousMediaLab is divided into seven files of *Python* code. Each file corresponds to a different task. Main class and definitions of all shared between subclasses methods are contained in *lab.py*. The codes for simulation of the well-mixed reactor and 1-dimensional reactive transport are located in *batch.py* and *column.py*, respectively. Files *desolver.py* and *equilibriumsolver.py* contain methods for computation of kinetic and equilibrium reactions. Additional *calibrator.py* and *plotter.py* files contain methods for calibration based on measured data and plotting of the modelling

results.

PorousMediaLab is distributed through Python package manager *pip* and requires Python version 3.5 or higher. The user can install Python via official website (`python.org`) or as a part of Python Data Science Distribution package *Anaconda* (`anaconda.com`). When the requirements are met, the user can install the toolbox by running the following command in the terminal: *pip install porousmedialab*. After successful installation *porousmedialab* package will be available as any other Python package, (e.g., *numpy, scipy*) via *import* command. The model can be executed on Windows, Linux, and Mac OS machines, and is open source and freely available under GNU General Public License (GPL). Source code, *Jupyter notebooks* with examples presented here and many others can be downloaded from git repository of the project (`github.com/biogeochemistry/PorousMediaLab`).

5.3 Examples

In this section three example calculations using PorousMediaLab are presented that demonstrate capabilities of the program: (1) titration of strong acid with the base, (2) simulation of anoxic freshwater wetland sediment (batch reactor) with measurements and parameters reported by Roden (2008), (3) freeze-thaw cycles of saturated soil column with transient temperature boundary conditions. Examples (1) and (2) demonstrate the reaction module with a simulation of the well-mixed reactor, whereas example (3) present the reactive modelling with 1-dimensional transport. In all examples, complete required input and only selected output are presented. Scripts for plotting graphs shown in the text can be found in the official GitHub repository of the project.

5.3.1 Acid Titration

This examples calculates distribution of aqueous species of phosphoric acid H_3PO_4 titrated with base NaOH (fig. 5.2a). In this numerical experiment, during the period of titration (30 hours) we add NaOH with the rate of 10 mM per hour. The essential data needed for a speciation calculation are the initial concentration of H_3PO_4 and pKa values

(table 5.1).

The input file for this example calculation is as follows:

```
1   from porousmedialab.batch import Batch
2   bl = Batch(tend=30, dt=0.1)
3   bl.add_species(name='H3PO4', init_conc=0.1)
4   bl.add_species(name='H2PO4', init_conc=0)
5   bl.add_species(name='HPO4', init_conc=0)
6   bl.add_species(name='PO4', init_conc=0)
7   bl.add_species(name='Na', init_conc=0)
8   bl.add_species(name='NaOH', init_conc=0)
9   bl.add_acid(species=['H3PO4', 'H2PO4', 'HPO4', 'PO4'], pKa=[2.15, 7.20, 12.38])
10  bl.add_acid(species=['Na', 'NaOH'], charge=1, pKa=[13.8])
11  bl.dcdt['NaOH'] = '0.01'
12  bl.solve()
13
```

In the first line of the code (LOC 1), required *Batch* class is imported from *porousmedialab* library, and an instance of *Batch* is created with the total time of simulation *tend* and the time-step *dt* (LOC 2). All necessary species with corresponding initial concentrations are introduced using method *add_species* (LOC 3-8). Here, the user should give the element name and an initial concentration, and it is up to the user to choose the names for the species as they are not strictly defined. In this example, H^+ and OH^- are not explicitly specified, H^+ is calculated using equilibrium solver and OH^- is estimated internally using K_w. The corresponding pKs of the H_3PO_4 are provided in LOC 9. It should be noted that base reaction was written as an acid reaction (i.e., $Na^+ + H_2O \longleftrightarrow NaOH + H^+$) and added NaOH as an acid with *charge* keyword argument, which is the charge of the fully protonated species (LOC 10). Furthermore, due to NaOH is the strong base with pKb 0.2, the user could define Na^+ as a sole ion via command *bl.add_ion(name='Na', charge=1)* without considering dissociation of NaOH. Later, the rate of change 10 mM of NaOH per hour is set (LOC 10). Finally, LOC 11 starts the computation of the numerical

no.	Equilibrium Reaction	log K
R_1	$H_3PO_4 \longleftrightarrow H_2PO_4^- + H^+$	2.15
R_2	$H_2PO_4^- \longleftrightarrow HPO_4^{2-} + H^+$	7.20
R_3	$HPO_4^{2-} \longleftrightarrow PO_4^{3-} + H^+$	12.38
R_4	$NaOH \longleftrightarrow Na^+ + OH^-$	0.2
R_5	$H_2O \longleftrightarrow H^+ + OH^-$	14

Table 5.1: Reactions considered in the example of acid titration with the base.

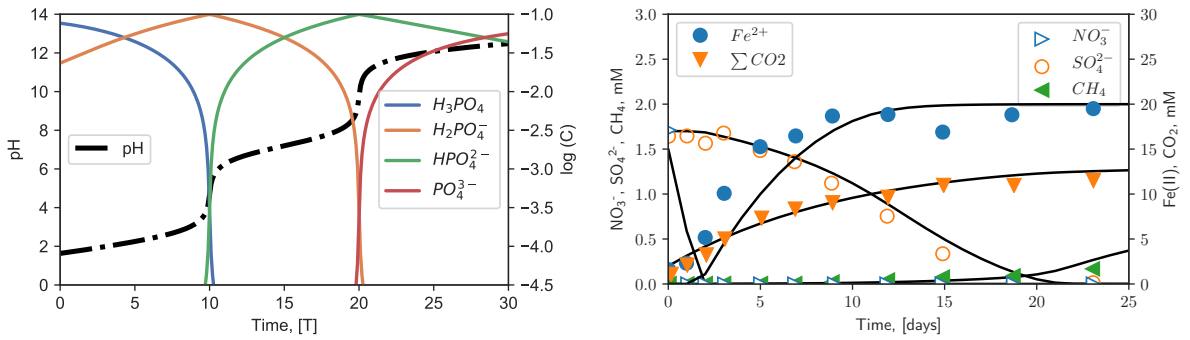

(a) Titration of H_3PO_4 with NaOH

(b) Anoxic freshwater sediment

Figure 5.2: The output generated by the the program in the example (a) titration of strong acid with base, (b) simulation of anoxic freshwater sediment as reported by Roden (2008). The parameters used in (b) are from the original work.

experiment.

By solving the electroneutrality equation at each time step, PorousMediaLab estimates pH and corresponding ionization fractions of acids. The titration curve relating pH and quantity of acid fractions during the numerical experiment can be constructed (Figure 5.2a).

Plotting methods and other useful keywords can be found in the supplemental information (Appendix D.2) or in the GitHub repository of the project. Current and many other examples are available there.

5.3.2 Organic Matter Degradation in Batch Reactor

Here, we demonstrate the application of the kinetic rate laws in PorousMediaLab throughout the simulation of the particulate organic carbon (POC) degradation with a set of terminal electron acceptors in the slurry of anoxic wetland sediment (Roden, 2008).

No.	Reaction
R_1	$\mathrm{CH_2O} + \frac{4}{5}\mathrm{NO_3^-} \longrightarrow \frac{2}{5}\mathrm{N_2(aq)} + \frac{2}{5}\mathrm{H_2O} + \mathrm{HCO_3^-} + \frac{1}{5}\mathrm{H^+}$
R_2	$\mathrm{CH_2O} + 4\,\mathrm{Fe(OH)_3} + 7\,\mathrm{H^+} \longrightarrow \mathrm{HCO_3^-} + 4\,\mathrm{Fe_2^+} + 10\,\mathrm{H_2O}$
R_3	$\mathrm{CH_2O} + \frac{1}{2}\mathrm{SO_4^{2-}} \longrightarrow \frac{1}{2}\mathrm{HS^-} + \mathrm{HCO_3^-} + \frac{1}{2}\mathrm{H^+}$
R_4	$\mathrm{CH_2O} \longrightarrow \frac{1}{2}\mathrm{CH_4} + \frac{1}{2}\mathrm{CO_2}$

Table 5.2: Reactions in a slurry (batch reactor) of anoxic freshwater wetland sediment with sequential consumption of electron acceptors considered by Roden (2008).

In the original work, the slurry in the batch reactor was amended with 1 wt % of POC (heat-killed yeast), and organic matter decay was modelled according to first-order rate law using Monod rate equation:

$$R_i = k_1[POC]\frac{[EA]_i}{[EA]_i + K_m}\prod_{j=1}^{N}\frac{K_{in}}{[EA]_j + K_{in}} \tag{5.2}$$

where k_1 – first-order rate constant, $[POC]$ – concentration of organic matter, $[EA]$ concentration of electron acceptor (*e.g.*, nitrate, iron oxyhydroxide, or sulphate), K_m – half saturation constant. Inhibition terms K_{in} are used for simulation of the sequential oxidation of the organic matter degradation with nitrate, iron oxyhydroxide, and sulphate, followed by methanogenesis (Table 5.2). The experimental data and results of simulation are shown in Figure 5.2b.

The code of the simulation is the following:

```
1   from porousmedialab.batch import Batch
2   bl = Batch(tend=25, dt=1)
3   bl.add_species(name='POC', init_conc=12e-3)
4   bl.add_species(name='CO2', init_conc=2e-3)
5   bl.add_species(name='Fe2', init_conc=0)
6   bl.add_species(name='NO3', init_conc=1.5e-3)
7   bl.add_species(name='Fe3', init_conc=2e-2)
8   bl.add_species(name='SO4', init_conc=1.7e-3)
9   bl.add_species(name='CH4', init_conc=0)
10  bl.constants['Km_NO3'] = 1e-6
11  bl.constants['Km_Fe3'] = 2e-3
12  bl.constants['Km_SO4'] = 3e-5
13  bl.constants['k1'] = 0.1
14  bl.rates['r1'] = 'k1 * POC * NO3 / (Km_NO3 + NO3)'
15  bl.rates['r2'] = 'k1 * POC *Fe3 / (Km_Fe3 +Fe3) * Km_NO3 / (Km_NO3 + NO3)'
16  bl.rates['r3'] = 'k1 * POC * SO4 / (Km_SO4 + SO4) * Km_Fe3 / (Km_Fe3 +Fe3) * Km_NO3 / (Km_NO3 + NO3
    )'
17  bl.rates['r4'] = 'k1 * POC * Km_SO4 / (Km_SO4 + SO4) * Km_Fe3 / (Km_Fe3 +Fe3) * Km_NO3 / (Km_NO3 +
    NO3)'
18  bl.dcdt['POC'] = '- r1 - r2 - r3 - r4'
19  bl.dcdt['NO3'] = '- 0.8 * r1'
20  bl.dcdt['Fe3'] = '- 4 * r2'
21  bl.dcdt['Fe2'] = '4 * r2'
22  bl.dcdt['SO4'] = '- 0.5 * r3'
23  bl.dcdt['CO2'] = 'r1 + r2 + r3 + 0.5 * r4'
24  bl.dcdt['CH4'] = '0.5 * r4'
25  bl.solve()
26
```

In LOC 1, the *Batch* class is imported from the *porousmedialab* library, and an instance of *Batch* is created with the total time of the simulation of 40 *days* and with the

time-step of one *day*. In LOC from 3 to 10, the species are added using instance method *add_species* with keyword arguments *name* and *init_conc* introducing desired names and initial concentrations. In LOC 10-13, half-saturation constants of electron acceptors and a first-order rate constant of the organic matter degradation are set using instance method *constants*. In LOC 14-17, the rate laws of the reactions are introduced with instance method *rates* using the names of species and constants defined in the previous lines. Rate expressions of reaction equations for each species are written in LOC 18-24, where coefficients in front of the rates are defined in the stoichiometry of the corresponding reactions (Table 5.2). Finally, LOC 25 starts the simulation.

In this example, PorousMediaLab simulates the sequential consumption with the aid of inhibition terms imposed in the kinetic rate laws (Equation 5.2, and LOC 15-17). Simulation shows the typical pattern of the sequential consumption of the terminal electron acceptors, from the most energy-yielding nitrate to the least favorable sulphate, followed by methanogenesis.

5.3.3 Freeze-Thaw Cycles in the Soil Column

The example demonstrates an implementation of one-dimensional transport in the saturated soil column with transient boundary conditions. Vertical soil column consists of the organic matter and two layers of the iron inclusions, where oxygen penetrates only from the top of the column via molecular diffusion. Organic matter is degraded via two pathways, aerobic degradation and oxidation with iron, producing inorganic carbon (Table 5.3). In the model, organic matter degradation rates are simulated via first-order rate law using Monod-type rate equation with temperature dependence factor Q_{10}:

$$R_T = R_\circ \cdot Q_{10}^{\left(\frac{T-T_\circ}{10}\right)} \tag{5.3}$$

where $R_\circ$ – rate of the reaction at the reference temperature $T_\circ$ (Equation 5.2), R_T – rate of the reaction at the temperature T. Conversion of dissolved carbon dioxide CO_2(aq) to gas CO_2(g) is calculated with Henry law equilibrium expression.

no.	Reaction
R_1	$CH_2O + O_2 \longrightarrow CO_2(aq) + H_2O$
R_2	$CH_2O + 4\,Fe(OH)_3 + 7\,H^+ \longrightarrow 4\,{Fe_2}^+ + CO_2(aq) + 11\,H_2O$
R_3	$Fe^{2+} + \frac{1}{4}O_2 + 2\,{HCO_3}^- + \frac{1}{2}H_2O \longrightarrow Fe(OH)_3 + 2\,CO_2(aq)$
R_4	$CO(aq) \longleftrightarrow CO_2(g)$

Table 5.3: Reactions considered during freeze-thaw cycles in the soil column: (1) and (2) organic matter degradation with oxygen and iron are modelled via first-order rate law using Monod rate equation, (3) oxidation of reduced Fe(II) is modelled via bi-molecular rate expression, (4) conversion of inorganic carbon to CO2(g) is calculated with Henry law equilibrium expression.

In our example, freeze-thaw cycles are simulated by changing the temperature at the top of the soil column. During the freezing period, the temperature at the top fluctuates between -15°C and -5°C, and it is assumed that the formation of ice restricts oxygen diffusion into the soil column and bocks escape of carbon dioxide (gas). Thus, using zero flux boundary condition, we simulate a non-permeable physical barrier to gas exchange on the top of the soil column. During the thaw period, the temperature at the top of the soil column fluctuates from 0°C to 10°C simulating daily temperature change. During this period, the top of the soil column is permeable, and the absence of a physical barrier promotes gas exchange.

The input file for this example simulation is as follows:

```
from porousmedialab.column import Column
L = 40
phi = 0.8
t = 27 / 365
dx = 0.2
dt = 1e-5
ftc = Column(L, dx, t, dt)
import numpy as np
x = np.linspace(0, L, L / dx + 1)
Fe3_init = np.zeros(x.size)
Fe3_init[x > 5] = 75; Fe3_init[x > 15] = 0; Fe3_init[x > 25] = 75; Fe3_init[x > 35] = 0
ftc.add_species(theta=1-phi, name='FeOH3', D=1, init_conc=Fe3_init, bc_top_value=0, bc_top_type='flux', bc_bot_value=0, bc_bot_type='flux')
ftc.add_species(theta=phi, name='O2', D=368, init_conc=0, bc_top_value=0.231, bc_top_type='dirichlet', bc_bot_value=0, bc_bot_type='flux')
ftc.add_species(theta=phi, name='TIC', D=320, init_conc=0, bc_top_value=0, bc_top_type='flux', bc_bot_value=0, bc_bot_type='flux')
ftc.add_species(theta=phi, name='Fe2', D=127, init_conc=0, bc_top_value=0, bc_top_type='flux', bc_bot_value=0, bc_bot_type='flux')
ftc.add_species(theta=1-phi, name='OM', D=1, init_conc=15, bc_top_value=0, bc_top_type='flux', bc_bot_value=0, bc_bot_type='flux')
ftc.add_species(theta=phi, name='CO2g', D=320, init_conc=0, bc_top_value=0, bc_top_type='flux', bc_bot_value=0, bc_bot_type='flux')
```

```
    ftc.add_species(theta=phi, name='Temperature', D=281000, init_conc=5, bc_top_value=5., bc_top_type='constant', bc_bot_value=0, bc_bot_type='flux')
    ftc.henry_equilibrium('TIC', 'CO2g', Hcc=0.166)
    ftc.constants['k_OM'] = 1
    ftc.constants['Km_O2'] = 20e-3
    ftc.constants['Km_FeOH3'] = 10
    ftc.constants['k8'] = 1.4e+5
    ftc.constants['Q10'] = 4
    ftc.constants['CF'] = (1-phi)/phi
    ftc.rates['r1'] = 'Q10**((Temperature-5)/10) * k_OM * OM * O2 / (Km_O2 + O2)'
    ftc.rates['r2'] = 'Q10**((Temperature-5)/10) * k_OM * OM * FeOH3 / (Km_FeOH3 + FeOH3) * Km_O2 / (Km_O2 + O2)'
    ftc.rates['r3'] = 'k8 * O2 * Fe2'
    ftc.dcdt['OM'] = '-r1-r2'
    ftc.dcdt['O2'] = '-r1-0.25*r3'
    ftc.dcdt['FeOH3'] = '-4*r2+r3/CF'
    ftc.dcdt['Fe2'] = '-r3+4*r2*CF'
    ftc.dcdt['TIC'] = 'r1+r2*CF'
    for i in range(1, len(ftc.time)):
        day_of_bi_week = (ftc.time[i]*365) % 14
        if day_of_bi_week < 7:
            ftc.change_boundary_conditions('Temperature', i,  bc_top_value=5  + 5 * np.sin(np.pi * 2 * ftc.time[i] * 365), bc_top_type='constant', bc_bot_value=0, bc_bot_type='flux')
        else:
            ftc.change_boundary_conditions('Temperature', i,  bc_top_value=-10  + 5 * np.sin(np.pi * 2 * ftc.time[i] * 365), bc_top_type='constant', bc_bot_value=0, bc_bot_type='flux')
        if ftc.Temperature.bc_top_value < 0:
            ftc.change_boundary_conditions('O2', i, bc_top_value=0, bc_top_type='flux', bc_bot_value=0, bc_bot_type='flux')
            ftc.change_boundary_conditions('CO2g', i, bc_top_value=0, bc_top_type='flux', bc_bot_value=0, bc_bot_type='flux')
        else:
            ftc.change_boundary_conditions('O2', i, bc_top_value=0.231, bc_top_type='constant', bc_bot_value=0, bc_bot_type='flux')
            ftc.change_boundary_conditions('CO2g', i, bc_top_value=0, bc_top_type='constant', bc_bot_value=0, bc_bot_type='flux')
        ftc.integrate_one_timestep(i)

```

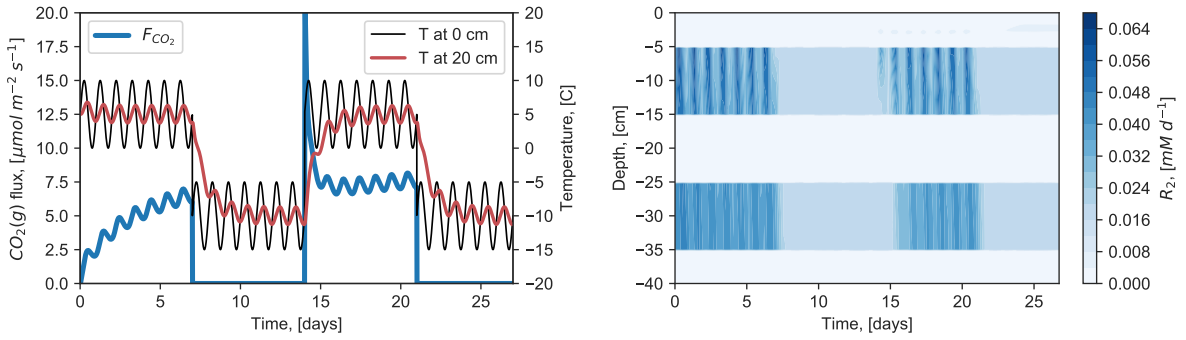

(a) Temperature and CO_2 flux

(b) Rate $r2$

Figure 5.3: Results of the freeze-thaw cycles simulation of the saturated soil column: (a) carbon dioxide flux at the top of the soil column, temperature at the top and in the middle of the soil column, (b) rate of Fe(II) concentration change in time the soil column. The plots are produced using built-in commands (Appendix D.2).

In LOC 1, class *Column* is imported from the *porousmedialab* library. In LOC 2-6, the length of the column L, porosity of the soil *phi*, the total time of simulation t, spatial dx and temporal dt resolution are assigned. In LOC 7, an instance of *Column* is created. In LOC 8-11, the vector of the initial $Fe(OH)_3$ profile *Fe3_init* is created with iron inclusions at the depths from 5 to 15 *cm* and from 25 to 35 *cm*. In LOC 12-17, all required for simulation species are created and added in the *Column*. When species are introduced, the user should provide the porosity *phi* for dissolved species and $(1-phi)$ for solid species, name, initial concentration value or profile, types and values for the top and bottom boundary conditions. The keyword argument *name* gives a reactant desired name, *init_conc* – an initial concentration profile. The profile of *init_conc* can be either scalar which specifies flat concentration profile with a given value or a vector (*e.g.*, see initial profile of *Fe3_init*). The boundary *bc_top_type* and *bc_bot_type* condition type can have either *Dirichlet* (constant value) or *Neumann* (flux) type. Using keyword *bc_top_value* and *bc_bot_value*, the user provides the values of the concentration or flux at the top and bottom boundaries, respectively. In LOC 19, using *henry_equilibrium* instance method, the user specifies partitioning of carbon dioxide using Henry's law constant H^{cc}. In LOC 20-24, half-saturation constants of electron acceptors and first-order rate constant of organic matter degradation, second-order rate constant of iron oxidation, and temperature dependence factor are set using instant method *constants*. In LOC 25, conversion factor CF is introduced in order to account for interface dissolution-precipitation reactions. The rate laws of reactions 1-3 (Table 5.3) are introduced with instance method *rates* using the names of species and constants defined in the previous lines (LOC 26-28). Then, in LOC from 28 to 33, the mass conservation equations are written for all species of interest using instance method *dcdt*. Now, all the information required to start the simulation is provided, yet the user needs to define conditions of the top boundary changes to simulate freeze-thaw cycles.

The code written in LOC 33-46 accounts for the freeze-thaw cycles and changing boundary conditions. First, in order to provide the user access to variables at each time-step, the *for*-loop with *ftc.time* is introduced (LOC 34). In LOC 35 and 36, the program

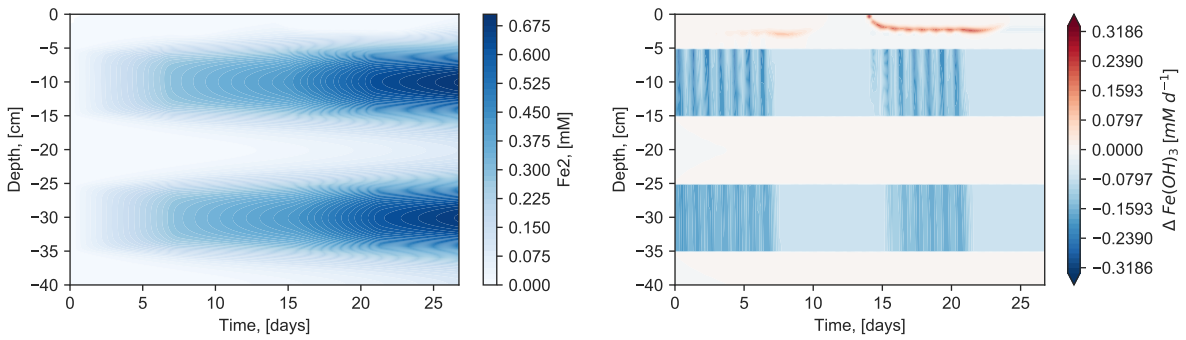

(a) Fe(II) concentration

(b) Fe(III) accumulation rates

Figure 5.4: Results of the freeze-thaw cycles simulation of the saturated soil column: (a) temperature dependent rate of organic matter degradation with iron (table 5.3), (b) Fe(III) accumulation rate in the saturated soil column. The source of Fe (III) is oxidation of ferrous Fe with oxygen (R_3) while the sink is the reduction of Fe(III) with organic matter (R_2).

checks if the current time-step is the first or second week of bi-weekly simulation. During the first week, the top boundary temperature follows the daily sinusoidal change from $0°C$ to $10°C$ (LOC 37); if it is a second week (LOC 39), then the temperature at the top boundary fluctuates from -15°C to -5°C (Figure 5.3a). In LOC 40-45, the program routinely checks if the top boundary temperature is below 0°, then the boundary condition for oxygen and carbon dioxide (gas) are changed to no flux boundary. Otherwise, if the temperature is above $0°C$, then the boundary conditions are changed to constant values and assigned corresponding concentrations of oxygen and carbon dioxide (LOC 44-45). In LOC 46, the program executes one time-step in the *ftc.time* loop.

During the first seven days of the numerical experiment, the temperature at the top of the soil column fluctuates between $0°C$ to $10°C$ (Figure 5.3a). Due to the limited conductivity of soil saturated with water, the temperature at the deeper depths fluctuates to a less extent. As a result, the rates of organic matter degradation R_1 (not shown) and R_2 also varies (Figure 5.4a). Furthermore, freezing and thawing periods result in the stepwise accumulation of ferrous Fe (Figure 5.4b). Thus, after the first freezing period (day 14), oxygen diffusively penetrates in the column and oxidizes accumulated ferrous Fe forming iron oxyhydroxide (Figure 5.3b). Moreover, the effect of the impermeable top boundary during the freezing period (day 7-13) results in carbon dioxide (gas) flux spike

on day 14 (Figure 5.3a).

5.4 PorousMediaLab Applicability, Limitations And Perspectives

PorousMediaLab can simulate zero-dimensional (*e.g.*, batch and flow-through reactors, and mass balance models) and one-dimensional (*e.g.*, soil and sediment columns, contaminant groundwater flow) systems with equilibrium and kinetic reaction terms. The tool will be useful for scientists and students who are going in the laboratory to test their hypotheses and obtain qualitative information before the actual experiments. The options of PorousMediaLab to define the kinetic rate laws of reactions and identify the parameters present the possibility to gain quantitative knowledge after the experiments.

The inventory of PorousMediaLab functionalities is planned to be expanded to perform a sensitivity analysis of the input parameters. Preliminary work is already initiated, and implementation of the Fourier Amplitude Sensitivity Test (Saltelli and Bolado, 1998) is under development. Moreover, a large number of sensitivity test simulations would require extensive computational power. Therefore, it is planned to introduce parallel computation by using multiprocessing libraries on distributed and shared memory systems. The other important milestone in the development of the PorousMediaLab library is to include unsaturated flow transport for simulation of water table fluctuations in the soil column. Possibility of the unsaturated flow transport calculations will significantly expand the application domain of the framework.

5.5 Summary

Tested against analytical solutions, PorousMediaLab is a robust and efficient suite of simulators for solving diverse scientific and practical applications related to aquatic chemistry. PorousMediaLab is a core component of the numerical experiments presented in this thesis. In the preliminary design of the coupled MyLake-Sediment model of Chapter 2, PorousMediaLab was applied to design reaction network, estimate fluxes, reaction time-scales, and internal nutrient load in the sediment. Also, PorousMediaLab is used in

Chapter 3 to simulate the reaction rates using a novel approach based on the thermodynamic switch function. By incorporating dynamic estimations of Gibbs Free Energy of particular reactions that are accessible in PorousMediLab (Appendix D.3), it was possible to estimate the power of the catabolic reactions presented in the chapter. In Chapter 4, the PorousMediaLab is used to simulate water and chloride mass balance of Lake Erie to estimate inter-basin exchange rates. Thus, the capabilities of performing simulations, analysis, and parameter estimations make PorousMediaLab useful as a flexible research tool in designing, developing, and quantifying mechanistic reaction models of aquatic environments.

Chapter 6

Conclusions and Perspectives

6.1 Synthesis of Major Findings

The primary aim of this thesis was to investigate the impact of the different processes at the different scales on the phosphorus cycle in lakes. In Chapter 2, I showed that in Lake Vansjø, phosphorus dynamics is driven by internal loading and iron recycling, while vulnerable to the reduction of ice cover. To achieve that, I expanded the existing MyLake model by incorporating a sediment diagenesis module. I developed the continuous reaction network that couples the water column and sediment biogeochemistry. In the modelling scenarios, I assessed the importance of the sediment processes and the effects of the climatic and anthropogenic drivers on water quality in Lake Vansjø. I stressed the importance of the accumulated phosphorus in controlling timing and magnitude of the biogeochemical lake response to external forcing, including projected changes in the air temperature, disappearing ice cover, and potential management interventions. The code of the new coupled model is open-source, and it is available for lake and sediment modelers.

In Chapter 3, I showed that on the scales of microbial systems, the respiration reactions can adequately be described by the power produced in catabolic reactions. I demonstrated that the intensity of the specific catabolic reaction pathways may exert substantial control on biogeochemical cycles by regulating the availability of the electron donors and acceptors, adsorption sites, secondary minerals, and alkalinity. To achieve that, I developed a new conceptual model to simulate the preferential catabolic reaction

pathways in the microbial reaction networks. In the presented model, I substantially decreased the number of assumptions that are often subjective to specific case studies. It allowed significantly improve the robustness, transferability, and generalization of the model-derived parameters. In contrast to efforts to simulate biogeochemical reaction pathways by kinetic formulations, I demonstrate that new thermodynamically based formulations can be applied to describe the microbial respiration. Those findings are crucial for the accurate prediction of biogeochemical cycles in aquatic environments driven by microbial metabolism.

In Chapter 4, I showed that on the regional scale, weather defines hydrodynamic flush rates and water circulation patterns, which in turn controls the phosphorus transport in Lake Erie. That is, precipitation controls the release of phosphorus from the watershed in the spring, while wind governs the water circulation and transport of the phosphorus released from sediment in the central basin. Both have an impact on algal blooms. Also, I showed that due to the large surface area of the Laurentian Great Lakes watershed, climate and weather in the upper Laurentian Great Lakes regulates changes in the water level of Lake Erie. Daily estimates of all hydrological components of the Lake Erie water balance for the period from 1996 to 2017 are uploaded for the open access.

Finally, I developed PorousMediaLab, a tool for designing, developing, and quantifying the mechanisms of reactive transport within the aquatic environments (Chapter 5). PorousMediaLab is the core component of the numerical investigations presented in the thesis. in Chapter 2, PorousMediaLab was applied to design and test the reaction network, estimate fluxes at the sediment-water interface, and reaction timescales. In Chapter 3, PorousMediaLab was used to simulate the reaction rates using a novel approach based on the thermodynamic switch function. With the thermodynamic library that is accessible in PorousMediaLab, I estimated the energy supply rate of the catabolic reactions. Furthermore, in Chapter 4, PorousMediaLab was used to build a mass balance model and to improve the current understanding of the inter-basin exchange. Overall, within this thesis, the PorousMediaLab framework has been tested with analytical solutions and by reproducing experimental results. The open-source framework is publicly available, and

it is used in various projects by Ecohydrology research group members.

6.2 Research Perspectives

The immediate continuation of the research should focus on the three following areas: (1) improving the reactive modelling of microbial system in lakes, (2) estimating methane fluxes from small lakes, (3) simulation of the lake restoration practices.

6.2.1 Improving the Reactive Modelling of Microbial System in Lakes

The research presented in Chapter 2 in this thesis relies on the use of the inhibition terms to represent the microbial redox reactions. However, in Chapter 3, I showed that using inhibition terms involve a wide range of assumptions to prioritize one reaction over another, whereas they may lack generalization and may underrepresent the environmental changes. Therefore, incorporating the thermodynamic switch function, developed in Chapter 3, would improve the predictive capacity and applicability of the coupled-lake sediment model to wide the range of the environmental conditions.

In state-of-the-art aquatic models, anoxic and aerobic microbial oxidation of the methane, sulfide, ferrous iron, ammonia, pyrite, and other reduced elements are entirely disregarded (Barker and Fritz, 1981, Ende and Gemerden, 1993, Jia and Conrad, 2009, Konhauser et al., 2011). Together these processes have control over the cycling of major nutrients (*e.g.*, carbon, oxygen, phosphorus, nitrogen, sulfur) in marine and freshwater environments. An interplay of such reactions under different conditions may have substantial implications on ecosystem functioning. Thus, modelling of microbial oxidation reactions based on thermodynamic concepts outlined in Chapter 3 would improve predicting capacity of the existing process-based lake models.

6.2.2 Lake-Climate Feedback Loop: Methane Fluxes

In lakes, alongside availability and inputs of carbon, nitrogen, and phosphorus from the catchment, primary production and respiration depend on the geomorphology of the lake. Specifically, water column depth strongly affects sediment respiration making shallow lakes to be the most productive (Duarte and Prairie, 2005, Giorgio et al., 1999, Wetzel,

2001). Direct contact of the sediment with the upper mixed layer in shallow lakes favors mineralization over burial, resulting in production and over-saturation of carbon dioxide and methane, and escape to the atmosphere. Methane emissions from freshwater ecosystems to the atmosphere are comparable in magnitude to the net production of terrestrial ecosystems (Tranvik et al., 2009). Empirical estimations suggest that freshwater environments contribute about one-fifth of the total methane flux to the atmosphere (Khalil and Shearer, 2000). As such, climate warming and increasing water temperature in lakes could amplify a feedback loop where warming enhances methane emission contributing to climate change (Lambrecht et al., 2019).Thus, with addition of rooted vegetation and ebullition processes that are known to be significant, the coupled Lake-Sediment model described in Chapter 2 can be applied to estimate the effect of climate warming on methane fluxes and suggest management solutions to reduce emissions from lakes.

6.2.3 Modelling Before Actions: Lake Restoration

Most of the lake restoration approaches are very radical, intrusive, and expensive methods, causing extinctions of organisms (Gołdyn et al., 2014). Even so, in many cases, the restoration measures have not necessarily led to the desired improvement, and lakes needed additional protective measures (Jeppesen et al., 1991, Lürling et al., 2016, Sondergaard, 2007). The lack of comprehensive studies of the restoration practices using processed based-models severely limits our ability to understand what ecological processes are at stake and what are the potential feedbacks. Moreover, an essential requirement for obtaining success and long-term effects after restoration measures is understanding what specific processes in the particular lake govern the degradation of water quality. Therefore, there is a need for mechanistic simulations of the restoration practices before actual implementation in place to determine the minimally invasive measures.

References

Abtew, W. and P. Trimble (2010). El Nino – Southern Oscillation Link to South Florida Hydrology and Water Management Applications. *Water Resources Management 24*(15), 4255–4271.

Achtnich, C. and A. Schuhmann (1995). Role of interspecies H2 transfer to sulfate and ferric iron-reducing bacteria in acetate consumption in anoxic paddy soil. *FEMS Microbiology Ecology 16*(1), 61–70.

Adrian, R., C. M. O'Reilly, H. Zagarese, S. B. Baines, D. O. Hessen, W. Keller, D. M. Livingstone, R. Sommaruga, D. Straile, E. Van Donk, G. A. Weyhenmeyer, and M. Winder (2009). Lakes as sentinels of climate change. *Limnology and Oceanography 54*(6), 2283–2297.

Aguilera, D. R., P. Jourabchi, C. Spiteri, and P. Regnier (2005). A knowledge-based reactive transport approach for the simulation of biogeochemical dynamics in Earth systems. *Geochemistry, Geophysics, Geosystems 6*(7).

Ahlgren, J., K. Reitzel, H. De Brabandere, A. Gogoll, and E. Rydin (2011). Release of organic P forms from lake sediments. *Water Research 45*(2), 565–572.

Ahring, B. K. and P. Westermann (1987). Kinetics of butyrate, acetate, and hydrogen metabolism in a thermophilic, anaerobic, butyrate-degrading triculture. *Applied and Environmental Microbiology 53*(2), 434–439.

Aiba, S., M. Shoda, and M. Nagatani (1968). Kinetics of product inhibition in alcohol fermentation. *Biotechnology and Bioengineering 10*(6), 845–864.

Akbarzadeh, Z., A. M. Laverman, F. Rezanezhad, M. Raimonet, E. Viollier, B. Shafei, and P. Van Cappellen (2018). Benthic nitrite exchanges in the Seine River (France): An early diagenetic modeling analysis. *The Science of the Total Environment 628-629*, 580–593.

Algar, C. K. and J. J. Vallino (2014). Predicting microbial nitrate reduction pathways in coastal sediments. *Aquatic Microbial Ecology 71*(3), 223–238.

Amirbahman, A., B. A. Lake, and S. A. Norton (2012). Seasonal phosphorus dynamics in the surficial sediment of two shallow temperate lakes: a solid-phase and pore-water study. *Hydrobiologia 701*(1), 65–77.

Arndt, S., B. B. Jørgensen, D. E. LaRowe, J. J. Middelburg, R. D. Pancost, and P. Regnier (2013). Quantifying the degradation of organic matter in marine sediments: A review and synthesis. *Earth-Science Reviews 123*, 53–86.

Atkin, O. K. and M. G. Tjoelker (2003). Thermal acclimation and the dynamic response of plant respiration to temperature. *Trends in Plant Science 8*(7), 343–351.

Austin, J. and S. Colman (2008). A century of temperature variability in Lake Superior. *Limnology and Oceanography 53*(6), 2724–2730.

Ayora, C., C. Taberner, M. W. Saaltink, and J. Carrera (1998). The genesis of dedolomites: a discusion based on reactive transport modeling. *Journal of Hydrology 209*(1-4), 346–365.

Barker, J. F. and P. Fritz (1981, September). Carbon isotope fractionation during microbial methane oxidation. *Nature 293*(5), 289–291.

Beletsky, D., N. Hawley, and Y. R. Rao (2013). Modeling summer circulation and thermal structure of Lake Erie. *Journal of Geophysical Research: Oceans 118*(11), 6238–6252.

Bengtsson, L., V. Fortin, A. D. Gronewold, Y. Tanino, B. Surridge, N. Watson, R. W. Herschy, G. Gergov, M.-k. Woo, K. Young, L. Lundin, and L. Cavaleri (2012). Water

Balance of the Laurentian Great Lakes. In *Encyclopedia of Lakes and Reservoirs*, pp. 864–869. Springer Netherlands.

Benndorf, J. (1995). Possibilities and Limits for Controlling Eutrophication by Biomanipulation. *Internationale Revue der gesamten Hydrobiologie und Hydrographie 80*(4), 519–534.

Bentsen, M., I. Bethke, J. B. Debernard, T. Iversen, A. Kirkevaag, O. Seland, H. Drange, C. Roelandt, I. A. Seierstad, C. Hoose, and J. E. Kristjansson (2013). The Norwegian Earth System Model, NorESM1-M – Part 1: Description and basic evaluation of the physical climate. *Geoscientific Model Development 6*(3), 687–720.

Berg, P. (2003). Dynamic Modeling of Early Diagenesis and Nutrient Cycling. A Case Study in an Artic Marine Sediment. *American Journal of Science 303*(10), 905–955.

Berner, R. A. (1980). *Early diagenesis: a theoretical approach*. Number 1. Princeton University Press.

Bertilsson, S., A. Burgin, C. C. Carey, S. B. Fey, H.-P. Grossart, L. M. Grubisic, I. D. Jones, G. Kirillin, J. T. Lennon, A. Shade, and R. L. Smyth (2013). The under-ice microbiome of seasonally frozen lakes. *Limnology and Oceanography 58*(6), 1998–2012.

Bethke, C. M., D. Ding, Q. Jin, and R. a. Sanford (2008). Origin of microbiological zoning in groundwater flows. *Geology 36*(9), 739–742.

Bethke, C. M., R. a. Sanford, M. F. Kirk, Q. Jin, and T. M. Flynn (2011). The thermodynamic ladder in geomicrobiology. *American Journal of Science 311*(3), 183–210.

Blanch, H. W. (1981). Invited Review Microbial Growth Kinetics. *8*(4-6), 181–211.

Bocaniov, S. A., L. F. Leon, Y. R. Rao, D. J. Schwab, and D. Scavia (2016). Simulating the effect of nutrient reduction on hypoxia in a large lake (Lake Erie, USA-Canada) with a three-dimensional lake model. *Journal of Great Lakes Research 42*(6), 1228–1240.

Bocaniov, S. A., D. S. W. R. Research, and 2018 (2018). Nutrient Loss Rates in Relation to Transport Time Scales in a Large Shallow Lake (Lake St. Clair, USA—Canada): Insights From a Three-Dimensional Model. *Wiley Online Library 54*(6), 3825–3840.

Boon, B. and H. Laudelout (1962). Kinetics of nitrite oxidation by Nitrobacter winogradskyi. *The Biochemical journal 85*(3), 440–447.

Boström, B., J. M. Andersen, S. Fleischer, and M. Jansson (1988). Exchange of phosphorus across the sediment-water interface. *Hydrobiologia 170*(1), 229–244.

Bostrom, B., J. M. Andersen, S. Fleischer, and M. Jansson (1988). Exchange of phosphorus across the sediment-water interface. *Hydrobiologia 170*(1), 229–244.

Boudreau, B. P. (1996). A method-of-lines code for carbon and nutrient diagenesis in aquatic sediments. *Computers & Geosciences 22*(5), 479–496.

Boudreau, B. P. (1997). *Diagenetic Models and Their Implementation*.

Bruggeman, J. and K. Bolding (2014). A general framework for aquatic biogeochemical models. *Environmental Modelling & Software 61*, 249–265.

Bryhn, A. C. and L. Haakanson (2007). A Comparison of Predictive Phosphorus Load-Concentration Models for Lakes. *Ecosystems 10*(7), 1084–1099.

Burns, D., T. Vitvar, J. McDonnell, J. Hassett, J. Duncan, and C. Kendall (2005). Effects of suburban development on runoff generation in the Croton River basin, New York, USA. *Journal of Hydrology 311*(1-4), 266–281.

Butcher, J. B., D. Nover, T. E. Johnson, and C. M. Clark (2015). Sensitivity of lake thermal and mixing dynamics to climate change. *Climatic Change 129*(1-2), 295–305.

Canavan, R. W., C. P. Slomp, P. Jourabchi, P. Van Cappellen, A. M. Laverman, and G. A. van den Berg (2006). Organic matter mineralization in sediment of a coastal freshwater lake and response to salinization. *Geochimica et Cosmochimica Acta 70*(11), 2836–2855.

Canfield, D. E., E. Kristensen, and B. Thamdrup (2005). Aquatic geomicrobiology. *Advances in marine biology 48*, 1–599.

Canfield, D. E. and B. Thamdrup (2009). Towards a consistent classification scheme for geochemical environments, or, why we wish the term 'suboxic' would go away. *Geobiology 7*(4), 385–392.

Carvalho, L., C. McDonald, C. de Hoyos, U. Mischke, G. Phillips, G. Borics, S. Poikane, B. Skjelbred, A. L. Solheim, J. Van Wichelen, and A. C. Cardoso (2013). Sustaining recreational quality of European lakes: minimizing the health risks from algal blooms through phosphorus control. *The Journal of Applied Ecology 50*(2), 315–323.

Chapra, S. C. and D. M. Dolan (2012). Great Lakes total phosphorus revisited: 2. Mass balance modeling. *Journal of Great Lakes Research 38*(4), 741–754.

Chen, C., G. Cowles, and R. C. Beardsley (2006). An unstructured grid, finite-volume coastal ocean model: FVCOM User Manual.

Chen, J., F. P. Brissette, and R. Leconte (2010). A daily stochastic weather generator for preserving low-frequency of climate variability. *Journal of Hydrology 388*(3-4), 480–490.

Christensen, T. H., P. L. Bjerg, S. A. Banwart, R. Jakobsen, G. Heron, and H. J. Albrechtsen (2000). Characterization of redox conditions in groundwater contaminant plumes. *Journal of Contaminant Hydrology 45*(3-4), 165–241.

Cloern, J. E., C. Grenz, and L. V. Lucas (1995). An empirical model of the phytoplankton chlorophyll : carbon ratio-the conversion factor between productivity and growth rate. *Limnology and Oceanography 40*(7), 1313–1321.

Cole, T. M. and S. A. Wells (2006). CE-QUAL-W2: A two-dimensional, laterally averaged, hydrodynamic and water quality model, version 3.5.

Conley, D. J., H. W. Paerl, R. W. Howarth, D. F. Boesch, S. P. Seitzinger, K. E. Havens, C. Lancelot, and G. E. Likens (2009). Controlling Eutrophication: Nitrogen and Phosphorus. *Science 323*(5917), 1014–1015.

Correll, D. (1999). Phosphorus: A Rate Limiting Nutrient In Surface Waters. *Poultry Science 78*(5), 674–682.

Couture, R.-M., H. A. De Wit, K. Tominaga, P. Kiuru, and I. Markelov (2015). Oxygen dynamics in a boreal lake responds to long-term changes in climate, ice phenology, and DOC inputs. *Journal of Geophysical Research: Biogeosciences 120*(11), 2441–2456.

Couture, R.-M., R. Fischer, P. Van Cappellen, and C. Gobeil (2016). Non-steady state diagenesis of organic and inorganic sulfur in lake sediments. *Geochimica et Cosmochimica Acta 194*(C), 15–33.

Couture, R.-M., C. Gobeil, and A. Tessier (2010). Arsenic, iron and sulfur co-diagenesis in lake sediments. *Geochimica et Cosmochimica Acta 74*(4), 1238–1255.

Couture, R.-M., S. Jannicke Moe, Y. Lin, O. Kaste, S. Haande, and A. L. Solheim (2018). Simulating water quality and ecological status of Lake Vansjo, Norway, under land-use and climate change by linking process-oriented models with a Bayesian network. *The Science of the Total Environment 621*, 713–724.

Couture, R.-M., B. Shafei, P. Van Cappellen, A. Tessier, and C. Gobeil (2010). Non-steady state modeling of arsenic diagenesis in lake sediments. *Environmental Science & Technology 44*(1), 197–203.

Couture, R.-M., K. Tominaga, J. Starrfelt, S. Jannicke Moe, O. Kaste, and R. F. Wright (2014). Modelling phosphorus loading and algal blooms in a Nordic agricultural catchment-lake system under changing land-use and climate. *Environmental Science. Processes & Impacts 16*(7), 1588–1599.

Croley, T. E. (1989). Verifiable evaporation modeling on the Laurentian Great Lakes. *Water resources research 25*(5), 781–792.

Croley, T. E. (2005). Recent Great Lakes Evaporation Model Estimates. In *Impacts of Global Climate Change*.

Dale, A. W., V. J. Bertics, T. Treude, S. Sommer, and K. Wallmann (2013). Modeling benthic–pelagic nutrient exchange processes and porewater distributions in a seasonally hypoxic sediment: evidence for massive phosphate release by Beggiatoa? *Biogeosciences 10*(2), 629–651.

de Wit, H. A., R.-M. Couture, L. Jackson-Blake, M. N. Futter, S. Valinia, K. Austnes, J.-L. Guerrero, and Y. Lin (2018). Pipes or chimneys? For carbon cycling in small boreal lakes, precipitation matters most. *Limnology and Oceanography Letters 3*(3), 275–284.

del Giorgio, P. and P. Williams (2005). *Respiration in Aquatic Ecosystems*. OUP Oxford.

Delworth, T. L., A. Rosati, W. Anderson, A. J. Adcroft, V. Balaji, R. Benson, K. Dixon, S. M. Griffies, H.-C. Lee, R. C. Pacanowski, G. A. Vecchi, A. T. Wittenberg, F. Zeng, and R. Zhang (2012). Simulated Climate and Climate Change in the GFDL CM2.5 High-Resolution Coupled Climate Model. *Journal of Climate 25*(8), 2755–2781.

DeMarchi, C., Q. Dai, M. Mello, and T. S. Hunter (2009). Estimate ofoverlake precipitation and basin runoff uncertainty. *Report to the International Upper Great Lakes Study Hydroclimate Technical Working Group Tasks 3.1.2 and 3.3.3*.

Derecki, J. A. (1976a). Heat Storage and Advection in Lake Erie. *Water Resources Research 12*(6), 1144–1150.

Derecki, J. A. (1976b). Multiple estimates of lake erie evaporation. *Journal of Great Lakes Research 2*(1), 124–149.

Dibike, Y., T. Prowse, T. Saloranta, and R. Ahmed (2011). Response of Northern Hemisphere lake-ice cover and lake-water thermal structure patterns to a changing climate. *Hydrological Processes 25*(19), 2942–2953.

DiChristina, T. J. (1992). Effects of nitrate and nitrite on dissimilatory iron reduction by Shewanella putrefaciens 200. *Journal of bacteriology 174*(6), 1891–1896.

Dijkstra, N., M. Hagens, M. Egger, and C. P. Slomp (2018). Post-depositional formation of vivianite-type minerals alters sediment phosphorus records. *Biogeosciences 15*(3), 861–883.

Dillon, P. J. and F. H. Rigler (1974). The Phosphorus-Chlorophyll Relationship In Lakes. *Limnology and Oceanography 19*, 767–773.

Dithmer, L., A. S. Lipton, K. Reitzel, T. E. Warner, D. Lundberg, and U. G. Nielsen (2015). Characterization of phosphate sequestration by a lanthanum modified bentonite clay: a solid-state NMR, EXAFS, and PXRD study. *Environmental Science & Technology 49*(7), 4559–4566.

Dittrich, M., A. Chesnyuk, A. Gudimov, J. McCulloch, S. Quazi, J. Young, J. Winter, E. Stainsby, and G. Arhonditsis (2013). Phosphorus retention in a mesotrophic lake under transient loading conditions: Insights from a sediment phosphorus binding form study. *Water Research 47*(3), 1433–1447.

Dittrich, M., B. Wehrli, and P. Reichert (2009). Lake sediments during the transient eutrophication period: Reactive-transport model and identifiability study. *Ecological Modelling 220*(20), 2751–2769.

Doan, P. T. K., S. B. Watson, S. Markovic, A. Liang, J. Guo, S. Mugalingam, J. Stokes, A. Morley, W. Zhang, G. B. Arhonditsis, and M. Dittrich (2018). Phosphorus retention and internal loading in the Bay of Quinte, Lake Ontario, using diagenetic modelling. *Science of The Total Environment 636*, 39–51.

Doolittle, H. A., S. A. Norton, L. C. Bacon, H. A. Ewing, and A. Amirbahman (2018). The internal and watershed controls on hypolimnetic sediment phosphorus release in Lake Auburn, Maine, USA. *Lake and Reservoir Management 34*(3), 258–269.

Duarte, C. M. and Y. T. Prairie (2005). Prevalence of Heterotrophy and Atmospheric CO2 Emissions from Aquatic Ecosystems. *Ecosystems 8*(7), 862–870.

Dufresne, J.-L., M.-A. Foujols, S. Denvil, A. Caubel, O. Marti, O. Aumont, Y. Balkanski, S. Bekki, H. Bellenger, R. Benshila, S. Bony, L. Bopp, P. Braconnot, P. Brock-

mann, P. Cadule, F. Cheruy, F. Codron, A. Cozic, D. Cugnet, N. de Noblet, J.-P. Duvel, C. Ethe, L. Fairhead, T. Fichefet, S. Flavoni, P. Friedlingstein, J.-Y. Grandpeix, L. Guez, E. Guilyardi, D. Hauglustaine, F. Hourdin, A. Idelkadi, J. Ghattas, S. Joussaume, M. Kageyama, G. Krinner, S. Labetoulle, A. Lahellec, M.-P. Lefebvre, F. Lefevre, C. Levy, Z. X. Li, J. Lloyd, F. Lott, G. Madec, M. Mancip, M. Marchand, S. Masson, Y. Meurdesoif, J. Mignot, I. Musat, S. Parouty, J. Polcher, C. Rio, M. Schulz, D. Swingedouw, S. Szopa, C. Talandier, P. Terray, N. Viovy, and N. Vuichard (2013). Climate change projections using the IPSL-CM5 Earth System Model: from CMIP3 to CMIP5. *Climate Dynamics 40*(9-10), 2123–2165.

Eichenlaub, V. L. (1979). *Weather and climate of the Great Lakes region*. Univ of Notre Dame Pr.

Ende, F. P. and H. Gemerden (1993, October). Sulfide oxidation under oxygen limitation by a thiobacillus thioparus isolated from a marine microbial mat. *FEMS Microbiology Ecology 13*(1), 69–77.

Engstrom, D. R. (2005). Long-term Changes in Iron and Phosphorus Sedimentation in Vadnais Lake, Minnesota, Resulting from Ferric Chloride Addition and Hypolimnetic Aeration. *Lake and Reservoir Management 21*(1), 95–105.

Fang, X. and H. G. Stefan (2009). Simulations of climate effects on water temperature, dissolved oxygen, and ice and snow covers in lakes of the contiguous U.S. under past and future climate scenarios. *Limnology and Oceanography 54*(6part2), 2359–2370.

Ferro, I. (2003). Cycling of iron and manganese in freshwater, estuarine and deep sea sediments. *Thesis*.

Filippelli, G. M. (2008). The Global Phosphorus Cycle: Past, Present, and Future. *Elements 4*(2), 89–95.

Forget, G., J. M. Campin, P. Heimbach, C. N. Hill, R. M. Ponte, and C. Wunsch (2015). ECCO version 4: an integrated framework for non-linear inverse modeling and global ocean state estimation. *Geoscientific Model Development Discussions 8*(5), 3653–3743.

Fragoso Jr., C. R., E. H. Van Nes, J. H. Janse, and D. da Motta Marques (2009). IPH-TRIM3D-PCLake: A three-dimensional complex dynamic model for subtropical aquatic ecosystems. *Environmental Modelling & Software 24*(11), 1347–1348.

Franz, D., I. Mammarella, J. Boike, G. Kirillin, T. Vesala, N. Bornemann, E. Larmanou, M. Langer, and T. Sachs (2018). Lake-atmosphere heat flux dynamics of a thermokarst lake in arctic Siberia. *Journal of Geophysical Research: Atmospheres*.

Froelich, P., G. Klinkhammer, M. a. a. Bender, N. Luedtke, G. R. Heath, D. Cullen, P. Dauphin, D. Hammond, B. Hartman, and V. Maynard (1979). Early oxidation of organic matter in pelagic sediments of the eastern equatorial atlantic: suboxic diagenesis. *43*(7), 1075–1090.

Fuechslin, H. P., C. Schneider, and T. Egli (2012). In glucose-limited continuous culture the minimum substrate concentration for growth, s(min), is crucial in the competition between the enterobacterium Escherichia coli and Chelatobacter heintzii, an environmentally abundant bacterium. *The ISME Journal 6*(4), 777–789.

Fuhrer, T., E. Fischer, and U. Sauer (2005). Experimental Identification and Quantification of Glucose Metabolism in Seven Bacterial Species. *Journal of bacteriology 187*(5), 1581–1590.

Gallagher, K. L., C. Dupraz, and P. T. Visscher (2014). Two opposing effects of sulfate reduction on carbonate precipitation in normal marine, hypersaline, and alkaline environments: COMMENT. *Geology 42*(1), e313–e314.

Gebre, S., T. Boissy, and K. Alfredsen (2014). Sensitivity of lake ice regimes to climate change in the Nordic region. *The Cryosphere 8*(4), 1589–1605.

Gemmell, B. J., G. Oh, E. J. Buskey, and T. A. Villareal (2016). Dynamic sinking behaviour in marine phytoplankton: rapid changes in buoyancy may aid in nutrient uptake. *Proceedings of the Royal Society B: Biological Sciences 283*(1840), 20161126.

George, D. G. and C. S. Reynolds (1997). Zooplankton-phytoplankton interactions: the case for refining methods, measurements and models. *Aquatic Ecology 31*(1), 59–71.

Giorgio, P. A. D., J. J. Cole, N. F. Caraco, and R. H. Peters (1999). Linking Planktonic Biomass and Metabolism to Net Gas Fluxes in Northern Temperate Lakes. *Ecology 80*(4), 1422.

Giraldo-Gomez, E., S. Goodwin, and M. S. Switzenbaum (1992). Influence of mass transfer limitations on determination of the half saturation constant for hydrogen uptake in a mixed-culture CH4-producing enrichment. *Biotechnology and Bioengineering 40*(7), 768–776.

Gołdyn, R., S. Podsiadłowski, R. Dondajewska, and A. Kozak (2014). The sustainable restoration of lakes—towards the challenges of the Water Framework Directive. *Ecohydrology & Hydrobiology 14*(1), 68–74.

Groisman, P. Y. and D. R. Legates (1994). The Accuracy of United States Precipitation Data. *Bulletin of the American Meteorological Society 75*(2), 215–227.

Gronewold, A. D., J. Bruxer, D. Durnford, J. P. Smith, A. H. Clites, F. Seglenieks, S. S. Qian, T. S. Hunter, and V. Fortin (2016). Hydrological drivers of record-setting water level rise on Earth's largest lake system. *Water Resources Research 52*(5), 4026–4042.

Gudasz, C., D. Bastviken, K. Steger, K. Premke, S. Sobek, and L. J. Tranvik (2010). Temperature-controlled organic carbon mineralization in lake sediments. *Nature 466*(7), 478–481.

Gudimov, A., D.-K. Kim, J. D. Young, M. E. Palmer, M. Dittrich, J. G. Winter, E. Stainsby, G. B. Arhonditsis, M. E. Palmer, J. G. Winter, and E. Stainsby (2015). Examination of the role of dreissenids and macrophytes in the phosphorus dynamics of Lake Simcoe, Ontario, Canada. *Ecological Informatics 26*, 36–53.

Gudimov, A., J. McCulloch, J. Chen, P. Doan, G. Arhonditsis, and M. Dittrich (2016). Modeling the interplay between deepwater oxygen dynamics and sediment diagenesis in a hard-water mesotrophic lake. *Ecological Informatics 31*, 59–69.

Gulati, R. D., E. H. R. R. Lammens, M.-L. Meijer, and E. Van Donk (Eds.) (1990).

Biomanipulation Tool for Water Management. Proceedings of an International Conference held in Amsterdam, The Netherlands, 8–11 August, 1989. Dordrecht: Springer Netherlands.

Gulati, R. D., L. Miguel Dionisio Pires, and E. van Donk (2012). Restoration of Freshwater Lakes. In *Restoration Ecology*, pp. 233–247.

Guyer, J. E., D. Wheeler, and J. A. Warren (2009). Fipy: Partial differential equations with python. *Computing in Science & Engineering 11*(3), 6–15.

Haande, S., S. Jannicke Moe, and R.-M. Couture (2016). Phytoplankton and other monitoring data from Lake VansjO. *Freshwater Metadata Journal*, 1–8.

Hadley, K. R., A. M. Paterson, R. I. Hall, and J. P. Smol (2012). Effects of multiple stressors on lakes in south-central Ontario: 15 years of change in lakewater chemistry and sedimentary diatom assemblages. *Aquatic Sciences 75*(3), 349–360.

Haeckel, M., B. P. Boudreau, and K. Wallmann (2007). Bubble-induced porewater mixing: A 3-d model for deep porewater irrigation. Technical Report 21.

Håkanson, L. (1986). The swedish coastal zone project: sediment types and morphometry. In *Sediments and Water Interactions*, pp. 35–51. Springer.

Hampton, S. E., A. W. E. Galloway, S. M. Powers, T. Ozersky, K. H. Woo, R. D. Batt, S. G. Labou, C. M. O'Reilly, S. Sharma, N. R. Lottig, E. H. Stanley, R. L. North, J. D. Stockwell, R. Adrian, G. A. Weyhenmeyer, L. Arvola, H. M. Baulch, I. Bertani, L. L. Bowman, C. C. Carey, J. Catalan, W. Colom-Montero, L. M. Domine, M. Felip, I. Granados, C. Gries, H.-P. Grossart, J. Haberman, M. Haldna, B. Hayden, S. N. Higgins, J. C. Jolley, K. K. Kahilainen, E. Kaup, M. J. Kehoe, S. MacIntyre, A. W. Mackay, H. L. Mariash, R. M. McKay, B. Nixdorf, P. NOGES, T. Noges, M. Palmer, D. C. Pierson, D. M. Post, M. J. Pruett, M. Rautio, J. S. Read, S. L. Roberts, J. Rücker, S. Sadro, E. A. Silow, D. E. Smith, R. W. Sterner, G. E. A. Swann, M. A. Timofeyev, M. Toro, M. R. Twiss, R. J. Vogt, S. B. Watson, E. J. Whiteford, and M. A. Xenopoulos (2017). Ecology under lake ice. *Ecology Letters 20*(1), 98–111.

Hampton, S. E., M. V. Moore, T. Ozersky, E. H. Stanley, C. M. Polashenski, and A. W. E. Galloway (2015). Heating up a cold subject: Prospects for under-ice plankton research in lakes. *Journal of Plankton Research 37*(2), 277–284.

Havens, K. E. and H. W. Paerl (2015). Climate Change at a Crossroad for Control of Harmful Algal Blooms. *Environmental Science & Technology 49*(21), 12605–12606.

Herschy, R. W. (1971). *The magnitude of errors at flow measurement stations*. Water Resources Board.

Hieltjes, A. H. M. and L. Lijklema (1980). Fractionation of Inorganic Phosphates in Calcareous Sediments1. *Journal of Environmental Quality 9*(3), 405.

Hipsey, M. R., L. C. Bruce, C. Boon, B. Busch, C. C. Carey, D. P. Hamilton, P. C. Hanson, J. S. Read, E. de Sousa, M. Weber, and L. A. Winslow (2017). A General Lake Model (GLM 2.4) for linking with high-frequency sensor data from the Global Lake Ecological Observatory Network (GLEON). *Geoscientific Model Development Discussions*, 1–60.

Hodges, B. R. (2009). Hydrodynamical Modeling. In *Encyclopedia of Inland Waters*, pp. 613–627. Elsevier.

Hoehler, T. M., M. J. Alperin, D. B. Albert, and C. S. Martens (1998). Thermodynamic control on hydrogen concentrations in anoxic sediments. *Geochimica et Cosmochimica Acta 62*(10), 1745–1756.

Horton, R. E. (1927). *Hydrology of the Great Lakes*. Sanitary District of Chicago.

Hu, F., K. Bolding, J. Bruggeman, E. Jeppesen, M. R. Flindt, L. van Gerven, J. H. Janse, A. B. G. Janssen, J. J. Kuiper, W. M. Mooij, and D. Trolle (2016). FABM-PCLake – linking aquatic ecology with hydrodynamics. *Geoscientific Model Development 9*(6), 2271–2278.

Huisman, J., H. C. P. Matthijs, and P. M. Visser (2005). *Harmful Cyanobacteria*, Volume 3 of *Aquatic Ecology Series*. Springer.

Huisman, J. and F. J. Weissing (1999). Biodiversity of plankton by species oscillations and chaos. *Nature 402*(6), 407–410.

Hülsmann, S., K. Rinke, and W. M. Mooij (2005). A quantitative test of the size efficiency hypothesis by means of a physiologically structured model. *Oikos 110*(1), 43–54.

Humphrey, A. E. (1972). The kinetics of biosystems: a review.

Huser, B. J., S. Egemose, H. Harper, M. Hupfer, H. Jensen, K. M. Pilgrim, K. Reitzel, E. Rydin, and M. Futter (2016). Longevity and effectiveness of aluminum addition to reduce sediment phosphorus release and restore lake water quality. *Water research 97*, 122–132.

Iho, A., L. Ahlvik, P. Ekholm, J. Lehtoranta, and P. Kortelainen (2017). Optimal Phosphorus Abatement Redefined: Insights From Coupled Element Cycles. *Ecological Economics 137*, 13–19.

Ingvorsen, K., a. J. Zehnder, and B. B. Jørgensen (1984). Kinetics of Sulfate and Acetate Uptake by Desulfobacter postgatei. *Applied and Environmental Microbiology 47*(2), 403–408.

IPCC Report (2018). Global Warming of 1.5C. *An IPCC Special Report on the Impacts of Global Warming of 1.5C Above Pre-industrial Levels and Related Global Greenhouse Gas Emission Pathways*.

Jackson-Blake, L. A. and J. Starrfelt (2015). Do higher data frequency and Bayesian autocalibration lead to better model calibration? Insights from an application of INCA-P, a process-based river phosphorus model. *Journal of Hydrology 527*, 641–655.

James, W. F. (2017). Internal phosphorus loading contributions from deposited and resuspended sediment to the Lake of the Woods. *Lake and Reservoir Management 33*(4), 347–359.

Janssen, A. B. G., G. B. Arhonditsis, A. Beusen, K. Bolding, L. Bruce, J. Bruggeman, R.-M. Couture, A. S. Downing, J. Alex Elliott, M. A. Frassl, G. Gal, D. J. Gerla, M. R.

Hipsey, F. Hu, S. C. Ives, J. H. Janse, E. Jeppesen, K. D. Johnk, D. Kneis, X. Kong, J. J. Kuiper, M. K. Lehmann, C. Lemmen, D. ozkundakci, T. Petzoldt, K. Rinke, B. J. Robson, R. Sachse, S. A. Schep, M. Schmid, H. Scholten, S. Teurlincx, D. Trolle, T. A. Troost, A. A. Van Dam, L. P. A. Van Gerven, M. Weijerman, S. A. Wells, and W. M. Mooij (2015). Exploring, exploiting and evolving diversity of aquatic ecosystem models: a community perspective. *Aquatic Ecology 49*(4), 513–548.

Janssen, A. B. G., S. Teurlincx, A. H. W. Beusen, M. A. J. Huijbregts, J. Rost, A. M. Schipper, L. M. S. Seelen, W. M. Mooij, and J. H. Janse (2019). PCLake+: A process-based ecological model to assess the trophic state of stratified and non-stratified freshwater lakes worldwide. *Ecological Modelling 396*, 23–32.

Jarvie, H. P., L. T. Johnson, A. N. Sharpley, D. R. Smith, D. B. Baker, T. W. Bruulsema, and R. Confesor (2017). Increased Soluble Phosphorus Loads to Lake Erie: Unintended Consequences of Conservation Practices? *Journal of Environment Quality 46*(1), 123.

Jeppesen, E., P. Kristensen, J. Jensen, M. Søndergaard, E. Mortensen, and T. Lauridsen (1991). Recovery resilience following a reduction in external phosphorus loading of shallow, eutrophic danish lakes: duration, regulating factors and methods for overcoming resilience. *Memorie dell'Istituto Italiano di Idrobiologia 48*, 127–148.

Jeppesen, E., M. Meerhoff, T. A. Davidson, D. Trolle, M. Sondergaard, T. L. LAURIDSEN, M. Beklioglu, S. Brucet, P. Volta, I. González-Bergonzoni, and A. Nielsen (2014). Climate change impacts on lakes: an integrated ecological perspective based on a multifaceted approach, with special focus on shallow lakes. *Journal of Limnology 73*(s1).

Jia, Z. and R. Conrad (2009, July). Bacteriarather than Archaeadominate microbial ammonia oxidation in an agricultural soil. *Environmental Microbiology 11*(7), 1658–1671.

Jöhnk, K. D., J. Huisman, J. Sharples, B. Sommeijer, P. M. Visser, and J. M. Stroom (2008). Summer heatwaves promote blooms of harmful cyanobacteria. *Global Change Biology 14*(3), 495–512.

Jones, E., T. Oliphant, P. Peterson, et al. (2001). SciPy: Open source scientific tools for Python.

Jørgensen, S. E. (2008). Overview of the model types available for development of ecological models. *Ecological Modelling 215*(1-3), 3–9.

Jørgensen, S. E. (2010). A review of recent developments in lake modelling. *Ecological Modelling 221*(4), 689–692.

Jourabchi, P. (2007). New Developments in Early Diagenetic Modeling : pH Distributions, Calcite Dissolution and Compaction.

Karatayev, A. Y., L. E. Burlakova, and D. K. Padilla (2014). Zebra versus quagga mussels: a review of their spread, population dynamics, and ecosystem impacts. *Hydrobiologia 746*(1), 97–112.

Katsev, S. (2017). When large lakes respond fast: A parsimonious model for phosphorus dynamics. *Journal of Great Lakes Research 43*(1), 199–204.

Katsev, S. and M. Dittrich (2013). Modeling of decadal scale phosphorus retention in lake sediment under varying redox conditions. *Ecological Modelling 251*, 246–259.

Katsev, S., I. Tsandev, I. L'Heureux, and D. G. Rancourt (2006). Factors controlling long-term phosphorus efflux from lake sediments: Exploratory reactive-transport modeling. *Chemical Geology 234*(1-2), 127–147.

Khalil, M. A. K. and M. J. Shearer (2000). Sources of Methane: An Overview. In *Atmospheric Methane*, pp. 98–111. Berlin, Heidelberg: Springer Berlin Heidelberg.

Kiuru, P., A. Ojala, I. Mammarella, J. Heiskanen, M. Kämäräinen, T. Vesala, and T. Huttula (2018). Effects of Climate Change on CO2 Concentration and Efflux in a Humic Boreal Lake: A Modeling Study. *Journal of Geophysical Research: Biogeosciences 123*(7), 2212–2233.

Konhauser, K. O., A. Kappler, and E. E. Roden (2011). Iron in Microbial Metabolisms. *Elements 7*(2), 89–93.

Kopáček, J., J. Borovec, J. Hejzlar, K.-U. Ulrich, S. A. Norton, and A. Amirbahman (2005). Aluminum Control of Phosphorus Sorption by Lake Sediments. *Environmental Science & Technology 39*(22), 8784–8789.

Koski-Vähälä, J. and H. Hartikainen (2001). Assessment of the Risk of Phosphorus Loading Due to Resuspended Sediment. *Journal of Environment Quality 30*(3), 960.

Lake, B. A., K. M. Coolidge, S. A. Norton, and A. Amirbahman (2007). Factors contributing to the internal loading of phosphorus from anoxic sediments in six Maine, USA, lakes. *Science of The Total Environment 373*(2-3), 534–541.

Lam, D. C. L., W. M. Schertzer, and A. S. Fraser (1987). Oxygen Depletion in Lake Erie: Modeling the Physical, Chemical, and Biological Interactions, 1972 and 1979. *Journal of Great Lakes Research 13*(4), 770–781.

Lambrecht, N., S. Katsev, C. Wittkop, S. J. Hall, C. S. Sheik, A. Picard, M. Fakhraee, and E. D. Swanner (2019, October). Biogeochemical and physical controls on methane fluxes from two ferruginous meromictic lakes. *Geobiology 2*(1), 57.

LaRowe, D. E. and J. P. Amend (2015). Catabolic rates, population sizes and doubling/replacement times of microorganisms in natural settings. *American Journal of Science 315*(3), 167–203.

LaRowe, D. E., A. W. Dale, J. P. Amend, and P. Van Cappellen (2012). Thermodynamic limitations on microbially catalyzed reaction rates. *Geochimica et Cosmochimica Acta 90*, 96–109.

Lawrence, C., C. Steefel, and K. Maher (2014). Abiotic/Biotic Coupling in the Rhizosphere: A Reactive Transport Modeling Analysis. *Procedia Earth and Planetary Science 10*, 104–108.

Lehtoranta, J., P. Ekholm, and H. Pitkanen (2009). Coastal Eutrophication Thresholds: A Matter of Sediment Microbial Processes. *AMBIO: A Journal of the Human Environment 38*(6), 303–308.

Li, J., Y. Zhang, and S. Katsev (2018). Phosphorus recycling in deeply oxygenated sediments in Lake Superior controlled by organic matter mineralization. *Limnology and Oceanography 63*, 1372–1385.

Lindenschmidt, K.-E., H. M. Baulch, and E. Cavaliere (2018). River and Lake Ice Processes-Impacts of Freshwater Ice on Aquatic Ecosystems in a Changing Globe. *Water 10*(11).

Livingstone, D. M. (2003). Impact of secular climate change on the thermal structure of a large temperate Central European lake. *Climatic Change 57*(1-2), 205–225.

Livingstone, D. M. (2008). A Change of Climate Provokes a Change of Paradigm: Taking Leave of Two Tacit Assumptions about Physical Lake Forcing. *International Review of Hydrobiology 93*(4-5), 404–414.

Loh, P. (2013). Evaluating relationships between sediment chemistry and anoxic phosphorus and iron release across three different water bodies. *Inland Waters 3*(1), 105–118.

Los, F. J., M. T. Villars, and M. W. M. Van der Tol (2008). A 3-dimensional primary production model (BLOOM/GEM) and its applications to the (southern) North Sea (coupled physical–chemical–ecological model). *Journal of Marine Systems 74*(1-2), 259–294.

Lovley, D. R., F. H. Chapelle, and J. C. Woodward (1994). Use of dissolved h2 concentrations to determine distribution of microbially catalyzed redox reactions in anoxic groundwater. *Environmental Science & Technology 28*(7), 1205–1210.

Lovley, D. R. and S. Goodwin (1988). Hydrogen concentrations as an indicator of the predominant terminal electron-accepting reactions in aquatic sediments. *Geochimica et Cosmochimica Acta 52*(12), 2993–3003.

Ludsin, S. A., M. W. Kershner, K. A. Blocksom, R. L. Knight, and R. A. Stein (2001). Life After Death in Lake Erie: Nutrient Controls Drive Fish Species Richness, Rehabilitation. *Ecological Applications: a Publication of the Ecological Society of America 11*(3), 731.

Lürling, M., E. Mackay, K. Reitzel, and B. M. Spears (2016). Editorial – A critical perspective on geo-engineering for eutrophication management in lakes. *Water research 97*, 1–10.

Mackay, E., S. Maberly, G. Pan, K. Reitzel, A. Bruere, N. Corker, G. Douglas, S. Egemose, D. Hamilton, T. Hatton-Ellis, B. Huser, W. Li, S. Meis, B. Moss, M. Lurling, G. Phillips, S. Yasseri, and B. Spears (2014). Geoengineering in lakes: welcome attraction or fatal distraction? *Inland Waters 4*(4), 349–356.

Mackenzie, F. T., L. M. Ver, and A. Lerman (2002). Century-scale nitrogen and phosphorus controls of the carbon cycle. *Chemical Geology 190*(1-4), 13–32.

Maerki, M., B. Müller, C. Dinkel, and B. Wehrli (2009). Mineralization Pathways in Lake Sediments with Different Oxygen and Organic Carbon Supply. *Limnology and Oceanography 54*(2), 428–438.

Magnuson, J. J. (2000). Historical Trends in Lake and River Ice Cover in the Northern Hemisphere. *Science 289*(5485), 1743–1746.

Magnuson, J. J., D. M. Robertson, B. J. Benson, R. H. Wynne, D. M. Livingstone, T. Arai, R. A. Assel, R. G. Barry, V. Card, V, E. Kuusisto, N. G. Granin, T. D. Prowse, K. M. Stewart, and V. S. Vuglinski (2000). Historical trends in lake and river ice cover in the northern hemisphere. *Science 289*(5485), 1743–1746.

Mainville, A. and M. R. Craymer (2005). Present-day tilting of the Great Lakes region based on water level gauges. *Geological Society of America Bulletin 117*(7), 1070–.

Mantzouki, E., M. Lürling, J. Fastner, L. de Senerpont Domis, and E. Wilk-Wo zniak (2018). Temperature Effects Explain Continental Scale Distribution of Cyanobacterial Toxins. *Toxins 10*(4), 156.

Markelov, I. (2019). Porousmedialab: The toolbox for batch and one-dimensional reactive transport modelling. *Github*.

Markelova, E., R.-M. Couture, C. T. Parsons, I. Markelov, B. Madé, P. V. Cappellen, and L. Charlet (2018). Speciation dynamics of oxyanion contaminants (as, sb, cr) in argillaceous suspensions during oxic-anoxic cycles. *Applied Geochemistry 91*, 75 – 88.

Matisoff, G., E. M. Kaltenberg, R. L. Steely, S. K. Hummel, J. Seo, K. J. Gibbons, T. B. Bridgeman, Y. Seo, M. Behbahani, W. F. James, L. T. Johnson, P. Doan, M. Dittrich, M. A. Evans, and J. D. Chaffin (2016). Internal loading of phosphorus in western Lake Erie. *Journal of Great Lakes Research 42*(4), 775–788.

Matisoff, G., S. B. Watson, J. Guo, A. Duewiger, and R. Steely (2017). Sediment and nutrient distribution and resuspension in Lake Winnipeg. *Science of The Total Environment 575*, 173–186.

Matzinger, A., B. Muller, P. Niederhauser, M. Schmid, and A. Wuest (2010). Hypolimnetic oxygen consumption by sediment-based reduced substances in former eutrophic lakes. *Limnology and Oceanography 55*(5), 2073–2084.

Mayer, K. U., S. G. Benner, E. O. Frind, S. F. Thornton, and D. N. Lerner (2001). Reactive transport modeling of processes controlling the distribution and natural attenuation of phenolic compounds in a deep sandstone aquifer. *Journal of Contaminant Hydrology 53*(3-4), 341–368.

McAuliffe, T. F., R. J. Lukatelich, A. J. McComb, and S. Qiu (1998). Nitrate applications to control phosphorus release from sediments of a shallow eutrophic estuary: an experimental evaluation. *Marine and Freshwater Research 49*(6), 463–473.

McCulloch, J., A. Gudimov, G. Arhonditsis, A. Chesnyuk, and M. Dittrich (2013). Dynamics of P-binding forms in sediments of a mesotrophic hard-water lake: Insights from non-steady state reactive-transport modeling, sensitivity and identifiability analysis. *Chemical Geology 354*, 216–232.

Megonigal, J. P., M. E. Hines, and P. T. Visscher (2003). Anaerobic Metabolism: Linkages to Trace Gases and Aerobic Processes. Elsevier.

Mellor, G. L., S. M. Häkkinen, T. Ezer, and R. C. Patchen (2002). A Generalization of a Sigma Coordinate Ocean Model and an Intercomparison of Model Vertical Grids. In *Ocean Forecasting*, pp. 55–72. Berlin, Heidelberg: Springer, Berlin, Heidelberg.

Meredith, D. D. (1975). Temperature Effects on Great Lakes Water Balance Studies . *American Water Resources Association 11*(1), 60–68.

Michalak, A. M., E. J. Anderson, D. Beletsky, S. Boland, N. S. Bosch, T. B. Bridgeman, J. D. Chaffin, K. Cho, R. Confesor, I. Daloglu, J. V. DePinto, M. A. Evans, G. L. Fahnenstiel, L. He, J. C. Ho, L. Jenkins, T. H. Johengen, K. C. Kuo, E. LaPorte, X. Liu, M. R. McWilliams, M. R. Moore, D. J. Posselt, R. P. Richards, D. Scavia, A. L. Steiner, E. Verhamme, D. M. Wright, and M. A. Zagorski (2013). Record-setting algal bloom in Lake Erie caused by agricultural and meteorological trends consistent with expected future conditions. *Proceedings of the National Academy of Sciences 110*(16), 6448–6452.

Moe, S. J., S. Jannicke Moe, S. Haande, and R.-M. Couture (2016). Climate change, cyanobacteria blooms and ecological status of lakes: A Bayesian network approach. *Ecological Modelling 337*, 330–347.

Moeini, M. H. and A. Etemad-Shahidi (2007). Application of two numerical models for wave hindcasting in Lake Erie. *Applied Ocean Research 29*(3), 137–145.

Molot, L. A., S. B. Watson, I. F. Creed, C. G. Trick, S. K. McCabe, M. J. Verschoor, R. J. Sorichetti, C. Powe, J. J. Venkiteswaran, and S. L. Schiff (2014). A novel model for cyanobacteria bloom formation: the critical role of anoxia and ferrous iron. *Freshwater Biology 59*(6), 1323–1340.

Monod, J. (1950). La technique de culture continue: theorie et applications. *Ann. Inst. Pasteur 79*.

Mooij, W. M., D. Trolle, E. Jeppesen, G. Arhonditsis, P. V. Belolipetsky, D. B. R. Chitamwebwa, A. G. Degermendzhy, D. L. DeAngelis, L. N. De Senerpont Domis, A. S.

Downing, J. A. Elliott, C. R. Fragoso, U. Gaedke, S. N. Genova, R. D. Gulati, L. Hakanson, D. P. Hamilton, M. R. Hipsey, J. t Hoen, S. Hülsmann, F. H. Los, V. Makler-Pick, T. Petzoldt, I. G. Prokopkin, K. Rinke, S. A. Schep, K. Tominaga, A. A. Van Dam, E. H. Van Nes, S. A. Wells, and J. H. Janse (2010). Challenges and opportunities for integrating lake ecosystem modelling approaches. *Aquatic Ecology 44*(3), 633–667.

Mosley, L. M. (2015). Drought impacts on the water quality of freshwater systems; review and integration. *Earth-Science Reviews 140*, 203–214.

Mueller, H., D. P. Hamilton, and G. J. Doole (2016). Evaluating services and damage costs of degradation of a major lake ecosystem. *Ecosystem Services 22*, 370–380.

Neff, B. P. and J. R. Nicholas (2004). Uncertainty in the Great Lakes water balance. *Scientific Investigations Report* (2004-5100).

Nirupama, N. and S. P. Simonovic (2006). Increase of Flood Risk due to Urbanisation: A Canadian Example. *Natural Hazards 40*(1), 25–41.

Niu, Q., M. Xia, E. S. Rutherford, D. M. Mason, E. J. Anderson, and D. J. SCHWAB (2015). Investigation of interbasin exchange and interannual variability in Lake Erie using an unstructured-grid hydrodynamic model. *Journal of Geophysical Research: Oceans 120*(3), 2212–2232.

Nurnberg, G. K., B. D. LaZerte, P. S. Loh, and L. A. Molot (2013). Quantification of internal phosphorus load in large, partially polymictic and mesotrophic Lake Simcoe, Ontario. *Journal of Great Lakes Research 39*(2), 271–279.

Obenour, D. R., A. D. Gronewold, C. A. Stow, and D. SCAVIA (2014). Using a Bayesian hierarchical model to improve Lake Erie cyanobacteria bloom forecasts. *Water Resources Research 50*(10), 7847–7860.

Obertegger, U., B. Obrador, and G. Flaim (2017). Dissolved oxygen dynamics under ice: Three winters of high-frequency data from l ake t ovel, i taly. *Water Resources Research 53*(8), 7234–7246.

Ogata, A. and R. B. Banks (1961). A solution of the differential equation of longitudinal dispersion in porous media. *Geological survey professional*, paper411–A.

O'Reilly, C. M., S. Sharma, D. K. Gray, S. E. Hampton, J. S. Read, R. J. Rowley, P. Schneider, J. D. Lenters, P. B. McIntyre, B. M. Kraemer, G. A. Weyhenmeyer, D. Straile, B. Dong, R. Adrian, M. G. Allan, O. Anneville, L. Arvola, J. Austin, J. L. Bailey, J. S. Baron, J. D. Brookes, E. Eyto, M. T. Dokulil, D. P. Hamilton, K. Havens, A. L. Hetherington, S. N. Higgins, S. Hook, e. L. R. Izmest, K. D. Joehnk, K. Kangur, P. Kasprzak, M. Kumagai, E. Kuusisto, G. Leshkevich, D. M. Livingstone, S. MacIntyre, L. May, J. M. Melack, N. D. C. Mueller, M. Naumenko, P. Noges, T. Noges, R. P. North, P.-D. Plisnier, A. Rigosi, A. Rimmer, M. Rogora, L. G. Rudstam, J. A. Rusak, N. Salmaso, N. R. Samal, D. E. Schindler, S. G. Schladow, M. Schmid, S. R. Schmidt, E. Silow, M. E. Soylu, K. Teubner, P. Verburg, A. Voutilainen, A. Watkinson, C. E. Williamson, and G. Zhang (2015). Rapid and highly variable warming of lake surface waters around the globe. *Geophysical Research Letters 42*(24), 10,773–10,781.

Orihel, D. M., H. M. Baulch, N. J. Casson, R. L. North, C. T. Parsons, D. C. M. Seckar, and J. J. Venkiteswaran (2017). Internal phosphorus loading in Canadian fresh waters: a critical review and data analysis. *Canadian Journal of Fisheries and Aquatic Sciences 74*(12), 2005–2029.

Orihel, D. M., D. W. Schindler, N. C. Ballard, L. R. Wilson, and R. D. Vinebrooke (2016). Experimental iron amendment suppresses toxic cyanobacteria in a hypereutrophic lake. *Ecological applications: a publication of the Ecological Society of America 26*(5), 1517–1534.

Ostrofsky, M. L. (2019). Predicting internal phosphorus loading in stratified lakes. *Aquatic Sciences 81*(1), 1–9.

Otsuki, A. and R. G. Wetzel (2003). Coprecipitation Of Phosphate With Carbonates In A Marl Lake. *Limnology and Oceanography 17*(5), 763–767.

Paerl, H. W. and J. Huisman (2008). CLIMATE: Blooms Like It Hot. *Science 320*(5872), 57–58.

Pallud, C. and P. Van Cappellen (2006). Kinetics of microbial sulfate reduction in estuarine sediments. *Geochimica et Cosmochimica Acta 70*(5), 1148–1162.

Paludan, C. and H. S. Jensen (1995). Sequential extraction of phosphorus in freshwater wetland and lake sediment: Significance of humic acids. *Wetlands 15*(4), 365–373.

Paraska, D. W., M. R. Hipsey, and S. U. Salmon (2014). Sediment diagenesis models: Review of approaches, challenges and opportunities. *Environmental Modelling & Software 61*, 297–325.

Parkhurst, D. L. and C. A. J. Appelo (2013). Description of Input and Examples for PHREEQC Version 3–a Computer Program for Speciation, Batch-reaction, One-dimensional Transport, and Inverse Geochemical Calculations. *Geological Survey Techniques and Methods*.

Parry, M. L. (2007). *Climate Change 2007 - Impacts, Adaptation and Vulnerability*. Working Group II Contribution to the Fourth Assessment Report of the IPCC. Cambridge University Press.

Parsons, C. T., F. Rezanezhad, D. W. O'Connell, and P. Van Cappellen (2017). Sediment phosphorus speciation and mobility under dynamic redox conditions. *Biogeosciences Discussions*, 1–36.

Pelletier, P. M. (1988). Uncertainties in the single determination of river discharge: a literature review. *Canadian Journal of Civil Engineering 15*(5), 834–850.

Penn, M. R., M. T. Auer, S. M. Doerr, C. T. Driscoll, C. M. Brooks, and S. W. Effler (2000). Seasonality in phosphorus release rates from the sediments of a hypereutrophic lake under a matrix of pH and redox conditions. *Canadian Journal of Fisheries and Aquatic Sciences 57*(5), 1033–1041.

Perez-Riverol, Y., M. Bai, F. da Veiga Leprevost, S. Squizzato, Y. M. Park, K. Haug, A. J. Carroll, D. Spalding, J. Paschall, M. Wang, N. del Toro, T. Ternent, P. Zhang, N. Buso, N. Bandeira, E. W. Deutsch, D. S. Campbell, R. C. Beavis, R. M. Salek, U. Sarkans, R. Petryszak, M. Keays, E. Fahy, M. Sud, S. Subramaniam, A. Barbera, R. C. Jiménez, A. I. Nesvizhskii, S.-A. Sansone, C. Steinbeck, R. Lopez, J. A. Vizcaíno, P. Ping, and H. Hermjakob (2017). Discovering and linking public omics data sets using the Omics Discovery Index. *Nature Biotechnology 35*(5), 406–409.

Peters, V. and R. Conrad (1996). Sequential reduction processes and initiation of CH4 production upon flooding of oxic upland soils. *Soil Biology and Biochemistry 28*(3), 371–382.

Petit, J. R., J. Jouzel, D. Raynaud, N. I. Barkov, J. M. Barnola, I. Basile, M. Bender, J. Chappellaz, M. Davis, G. Delaygue, M. Delmotte, V. M. Kotlyakov, M. Legrand, V. Y. Lipenkov, C. Lorius, L. PÉpin, C. Ritz, E. Saltzman, and M. Stievenard (1999). Climate and atmospheric history of the past 420,000 years from the Vostok ice core, Antarctica. *Nature 399*(6735), 429–436.

Poff, N. L., B. P. Bledsoe, and C. O. Cuhaciyan (2006). Hydrologic variation with land use across the contiguous United States: Geomorphic and ecological consequences for stream ecosystems. *Geomorphology 79*(3-4), 264–285.

Ponnamperuma, F. N. (1972). The chemistry of submerged soils. *Advances in Agronomy 24*, 29–96.

Prokopkin, I. G., W. M. Mooij, J. H. Janse, and A. G. Degermendzhy (2010). A general one-dimensional vertical ecosystem model of Lake Shira (Russia, Khakasia): description, parametrization and analysis. *Aquatic Ecology 44*(3), 585–618.

Quesada, A., W. F. Vincent, E. Kaup, J. E. Hobbie, I. Laurion, R. Pienitz, J. LÓPez-MartÍNez, and J. J. DuráN (2006). Landscape Control of High Latitude Lakes in a Changing Climate. In *Trends in Antarctic Terrestrial and Limnetic Ecosystems*, pp. 221–252. Dordrecht: Springer, Dordrecht.

Quinn, F. and J. Edstrom (2000). Great Lakes Diversions and Other Removals. *Canadian Water Resources Journal 25*(2), 125–151.

Quinn, F. H. (1979). Relative Accuracy of Connecting Channel Discharge Data with Application to Great Lakes Studies. *Journal of Great Lakes Research 5*(1), 73–77.

Quinn, F. H. and B. Guerra (1986). Current Perspectives on the Lake Erie Water Balance. *Journal of Great Lakes Research 12*(2), 109–116.

Recknagel, F., L. Cetin, and B. Zhang (2008). Process-based simulation library SALMO-OO for lake ecosystems. Part 1: Object-oriented implementation and validation. *Ecological Informatics 3*(2), 170–180.

Reeburgh, W. S. (1983). Rates of Biogeochemical Processes in Anoxic Sediments. *Annual Review of Earth and Planetary Sciences 11*(1), 269–298.

Regnier, P., P. Jourabchi, and C. P. Slomp (2003). Reactive-Transport modeling as a technique for understanding coupled biogeochemical processes in surface and subsurface. *Journal Of Geosciences 82*, 5–18.

Reitzel, K., J. Ahlgren, H. DeBrabandere, M. Waldeback, A. Gogoll, L. Tranvik, and E. Rydin (2006). Degradation rates of organic phosphorus in lake sediment. *Biogeochemistry 82*(1), 15–28.

Reitzel, K., H. S. Jensen, and S. Egemose (2013). pH dependent dissolution of sediment aluminum in six Danish lakes treated with aluminum. *Water research 47*(3), 1409–1420.

Reynolds, C. S., A. E. Irish, and J. A. Elliott (2001). The ecological basis for simulating phytoplankton responses to environmental change (PROTECH). *Ecological Modelling 140*(3), 271–291.

Rezanezhad, F., R.-M. Couture, R. Kovac, D. O'Connell, and P. V. Cappellen (2014). Water table fluctuations and soil biogeochemistry: An experimental approach using an automated soil column system. *Journal of Hydrology 509*, 245 – 256.

Rezanezhad, F., J. S. Price, W. L. Quinton, B. Lennartz, T. Milojevic, and P. Van Cappellen (2016). Structure of peat soils and implications for water storage, flow and solute transport: A review update for geochemists. *Chemical Geology 429*, 75–84.

Robson, B. J. (2014). State of the art in modelling of phosphorus in aquatic systems: Review, criticisms and commentary. *Environmental Modelling & Software 61*, 339–359.

Roden, E. E. (2006). Geochemical and microbiological controls on dissimilatory iron reduction. *Comptes Rendus Geoscience 338*(6-7), 456–467.

Roden, E. E. (2008). Microbiological Controls on Geochemical Kinetics 1: Fundamentals and Case Study on Microbial Fe(III) Oxide Reduction. In *Kinetics of Water-Rock Interaction*, pp. 335–415. New York, NY: Springer New York.

Roden, E. E. and R. G. Wetzel (1996). Organic carbon oxidation and suppression of methane production by microbial Fe(III) oxide reduction in vegetated and unvegetated freshwater wetland sediments. *Limnology and Oceanography 41*, 1733–1748.

Roden, E. E. and R. G. Wetzel (2002). Kinetics of microbial Fe(III) oxide reduction in freshwater wetland sediments. *Limnology and Oceanography 47*(1), 198–211.

Romero, J. R., J. P. Antenucci, and J. Imberger (2004). One- and three-dimensional biogeochemical simulations of two differing reservoirs. *Ecological Modelling 174*(1-2), 143–160.

Rucinski, D. K., J. V. De Pinto, D. Scavia, and D. Beletsky (2014). Modeling Lake Erie's hypoxia response to nutrient loads and physical variability. *Journal of Great Lakes Research 40*, 151–161.

Saaltink, M. W., F. Batlle, C. Ayora, J. Carrera, and S. Olivella (2004). RETRASO, a code for modeling reactive transport in saturated and unsaturated porous media. *Geologica Acta 2*(3), 235–251.

Saloranta, T. M. and T. Andersen (2007). MyLake—A multi-year lake simulation model

code suitable for uncertainty and sensitivity analysis simulations. *Ecological Modelling 207*(1), 45–60.

Saltelli, A. and R. Bolado (1998). An alternative way to compute Fourier amplitude sensitivity test (FAST). *Computational Statistics & Data Analysis 26*(4), 445–460.

Sander, R. (2015). Compilation of Henry's law constants (version 4.0) for water as solvent. *Atmospheric Chemistry and Physics 15*(8), 4399–4981.

Sauer, V. B. and R. W. Meyer (1992). *Determination of error in individual discharge measurements.*

Scavia, D., J. D. Allan, K. K. Arend, S. Bartell, D. Beletsky, N. S. Bosch, S. B. Brandt, R. D. Briland, I. Daloğlu, J. V. DePinto, D. M. Dolan, M. A. Evans, T. M. Farmer, D. Goto, H. Han, T. O. Höök, R. Knight, S. A. Ludsin, D. Mason, A. M. Michalak, R. P. Richards, J. J. Roberts, D. K. Rucinski, E. Rutherford, D. J. Schwab, T. M. Sesterhenn, H. Zhang, and Y. Zhou (2014). Assessing and addressing the re-eutrophication of Lake Erie: Central basin hypoxia. *Journal of Great Lakes Research 40*(2), 226–246.

Scavia, D., S. A. Bocaniov, A. Dagnew, C. Long, and Y.-C. Wang (2018). St. Clair-Detroit River system: Phosphorus mass balance and implications for Lake Erie load reduction, monitoring, and climate change. *Journal of Great Lakes Research.*

Schaus, M. H., M. J. Vanni, T. E. Wissing, M. T. Bremigan, J. E. Garvey, and R. A. Stein (2003). Nitrogen and phosphorus excretion by detritivorous gizzard shad in a reservoir ecosystem. *Limnology and Oceanography 42*(6), 1386–1397.

Schauser, I., M. Hupfer, and R. Brüggemann (2004). SPIEL—a model for phosphorus diagenesis and its application to lake restoration. *Ecological Modelling 176*(3-4), 389–407.

Schauser, I., M. Hupfer, and R. Brüggemann (2006). Sensitivity analysis with a phosphorus diagenesis model (SPIEL). *Ecological Modelling 190*, 87–98.

Schindler, D. W., S. E. Bayley, B. R. Parker, K. G. Beaty, D. R. Cruikshank, E. J. Fee, E. U. Schindler, and M. P. Stainton (1996). The effects of climatic warming on the properties of boreal lakes and streams at the Experimental Lakes Area, northwestern Ontario. *Limnology and Oceanography 41*(5), 1004–1017.

Schindler, D. W., K. G. Beaty, E. J. Fee, D. R. Cruikshank, E. R. DeBruyn, D. L. Findlay, G. A. Linsey, J. A. Shearer, M. P. Stainton, and M. A. Turner (1990). Effects of climatic warming on lakes of the central boreal forest. *Science 250*(4983), 967–970.

Schmid, M., S. Hunziker, and A. Wuest (2014). Lake surface temperatures in a changing climate: a global sensitivity analysis. *Climatic Change 124*(1-2), 301–315.

Schmid, M., I. Ostrovsky, and D. F. McGinnis (2017). Role of gas ebullition in the methane budget of a deep subtropical lake: What can we learn from process-based modeling? *Limnology and Oceanography 62*(6), 2674–2698.

Schrödinger, E. (1944). *What is Life? The Physical Aspect of the Living Cell*. Cambridge University Press.

Schutz, J., E. Rydin, and B. J. Huser (2017). A newly developed injection method for aluminum treatment in eutrophic lakes: Effects on water quality and phosphorus binding efficiency. *Lake and Reservoir Management 33*(2), 152–162.

Schwab, D. J., D. Beletsky, J. De Pinto, and D. M. Dolan (2009). A hydrodynamic approach to modeling phosphorus distribution in Lake Erie. *Journal of Great Lakes Research 35*(1), 50–60.

Scott, R. W. and F. A. Huff (1996). Impacts of the Great Lakes on regional climate conditions. *Journal of Great Lakes Research 22*(4), 845–863.

Senn, H., U. Lendenmann, M. Snozzi, G. Hamer, and T. Egli (1994). The growth of Escherichia coli in glucose-limited chemostat cultures: a re-examination of the kinetics. *Biochimica et Biophysica Acta 1201*(3), 424–436.

Shabbar, A., M. K. Atmosphere-Ocean, and 1996 (1996). The impact of el Nino-Southern oscillation on the temperature field over Canada: Research note. *Taylor & Francis 34*(2), 401–416.

Shabbar, A., B. Bonsal, and M. Khandekar (1997). Canadian Precipitation Patterns Associated with the Southern Oscillation. *Journal of Climate 10*(12), 3016–3027.

Sharma, S., D. K. Gray, J. S. Read, C. M. O'Reilly, P. Schneider, A. Qudrat, C. Gries, S. Stefanoff, S. E. HAMPTON, S. Hook, J. D. Lenters, D. M. Livingstone, P. B. McIntyre, R. Adrian, M. G. Allan, O. ANNEVILLE, L. Arvola, J. Austin, J. Bailey, J. S. Baron, J. Brookes, Y. Chen, R. Daly, M. Dokulil, B. Dong, K. Ewing, E. de Eyto, D. Hamilton, K. Havens, S. Haydon, H. Hetzenauer, J. Heneberry, A. L. Hetherington, S. N. Higgins, E. Hixson, L. R. Izmest'eva, B. M. Jones, K. KANGUR, P. Kasprzak, O. Köster, B. M. Kraemer, M. Kumagai, E. Kuusisto, G. Leshkevich, L. May, S. MacIntyre, D. Müller-Navarra, M. Naumenko, P. NOGES, T. Noges, P. Niederhauser, R. P. North, A. M. Paterson, P.-D. Plisnier, A. Rigosi, A. Rimmer, M. Rogora, L. Rudstam, J. A. Rusak, N. Salmaso, N. R. Samal, D. E. Schindler, G. Schladow, S. R. Schmidt, T. Schultz, E. A. Silow, D. STRAILE, K. Teubner, P. Verburg, A. Voutilainen, A. Watkinson, G. A. Weyhenmeyer, C. E. Williamson, and K. H. Woo (2015). A global database of lake surface temperatures collected by in situ and satellite methods from 1985–2009. *Scientific Data 2*(1), 1770.

Shimoda, Y., M. Ekram Azim, G. Perhar, M. Ramin, M. A. Kenney, S. Sadraddini, A. Gudimov, and G. B. Arhonditsis (2011). Our current understanding of lake ecosystem response to climate change: What have we really learned from the north temperate deep lakes? *Journal of Great Lakes Research 37*(1), 173–193.

Skarbøvik, E., S. Haande, and B. Bechmann, M.and Skjelbred (2019). Monitoring Morsa 2017–2018 (in Norwegian). *NIBIO 5*(30/2019), 64.

Smith, V. H., G. D. Tilman, and J. C. Nekola (1999). Eutrophication: impacts of excess nutrient inputs on freshwater, marine, and terrestrial ecosystems. *Environmental Pollution 100*(1-3), 179–196.

Smits, J. G. C. and J. K. L. van Beek (2013). ECO: a generic eutrophication model including comprehensive sediment-water interaction. *PloS One 8*(7), e68104.

Smolders, A. J. P., L. P. M. Lamers, E. C. H. E. Lucassen, G. Van Der Velde, and J. G. M. Roelofs (2006). Internal eutrophication: How it works and what to do about it—a review. *Chemistry and Ecology 22*(2), 93–111.

Smolders, A. J. P., R. C. Nijboer, and J. G. M. Roelofs (1995). Prevention of sulphide accumulation and phosphate mobilization by the addition of iron(II) chloride to a reduced sediment: an enclosure experiment. *Freshwater Biology 34*(3), 559–568.

Soetaert, K., P. M. J. Herman, and J. J. Middelburg (1996). A model of early diagenetic processes from the shelf to abyssal depths. *Geochimica et Cosmochimica Acta 60*(6), 1019–1040.

Soetaert, K., J. J. Middelburg, P. M. J. Herman, and K. Buis (2000). On the coupling of benthic and pelagic biogeochemical models. *Earth-Science Reviews 51*(1-4), 173–201.

Solheim, A. L., T. Rohrlack, M. Grung, A. Hobæk, H. Bennion, A. Burgess, and H. Yang (2006). Study on reference condition and development of eutrophication in lake vansjø, (in norwegian). *NIVA report 5145-2006*.

Sondergaard, M. (2007). Nutrient dynamics in lakes - with emphasis on phosphorus, sediment and lake restoration (Disertation). pp. 1–74.

Sondergaard, M., J. P. Jensen, and E. Jeppesen (2003). Role of sediment and internal loading of phosphorus in shallow lakes. *Hydrobiologia 506*(1), 135–145.

Sondergaard, M., L. Liboriussen, A. R. Pedersen, and E. Jeppesen (2008). Lake Restoration by Fish Removal: Short- and Long-Term Effects in 36 Danish Lakes. *Ecosystems 11*(8), 1291–1305.

Steefel, C., D. Depaolo, and P. Lichtner (2005). Reactive transport modeling: An essential tool and a new research approach for the Earth sciences. *Earth and Planetary Science Letters 240*(3-4), 539–558.

Steefel, C. I. and P. Van Cappellen (1998). Reactive transport modeling of natural systems: Preface. *Journal of Hydrology 209*(1-4), 1–7.

Stefan, H. G., X. Fang, and J. G. Eaton (2001). Simulated Fish Habitat Changes in North American Lakes in Response to Projected Climate Warming. *Transactions of the American Fisheries Society 130*(3), 459–477.

Stegen, J. C., J. K. Fredrickson, M. J. Wilkins, A. E. Konopka, W. C. Nelson, E. V. Arntzen, W. B. Chrisler, R. K. Chu, R. E. Danczak, S. J. Fansler, D. W. Kennedy, C. T. Resch, and M. Tfaily (2016). Groundwater-surface water mixing shifts ecological assembly processes and stimulates organic carbon turnover. *Nature Communications 7*, 11237.

Stumpf, R. P., T. T. Wynne, D. B. Baker, and G. L. Fahnenstiel (2012). Interannual Variability of Cyanobacterial Blooms in Lake Erie. *PLoS ONE 7*(8), e42444–.

Stuum, W. and J. J. Morgan (1996). *Aquatic chemistry: chemical equilibria and rates in natural waters*. Wiley/Interscience Publication.

Testa, J. M., D. C. Brady, D. M. Di Toro, W. R. Boynton, J. C. Cornwell, and W. M. Kemp (2013). Sediment flux modeling: Simulating nitrogen, phosphorus, and silica cycles. *Estuarine, Coastal and Shelf Science 131*(c), 245–263.

Thornton, S. F., S. Quigley, M. J. Spence, S. A. Banwart, S. Bottrell, and D. N. Lerner (2001). Processes controlling the distribution and natural attenuation of dissolved phenolic compounds in a deep sandstone aquifer. *Journal of Contaminant Hydrology 53*(3-4), 233–267.

Thullner, M., A. W. Dale, and P. Regnier (2009). Global-scale quantification of mineralization pathways in marine sediments: A reaction-transport modeling approach. *Geochemistry, Geophysics, Geosystems 10*(10).

Tranvik, L. J., J. A. Downing, J. B. Cotner, S. A. Loiselle, R. G. Striegl, T. J. Ballatore, P. Dillon, K. Finlay, K. Fortino, L. B. Knoll, P. L. Kortelainen, T. Kutser, S. Larsen,

I. Laurion, D. M. Leech, S. Leigh McCallister, D. M. McKnight, J. M. Melack, E. Overholt, J. A. Porter, Y. Prairie, W. H. Renwick, F. Roland, B. S. Sherman, D. W. Schindler, S. Sobek, A. Tremblay, M. J. Vanni, A. M. Verschoor, E. von Wachenfeldt, and G. A. Weyhenmeyer (2009). Lakes and reservoirs as regulators of carbon cycling and climate. *Limnology and Oceanography 54*(6part2), 2298–2314.

Trolle, D., D. P. Hamilton, C. A. Pilditch, I. C. Duggan, and E. Jeppesen (2011). Predicting the effects of climate change on trophic status of three morphologically varying lakes: Implications for lake restoration and management. *Environmental Modelling & Software 26*(4), 354–370.

Trolle, D., H. Skovgaard, and E. Jeppesen (2008). The Water Framework Directive: Setting the phosphorus loading target for a deep lake in Denmark using the 1D lake ecosystem model DYRESM–CAEDYM. *Ecological Modelling 219*(1-2), 138–152.

Tromp, T. K., P. Van Cappellen, and R. M. Key (1995). A global model for the early diagenesis of organic carbon and organic phosphorus in marine sediments. *Geochimica et Cosmochimica Acta 59*(7), 1259–1284.

Vallino, J. J. (2010). Ecosystem biogeochemistry considered as a distributed metabolic network ordered by maximum entropy production. *Philosophical transactions of the Royal Society of London. Series B, Biological sciences 365*(1545), 1417–1427.

Vallino, J. J. and C. K. Algar (2016). The Thermodynamics of Marine Biogeochemical Cycles: Lotka Revisited. *Annual Review of Marine Science 8*(1), 333–356.

Van Cappellen, P. and C. P. Slomp (2004). Nutrient inputs to the coastal ocean through submarine groundwater discharge: controls and potential impact. *Journal of Hydrology 295*(1-4), 64–86.

Van Cappellen, P. and Y. Wang (1996). Cycling of iron and manganese in surface sediments; a general theory for the coupled transport and reaction of carbon, oxygen, nitrogen, sulfur, iron, and manganese. *American Journal of Science 296*(3), 197–243.

Van Nes, E. H., E. H. R. R. Lammens, and M. Scheffer (2002). PISCATOR, an individual-based model to analyze the dynamics of lake fish communities. *Ecological Modelling 152*(2), 261–278.

Van Nes, E. H., M. Scheffer, M. S. van den Berg, and H. Coops (2003). Charisma: a spatial explicit simulation model of submerged macrophytes. *Ecological Modelling 159*(2-3), 103–116.

Vanderborght, J.-P., I. M. Folmer, D. R. Aguilera, T. Uhrenholdt, and P. Regnier (2007). Reactive-transport modelling of C, N, and O2 in a river–estuarine–coastal zone system: Application to the Scheldt estuary. *Marine Chemistry 106*(1-2), 92–110.

Verschoor, M. J., C. R. Powe, E. McQuay, S. L. Schiff, J. J. Venkiteswaran, J. Li, and L. A. Molot (2017). Internal iron loading and warm temperatures are preconditions for cyanobacterial dominance in embayments along Georgian Bay, Great Lakes. *Canadian Journal of Fisheries and Aquatic Sciences*, 1–15.

Vijayagopal, V. and T. Viruthagiri (2005). Batch kinetic studies in phenol biodegradation and comparison. *Indian Journal of Biotechnology*.

Visser, P. M., J. M. H. Verspagen, G. Sandrini, L. J. Stal, H. C. P. Matthijs, T. W. Davis, H. W. Paerl, and J. Huisman (2016). How rising CO and global warming may stimulate harmful cyanobacterial blooms. *Harmful Algae 54*, 145–159.

Vollenweider, R. A. (1976). Advances in defining critical loading levels for phosphorus in lake eutrophication. *Memorie dell'Istituto Italiano di Idrobiologia, Dott. Marco de Marchi Verbania Pallanza*.

Wang, J., H. Hu, D. Schwab, G. Leshkevich, D. BELETSKY, N. Hawley, and A. Clites (2010). Development of the Great Lakes Ice-circulation Model (GLIM): Application to Lake Erie in 2003–2004. *Journal of Great Lakes Research 36*(3), 425–436.

Wang, Y. and P. Van Cappellen (1996). A multicomponent reactive transport model of early diagenesis: Application to redox cycling in coastal marine sediments. *Geochimica et Cosmochimica Acta 60*(16), 2993–3014.

Warszawski, L., K. Frieler, V. Huber, F. Piontek, O. Serdeczny, and J. Schewe (2014). The Inter-Sectoral Impact Model Intercomparison Project (ISI-MIP): project framework. *Proceedings of the National Academy of Sciences of the United States of America 111*(9), 3228–3232.

Watson, I. A., S. E. Oswald, S. A. Banwart, R. S. Crouch, and S. F. Thornton (2005). Modeling the Dynamics of Fermentation and Respiratory Processes in a Groundwater Plume of Phenolic Contaminants Interpreted from Laboratory- to Field-Scale. *Environmental Science & Technology 39*(22), 8829–8839.

Watson, I. A., S. E. Oswald, K. U. Mayer, Y. Wu, and S. A. Banwart (2003). Modeling Kinetic Processes Controlling Hydrogen and Acetate Concentrations in an Aquifer-Derived Microcosm. *Environmental Science & Technology 37*(17), 3910–3919.

Wetzel, R. (2001). *Limnology: Lake and River Ecosystems*. Academic Press.

Wilfert, P., P. S. Kumar, L. Korving, G.-J. Witkamp, and M. C. M. van Loosdrecht (2015). The Relevance of Phosphorus and Iron Chemistry to the Recovery of Phosphorus from Wastewater: A Review. *Environmental Science & Technology 49*(16), 9400–9414.

Winder, M. and U. Sommer (2012). Phytoplankton response to a changing climate. *Hydrobiologia 698*(1), 5–16.

Winslow, L. A., T. H. Leach, and K. C. Rose (2018). Global lake response to the recent warming hiatus. *Environmental Research Letters 13*(5), 054005.

Winter, T. C. (1981). Uncertainties in Estimating the Water Balance of Lakes . *Journal of the American Water Resources Association / AWRA 17*(1), 82–115.

Winter, T. C. (1995). *Hydrological Processes and the Water Budget of Lakes*, pp. 37–62. Berlin, Heidelberg: Springer Berlin Heidelberg.

Woolway, R. I. and C. J. Merchant (2019). Worldwide Alteration of Lake Mixing Regimes in Response to Climate Change. *Nature Geoscience 12*(4), 271–276.

Woolway, R. I., G. A. Weyhenmeyer, M. Schmid, M. T. Dokulil, E. Eyto, S. C. Maberly, L. May, and C. J. Merchant (2019). Substantial increase in minimum lake surface temperatures under climate change. pp. 1–14.

Xiong, Y., R. Guilbaud, C. L. Peacock, R. P. Cox, D. E. Canfield, M. D. Krom, and S. W. Poulton (2019). Phosphorus cycling in lake cadagno, switzerland: A low sulfate euxinic ocean analogue. *Geochimica et Cosmochimica Acta*.

Yano, T., T. Nakahara, S. Kamiyama, and K. Yamada (1966). Kinetic Studies on Microbial Activities in Concentrated Solutions. Part. I. *Agricultural and Biological Chemistry 30*(1), 42–48.

Yao, H., R. Conrad, R. Wassmann, and H. U. Neue (1999). Effect of soil characteristics on sequential reduction and methane production in sixteen rice paddy soils from China, the Philippines, and Italy. *Biogeochemistry 47*(3), 269–295.

Yvon-Durocher, G., J. M. Caffrey, A. Cescatti, M. Dossena, P. del Giorgio, J. M. Gasol, J. M. Montoya, J. Pumpanen, P. A. Staehr, M. Trimmer, G. Woodward, and A. P. Allen (2012). Reconciling the temperature dependence of respiration across timescales and ecosystem types. *Nature 487*(7408), 472–476.

Zhang, Z., B. Sun, and B. E. Johnson (2015). Integration of a benthic sediment diagenesis module into the two dimensional hydrodynamic and water quality model – CE-QUAL-W2. *Ecological Modelling 297*, 213–231.

APPENDICES

Appendix A

Supporting Information for Chapter 2

A.1 Water Temperature Profiles

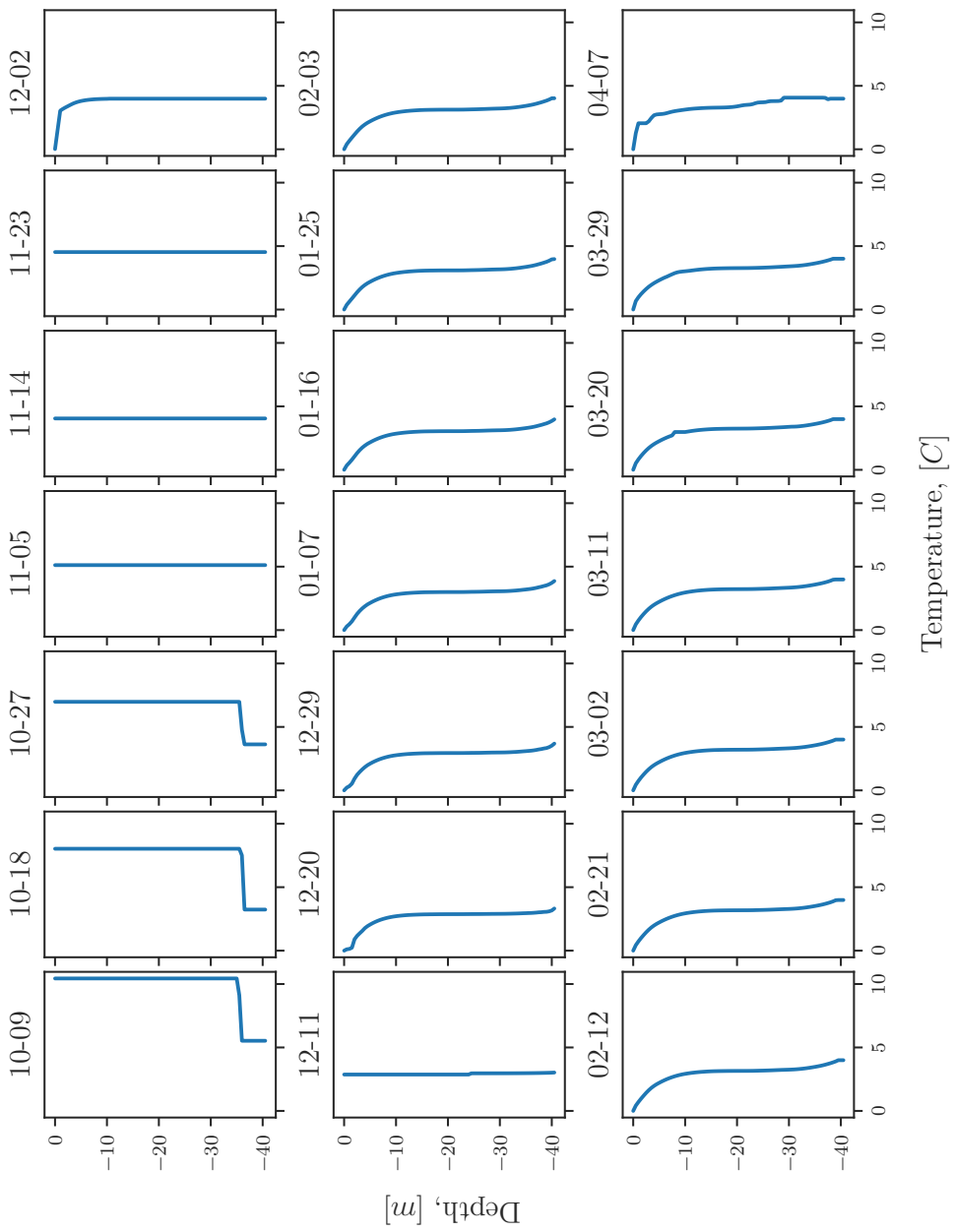

Figure A.1: Simulated water temperature profiles for the period from October, 2009 to April, 2010.

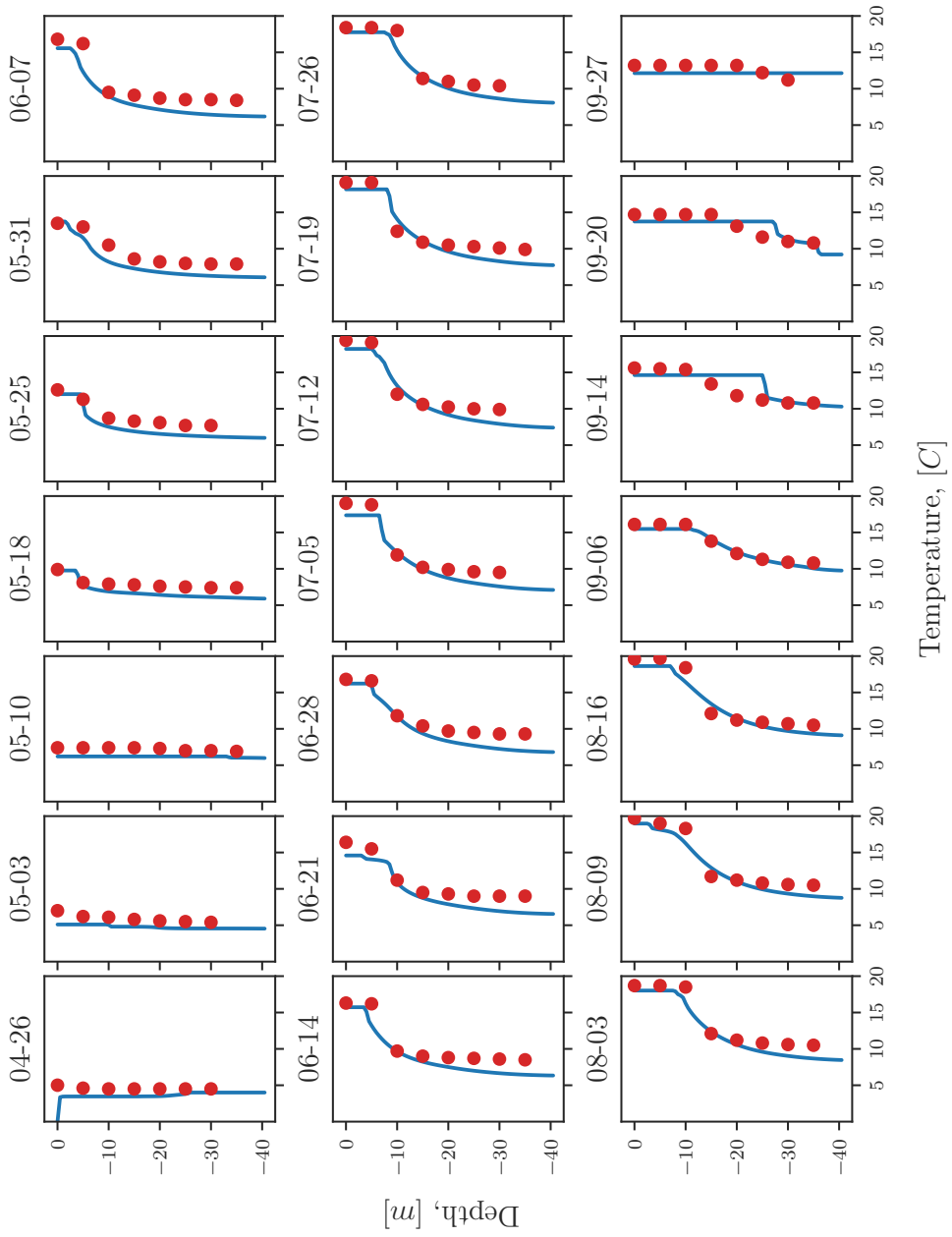

Figure A.2: Water temperature profiles observed and simulated for the period from April to October of 2010.

A.2 Downscaled Average Air Temperatures

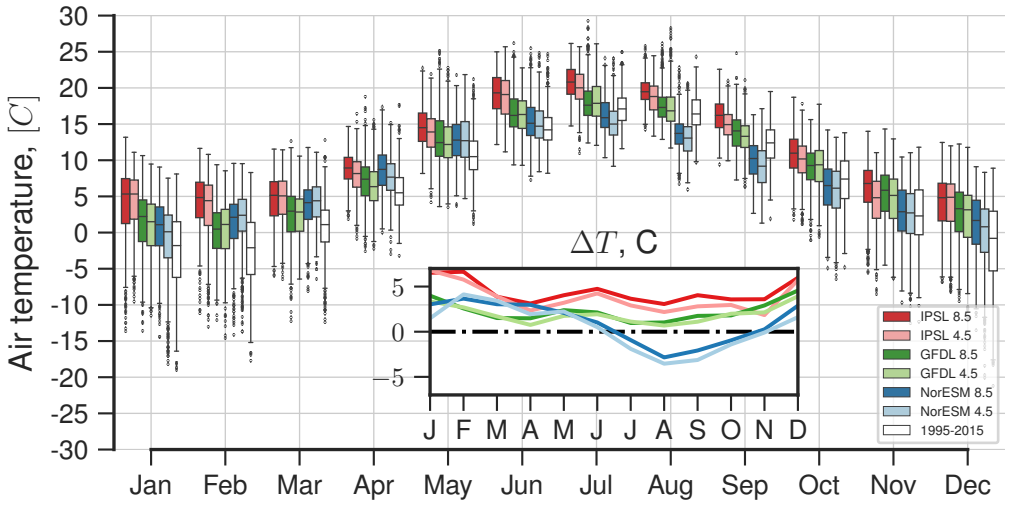

Figure A.3: Downscaled average air temperature according to IPSL, GFDL and NorESM climate models and corresponding representative concentration pathways (RCP) for the period 2050-2070. The historical values are average values over the period from 1995 to 2015.

A.3 Trends of Selected Model Variables

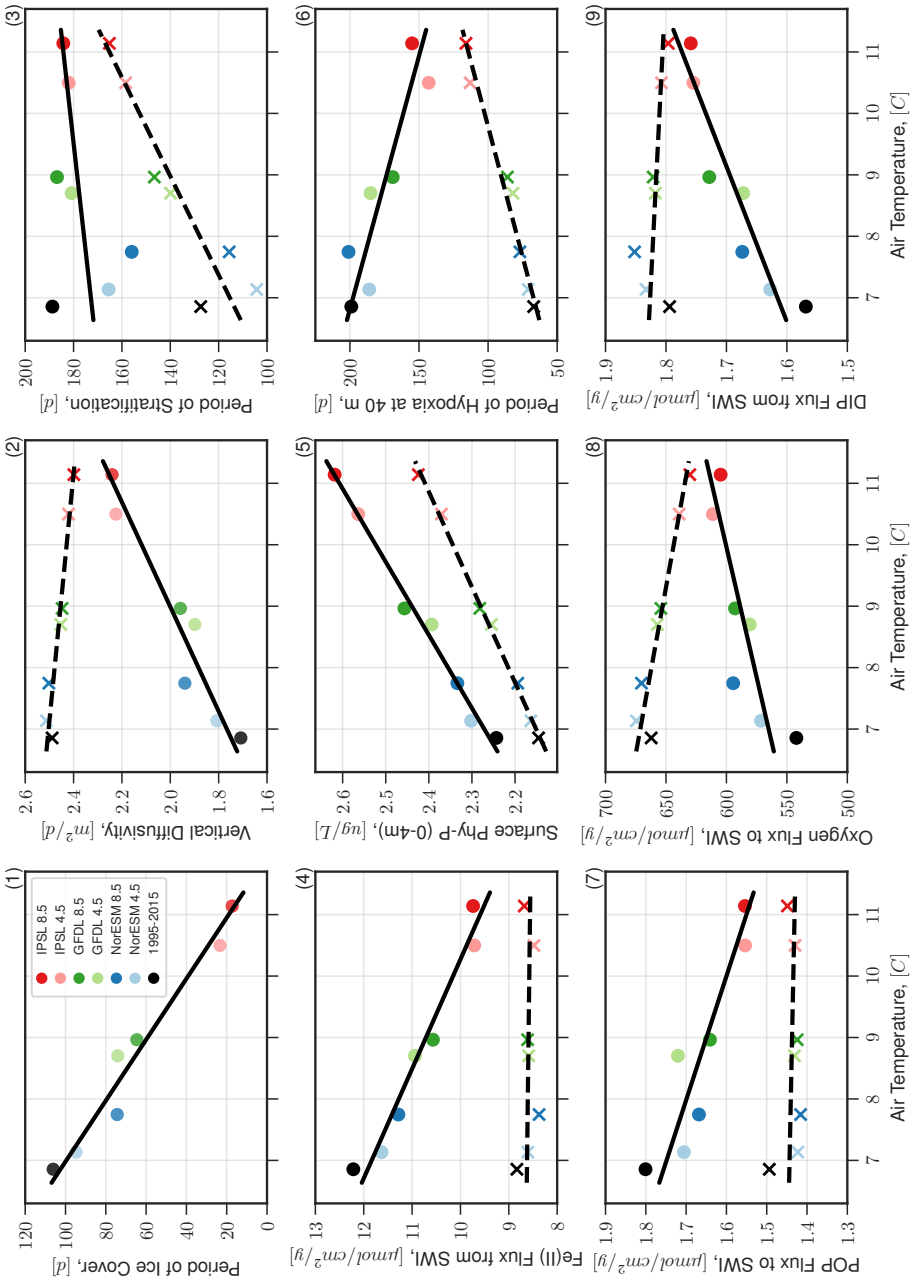

Figure A.4: Trends of selected MyLake-Sediment variables as a function of the projected average annual air temperatures, according to the three climate models, IPSL (red), GFDL (green), NorESM (blue), and for RCP 4.5 (light) and RCP 8.5 (dark). Dashed lines and crosses indicate the no-ice scenarios.

A.4 Response of The Model to an Abrupt Halt of All External P Loading

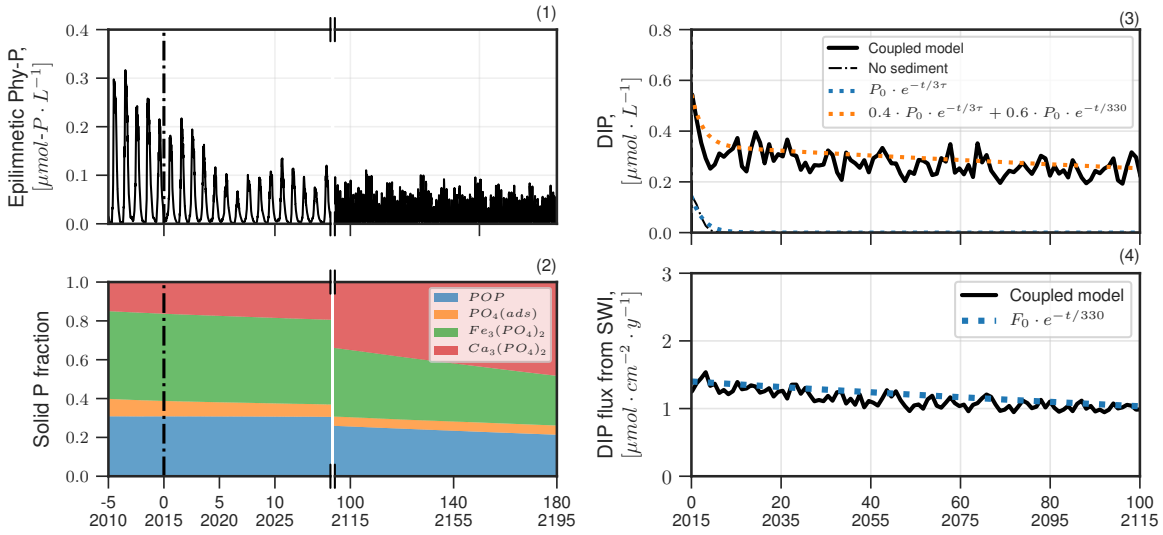

Figure A.5: Response of MyLake-Sediment to an abrupt halt of all external P loading in 2015. Left panels: (1) epilimnetic phytoplankton concentration, and (4) P-fractionation in the sediment column from 2010 to 2195. Right panel: (3) average DIP in water-column with and without the sediment module, and (4) benthic DIP flux. Dashed lines indicate best fit of half-life equation to modelled data as indicated in the text.

A.5 State Variables Of The Coupled MyLake-Sediment Model

Table A.1: State variables of the coupled MyLake-Sediment model.

Variable	**Description**	**Units**
Physical		
T	Temperature	$^{\circ}C$
K_z	Vertical diffusion	$m^2 \cdot d^{-1}$
Hi	Ice thickness	m
Hsi	Snow thickness	m
PAR	Irradiance	$mol \cdot m^{-2} \cdot d^{-1}$
Biological		
Phy-I	Phytoplankton (group 1)	$mM - P$
Phy-II	Phytoplankton (group 2)	$mM - P$
Chemical		
POP	Particulate organic phosphorus	$mmol - P \cdot L_s^{-1}$
DOP	Dissolved organic phosphorus	$mM - P$
POC	Particulate organic carbon	$mmol - C \cdot L_s^{-1}$
DOC	Dissolved organic carbon	$mM - C$
HPO_4^{2-}	Phosphate	mM
O_2	Dissolved oxygen	mM
NO_3^-	Nitrate	mM
$Fe(OH)_3$	First pool of iron oxide	$mmol \cdot L_s^{-1}$
FeOOH	Second pool of iron oxide	$mmol \cdot L_s^{-1}$
SO_4^{2-}	Sulfate	mM
NH_4^+	Ammonia	mM
Fe^{2+}	Ferrous Iron	mM
HS^-	Hydrogen sulfide	mM
FeS	Mackinawite	$mmol \cdot L_s^{-1}$
FeS_2	Pyrite	$mmol \cdot L_s^{-1}$
S_0	Sulfur	mM
S_8	Octasulfur	$mmol \cdot L_s^{-1}$
$Al(OH)_3$	Aluminum hydroxide	$mmol \cdot L_s^{-1}$
$PO_4{\equiv}Fe(OH)_3$	Sorbed phosphate on iron pool 1	$mmol \cdot L_s^{-1}$
$PO_4{\equiv}FeOOH$	Sorbed phosphate on iron pool 2	$mmol \cdot L_s^{-1}$
$PO_4{\equiv}Al(OH)_3$	Sorbed phosphate on Aluminum	$mmol \cdot L_s^{-1}$
Ca^{2+}	Calcium	$mmol \cdot L_s^{-1}$
$Ca_3(PO_4)_2$	Calcium phosphate	$mmol \cdot L_s^{-1}$
$CaCO_3$	Calcite	$mmol \cdot L_s^{-1}$
$Fe_3(PO_4)_2$	Vivianite	$mmol \cdot L_s^{-1}$
$FeCO_3$	Ferrous carbonate	$mmol \cdot L_s^{-1}$
OMS	Sulfurized organic matter	$mmol \cdot L_s^{-1}$

A.6 Parameters of The Physical And Phytoplankton Modules

Table A.2: Parameters of the physical and phytoplankton modules. PAR - photosynthetically active radiation with $\lambda \in [400, 700]$ nm, and non-PAR light, where $\lambda \notin [400, 700]$ nm. Source: C - calibrated, 1 - Saloranta and Andersen (2007).

Param.	Description	Value	Units	Source
	Physical Module			
a_k	Open water diffusion parameter	0.04165	–	1
a_k^{ice}	Under ice diffusion parameter	0.000898	–	1
N^2_{min}	Minimum stability frequency	$7 \cdot 10^{-5}$	s^{-2}	1
W_{str}	Wind shelter parameter	0.74	–	1
α_{ice}	Albedo of melting ice	0.3	–	1
α_{snow}	Albedo of melting snow	0.77	–	1
f_{par}	PAR fraction of the total short-wave energy	0.45	–	1
λ_i	PAR light attenuation coefficient for ice	5	m^{-1}	1
λ_s	PAR light attenuation coefficient for snow	15	m^{-1}	1
$\hat{\varepsilon}$	PAR light attenuation coefficient	1.0	m^{-1}	1
$\bar{\hat{\varepsilon}}$	non-PAR light attenuation coefficient	2.5	m^{-1}	1
w_s	Settling velocity for solids	0.1	$m \cdot d^{-1}$	C
d_{sed}	Sediment effective depth	17	m	C
φ_0	Porosity at SWI	0.98	–	C
φ_∞	Deep sediment porosity	0.85	–	C
τ	Porosity attenuation	0.5	cm^{-1}	C
w_{sed}	Sediment accumulation rate	0.1	$cm \cdot y^{-1}$	C
α	Bioirrigation constant	7.2	y^{-1}	C
	Phytoplankton Module			
$\mu'(20)$	Specific growth rate at $20°C$	1.5	d^{-1}	1
P'	Half saturation P level	12	$mg \cdot m^{-3}$	C
N'	Half saturation N level	12	$mg \cdot m^{-3}$	C
β	Optical cross-section	0.015	$m^2 \cdot mg^{-1}$	1
λ'	PAR saturation level	$3 \cdot 10^{-5}$	$mol \cdot m^{-2} \cdot s^{-1}$	1
$m(20)$	Loss rate at $20°C$	0.2	d^{-1}	1
w_p	Settling velocity	0.1	$m \cdot d^{-1}$	C

A.7 Statistical Metrics of The Coupled Model

Table A.3: Statistical metrics of the coupled model during calibration period of 2005-2010 and during verification period of 2010-2014: MAE - mean absolute error, Bias - mean percent bias, RMSE - root mean squared error, r - correlation coefficient, R^2 - coefficient of determination.

Variable	**Depth**	**MAE**	**Bias**	**RMSE**	**r**	**R^2**
Temperature, °C	0	1.11 / 1.03	-6.01 / -6.84	1.34 / 1.26	0.98 / 0.99	0.89 / 0.91
	5	0.96 / 1.09	-5.89 / -7.09	1.17 / 1.33	0.98 / 0.98	0.90 / 0.91
	10	0.99 / 1.11	-1.17 / -4.10	1.20 / 1.40	0.94 / 0.94	0.85 / 0.86
	15	1.11 / 0.96	-0.29 / -0.88	1.35 / 1.15	0.91 / 0.94	0.78 / 0.83
	20	1.07 / 0.89	-2.27 / -3.90	1.32 / 1.07	0.90 / 0.95	0.74 / 0.82
	25	1.06 / 0.91	-3.99 / -5.91	1.36 / 1.11	0.89 / 0.95	0.69 / 0.79
	30	1.11 / 1.00	-4.81 / -7.44	1.40 / 1.19	0.88 / 0.93	0.65 / 0.71
	35	1.12 / 1.20	-5.68 / -9.70	1.40 / 1.58	0.88 / 0.86	0.58 / 0.38
	40	1.02 / 1.67	-8.83 / -11.68	1.37 / 2.19	0.89 / 0.69	0.59 / -0.16
Oxygen, mg/L	0	1.38 / 0.75	-4.65 / -0.54	1.87 / 1.13	0.41 / 0.47	0.11 / 0.19
	5	1.48 / 0.72	-6.23 / -0.97	1.92 / 1.04	0.43 / 0.56	0.09 / 0.30
	10	1.77 / 1.15	-6.15 / 1.76	2.24 / 1.41	0.49 / 0.58	0.18 / 0.32
	15	1.94 / 1.44	-3.63 / 5.65	2.55 / 1.73	0.54 / 0.62	0.27 / 0.32
	20	1.96 / 1.52	-0.13 / 7.52	2.44 / 1.93	0.55 / 0.60	0.30 / 0.28
	25	1.95 / 1.57	0.00 / 6.90	2.48 / 2.14	0.56 / 0.53	0.32 / 0.19
	30	2.07 / 1.44	-4.03 / 3.25	2.74 / 2.11	0.51 / 0.59	0.24 / 0.30
	35	2.33 / 1.53	-10.65 / -4.72	3.04 / 2.18	0.45 / 0.65	0.11 / 0.39
	40	2.96 / 2.28	-31.74 / -8.30	3.57 / 3.12	0.60 / 0.51	-0.20 / 0.16
Phosphorus, µg/L						
Total	0-4	5.21 / 5.95	3.37 / -13.52	6.54 / 7.20	0.72 / 0.55	0.29 / -0.60
Dissolved	0-4	4.16 / 5.52	-42.05 / -54.49	5.09 / 6.33	0.60 / 0.64	-0.30 / -0.71
Particulate	0-4	4.06 / 2.67	20.67 / -5.50	5.22 / 3.37	0.48 / 0.41	-1.20 / -0.10
Phytoplankton	0-4	8.02 / 4.67	-36.45 / -14.85	11.03 / 5.91	0.49 / 0.44	-0.25 / -0.04

A.8 Parameters of The Reaction Network

Table A.4: Parameters of the reaction network. Source: C - calibrated or from 1 - *Canavan et al. [2006]*, 2 - *Van Cappellen and Wang [1996]*; 3 - *Atkin and Tjoelker [2003]*; 4 - *Dijkstra et al. [2018]*; 5 - *Couture et al. [2016]*; 6 - *Katsev and Dittrich [2013]*; 7 - lnl PhreeqC database, *Parkhurst and Apello [2014]*.

Parameter	Value	Units	Source	Literature Values	no.
Primary Redox Reactions					
$k(5)_{POP}$	2×10^{-1}	y^{-1}	C	$1 \times 10^{-2} - 4 \times 10^{1}$	R1-R6
$k(5)_{DOP}$	4×10^{-1}	y^{-1}	C		R1-R6
$k(5)_{POC}$	3×10^{-3}	y^{-1}	C	$2 \times 10^{-3} - 1.5 \times 10^{-1}$	R1-R6
$k(5)_{DOC}$	7×10^{-3}	y^{-1}	C		R1-R6
K_m^{O}	8×10^{-3}	mM	1	$8 \times 10^{-4} - 2 \times 10^{-2}$	R1-R6
$K_m^{\mathrm{N(V)}}$	1×10^{-2}	mM	1	$3 \times 10^{-3} - 2 \times 10^{-1}$	R2-R6
$K_m^{\mathrm{Fe(IIIa)}}$	1.5×10^{3}	$mmol \cdot L_s^{-1}$	C	$6 \times 10^{-1} - 5 \times 10^{3}$	R3-R6
$K_m^{\mathrm{Fe(IIIb)}}$	1×10^{4}	$mmol \cdot L_s^{-1}$	C	$5 \times 10^{1} - 2.3 \times 10^{4}$	R4-R6
$K_m^{\mathrm{S(VI)}}$	1	mM	1	$1.1 \times 10^{-2} - 1.6$	R5, R6
Q_{10}	2	–	3	$1.2 - 4$	R1-R6
$accel$	3×10^{2}	–	C	$1 - 1 \times 10^{2}$	R1, R2
Ψ	1.5×10^{-3}	–	4	$1.5 \times 10^{-3} - 7.5 \times 10^{-2}$	R5, R6
Secondary Redox Reactions					
k_{tsox}	1×10^{6}	$mM^{-1} \cdot y^{-1}$	1	$1.6 \times 10^{2} - 1.6 \times 10^{6}$	R11
k_{tsfe}	2.5	$mM^{-1} \cdot y^{-1}$	1	$2.5 - 9.5 \times 10^{1}$	R12
k_{feox}	5×10^{4}	$mM^{-1} \cdot y^{-1}$	1	$3.5 \times 10^{2} - 1.6 \times 10^{7}$	R13
k_{amox}	2×10^{4}	$mM^{-1} \cdot y^{-1}$	1	$5 \times 10^{3} - 7.9 \times 10^{4}$	R14
k_{ch4o2}	1×10^{7}	$mM^{-1} \cdot y^{-1}$	1	1×10^{7}	R15
k_{ch4so4}	1×10^{-1}	$mM^{-1} \cdot y^{-1}$	1	$1 \times 10^{-1} - 10^{7}$	R16
Mineral precipitation - dissolution reactions					
k_{oms}	1.6×10^{-2}	$mM^{-1} \cdot y^{-1}$	5	$1.6 \times 10^{-2} - 7.8 \times 10^{-2}$	R21
k_{spre}	2.5×10^{3}	y^{-1}	5	$2.5 \times 10^{3} - 3.6 \times 10^{3}$	R22a
k_{sdis}	1×10^{-1}	y^{-1}	5	1×10^{-1}	R22b
k_{fes2ox}	2×10^{2}	$L_s \cdot mmol^{-1} \cdot y^{-1}$	6	2×10^{2}	R23
k_{fespre}	1×10^{-1}	$L_s \cdot mmol^{-1} \cdot y^{-1}$	5	$1 \times 10^{-1} - 1 \times 10^{2}$	R24
k_{fesox}	2×10^{4}	$L_s \cdot mmol^{-1} \cdot y^{-1}$	1	$1 \times 10^{3} - 2 \times 10^{4}$	R25
$k_{fes2pre}$	1.3	$mmol \cdot L_s^{-1} \cdot y^{-1}$	1	$2 \times 10^{-1} - 3.3$	R26
k_{fepre}	2.5×10^{-3}	$mmol \cdot L_s^{-1} \cdot y^{-1}$	6	$2.5 \times 10^{-3} - 2.2 \times 10^{1}$	R27a
k_{fedis}	1×10^{-3}	y^{-1}	1	1×10^{-3}	R27b
K_{FeS}	9.6×10^{3}	–	1	$2.5 \times 10^{3} - 4.9 \times 10^{4}$	R27a, R27b
k_{CCpre}	1×10^{-1}	$mmol \cdot L_s^{-1} \cdot y^{-1}$	6	1×10^{-1}	R28a
k_{CCdis}	1.25×10^{-1}	y^{-1}	6	$5 \times 10^{-2} - 1.25 \times 10^{-1}$	R28b
K_{CC}	5×10^{-15}	mM^2	7	5×10^{-15}	R28a, R29b
k_{FCpre}	1.8×10^{2}	$mmol \cdot L_s^{-1} \cdot y^{-1}$	2	$6.5 \times 10^{-2} - 1.8 \times 10^{2}$	R29a
k_{FCdis}	2.5×10^{-1}	y^{-1}	2	$5 \times 10^{-2} - 2.5 \times 10^{-1}$	R29b
K_{FC}	3.9×10^{-15}	mM^2	2	3.9×10^{-15}	R29a, R29b
Phosphorus sorption and precipitation reactions					
$k_{psorb}^{Fe(IIIa)}$	5	$mM^{-1} \cdot y^{-1}$	C	–	R31a
$k_{psorb}^{Fe(IIIb)}$	5	$mM^{-1} \cdot y^{-1}$	C	–	R32a
k_{psorb}^{Al}	5	$mM^{-1} \cdot y^{-1}$	C	–	R35a
k_{vivpre}	1.1×10^{-2}	$mmol \cdot L_s^{-1} \cdot y^{-1}$	C	2.5×10^{-4}	R33a
k_{vivdis}	5.3×10^{-3}	y^{-1}	C	1.0	R33b
K_{viv}	1.9×10^{-14}	mM^3	7	1.9×10^{-14}	R33a, R33b
k_{apapre}	1.4×10^{-6}	$mmol \cdot L_s^{-1} \cdot y^{-1}$	C	–	R34a
k_{apadis}	3.7×10^{-2}	y^{-1}	C	–	R34b
K_{apa}	6×10^{-20}	mM^3	7	5.9×10^{-14}	R34a, R34b

A.9 Physical Transport Properties of The Solute Constituents

Table A.5: Molecular diffusion coefficients at $5°C$ for solute constituents used in the sediment module. Diffusion coefficients for ions were corrected for temperature using linear regression according to *Boudreau* [1997], for non-charged species – using empirical correlation of Wilke and Chang as corrected by Hayduk and Laudie [*Boudreau, 1997*]. Units are $cm^2\ y^{-1}$.

Species	$D_\circ$	Species	$D_\circ$	Species	$D_\circ$	Species	$D_\circ$
DOP	85	NH_3	398	HS^-	280	CO_3^{2-}	167
HPO_4^{2-}	105	NH_4^+	363	S_0	210	CO_2(aq)	310
DOC	85	Fe^{2+}	127	CH_4(aq)	308		
O_2	369	SO_4^{2+}	190	Ca^{2+}	141		
NO_3^-	359	H_2S	294	HCO_3^-	202		

Appendix B

Supporting information for Chapter 3

B.1 Parameter values used in the simulations

no	$\bar{r}$, $\left[\frac{mol}{mol-C \cdot s}\right]$	literature values	K_m^S	literature values	K_m^{EA}	literature values
R1G	$2.8 \cdot 10^{-6}$[x]	$5.5 \cdot 10^{-5}$ – $1.6 \cdot 10^{-3}$[r]	0.1 mM[x]	0.2 μM – 0.55 mM[p,q]	8 μM[x]	1 μM – 100 μM[f,n]
R2G	$2.8 \cdot 10^{-6}$[x]	$5.5 \cdot 10^{-5}$ – $1.6 \cdot 10^{-3}$[r]	0.1 mM[x]	0.2 μM – 0.55 mM[p,q]	1 μM[x]	1 μM – 80 μM[f,n]
R3G	$2.8 \cdot 10^{-6}$[x]	$5.5 \cdot 10^{-5}$ – $1.6 \cdot 10^{-3}$[r]	0.1 mM[x]	0.2 μM – 0.55 mM[p,q]	-	-
R1P	$3.1 \cdot 10^{-6}$[x]	$3.8 \cdot 10^{-8}$[i]	6.6 μM[x]	1 μM – 0.11 mM[d,j]	-	-
R1A	$3.8 \cdot 10^{-4}$[x]	$1 \cdot 10^{-4}$[i]	0.2 mM[x]	60 μM – 0.5 mM[o,m]	8 μM[x]	1 μM – 100 μM[f,n]
R2A	$4.0 \cdot 10^{-4}$[x]	$2 \cdot 10^{-5}$[i]	0.2 mM[x]	60 μM – 0.5 mM[o,m]	1 μM[x]	1 μM – 80 μM[f,n]
R3A	$1.7 \cdot 10^{-6}$[x]	$9 \cdot 10^{-8}$[i]	0.2 mM[x]	60 μM – 0.5 mM[o,m]	110 μM[x]	3 μM – 0.25 mM[e,g,h,n]
R4A2	$2.4 \cdot 10^{-7}$[x]	$4 \cdot 10^{-7}$ – $1.5 \cdot 10^{-5}$[i,m]	0.2 mM[x]	60 μM – 0.5 mM[o,m]	110 μM[x]	3 μM – 0.25 mM[e,g,h,n]
R5A	$1.3 \cdot 10^{-5}$[x]	10^{-5} – 10^{-3}[i,m]	0.2 mM[x]	60 μM – 0.5 mM[o,m]	0.2 mM[x]	60 μM – 1 mM[c,h,l,n]
R6A	$3.8 \cdot 10^{-7}$[x]	$8 \cdot 10^{-7}$ – $3 \cdot 10^{-4}$[i,m]	0.2 mM[x]	60 μM – 5 mM [o,m]	-	-
R1H	$3.8 \cdot 10^{-4}$[x]	10^{-3}[i]	8 nM[x]	1 nM – 0.6 mM[a,b]	8 μM[x]	1 μM – 100 μM[f,n]
R2H	$3.7 \cdot 10^{-4}$[x]	10^{-3}[i]	8 nM[x]	1 nM – 0.6 mM[a,b]	1 μM[x]	2 μM – 80 μM[f,n]
R3H	$2.3 \cdot 10^{-6}$[x]	$1.1 \cdot 10^{-4}$[i]	8 nM[x]	1 nM – 0.6 mM[a,b]	110 μM[x]	3 μM – 0.25 mM[e,g,h,n]
R4H	$5.4 \cdot 10^{-7}$[x]	$5 \cdot 10^{-4}$[i]	8 nM[x]	1 nM – 0.6 mM[a,b]	110 μM[x]	3 μM – 0.25 mM[e,g,h,n]
R5H	$3.5 \cdot 10^{-5}$[x]	$9 \cdot 10^{-4}$[i]	8 nM[x]	1 nM – 0.6 mM[a,b]	0.2 mM[x]	60 μM – 1 mM[c,h,l,n]
R6H	$8.0 \cdot 10^{-6}$[x]	10^{-3}[i]	8 nM[x]	1 nM – 0.6 mM[a,b]	-	-

Table C1: Kinetic parameters of microbial reactions used in the models of contaminant plume (batch reactor; Watson et al., 2003) and freshwater sediment (column). Biomass yield coefficients are taken from Watson et al., 2003. Membrane voltage potential, $\Delta\Psi$, equals 160 mV for all reactions including fermentation. The rate law and parameters for secondary reactions such as iron oxidation with oxygen and mackinawite formation are taken from (Couture et al., 2015). Henry constants for H_2(aq) and CH_4(aq) are taken from Sander (2015). Range of kinetic parameters are taken from: [a]Ahring and Westermann (1987), [b]Giraldo-Gomez et al. (1992), [c]Wang and Van Cappellen (1996), [d]Mayer et al. (2001), [e]Roden and Wetzel (2002), [f]Berg (2003), [g]Ferro (2003), [h]Schauser et al. (2004), [i]Watson et al. (2005, 2003), [j]Vijayagopal and Viruthagiri (2005), [k]Roden (2006), [l]Pallud and Van Cappellen (2006), [m]Bethke et al. (2008), [n]Katsev and Dittrich (2013), [o]Ingvorsen et al. (1984), [p]Fuechslin et al. (2012), [q]Senn et al. (1994), [r]Fuhrer et al. (2005), [x]calibrated to match Watson et al. (2003) experimental results.

Table C2: Initial concentrations and boundary conditions used in the model of lacustrine sediment. The porosity of the sediment column is assumed to be constant and equal 0.8. The burial rate is 0.2 cm/y. C_0 – is the initial concentration, BC(t) and BC(b) – boundary condition values and types the top (t) and bottom (b), respectively.

name	**variable**	$\mathbf{C_0}$, $\left[\frac{\mathbf{mol}}{\mathbf{L}}\right]$	**BC(t)**, $\left[\frac{\mathbf{mol}}{\mathbf{cm^2 \cdot y}}\right]$		**BC(b)**, $\left[\frac{\mathbf{mol}}{\mathbf{cm^2 \cdot y}}\right]$	
Biomass						
Aerobs	X_A	$5 \cdot 10^{-4}$	0	Flux	0	Flux
Fermenters	X_F	$5 \cdot 10^{-4}$	0	Flux	0	Flux
Nitrate reducers	X_N	$5 \cdot 10^{-4}$	0	Flux	0	Flux
Iron reducers	X_I	$5 \cdot 10^{-4}$	0	Flux	0	Flux
Sulfate reducers	X_S	$5 \cdot 10^{-4}$	0	Flux	0	Flux
Methanogens	X_M	$5 \cdot 10^{-5}$	0	Flux	0	Flux
Solids						
Organic matter	OM	10^{-5}	$7 \cdot 10^{-5}$	Flux	0	Flux
Iron mineral	FeOOH	10^{-3}	10^{-7}	Flux	0	Flux
Adsorbed iron	$=Fe^{2+}$	10^{-10}	0	Flux	0	Flux
Dissolved						
Glucose	$C_6H_{12}O_6$	10^{-6}	0	Flux	0	Flux
Acetate	CH_3COO^-	10^{-6}	0	Flux	0	Flux
Hydrogen	$H_2(aq)$	10^{-6}	0	Flux	0	Flux
Oxygen	O_2	10^{-6}	$3 \cdot 10^{-4}$	Constant	0	Flux
Nitrate	$NO_3{}^-$	10^{-6}	10^{-4}	Constant	0	Flux
Ferrous iron	Fe^{2+}	10^{-6}	0	Flux	0	Flux
Sulfide	HS^-	10^{-6}	0	Flux	0	Flux
Sulfate	$SO_4{}^{2-}$	10^{-4}	10^{-4}	Constant	0	Flux
Methane	$CH_4(aq)$	10^{-12}	10^{-12}	Constant	0	Flux

Table C3: Molecular diffusion coefficients at $10°C$ for solute constituents used in the sediment example. Diffusion coefficients for ions were corrected for temperature using linear regression according to Boudreau (1997), for non-charged species – using empirical correlation of Wilke and Chang as corrected by Hayduk and Laudie (Boudreau, 1997). Units are $cm^2\ y^{-1}$.

species	$\mathbf{D_\circ}$	**species**	$\mathbf{D_\circ}$	**species**	$\mathbf{D_\circ}$
$C_6H_{12}O_6$	85	HS^-	280	O_2	369
CH_3COO^-	100	$SO_4{}^{2+}$	190	$NO_3{}^-$	363
$H_2(aq)$	1132	$CH_4(aq)$	391	Fe^{2+}	127

B.2 Results of the reproduced model and the model with the thermodynamic switch function

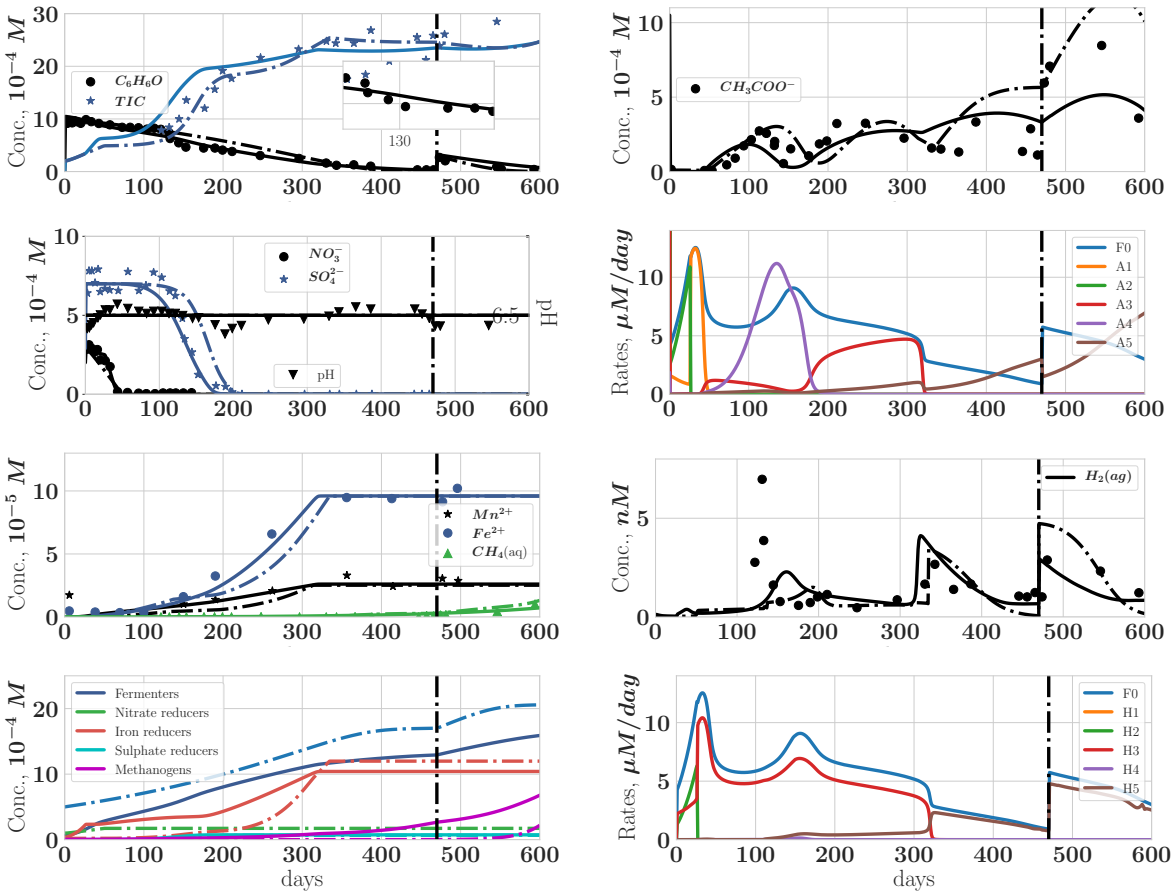

Figure C1: Results of reproduced Watson et al. (2003) model (dashed line) and model with thermodynamic switch function (solid lines). Symbols are experimental data from Watson et al. (2003). For the additional information, refer to the original work.

Appendix C

Supporting Information for Chapter 4

C.1 Characteristics of water gauging stations used for the estimation of the water runoff for the period 2003-2017

Table C1: Characteristics of water gauging stations used for the estimation of the water runoff for the period 2003-2017.

Basin	Side	Name	Code	Coordinates		Area, km^2	Coverage, *days*	Statistical Characteristics of Measurements, *cms*						
				Latitude	Longitude			mean	SD	min	25%	50%	75%	max
SCR	US	St. Clair River At Port Huron, MI	04159130	42.986974	-82.424637	576014	2765	5090.5	624.9	2452.8	4760	5096	5488	6720
SCR	US	Black River Near Jeddo, MI	04159492	43.150860	-82.624647	1202	5479	8.6	18.7	0.2	1.1	2.6	7.7	278.9
SCR	US	Mill Creek Near Avoca, MI	04159900	43.054471	-82.734649	438	5479	3	5.5	0.1	0.4	1	3	95.2
SCR	US	Belle River At Memphis, MI	04160600	42.900862	-82.769091	391	5479	3.1	5.4	0.2	0.6	1.2	3	72.2
SCR	CA	St. Clair River At Port Huron, ON	02GG014	42.986939	-82.424721	576013	1507	4971.9	431.7	2890	4790	5010	5240	6340
LSC	US	Clinton River At Moravian Drive At Mt. Clemens, MI	04165500	42.595867	-82.908810	1901	5479	19.4	21.2	1.6	7.7	12.6	23.5	350
LSC	US	North Branch Clinton River Near Mt. Clemens, MI	04164500	42.629200	-82.888810	515	5479	4.6	8.3	0	0.7	1.7	4.6	173.6
LSC	CA	Thames River At Thamesville, ON	02GE003	42.544861	-81.967270	4370	5479	59	80.5	5.9	15.8	28.9	65.5	893
LSC	CA	Thames River Near Dutton, ON	02GE006	42.730690	-81.577469	3820	4658	53.2	70.8	5.9	15.2	26.2	60	766
LSC	CA	Thames River At Byron, ON	02GE002	42.962502	-81.331780	3080	5479	44.7	67	4.4	12.4	21.3	48.2	856
LSC	CA	Sydenham River At Florence, ON	02GG003	42.650612	-82.008392	1150	5479	12.7	21.4	0.2	1.8	4.7	12.4	227
LSC	CA	Sydenham River Near Alvinston, ON	02GG002	42.830810	-81.851723	701	5479	7.9	13.6	0.5	1.5	3	7.5	174
LSC	CA	Bear Creek Below Brigden, ON	02GG009	42.812031	-82.298424	536	5479	5.8	12.4	0	0.4	1.4	5.2	206
LSC	CA	Bear Creek Near Petrolia, ON	02GG006	42.905830	-82.119110	249	5479	2.9	7.6	0	0.2	0.6	2	140
LSC	CA	Black Creek Near Bradshaw, ON	02GG013	42.762440	-82.259216	213	4262	2.6	6.6	0	0.1	0.3	1.5	109
LSC	CA	Mcgregor Creek Near Chatham, ON	02GE007	42.383499	-82.095062	204	3945	2.2	5.8	0	0.1	0.4	1.4	81.5
LSC	CA	Sydenham River At Strathroy, ON	02GG005	42.958859	-81.627136	171	5479	2.1	3.7	0.1	0.6	0.9	2	52.4
LSC	CA	Ruscom River Near Ruscom Station, ON	02GH002	42.211498	-82.629143	125	5479	1.1	3.1	0	0.1	0.2	0.6	46.4
DR	US	Detroit River At Fort Wayne At Detroit, MI	04165710	42.298094	-83.092700	592590	1299	5833.3	1016.9	3024	5124	6216	6636	7588
DR	US	River Rouge At Detroit, MI	04166500	42.373092	-83.254651	484	5479	4.5	6.1	0.5	1.5	2.6	4.8	142.5
DR	US	Middle River Rouge Near Garden City, MI	04167000	42.348093	-83.311597	259	5479	3	3.6	0.4	1.1	1.8	3.3	72.5
DR	US	Lower River Rouge At Dearborn, MI	04168400	42.308371	-83.252706	236	2805	3	3.6	0	1.2	1.8	3.1	56.6
DR	US	Ecorse River At Dearborn Heights, MI	04168580	42.269483	-83.289652	26	5479	0.2	0.5	0	0	0.1	0.2	10.1
DR	CA	Canard River Near Lukerville, ON	02GH003	42.158970	-83.018890	159	5479	1.9	5	0	0.1	0.2	1.1	84.8
DR	CA	Little River At Windsor, ON	02GH011	42.309860	-82.928497	55	5052	0.7	1.8	0	0.1	0.1	0.5	28.7
DR	CA	Turkey Creek At Windsor, ON	02GH004	42.260502	-83.039833	30	3268	0.4	0.6	0	0.1	0.1	0.3	7.7
DR	CA	Turkey Creek At South Windsor, ON	02GH016	42.264080	-83.032417	15	277	0.4	1.4	0	0.1	0.1	0.2	19.7
WB	US	Maumee River At Waterville, OH	04193500	41.500053	-83.712715	16395	5479	185.2	291.7	1.5	23.8	65	209	2634.8
WB	US	River Raisin Near Monroe, MI	04176500	41.960601	-83.531046	2699	5479	24	31.4	1.4	5.8	11.8	28.3	358.4
WB	US	Huron River At Ann Arbor, MI	04174500	42.286982	-83.733830	1888	5479	15.3	11.6	0.9	7.4	11.9	19.9	91.6
WB	US	Portage River Near Elmore, OH	04195820	41.491162	-83.224645	1279	5479	16.4	35.9	0.1	1.2	3.9	12.9	366.8
WB	US	Ottawa River At University Of Toledo, Toledo, OH	04177000	41.659681	-83.612547	388	5479	3.7	7.2	0.1	0.4	1.2	3.4	77.8
WB	US	Lower River Rouge At Inkster, MI	04168000	42.300593	-83.300208	215	5022	3	3.8	0	1.2	1.7	3.1	58.5
WB	US	Otter Creek At La Salle, MI	04176605	41.866990	-83.453544	132	3195	1.4	3	0	0.1	0.4	1.4	54
WB	US	Wolf Creek At Holland, OH	04193999	41.609444	-83.684167	64	1109	0.9	1.5	0	0.2	0.4	0.9	17.9
WB	US	Malletts Creek At Ann Arbor, MI	04174518	42.264761	-83.688273	28	5479	0.3	0.6	0	0.1	0.1	0.3	21.7

Table C1: (Continued)

Basin	Side	Name	Code	Coordinates		Area, km^2	Coverage, *days*	Statistical Characteristics of Measurements, *cms*						
				Latitude	Longitude			mean	SD	min	25%	50%	75%	max
CB	US	Sandusky River Near Fremont, OH	04198000	41.307831	-83.158809	3240	5479	42.1	79.5	0.7	4.4	12.1	38.4	728
CB	US	Cuyahoga River Near Newburgh Heights, OH	04208504	41.462552	-81.680963	2041	5103	41	38.3	7.2	17.8	28.3	48.6	448
CB	US	Grand River Near Painesville, OH	04212100	41.718934	-81.227879	1774	5479	31.7	46.1	0.3	4.5	13.4	39.9	630
CB	US	Black River At Elyria, OH	04200500	41.380324	-82.104593	1026	5479	13.2	29.5	0.1	1.1	3.5	10.6	341.6
CB	US	Huron River At Milan, OH	04199000	41.300885	-82.608233	961	5479	12.3	28.4	0.2	1.5	3.7	9.5	411.6
CB	US	Rocky River Near Berea, OH	04201500	41.407548	-81.882638	692	5479	11.5	23.7	0.3	2	4.2	9.9	417.2
CB	US	Vermilion River Near Vermilion, OH	04199500	41.381990	-82.316827	679	5479	9.2	21.7	0	0.8	2.6	7.6	322
CB	US	Chagrin River At Willoughby, OH	04209000	41.630881	-81.403445	637	5479	13.2	22.5	0.9	3	6	12.7	319.2
CB	US	Conneaut Creek At Conneaut, OH	04213000	41.926999	-80.603966	453	5479	9	15.4	0.1	1.4	4	9.8	253.7
CB	US	Euclid Creek At Cleveland, OH	04208700	41.582272	-81.558734	60	2332	1.1	2.3	0.1	0.3	0.5	1	39.8
CB	US	Old Woman Creek At Berlin Rd Near Huron, OH	04199155	41.348383	-82.513782	57	5479	0.7	2	0	0	0.2	0.5	33.3
CB	US	Abram Creek At Kolthoff Drive At Brook Park, OH	04201526	41.393056	-81.850278	21	1645	0.3	0.6	0	0.1	0.1	0.3	5.6
CB	CA	Big Otter Creek Near Calton, ON	02GC026	42.710670	-80.840813	665	5479	9.1	11.5	1.6	3.2	5.3	9.8	152
CB	CA	Big Otter Creek At Tillsonburg, ON	02GC010	42.857311	-80.723579	354	5479	4.5	6.5	0.4	1.4	2.3	4.6	102
CB	CA	Kettle Creek At St. Thomas, ON	02GC002	42.777691	-81.213997	331	5479	3.9	9.2	0.1	0.4	1	3.1	139
CB	CA	Catfish Creek Near Sparta, ON	02GC018	42.746078	-81.056938	295	5435	3.5	8.1	0.1	0.4	1.1	2.9	170
CB	CA	Kettle Creek Above St. Thomas, ON	02GC029	42.835190	-81.134720	134	5479	1.6	3.9	0	0.1	0.4	1.2	64.3
CB	CA	Catfish Creek At Aylmer, ON	02GC030	42.773750	-80.982674	127	5479	1.5	3.2	0	0.2	0.5	1.3	66.4
CB	CA	Dodd Creek Below Paynes Mills, ON	02GC031	42.787392	-81.267502	100	5479	1.2	3	0	0.1	0.3	0.9	50.6
CB	CA	Silver Creek Near Grovesend, ON	02GC036	42.675831	-80.953331	40	3653	0.5	0.7	0.1	0.2	0.3	0.5	17.8
EB	US	Cattaraugus Creek At Gowanda, NY	04213500	42.463333	-78.934167	1129	5479	23.1	30.1	2	7.7	14.5	26.4	515.2
EB	US	Buffalo Creek At Gardenville, NY	04214500	42.854722	-78.755000	368	3651	6.4	10.6	0.1	1.4	3.1	6.6	152.9
EB	US	Cazenovia Creek At Ebenezer, NY	04215500	42.829722	-78.775000	350	5479	7.8	14.1	0.1	1.5	3.6	7.7	250.6
EB	US	Cayuga Creek Near Lancaster, NY	04215000	42.890000	-78.645000	250	5479	4.5	8.9	0	0.6	1.9	4.3	124.3
EB	CA	Grand River At Brantford, ON	02GB001	43.132721	-80.267311	5200	5479	65.5	74.8	11.7	26.4	39	73	1000
EB	CA	Grand River At Galt, ON	02GA003	43.353111	-80.315750	3520	5479	45.1	54.4	6.4	18	25.5	48.5	780
EB	CA	Big Creek Near Walsingham, ON	02GC007	42.685612	-80.538467	567	5479	7.4	5.5	1.6	4	5.9	8.9	75.4
EB	CA	Nanticoke Creek At Nanticoke, ON	02GC022	42.809921	-80.076172	177	4765	1.9	2.7	0	0.4	1	2.3	39.8
EB	CA	Mckenzie Creek Near Caledonia, ON	02GB010	43.033939	-79.949806	173	5479	2.1	3.3	0	0.4	0.9	2.1	38.9
EB	CA	Lynn River At Simcoe, ON	02GC008	42.823330	-80.289436	144	5479	1.8	1.2	0.6	1.1	1.5	2.2	21.1
EB	CA	Venison Creek Near Walsingham, ON	02GC021	42.653359	-80.548439	68	3646	1.4	1	0.5	0.8	1.1	1.6	8.4
EB	CA	Young Creek Near Vittoria, ON	02GC014	42.765751	-80.294579	66	2097	0.8	0.5	0.3	0.5	0.7	1	7
NR	US	Niagara River At Buffalo, NY	04216000	42.877778	-78.916389	682980	5478	5761.2	551.3	3808	5376	5712	6076	8176
NR	US	Tonawanda Creek At Rapids, NY	04218000	43.093056	-78.636111	904	5479	13.9	18.2	0.3	2.9	7.6	16.8	159.3
NR	US	Ellicott Creek Below Williamsville, NY	04218518	42.977778	-78.763611	211	5479	4.3	5.9	0.3	1.3	2.5	4.6	74.8
NR	CA	Niagara River At Queenston, ON	02HA003	43.156941	-79.047218	686000	5479	5860	568.9	3910	5460	5820	6200	8190
NR	CA	Niagara River At Fort Erie, ON	02HA013	42.930279	-78.914169	683000	585	5778.8	619.1	3900	5340	5740	6220	8460
NR	CA	Welland Canal Diversion From Lake Erie, ON	02HA019	42.950001	-79.216667	683000	5386	190.6	51.2	19.1	152	199	234	304
NR	CA	Welland River Below Caistor Corners, ON	02HA007	43.021778	-79.618019	223	5470	2.6	6.2	0	0.1	0.4	2	82.5
NR	CA	Oswego Creek At Canborough, ON	02HA024	42.991310	-79.678253	83	2647	1.2	3.1	0	0	0.1	0.8	50

C.2 Annual and monthly average values of evaporation

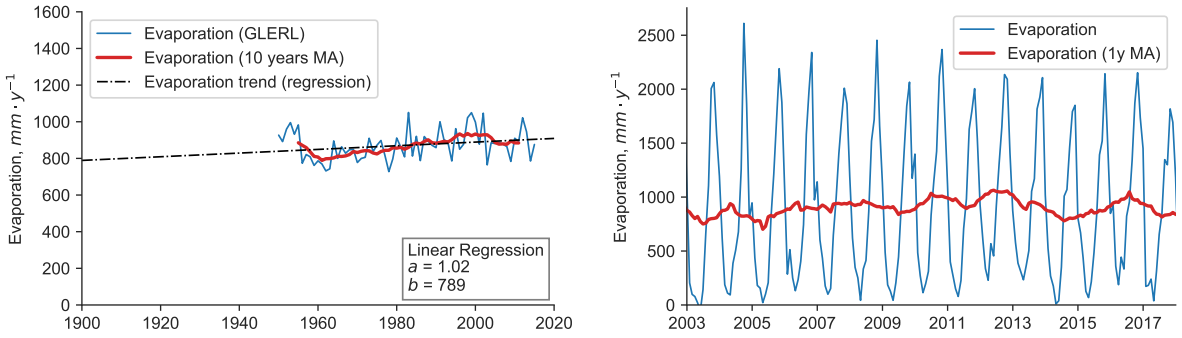

Figure C1: a) Historical 1900-2017 annual and b) 2003-2017 monthly average values of evaporation in Lake Erie as reported by NOAA (blue lines), as well as the trends estimated by linear regression (dashed black line) and moving averages (red lines).

C.3 Water level

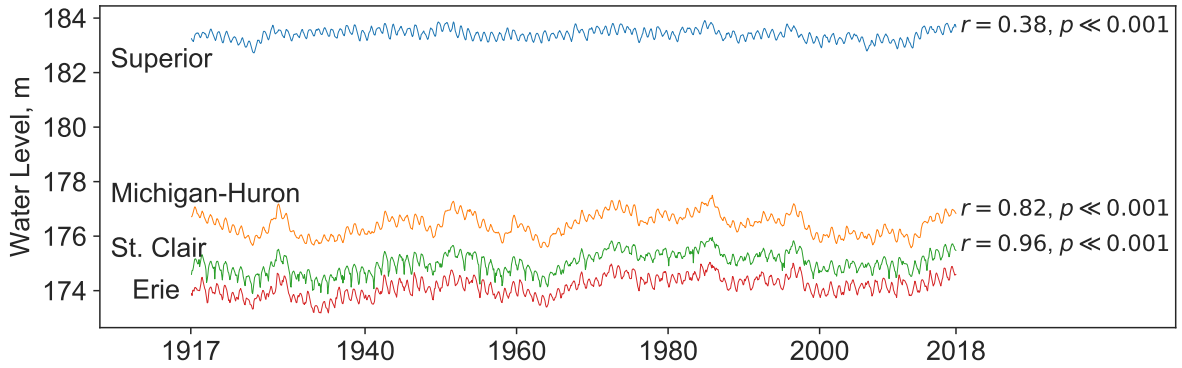

Figure C2: Historical water levels of the LGLs above of Lake Erie and their Pearson correlation coefficient with respect to the water level of Lake Erie.

C.4 Correlation of annual change of water level of Lake Erie with El Niño - Southern Oscillation Index

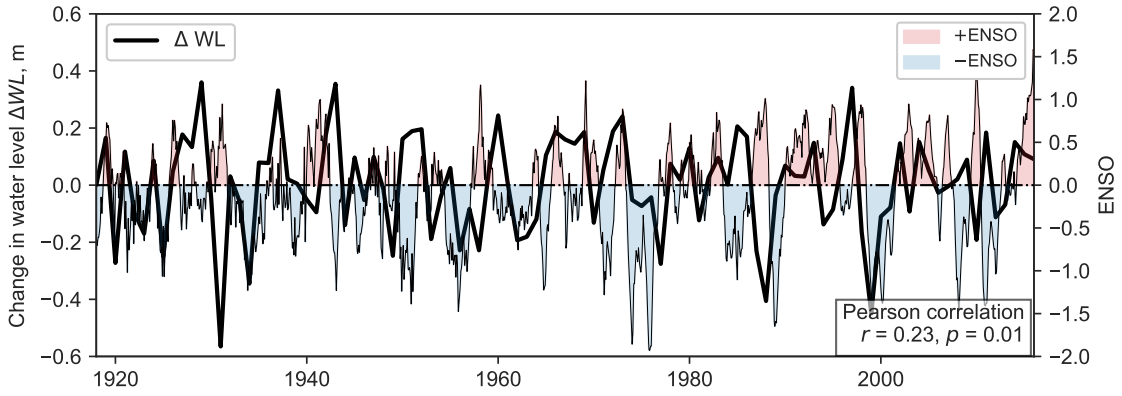

Figure C3: Correlation of annual change (derivative) of water level of Lake Erie with El Niño - Southern Oscillation Index (ENSO).

C.5 Overall water budget

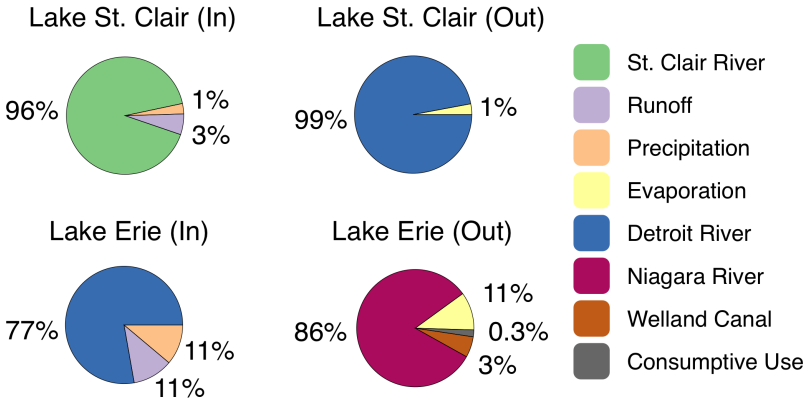

Figure C4: Pie charts of water budget for the period from 2003 to 2017.

C.6 Index of bloom severity

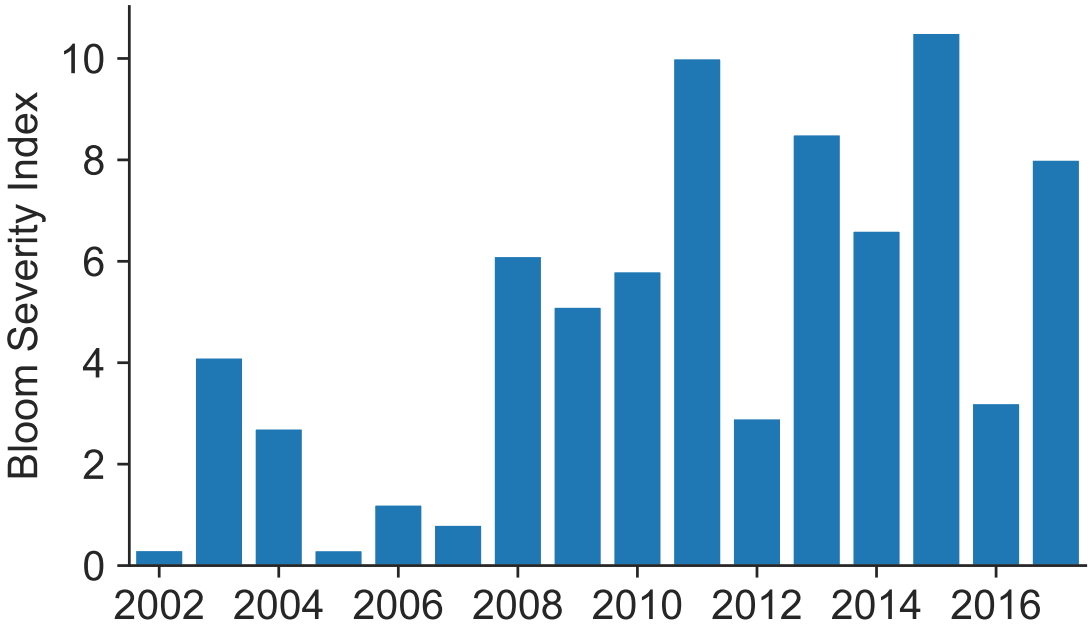

Figure C5: Index of bloom severity of Lake Erie as estimated by NOAA.

C.7 Comparison of precipitation and evaporation data provided by ERA5 and NOAA

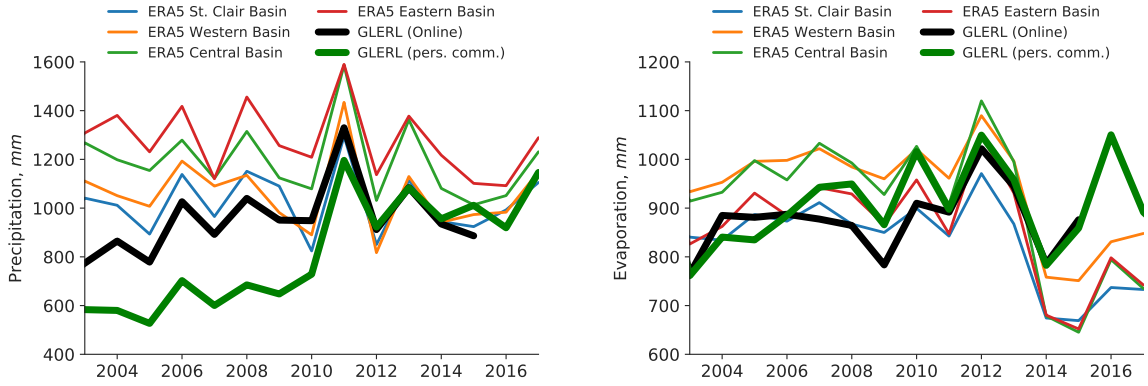

Figure C6: Comparison of (a) precipitation data and (b) evaporation data provided by ERA5 and NOAA.

Data on precipitation and evaporation was acquired from National Oceanic and Atmospheric Administration (NOAA) and European Centre for Medium- Range Weather Forecasts (ECMWF) ERA5 datasets. ERA5 is hourly gridded reanalysis data using 4D-Var data assimilation in ECMWF's Integrated Forecast System available from 1979. However, each method has unique sources of uncertainty and variability. We compare the values from these two sources in the supplemental material (fig. C6). As a part of Copernicus Earth observation programme, ECMWF provides estimates of a large number of oceanic, atmospheric, and land climate variables in 5th ECMWF Re-Analysis (ERA5) dataset (www.ecmwf.int). With high temporal and spatial resolution (hourly on 31 km grid), ERA5 combines historical observations into global estimates using modelling and data assimilation systems. Together with estimates of uncertainty, reanalysis includes estimate of precipitation and runoff from a Numerical Weather Prediction model, ground observations and satellite data. The uncertainty of these products are estimated using "Ensemble Spread" products to calculate daily gridded standard deviation over Lake Erie. Data used from this source includes main daily precipitation, evaporation, surface runoff, and cloud cover and the error bound estimates are 0.84 mm, 0.06 mm, 0.17 mm, and 0.2 percent, respectively. At present, ERA5 dataset is starting from 1979, while the entire

dataset from 1950 is expected to be available in late 2019.

C.8 Comparison of monthly average values of precipitation and runoff

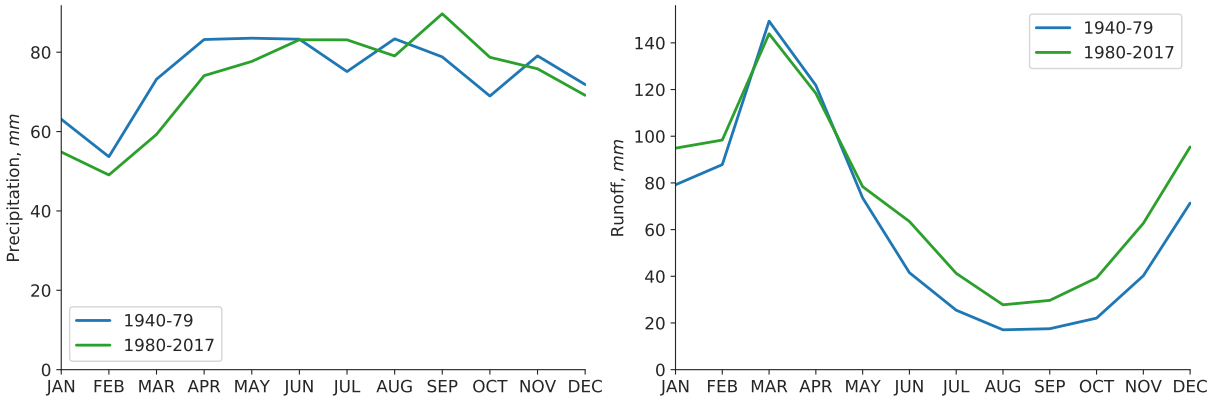

Figure C7: Monthly average values for the period 1940-79 compared with average values for the period from 1980-2017. (a) precipitation and (b) runoff as estimated by NOAA.

C.9 Average annual water outflow from Lake Erie

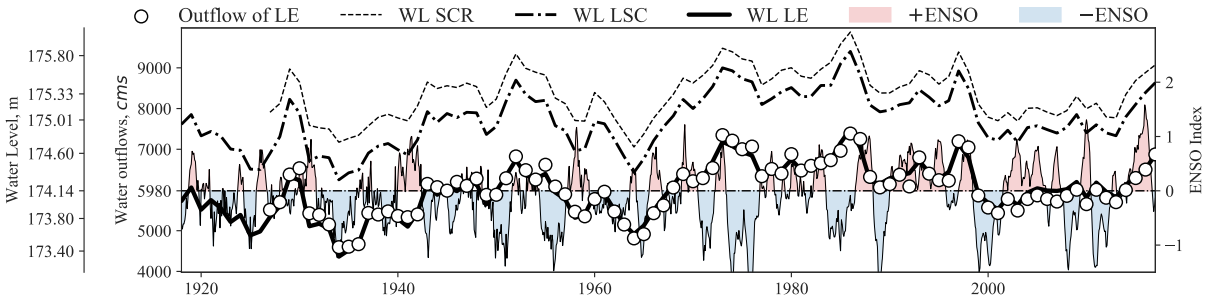

Figure C8: Average annual water outflow from Lake Erie for the period from 1917 to 2017 (black circles). The outflow estimated based on the Niagara River and Welland canal historical records. The thick black line represents water level obtained from the US Army Corps of Engineers. The thick dot-dashed black line represents the water level of Lake St. Clair (WL LSC). The thin dashed black line represents the water level of St. Clair River (WL SCR). The shaded blue and red areas represent the El Niño–Southern Oscillation Index (ENSO).

C.10 Detailed frequency analysis

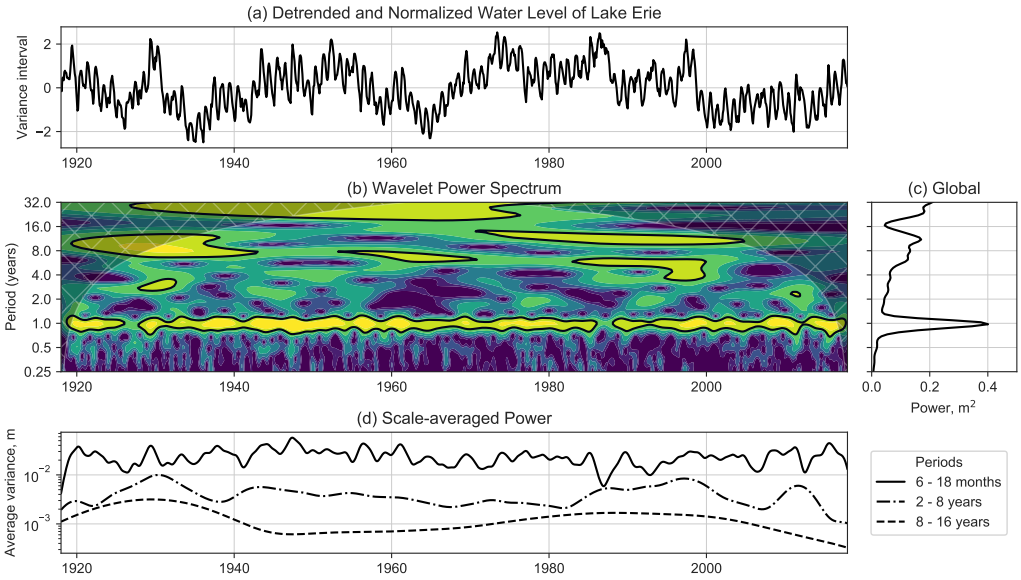

Figure C9: The local wavelet power spectrum analysis of Lake Erie water level for the period from 1917 to 2017. a) water level detrended and normalized to standard deviation, b) Morlet wavelet power spectrum, c) the global wavelet power spectra, d) the scale averaged wavelet spectrum.

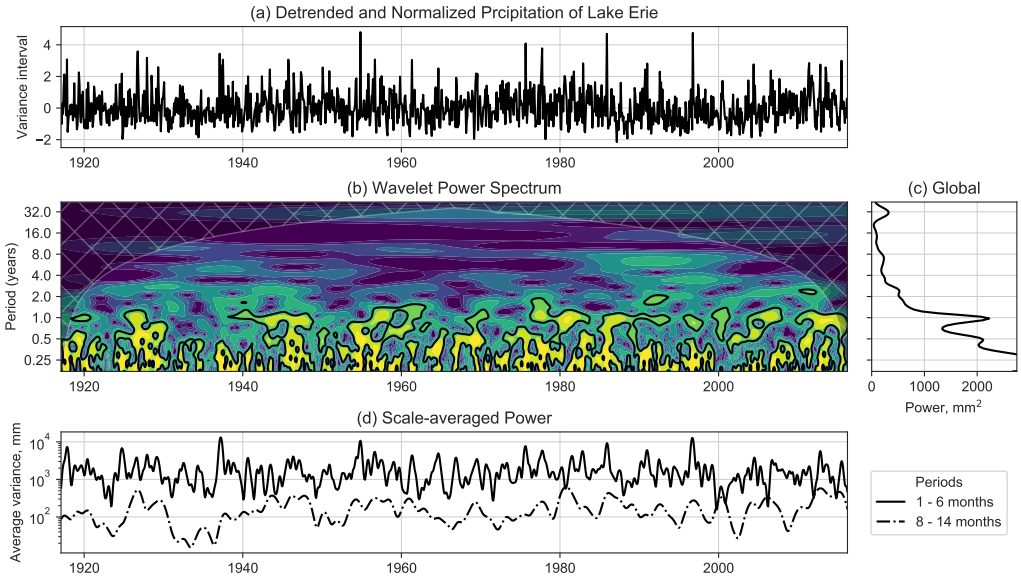

Figure C10: The local wavelet power spectrum analysis of over-lake precipitation of Lake Erie for the period from 1917 to 2017. a) precipitation detrended and normalized to standard deviation, b) Morlet wavelet power spectrum, c) the global wavelet power spectra, d) the scale averaged wavelet spectrum.

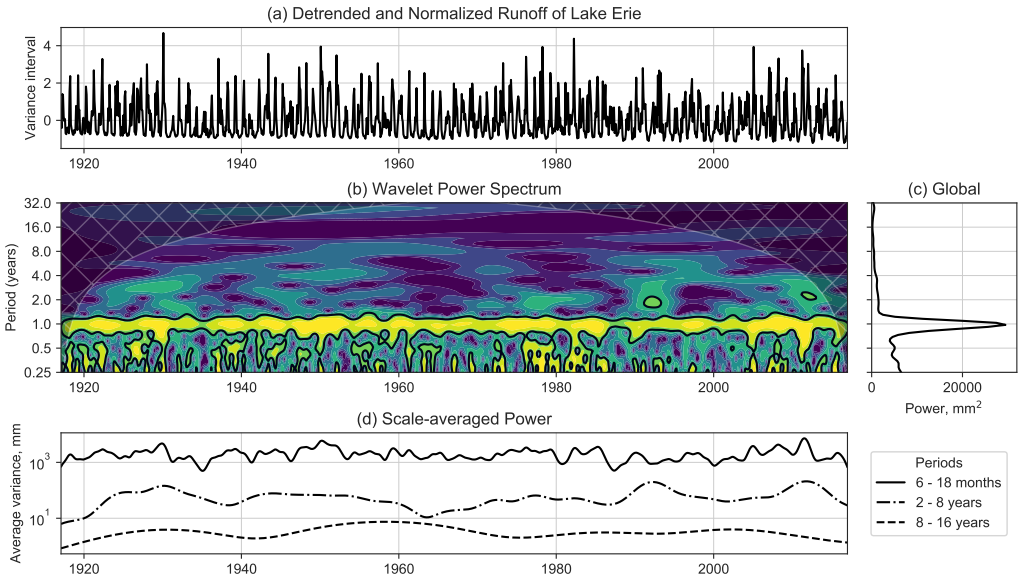

Figure C11: The local wavelet power spectrum analysis Lake Erie runoff for the period from 1917 to 2017. a) runoff detrended and normalized to standard deviation, b) Morlet wavelet power spectrum, c) the global wavelet power spectra, d) the scale averaged wavelet spectrum.

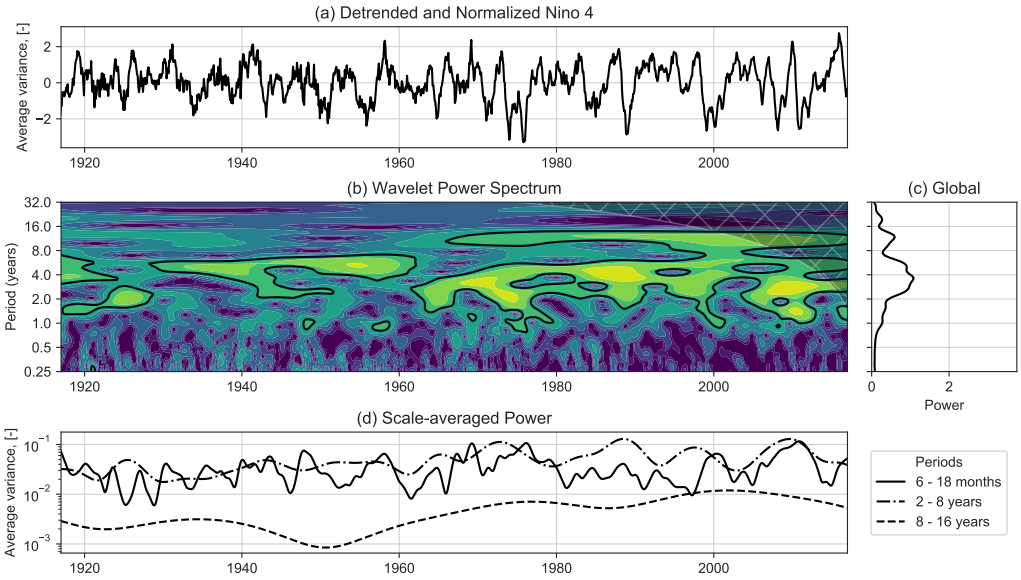

Figure C12: The local wavelet power spectrum analysis Lake Erie El Niño - Southern Oscillation Index (ENSO) for the period from 1917 to 2017. a) ENSO detrended and normalized to standard deviation, b) Morlet wavelet power spectrum, c) the global wavelet power spectra, d) the scale averaged wavelet spectrum.

C.11 Monthly average values of precipitation, evaporation and runoff of Lake St. Clair and Lake Erie.

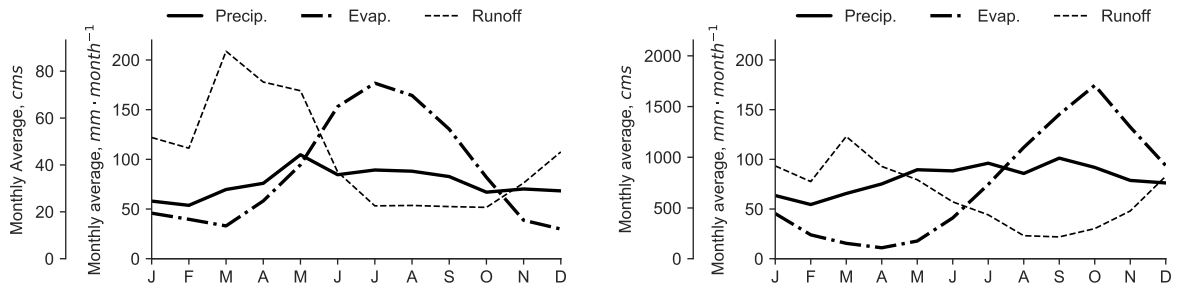

Figure C13: Monthly average values of precipitation, evaporation and runoff of (a) Lake St. Clair and (b) Lake Erie. The monthly average values are reported for the period from 2003 to 2017.

C.12 Monthly average values of precipitation, evaporation and runoff of Lake St. Clair and Lake Erie.

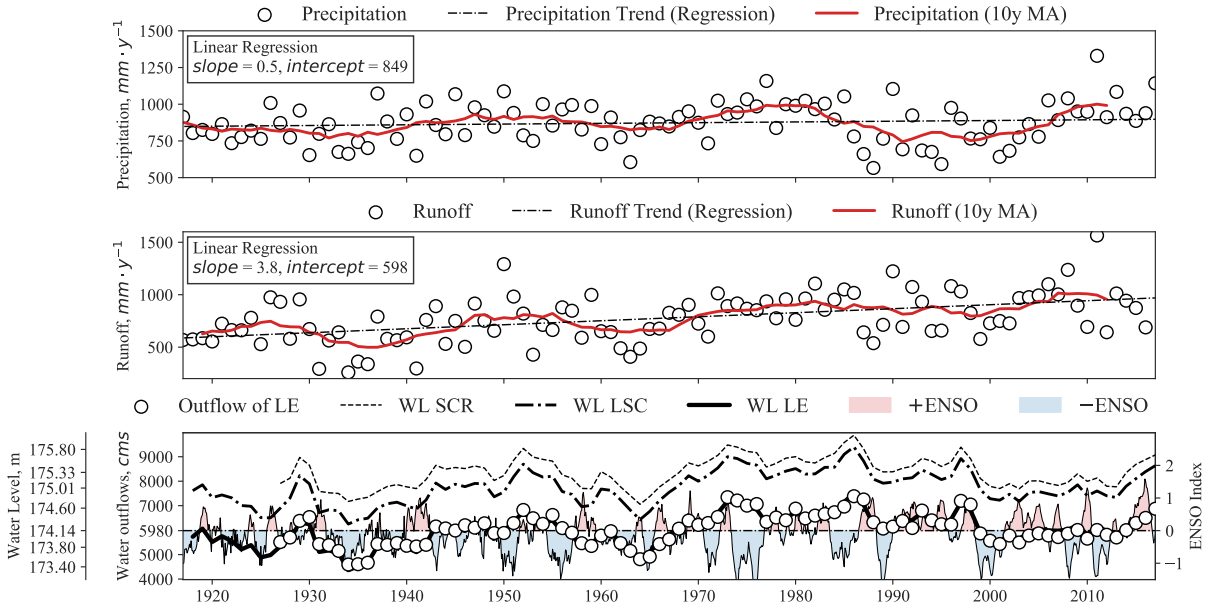

Figure C14: (A) Historical 1917-2017 monthly average values of precipitation over the Lake Erie (black circles), as well as the trend estimated by linear regression (dashed black line), and moving averages (red line). (B) Historical 1917-2017 monthly average values of runoff to the Lake Erie (black circles), linear regression trend (dashed black line), and moving averages (red line). (C) Average annual water outflow from Lake Erie for the period from 1980 to 2003 (black circles). The outflow estimated based on the Niagara River and Welland canal historical records. Thick black line represents water level obtained from the US Army Corps of Engineers. Thick dot-dashed black line represents the water level of Lake St. Clair (WL LSC). Thin dashed black line represents the water level of St. Clair River (WL SCR). The shaded blue and red areas represent El Niño–Southern Oscillation Index (ENSO).

Appendix D

Supporting Information for Chapter 5

D.1 Analytical Solutions

The numerical scheme results were verified against analytical solutions for transport and reaction problems. Analytical solutions for transport in 1-D flow field with diffusion without chemical reaction (Ogata and Banks, 1961):

$$C(x,t) = \frac{C_o}{2}\left[erfc\left(\frac{x-wt}{2\sqrt{Dt}}\right) + exp\left(\frac{wx}{D}\right)erfc\left(\frac{x-wt}{2\sqrt{Dt}}\right)\right] \tag{D.1}$$

where $erfc$ – is the complimentary error function. Figure D1a compares analytical and numerical solutions for advective-diffusive transport with constant boundary condition C_o.

Analytical solution for first-order process:

$$C(t) = C_0 exp(-kt) \tag{D.2}$$

where k – is a first-order decay constant. Figure D1b compares analytical and numerical solutions for the first-order decay reaction.

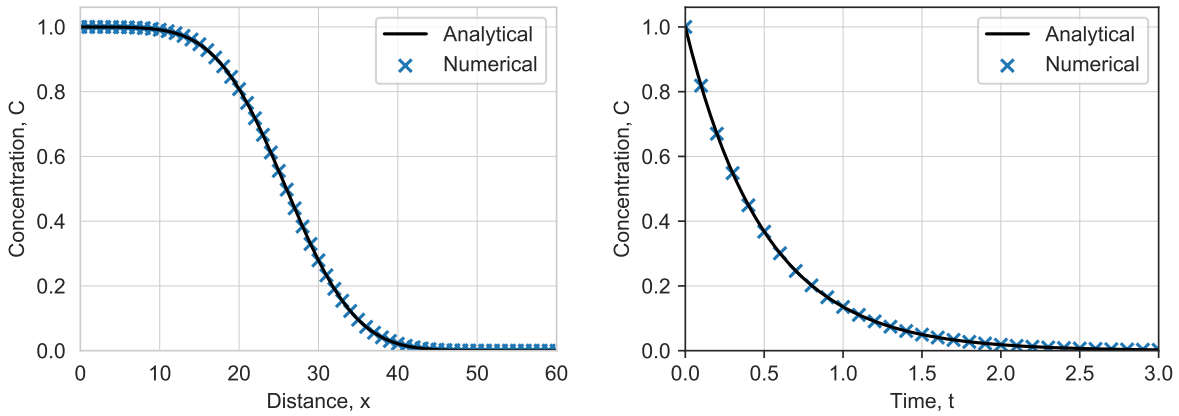

(a) Advective-diffusive transport (b) First-order decay

Figure D1: Comparison of numerical and analytical solutions for (a) transport and (b) reaction problems.

D.2 Methods' Names and Keywords Used in PorousMediaLab

D.2.1 Batch Class

- *batch = Batch(tend, dt)* – keyword initiates instance *batch* of master class *Batch*. User should provide total time of the simulation and time-step of the desired result. During the simulation the PorousMediaLab will adjust *dt* if integration methods do not converge at the provided time-step. The result will be returned at the time-step specified by the user. The name of the instance variable *batch* used in the examples is not strictly defined, user may chose any other convenient name;

- *batch.add_species(name, init_conc)* – an instance method that adds elements (reactive or trace) into the batch system. The user should provide the name of the element and initial concentration.

D.2.2 Column Class

- *column = Column(length, dx, tend, dt, w=0, ode_method='scipy')* – keyword initiates instance *column* of master class *Column*. The user should provide the length of the domain *length*, the mesh size *dx*, the total time of the simulation *tend* and time-step of the desired result *dt*. There are optional argument such as advective

velocity of all species *w* and ODE integration method *ode_method*. During the simulation, the PorousMediaLab will adjust *dt* if integration methods do not converge at the provided time-step. The result will be returned at the time-step specified by the user. The name of the instance variable *column* used in the examples is not strictly defined, the user may choose any other convenient name;

- *column.add_species(theta, name, init_conc, bc_top_value, bc_top_type, bc_bot_value, bc_bot_type, w)* – an instance method that adds elements (reactive or trace) into the *column*. The user should provide porosity *theta*, the name of the element *name*, initial concentration *init_conc*, top and bottom boundary conditions *bc_top_value*, *bc_top_type*, *bc_bot_value*, *bc_bot_type*. Advective velocity *w* – is an optional argument with default value of 0.

D.2.3 Common Methods of Batch and Column Class

- *instance.add_acid(species, pKa, charge)* – an instance method that adds acid and create an acid-base system. User should provide list of *species* (e.g., ['H3PO4', 'H2PO4', 'HPO4', 'PO4'], which were previously added in instance of *column* or *batch* via using method *add_speceis*), give a list of *pKa* values (e.g., [2.148, 7.198, 12.375]), and assign the charge of the most protonated element using keyword *charge*. Note that *instance* variable is declared variable during instantiation of the *Column* or *Batch* class and is not strictly defined, so that user may chose any other convenient name.

- *instance.add_ion(name, charge)* – an instance method that adds non-dissociative ion in acid-base system which is participating in the charge balance. Arguments: *name* – name of the chemical element, *charge* – charge of the ion (e.g., -3, -2, -1, +1, +2, +3, etc.).

- *instance.henry_equilibrium(aq, gas, Hcc)* – an instance method that adds linear partitioning between the aqueous and gaseous phase. Arguments: *aq* – name of aquatic species, *gas* – name of gaseous species, *Hcc* – Henry Law Constant.

- *instance.constants* – hash (dictionary-like) variable that assigns the names and values of constants used in the estimation of reaction rates.

- *instance.rates* – hash (dictionary-like) variable that assigns the names and values of rates used in the computation of mass-conservation equations.

- *instance.dcdt* – hash (dictionary-like) variable that assigns the names and values of the mass-conservation equations.

- *instance.solve()* – an instance method that solves the system of the transport and mass-conversation reaction equations in time from 0 till *tend*.

- *instance.integrate_one_timestep()* – an instance method that solves the system the transport mass-conversation reaction equations in time for one time-step *dt*. The method is useful for the numerical systems with transient parameters.

- *instance.reconstruct_rates()* – an instance method that reconstructs absolute values of the rates in *column.rates*.

- *instance.time* – array of time starting from 0 to *tend* with the step *dt*.

- *instance.NO3.concentration* – after the solution of the numerical equations user can access the solved variables by using dot notation. This example demonstrates access to an array of NO_3 concentration after the solution of the transport and mass-conversation reaction equations.

- *instance.save_results_in_hdf5()* – after the solution of the numerical equations user can save the results and parameters in HDF5 file *'results.h5'*.

D.2.4 Plotting Methods

- *instance.plot_profiles()* – the method plots resulting concentrations of batch and 1-dimensional simulations (*e.g.,* Figures 5.2b and 5.4a).

- *instance.plot_rates()* – the method that plots reaction rates in space and time of batch and 1-dimensional simulations (*e.g.,* Figure 5.3b).

- *instance.plot_deltas()* – the method plots deltas (relative change) of the concentrations in batch and 1-D simulations (*e.g.,* Figure 5.4b).

- *instance.plot_fractions()* – plots alpha fractions of the acid-base systems (*e.g.,* Figure 5.2a).

- *instance.plot_saturation_index()* – plots saturation indices of the minerals defined in the system.

D.3 Thermodynamic Library Accessible in PorousMediLab

Table C1: Thermodynamic properties of the chemical compounds. The units of Gibbs Free Energy and Enthalpy are $kJ \cdot mol^{-1}$, the units of Entropy are $J \cdot mol^{-1} \cdot K^{-1}$

Element	ΔG	ΔH	ΔS	**Element**	ΔG	ΔH	ΔS
$C_6H_{12}O_6$	-917.22	-1271	209.2	H_2(aq)	17.57	-4.18	57.7
C_6H_6O	-50.42	-165.1	144	H_2O	-237.18	-285.83	69.91
CH_3COO^-	-369.4	-486	86.6	HCO_3^-	-586.85	-692.0	91.2
CH_3COOH	-389.4	-484.5	159.8	HS^-	12.05	-17.6	62.8
CH_4(aq)	-34.39	-89.04	83.7	Mn^{2+}	-228.1	-220.8	-73.6
CH_4(g)	-50.79	-74.8	186	MnO_2	-465.1	-520	53.1
CO_2(aq)	-394.37	-393.5	213.6	N_2(g)	18.2	-10.4	95.8
CO_3^{2-}	-527.9	-677.1	-56.9	NO_3^-	-111.3	-207.4	146.4
αFeOOH	-488.6	-559.3	60.5	O_2	16.40	-11.17	111
γFeOOH	-480.1	-549.3	65.1	SO_4^{2-}	-744.6	-909.2	20.1
Fe^{2+}	-78.9	-89.10	138				

Table C2: Gibbs Free Energy of the half-reactions at standard conditions. The units are $kJ \cdot mol^{-1} \cdot e^{-1}$.

Reaction	ΔG°
$Sb(OH)_6{}^- + 2\,e^- + 3\,H^+ \longrightarrow Sb(OH)_3 + 3\,H_2O$	-248.13
$24MnOOH + 72H^+ + 24\,e \longrightarrow 24\,Mn(2^+) + 48H_2O$	-146.27
$6\,O_2 + 24\,H^+ + 24\,e^- \longrightarrow 12\,H_2O$	-122.98
$CrO_{42}{}^- + 5\,H^+ + 3\,e^- \longrightarrow Cr(OH)_{30} + H_2O$	-120.33
$4.8NO_3{}^- + 28.8H^+ + 24\,e^- \longrightarrow 2.4N_2(aq) + 14.4H_2O$	-118.27
$2\,NO_3{}^- + 12\,H^+ + 10\,e^- \longrightarrow N_{20} + 6\,H_2O$	-118.27
$NO_2{}^- + 8\,H^+ + 6\,e^- \longrightarrow NH_4{}^+ + 2\,H_2O$	-86.36
$24\,Fe(OH)_3 + 72\,H^+ + 24\,e^- \longrightarrow 24\,Fe^{2+} + 72\,H_2O$	-84.56
$NO_3{}^- + 2\,H^+ + 2\,e^- \longrightarrow NO_2{}^- + H_2O$	-81.14
$24\gamma{-}FeOOH + 72\,H^+ + 24\,e^- \longrightarrow 24\,Fe^{2+} + 48\,H_2O$	-65.28
$HAsO_4{}^{2-} + 2\,e^- + 4\,H^+ \longrightarrow H_3AsO_3 + H_2O$	-55.25
$C_2H_5OH + H_2O \longrightarrow 2\,CO_2 + 12\,H^+ + 12\,e^-$	-30.76
$3\,SO_4{}^{2-} + 27\,H^+ + 24\,e^- \longrightarrow 3\,HS^- + 12\,H_2O$	-24.13
$3\,HCO_3{}^- + 27\,H^+ + 24\,e^- \longrightarrow 3\,CH_4(aq) + 9\,H_2O$	-20.09
$3\,CO_2 + 24\,H^+ + 24\,e^- \longrightarrow 3\,CH_4 + 6\,H_2O$	-14.62
$12\,H_2 \longrightarrow 24H^+ + 24e^-$	-8.6
$C_6H_{12}O_6 + 2\,H_2O \longrightarrow 2\,CH_3COO^- + 4\,H_2 + 2\,CO_2 + 2\,H^+ + 8\,e^-$	-7.93
$3\,C_6H_{12}O_6 + 12\,H_2O \longrightarrow 6\,CH_3COO^- + 6\,HCO_3{}^- + 36\,H^+ + 24\,e^-$	-5.6
$C_6H_{12}O_6 + 4H_2O \longrightarrow 2\,CH_3COO^- + 2\,HCO_3{}^- + 4\,H^+ + 4\,H_2$	3.0
$C_6H_{12}O_6 + 12\,H_2O \longrightarrow 6\,HCO_3{}^- + 30\,H^+ + 24\,e^-$	10.31
$C_2H_5OH + H_2O \longrightarrow CH_3COO^- + 5\,H^+ + 4\,e^-$	12.07
$3\,CH_3COO^- + 9\,H_2O \longrightarrow 3\,CO_2 + 3\,HCO_3{}^- + 24\,H^+ + 24\,e^-$	12.8
$3\,CH_3COO^- + 12\,H_2O \longrightarrow 6\,HCO_3{}^- + 27\,H^+ + 24\,e^-$	18.26

Table C3: Gibbs Free Energy of the full reactions at standard conditions. The units are $kJ \cdot mol^{-1} \cdot e^{-1}$.

Reaction	ΔG°
$C_6H_{12}O_6 + 24MnOOH + 42H^+ \longrightarrow 6\,HCO_3^- + 24\,Mn(2^+) + 36H_2O$	-135.96
$3\,C_6H_{12}O_6 + 6\,O_2 + 18\,H^+ \longrightarrow 6\,CH_3COO^- + 12\,H_2 + 6\,CO_2 + 6\,H_2O$	-130.91
$3\,C_6H_{12}O_6 + 6\,O_2 \longrightarrow 6\,CH_3COO^- + 6\,HCO_3^- + 12\,H^+$	-128.58
$C_6H_{12}O_6 + 6\,O_2 \longrightarrow 6\,HCO_3^- + 6\,H^+$	-112.67
$C_6H_{12}O_6 + 4.8NO_3^- + \longrightarrow 6\,HCO_3^- + 1.2H^+ + 2.4N_2(aq) + 2.4H_2O$	-107.96
$C_6H_{12}O_6 + 24\,Fe(OH)_3 + 42\,H^+ \longrightarrow 24\,Fe^{2+} + 6\,HCO_3^- + 60\,H_2O$	-74.25
$3\,C_6H_{12}O_6 + 24\,FeOOH + 66\,H^+ \longrightarrow 6\,CH_3COO^- + 12\,H_2 + 6\,CO_2 + 24\,Fe^{2+} + 42\,H_2O$	-73.21
$3\,C_6H_{12}O_6 + 24\,FeOOH + 36\,H^+ \longrightarrow 6\,CH_3COO^- + 24\,Fe^{2+} + 36\,H_2O + 6\,HCO_3^-$	-70.88
$C_6H_{12}O_6 + 24\,FeOOH + 42\,H^+ \longrightarrow 6\,HCO_3^- + 24\,Fe^{2+} + 36\,H_2O$	-54.97
$3\,C_6H_{12}O_6 + 3\,SO_4^{2-} + 21\,H^+ \longrightarrow 6\,CH_3COO^- + 12\,H_2 + 6\,CO_2 + 3\,HS^- + 6\,H_2O$	-32.07
$3\,C_6H_{12}O_6 + 3\,SO_4^{2-} \longrightarrow 6\,CH_3COO^- + 6\,HCO_3^- + 9\,H^+ + 3\,HS^-$	-29.73
$C_6H_{12}O_6 + 3\,SO_4^{2-} \longrightarrow 6\,HCO_3^- + 3\,HS^- + 3\,H^+$	-13.82
$C_6H_{12}O_6 + 4\,H_2O \longrightarrow 2\,CH_3COO^- + 2\,HCO_3^- + 4\,H^+ + 4\,H_2$	24.02
$C_6H_6O + 5H_2O \longrightarrow 3CH_3COO + 3\,H + 2H_2(aq)$	20.33
$C_6H_6O + 5H_2O \longrightarrow 3CH_3COOH + 2H_2(aq)$	103.75
$C_2H_5OH + 2Sb(OH)_6- + H+ \longrightarrow CH_3COO- + 2Sb(OH)_3 + 5H_2O$	-236.06
$C_2H_5OH + 3\,O_2 \longrightarrow 2\,CO_2 + 3\,H_2O$	-153.74
$C_2H_5OH + 4\,CrO_4^{2-} + 8\,H^+ \longrightarrow 2\,CO_2 + 4\,Cr(OH)_3 + 3\,H_2O$	-151.09
$C_2H_5OH + 2.4NO_3- + 2.4H+ \longrightarrow 2CO_2 + 1.2N_2 + 4.2H_2O$	-149.02
$C_2H_5OH + O_2 \longrightarrow CH_3COO^- + H^+ + H_2O$	-110.91
$C_2H_5OH + (4/3)CrO_{42}^- + \frac{5}{3}H^+ \longrightarrow CH_3COO^- + (4/3)Cr(OH)_3 + (1/3)H_2O$	-108.26
$C_2H_5OH + 0.8NO_3^- \longrightarrow CH_3COO^- + 0.2\,H^+ + 0.4N_2 + 1.4H_2O$	-106.2
$C_2H_5OH + \frac{1}{3}H+ + \frac{2}{3}NO_2- \longrightarrow \frac{1}{3}H_2O + CH_3COO- + \frac{2}{3}NH_4+$	-74.29
$C_2H_5OH + 2NO_3- \longrightarrow CH_3COO- + 2NO_2- + H_2O + H+$	-69.07
$C_2H_5OH + 3H+ + 2HAsO_42- \longrightarrow H_2O + CH_3COO- + 2H_3AsO_3$	-43.18

Table C3: (Continued)

Reaction	ΔG°
$CH_3COO^- + \frac{8}{5}NO_3{}^- + \frac{3}{5}H^+ \longrightarrow \frac{4}{5}N_2 + \frac{4}{5}H_2O + 2\,HCO_3{}^-$	-100.0
$CH_3COO^- + 4\,MnO_2 + 5\,H^+ \longrightarrow 4\,Mn^{2+} + 4\,H_2O + 2\,HCO_3{}^-$	-100.71
$3\,CH_3COO^- + 6\,O_2 \longrightarrow 6\,HCO_3{}^- + 3\,H^+$	-104.72
$3\,CH_3COO^- + 24\,FeOOH + 45\,H^+ \longrightarrow 24\,Fe^{2+} + 6\,HCO_3{}^- + 36\,H_2O$	-47.01
$3\,CH_3COO^- + 24\,FeOOH + 45\,H^+ \longrightarrow 24\,Fe^{2+} + 6\,HCO_3{}^- + 36\,H_2O$	-47.01
$3\,CH_3COO^- + 3\,SO_4{}^{2-} \longrightarrow 6\,HCO_3{}^- + 3\,HS^-$	-5.87
$CH_3COO^- + SO_{42}{}^- \longrightarrow HS^- + 2\,HCO_3{}^-$	-5.87
$3\,CH_3COO^- + 3\,H_2O \longrightarrow 3\,HCO_3{}^- + 3\,CH_4$	-1.82
$CH_3COO^- + H_2O \longrightarrow CH_4 + HCO_3$	-1.82
$CH_3COO^- + H_2O \longrightarrow CH_4 + HCO_3$	0.63
$3\,CH_3COOH + 4NO_3{}^- \longrightarrow 6HCO_3- + 2N_2 + 6H+$	-77.84
$CH_3COOH + 2MnO_2 \longrightarrow 2HCO_3- + 2Mn + 2H+$	-38.77
$6\,CH_2O + 4.8NO_3{}^- \longrightarrow 2.4N_2(aq) + 2.4H_2O + 6HCO_3{}^- + 1.2H^+$	-104.18
$6\,CH_2O + 24\,Fe(OH)_3 + 42\,H^+ \longrightarrow 24\,Fe^{2+} + 60\,H_2O + 6HCO_3{}^-$	-70.48
$6\,CH_2O + 3\,SO_4{}^{2-} \longrightarrow 3\,HS^- + 6HCO_3{}^- + 3\,H^+$	-10.05
$9\,CH_2O + 3H_2O \longrightarrow 5CH_4 + 4HCO_3$	-8.23
$12\,H_2(aq) + 6\,O_2 \longrightarrow 12\,H_2O$	-131.58
$H_2(aq) + MnO_2 + 2\,H^+ \longrightarrow 2\,H_2O + Mn^{2+}$	-127.58
$H_2(aq) + 0.4\,NO_3{}^- + 0.4\,H^+ \longrightarrow 1.2\,H_2O + 0.2\,N_2$	-126.87
$H_2(aq) + 2\,FeOOH + 4\,H^+ \longrightarrow 4\,H_2O + 2\,Fe^{2+}$	-82.4
$12\,H_2(aq) + 24\,FeOOH + 48\,H^+ \longrightarrow 24\,Fe^{2+} + 48\,H_2O$	-73.88
$H_2(aq) + 0.25\,CO_{32}{}^- + 0.5\,H^+ \longrightarrow 0.75\,H_2O + 0.25\,CH_4$	-35.96
$12\,H_2(aq) + SO_4{}^{2-} + 3\,H^+ \longrightarrow 3\,HS^- + 12\,H_2O$	-32.74
$H_2(aq) + 0.25\,SO_{42}{}^- + 0.25\,H^+ \longrightarrow H_2O + 0.25\,HS^-$	-32.74
$12\,H_2(aq) + 3\,CO_2 \longrightarrow 3\,CH_4 + 6\,H_2O$	-23.22
$H_2(aq) + 0.25\,HCO_{32}{}^- + 0.25\,H^+ \longrightarrow 0.75\,H_2O + 0.25\,CH_4$	-28.69
$CO_2(aq) + 4H_2(aq) \longrightarrow CH_4(aq) + 2H_2O$	-185.76
$MnO_2 + 2\,Fe^{2+} + 2\,H_2O \longrightarrow Mn^{2+} + 2\,FeOOH + 2\,H^+$	-318.32